Contents

Abbreviations and Acronyms

ADC	Analogue-to-Digital Converter
ASK	Amplitude Shift Keying
AWGN	Additive White Gaussian Noise
BER	Bit Error Rate
BPF	Band-Pass Filter
BPSK	Binary Phase Shift Keying
BS	Base Station
cdf	Cumulative Density Function
CDMA	Code Division Multiple Access
CLT	Central Limit Theorem
DAC	Digital-to-Analogue Converter
DFT	Discrete Fourier Transform
DS-CDMA	Direct Sequence Code Division Multiple Access
DSP	Digital Signal Processor/Processing
DS-SS	Direct Sequence Spread Spectrum
FDMA	Frequency Division Multiple Access
FEC	Forward Error Correction
FFT	Fast Fourier Transform
GSM	Global System for Mobile communication
ICI	Inter-Carrier Interference
IDFT	Inverse Discrete Fourier Transform
IFFT	Inverse Fast Fourier Transform
INR	Interference-to-Noise Ratio
i.r.v.	Independent Random Variable
ISI	Inter-Symbol Interference
ISM	Industrial, Scientific and Medical
LOS	Line Of Sight
LPF	Low-Pass Filter
LTE	Long Term Evolution
MAI	Multiple Access Interference
MIMO	Multi-Input Multi-Output
MS	Mobile Station
NBI	Narrowband Interference/Interferer

NLOS	Non-Line Of Sight
OFDM	Orthogonal Frequency Division Multiplexing
OFDMA	Orthogonal Frequency Division Multiple Access
OFDMI	Orthogonal Frequency Division Multiplexing Interference/Interferer
PAPR	Peak-to-Average-Power Ratio
pdf	Probability Density Function
PHY	Physical layer
QAM	Quadrature Amplitude Modulation
QPSK	Quadrature Phase Shift Keying
RF	Radio Frequency
RSS	Received Signal Strength
Rx	Receiver
SC-FDMA	Single Carrier Frequency Division Multiple Access
SER	Symbol Error Rate
SINR	Signal-to-Interference-and-Noise Ratio
SIR	Signal-to-Interference Ratio
SNR	Signal-to-Noise Ratio
TDMA	Time Division Multiple Access
Tx	Transmitter
WCS	Wireless Communication System
WiMAX	Worldwide Interoperability for Microwave Access
WLAN	Wireless Local Area Network
WMAN	Wireless Metropolitan Area Network
WPAN	Wireless Personal Area Network

Nomenclature

a_k	Channel gain for the kth frequency bin for the desired OFDM transmission.
b	The number of data bits per mapped symbol.
c	Speed of light ($\approx 3 \times 10^8$ metres/second).
$D_{i,g}^{(\ell)}$	Complex envelope of the ℓth modulated data symbol of the gth subcarrier of the ith OFDM interfering signal.
D_k	Data modulation of the kth subcarrier for the desired OFDM transmission.
E_b	Energy of data bit.
E_s	Energy of data symbol.
G_i	Number of subcarriers for the ith OFDM interfering system.
$h(t)$	Channel impulse response.
I_k	Post-DFT interference component for the kth frequency bin.
J	Number of interferers.
j	$\sqrt{-1}$.
K	Number of desired OFDM subcarriers set to zero for spectral blanking.
M	QAM level for the desired OFDM signal, e.g. M =2 for BPSK and M =16 for 16QAM mapping schemes.
N	Number of subcarriers for desired OFDM system.
n	Time domain sample index.
P_b	Probability of bit error.
P_b^I	Probability of bit error in the in-phase channel.
P_b^{MC}	Probability of bit error produced by the Monte Carlo numerical model.
P_b^Q	Probability of bit error in the quadrature channel.
P_s	Probability of symbol error.

P_s^I	Probability of symbol error in the in-phase channel.
P_s^{MC}	Probability of symbol error produced by the Monte Carlo numerical model.
P_s^Q	Probability of symbol error in the quadrature channel.
R_k	Post-DFT signal for the kth frequency bin.
r_n	Received, sampled, baseband OFDM signal.
R_s	Symbol rate.
T	OFDM symbol period.
T_g	Period of guard interval or cyclic prefix.
T_s	Period of OFDM data.
Z	QAM level for an interfering OFDM system.
α	Normalised frequency offset between an interfering carrier and an OFDM subcarrier. $\alpha \in [0, 1]$.
$\beta_{i,g}$	Amplitude of the gth subcarrier of the ith OFDM interferer.
Δ	The signal space separation distance between adjacent signal levels as well as the decision thresholds.
$\gamma_k^{(i)}$	The interference-to-noise ratio of the ith interferer at the kth frequency bin.
λ	The wavelength in metres.
ϕ_i	Constant phase offset between the ith OFDM interferer and the desired OFDM signal.
Ψ_k	The spectral leakage component in the kth frequency bin.
τ_i	Time offset between the ith OFDM interferer and the desired OFDM signal.
$\zeta_{i,g}$	Normalised frequency of the gth subcarrier of the ith OFDM interferer.
$\forall$	For all.
$\angle\{\cdot\}$	Complex argument.
$\Im\{\cdot\}$	The imaginary component.
$\Re\{\cdot\}$	The real component.
$\star$	Convolution operator.
$\mathcal{F}\{\cdot\}$	Fourier transform operator.
$\mathcal{F}^{-1}\{\cdot\}$	Inverse Fourier transform operator.
$\wedge$	Logical AND operator.
$\oplus$	Logical exclusive OR operator.

Chapter 1

Introduction

Wireless communications using radio technologies have been around for many decades, but it was cellular telephony that really fuelled their growth. It was in the 1960s that the cellular concept was conceived by AT&T Bell Laboratories, but it was not until the early 1980s that the first commercial cellular systems were launched and they used what is now referred to as first generation (1G) technology, e.g. the U.S. Advanced Mobile Phone System (AMPS) [1–4]. First generation cellular systems used analogue modulation techniques that were designed mainly for voice communications. Second generation (2G) systems, such as the European Global System for Mobile communications (GSM[1]) and the U.S. Interim Standard 95 (IS-95), emerged in the late 1980s and early 1990s and used digital communications technologies; these were more efficient and had larger capacities than first generation systems [5, pp. 4–9]. The technological advancements brought by the 2G cellular systems caused an explosive growth in cellular telephony by the mid 1990s [5, p. 25]. By the late 1990s, third generation (3G) cellular systems (e.g. UMTS[2] and HSPA[3]) were developed and they were designed mainly to send/receive information packets that enable voice and video telephony, internet streaming and file transfer [5, p. 37].

The rapid growth and success of 2G cellular systems proved the robustness of wireless communications and sparked the development of other forms of wireless communication systems and standards. Parallel to the development of 2G and 3G cellular systems in the licensed spectrum, the mid-late 1990s witnessed a growth in the development of wireless systems in the unlicensed radio spectrum, such as wireless local area networks (WLANs) [5, p. 25]. The availability of license-free radio spectra (such as the Industrial, Scientific and Medical (ISM) bands) provides a fertile ground for the development of a multitude of wireless systems and devices for personal and commercial use. The first decade of the 21st century has seen an exponential growth in the demand for high data rate, low cost, robust wireless systems. In response to this insatiable demand for mobile broadband connectivity, wireless systems and standards over the past decade focused on improving spectral efficiency. This dictated the change in the underlying technology from that which is based on Direct-Sequence Spread Spectrum (DS-SS) to ones based on *Orthogonal Frequency Division Multiplexing* (OFDM) [6, p. 2].

[1] GSM originally stood for Groupe Spécial Mobile [5, p. 549].

[2] Abbreviation for Universal Mobile Telecommunications System. Also known as Wideband Code Division Multiple Access (W-CDMA).

[3] Abbreviation for High-Speed Packet Access.

The advantages and benefits that come with OFDM (such as robustness against Inter-Symbol Interference (ISI) and high spectral efficiency) has made it the technology of choice for current and next generation mobile wireless systems. Most contemporary WLANs (e.g. IEEE 802.11n), fourth generation (4G) cellular systems, such as the Long Term Evolution (LTE and LTE-advanced), and wireless metropolitan area networks (WMANs), such as the Worldwide Interoperability for Microwave Access (WiMAX), use OFDM as their physical layer air interface technology [7, 8].

Wireless systems can be categorised by the coverage area they provide; these coverage areas range from the largest, macro-cells, to the smallest, femto-cells. Today, macro-cells are used to provide cellular coverage for large areas (typical radius 1 to 8 km) with low user density (e.g. rural areas) since they operate with relatively high transmit powers [5, pp. 86–96]. As user densities increase, smaller coverage cells are required to provide adequate system capacity through the application of frequency re-use [3]. Therefore, micro-cells are used in urban areas to provide cellular coverage with ranges of several hundred metres [5, pp. 86–96]. However, many wireless applications, such as WLANs and wireless personal area networks (WPANs) require coverage in indoor environments. These in-building environments typically have high user densities, and require even smaller cells (femto-cells) to provide wireless services to the many users typically encountered in in-building environments. It is this growing demand for wireless services in confined spaces of buildings and houses that is motivating research into systems which can provide ever more increasing reliability and performance.

There are, however, several universal limitations to the performance of wireless systems — these include environmental/propagation conditions (e.g. multipath fading), spectral availability, system capacity, user mobility, noise and *interference*. Wireless systems, by virtue of their communications channel being shared, are more prone to interference from neighbouring systems than wired systems. Systems operating in the license-exempt bands are even more susceptible to interference than those operating in licensed bands as it is not generally possible to control sources of interference. There are many forms of interference that a wireless system can be subjected to, such as co-channel interference, adjacent-channel interference, ISI, and multiple access interference (MAI) [5, pp. 67–76]. Of particular interest to the research in this thesis is co-channel interference, where interference takes place when two or more wireless systems use the same frequency band simultaneously (either knowingly or unknowingly).

The proliferation of wireless communication systems (especially in the license-exempt bands) and the increasing popularity of OFDM as a physical layer air interface technology are major motivations for the research presented here. This thesis is primarily focused on analysing the performance of OFDM-based wireless networks in the presence of co-channel interference. There are several metrics that are used to quantify the performance of a communication system; these include symbol and bit error rates[4], outage probability, and data throughput. These performance metrics can be quantified via three major methods:

1. Hardware testing, where the performance metric is measured using a system prototype on hardware;
2. Numerical modelling techniques such as Monte Carlo methods; and
3. Analytical expressions that predict the performance metric based on the system parameters.

[4]Sometimes used interchangeably with probabilities of symbol and bit error, as is the case in this thesis.

Each of these methods has its advantages and drawbacks: hardware testing can be time consuming and laborious but provides accurate results. Numerical modelling can be more convenient than hardware prototyping but depending on the resolution of the numerical model and the scenario parameters, the duration of numerical simulations could take anywhere between a few seconds and several days or longer. Understanding the performance metric patterns and trends can be a case of trial and error when using hardware prototyping and numerical models. Analytical expressions/models, on the other hand, are the most convenient and, typically, the fastest of the three methods. Also, analytical models allow a better understanding of the underlying mechanisms that affect the trends and patterns of the performance metric. The main disadvantage of analytical models is their inherent dependency on the set of assumptions and approximations used to derive them. Also, depending on the set of assumptions used, modelling a communication system analytically can be challenging.

Of particular interest in this thesis is the error rate (symbol and bit) performance of OFDM systems that are subjected to multiple *OFDM* Interferers (OFDMIs). The analysis is comprised of three stages: the first is the development of an accurate, fast and robust *analytical* model that describes the performance of OFDM systems in the presence of multiple interfering sources. The model can be used as a tool for design and optimisation of OFDM-based wireless networks. The second stage is the performance assessment of OFDM systems in indoor environments in the presence of internal and external interfering sources — implications on system deployment strategies are identified by the study. The final stage of the analysis is a qualitative and quantitative performance comparison between OFDM systems and DS-SS systems under identical environmental conditions. Such a comparison is of practical importance to radio engineers and system designers when considering upgrading existing DS-SS networks to OFDM-based ones.

The thesis is structured as follows:

Chapter 2 discusses the spectrum sharing techniques used by wireless systems to mitigate co-channel interference and lists some contemporary wireless communication systems and their various modes of operation. A brief historical background into the development of OFDM and multi-carrier transmission systems is provided. A flavour of current OFDM-related research topics are also presented followed by an outline of the main thesis contributions.

Chapter 3 reviews the technical principles of OFDM system architecture, implementation, advantages and challenges. These include mathematical representations of OFDM signals in the time and frequency domains, the concept of subcarrier orthogonality, ISI mitigation, analogue and digital implementation of OFDM on hardware, and synchronisation techniques.

Chapter 4 reviews the fundamentals of radio wave propagation mechanisms, narrowband and wideband radio channel characterisation techniques and issues, channel impairments, and channel models adopted in this thesis.

Chapter 5 describes the indoor environments considered in the thesis, the RF measurement campaigns conducted over the past decade that provided the channel models used in Chapters 6–9 followed by an overview of the investigation plan of the following chapters.

Chapter 6 derives analytical error rate (symbol and bit) expressions for M-ary QAM OFDM systems in the presence of multiple single-carrier narrowband interferers. The analytical expressions are validated against Monte Carlo numerical methods and the performance of OFDM subjected to narrowband interference is investigated.

The main thesis contributions are presented in Chapters 7–9 where Chapter 7 derives novel analytical error rate (symbol and bit) expressions for M-ary QAM OFDM systems in the presence of multiple Z-ary QAM OFDM interferers. Exact analytical expressions are derived along with analytical approximations that are more computationally efficient. An algorithm is proposed that is a hybrid of two approximation methods that provides fast error rate estimations with sufficient levels of accuracy. The analytical expressions are validated against Monte Carlo numerical methods.

Chapter 8 provides a performance assessment of OFDM systems in indoor environments in the presence of multiple internal OFDM interferers. Performance trends and optimum base station deployment configurations are identified. A performance comparison with DS-SS systems under identical environmental conditions is presented with key observations outlined.

Chapter 9 provides a performance assessment of OFDM systems in indoor environments in the presence of multiple external OFDM interferers. Performance trends are outlined and a performance comparison with DS-SS systems under identical environmental conditions is presented with key observations outlined.

Chapter 10 puts the research presented in this thesis into context with regard to the “big picture”. Recommendations for future work that would enhance and complement the thesis contributions are also presented. Concluding remarks are presented in Chapter 11.

Chapter 2

Wireless Communication Systems and Interference

2.1 Introduction

The performance of wireless communication systems (WCSs) is limited by two key elements: the presence of noise and, more importantly (for cellular systems and similar systems relying on spectrum sharing), the presence of interference in the radio channel [5, p. 67]. A good analogy that can be used to describe the operation and limitations of WCSs is face-to-face conversations. When two people have a conversation, typically, one person talks (analogous to the transmitter) and the other person listens (analogous to the receiver). The person speaking uses a common language (code) that both parties understand and then forms the words (data) using his/her vocal cords and mouth (transmitting antenna); the words, carried by the sound vibrations (carrier signal) travel through the air between the two people (channel) and is picked up the listener's ears (receiving antennas, with spatial diversity) and then comprehended by the listener's brain (decoding). However, if the two people are in an environment where there is a lot of background sound present (e.g. a construction site or a night club with loud music), the other sounds may well impair the listener's ability to hear the words clearly and therefore, the listener might not fully detect and understand all that was said to him/her (detection errors). This inability to correctly detect the conversation as a result of random external transmissions is akin to *noise* in the radio channel. Similarly, when other people, close by, start to have their own conversations, the words originating from the other conversations impair the listener's ability to hear and understand the words intended for him/her (detection errors) — this is akin to *interference* in the radio channel. In a sense, noise and interference have the same effect on a victim WCS, but interference can be viewed as a noise source that is intelligent/adaptive[1].

One way of dealing with noise and, particularly, interference is for the person speaking to speak more loudly (increase transmit power) to enhance the listener's ability to hear and comprehend the spoken words. This technique usually works if the conversation is hindered by noise only; however, when other people are talking nearby (e.g. in a busy night club), the sudden volume increase of one conversation will

[1] In this context, "adaptive" suggests that interference sources can be controlled and regulated. On the other hand, a noise source cannot be regulated, i.e. a noise source does not stop emitting noise due to external influences (e.g. thermal noise).

interfere more severely with the other conversations prompting the other speakers to speak more loudly as well creating a positive feedback loop. Similarly, in WCSs, increasing the transmit power to combat interference is not a very popular or successful technique [5, p. 68].

When two or more WCSs operate using the same spectrum at the same time, *co-channel* interference takes place [9, p. 11] — degrading both/all networks' performance levels. The levels of co-channel interference encountered is dependant on radio spectrum availability, as for WCSs to coexist harmoniously, the radio spectrum has to be *shared* between all these systems. Today, there is a multitude of WCSs in operation such as cellular networks, WLANs, WMANs, WPANs, broadcasting systems, etc. and they all have to coexist with each other with minimal interference effects.

Common techniques used by modern WCSs to share the radio spectrum are discussed in Section §2.2. A brief look at contemporary WCSs in use and their modes of operation is presented in Section §2.3. Section §2.4 presents the development history of multi-carrier transmission systems, including OFDM (the research focus of this thesis) followed by an outline of the thesis contributions in Section §2.5.

2.2 Spectrum Sharing

To avoid co-channel interference, the radio spectrum has to be shared between various wireless systems and users alike. Spectrum sharing is achieved on the system level (to ensure entire systems do not interfere with each and/or the same system does not interfere with itself) and on the user level (allowing users connected a single base station to share the spectrum harmoniously). Spectrum sharing on the system level is achieved via *frequency re-use* and on the user level with *multiple access* techniques.

2.2.1 The Frequency Re-Use Concept

Frequency re-use is very simple conceptually — the usable radio spectrum is divided into several frequency bands such that each base station (BS) uses just a single frequency band *and* neighbouring BSs must not use the same frequency bands [3]. Fig. 2.1 illustrates the concept of frequency re-use where a system spread over a geographic area is serviced by several BSs each assigned a frequency band. The coverage area provided by each BS is called a *cell* and is represented by a hexagonal shape[2]. The configuration in Fig. 2.1 is such that the entire usable spectrum is divided into seven frequency bands and each cell is surrounded by other cells using a different (or adjacent) frequency bands to avoid co-channel interference. To increase system capacity and to service a large geographic area, BSs limit their transmit power to ensure a small cell size. This allows the frequency bands to be reused in other locations such that co-channel cells (cells using the same frequency bands) are separated enough spatially that their signals are sufficiently attenuated by the time they arrive at the other co-channel cells — to use the same analogy as before, this is similar to two people having a conversation while other people are conversing a large distance away so their voices can barely be heard.

Increasing the frequency re-use factor (i.e. the number of frequency bands) increases the distance between co-channel cells, thus improving co-channel interference mitigation. However, increasing the frequency re-use factor reduces the capacity of each cell (since there is less bandwidth) and therefore, cells

[2]The hexagonal geometry of the cells is conceptual only. In reality, the cells are amorphous and their size is dependent on the geographic topography, the antennas used and system requirements [5, p. 58].

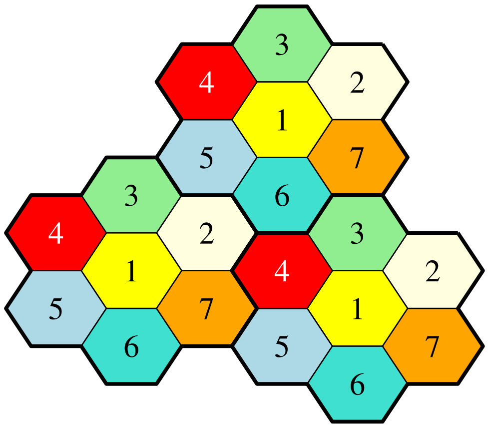

Figure 2.1: Frequency re-use concept illustration (adapted from [5, p. 59]). The frequency re-use factor is 1/7 since each cell contains one-seventh of the total available spectrum bands. Cells with similar numeric value (and colour) use the same frequency bands and are separated geographically to avoid co-channel interference.

are made smaller to support high density systems. While the cell size reduction supports high density wireless systems, it also means that mobile users will cross cell boundaries often (since the cells are small). Every time a mobile user crosses a cell boundary, a *hand-off* process has to be performed that adjusts the mobile device to the frequency band operated by the new cell [10, pp. 363–366]. The hand-off process increases the system complexity and can potentially disrupt the communications link and, therefore, too many hand-offs in a short span of time is not desirable. The frequency re-use concept is often referred to in the literature as the *cellular concept* and is (as the name suggests) the foundation of cellular telephony [3].

2.2.2 Multiple Access Techniques

Given that a finite amount of radio spectrum is allocated to an individual cell, the users connected to that cell have to share that spectrum simultaneously without causing severe degradation to the system performance [5, p. 447]. The methods used to provide multiple users simultaneous access to the finite frequency bandwidth within a cell are called *multiple access* techniques. There are three major multiple access techniques that modern WCSs use frequently: *Frequency Division Multiple Access* (FDMA), *Time Division Multiple Access* (TDMA), and *Code Division Multiple Access* (CDMA)[3].

Frequency Division Multiple Access (FDMA)

In FDMA [5, p. 449–452], each user is allocated an individual slice of the available radio spectrum called a channel as illustrated by Fig. 2.2a. FDMA channels are typically narrowband (30 kHz in AMPS[4]), and once assigned to an individual user, will be unavailable to other users (even if they are not being used) until the termination of the service. Since the channel is allocated for one user for a continuous

[3] There are other forms of multiple access techniques such as space division multiple access (SDMA) and frequency hopping multiple access (FHMA) that are not discussed in this thesis.

[4] Advanced Mobile Phone Service.

period of time, FDMA supports analogue modulation schemes. Tight filtering is required in FDMA systems to minimise interference from adjacent frequency bands (*adjacent-channel* interference). To relax the specifications of the filters needed in FDMA systems, the FDMA channels are typically separated in frequency by a *guard interval* or blank spectrum (not shown in Fig. 2.2a). A subset of FDMA is *Orthogonal*-FDMA (OFDMA[5]) that is popular with modern WCSs and is the focus of the research presented in this thesis. The development history of OFDM/OFDMA are discussed in Section §2.4 and the fundamental principles of OFDM/OFDMA are discussed in Chapter 3.

Time Division Multiple Access (TDMA)

In TDMA [5, p. 453–456], each user is allocated a time slot during which the user transmits and receives data using the cell's entire finite frequency spectrum as illustrated by Fig. 2.2b. The time slots are allocated cyclically to the users and thus the transmission in TDMA systems is non-contiguous, i.e. users transmit in bursts. This means that, unlike FDMA, analogue modulation schemes are not supported and digital modulation schemes are used instead which lead to increased system capacity and spectral efficiency. TDMA systems are more battery efficient than FDMA systems since the user's transmitter is typically switched off when not in use, which is most of the time. Because TDMA transmissions are slotted, the receivers have to be synchronised for each data burst, thus, unlike FDMA, a high synchronisation overhead is required for TDMA systems. Adding to the TDMA overhead are *guard slots*[6], which are necessary to separate users in time. Many WCSs use TDMA including IS-54 (Digital Advanced Mobile Phone System (DAMPS)) and the second generation (2G) cellular system Global System for Mobile communications (GSM).

Code Division Multiple Access (CDMA)

In CDMA [5, pp. 458–459], [11, pp. 479–499], users can transmit using the entire cell's frequency spectrum simultaneously as illustrated by Fig. 2.2c. To avoid Multiple Access Interference (MAI), each user is assigned a unique *spreading code* (also known as a spreading sequence) that is almost orthogonal to all other codes used by the other users — this is analogous to people talking in different languages. The spreading sequence is made up of *chips* and has a chip rate that is several orders of magnitude higher than the user's data rate (i.e. a much wider bandwidth than the original message's). The spreading sequences are sometimes referred to as pseudo-noise sequences since they are specifically designed so that their spectra look like that of noise. Multiple access using spread spectrum via pseudo-noise sequences is called direct-sequence CDMA (DS-CDMA)[7]. The spreading sequences also have special auto and cross-correlation properties [12, 13] such that their auto-correlation produces a very sharp peak and cross-correlation with other spreading sequences would result in virtually nothing.

Each user's data is multiplied by its unique spreading sequence, thus spreading its spectrum, and added to all other users' spread data before being transmitted. At the receiver, the uth user's data is extracted by correlating the received signal (a composite of all the users' spread data) with the same unique spreading code that was assigned to the uth user by the transmitter. The correlation output will comprise of positive

[5]When there is one user, it is called *orthogonal frequency division multiplexing* (OFDM).

[6]Time-domain equivalent to guard intervals in FDMA.

[7]Frequency hopping multiple access (FHMA) also uses spread spectrum but without pseudo-noise sequences.

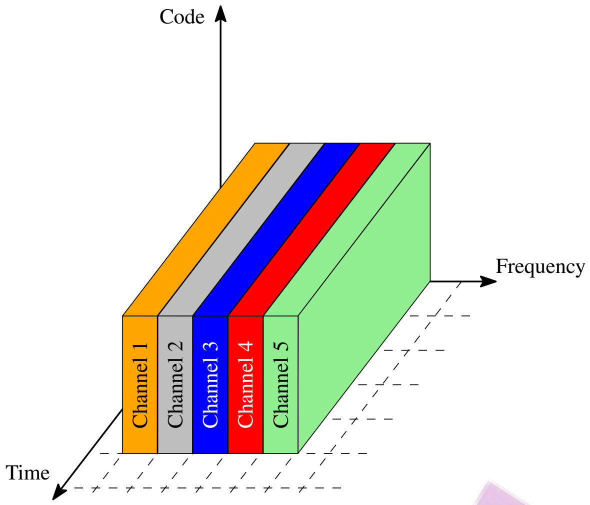

(a) FDMA (adapted from [5, p. 450]).

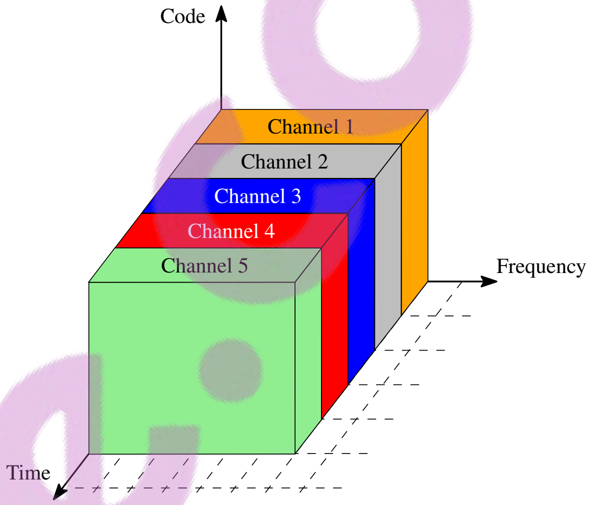

(b) TDMA (adapted from [5, p. 453]).

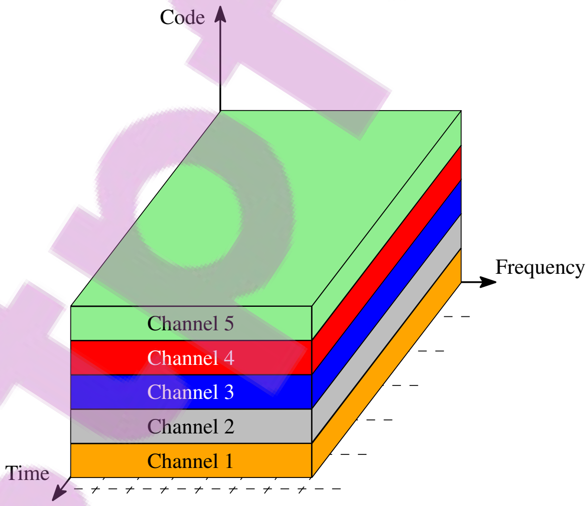

(c) CDMA (adapted from [5, p. 458]).

Figure 2.2: Multiple access techniques. Theoretically, there can be x number of channels, but only five are shown for each scheme.

and negative peaks (representing binary data) at the original data rate, i.e. the received signal is despread using the correlator.

Since the spreading sequences are not 100% mutually-orthogonal, their cross-correlation properties are non-ideal, thus MAI takes place. Unlike FDMA and TDMA, CDMA has a "soft" capacity limit, since servicing additional users raises the noise floor in a linear manner causing uniform performance degradation for all connected users. This means that for DS-CDMA systems, the limit to the number of users that can be supported is a property of the spreading sequences' mutual orthogonality. The ratio of the pseudo-noise sequence's bandwidth to that of the original data is called the *spreading factor* or *processing gain*, G_p. Increasing G_p improves the spreading sequences' mutual orthogonality but at the expense of data rate. DS-CDMA is a popular multiple access technique and many modern WCSs use it such as IS-95 (cdmaOne, 2.5G cellular system), and W-CDMA (3G cellular system).

2.3 Contemporary WCSs and their Modes of Operation

Table 2.1 lists some of the wireless communication systems and standards in operation today. It is worth noting that OFDM is a popular air interface technology, especially among the more recent wireless standards. Many of these wireless standards (e.g. WLANs, WPANs and even cellular systems) operate in indoor environments. Since the early 1990s, the Radio Systems Research Group in the Department of Electrical & Computer Engineering at The University of Auckland has been involved in evaluating wireless system performance in indoor settings and base station deployment optimisation strategies, e.g. [14–17]. However, all these studies focused on DS-CDMA, and thus DS-SS as the air interface technology. The popularity of OFDM coupled with the gap in understanding OFDM system performance in the presence of interference (especially OFDM interference) is a key motivation for the work presented in this thesis.

2.4 Development History of OFDM and Multi-Carrier Transmission Systems

Multi-carrier transmission systems were first developed in the 1960s to support military applications [29–31]. The commercial development of a multi-carrier transmission system where the carriers (also known as *subcarriers* or sub-channels) have overlapping spectra (i.e. an OFDM system[8]) was proposed by Chang [32, 33] and Saltzberg [34] and was then patented in United States in 1970 [35]. To avoid inter-carrier interference (ICI), the subcarriers are designed to be orthogonal to each other, hence the name *orthogonal* frequency division multiplexing (OFDM).

While the theory of OFDM was promising, there were challenges to its realisation. The complexity of the equipment needed to implement OFDM in the late 1960s (namely, the number of filters and modulators) was the main objection to its widespread use [19, p. 25]. In 1971, Weinstein and Ebert [36] proposed a method of implementing a discrete OFDM system using the discrete Fourier transform (DFT) which

[8]Technically, a FDMA system is a multi-carrier transmission system but the subcarriers do not have overlapping spectra.

Table 2.1: Summary of some contemporary wireless systems and standards [5, 18–20].

System/Standard	Type	Number of Carriers	Bandwidth (MHz)	PHY Protocol	Carrier Frequency (GHz)	Peak Data Rate (Mbps)
IEEE 802.11a [21]	WLAN	64	20/channel	OFDM	5	54
IEEE 802.11b [22]	WLAN	1	20/channel	DS-SS	2.4	11
IEEE 802.11g [23]	WLAN	64	20/channel	OFDM	2.4	54
IEEE 802.11n [24]	WLAN	128	40/channel	MIMO-OFDM	2.4, 5	600
GSM (2G)	Cellular	1	20	TDM	0.89 - 0.96	0.27/channel
W-CDMA (3G)	Cellular	1	5/channel	DS-SS	1.9 - 2.1	9
DAB [25]	Broadcast	192, 384,768, 1536	1.5/channel	OFDM	0.2 - 3	1.18
DVB-T2 [26]	Broadcast	1705, 6817	8/channel	OFDM	0.47 - 0.682	50
Bluetooth (IEEE 802.15.1) [27]	WPAN	1	83.5	FH-SS	2.4	1
ZigBee (IEEE 802.15.4)	WPAN	1	83.5	DS-SS	2.4	0.25
WiMAX (IEEE 802.16e) [8]	WMAN	128, 256, 512, 1024, 2048	20/channel	MIMO-OFDM	2.5 (US)	128
LTE (3.9G) [7], [28]	Cellular	12/ resource block	1.4, 3, 5, 10, 15, 20/channel	MIMO-OFDM & SC-FDM (uplink)	1.8 (Australia)	300 (4×4 MIMO)

greatly reduced the system complexity. Using the system proposed in [36], frequency division is achieved by baseband processing (as opposed to bandpass filtering) that can be easily implemented in the digital domain. In the 1980s, Hirosaki [37,38] developed methods of applying DFT to OFDM with multiplexed quadrature amplitude modulation (QAM).

The rise of OFDM as a popular physical layer air interface technology began in the 1990s with the advancements in digital signal processing techniques. Today, there are several standards and systems that use OFDM as their physical layer interface technology and they include [39, p. 636], [6, p. 2],

- Wired Systems
  - Very high bit rate digital subscriber line (VDSL);
  - Asymmetric digital subscriber line (ADSL);
  - Digital video broadcasting - cable (DVB-C and DVB-C2); and
  - Power-line digital subscriber line (PDSL).
- Wireless Systems (refer to Table 2.1)
  - Wireless local area networks (WLANs), such as IEEE 802.11a, IEEE 802.11g, IEEE 802.11n and the European high performance radio local area network (HIPERLAN/2);
  - Digital audio broadcasting (DAB and DAB+);
  - Terrestrial digital video broadcasting (DVB-T and DVB-T2);
  - Wireless personal area networks (WPANs), such as the ultra-wideband (UWB) IEEE 802.15a;
  - Wireless metropolitan area networks (WMANs), such as the worldwide interoperability for microwave access (WiMAX); and
  - Cellular systems, such as the 3rd Generation Partnership Project (3GPP) long term evolution (LTE and LTE-advanced).

OFDM is one of the most active areas of research today. Some of the current OFDM research areas in the literature, include: multi-input multi-output (MIMO) OFDM (e.g. [40–44]), interference analysis and mitigation/cancellation (e.g. [45–52]), coding and equalisation techniques (e.g. [53–58]) and synchronisation (e.g. [59–64]). Due to this emergence of OFDM technology in the wireless communications arena, it is important to evaluate the performance and reliability of OFDM based wireless systems in typical indoor environments since many OFDM based systems are used in indoor settings nowadays. The ability to evaluate the performance of OFDM in in-building environments gives radio engineers and system designers a powerful tool to optimise the deployment of wireless nodes in such environments to maximise coverage, speed and reliability of indoor wireless communications.

2.5 Thesis Contributions

The research presented in this thesis is focused on analysing the performance of OFDM-based wireless systems in the presence of interference. Two main interference sources are considered in this thesis:

the first are single-carrier narrowband interferers (NBIs). The second is OFDM interference (OFDMI), particularly same-type OFDMI (i.e. the interfering OFDM system is the same as the desired one, e.g. both are IEEE 802.11g WLANs).

There are three major research goals/objectives for this thesis:

1. To provide raw *analytical* error rate expressions (both symbol and bit error rates) for OFDM systems in the presence of multiple NBIs and same-type OFDMIs that are accurate, fast, robust and efficient. These analytical error rate expressions (also referred to as the analytical model) are developed to be *independent* of the other system stages (e.g. channel model, synchronisation algorithm, forward error correction (FEC) code, interleaving algorithm, and signal diversity scheme). This way, the analytical model is independent of the OFDM standard (e.g. WiMAX or IEEE 802.11g, etc.) and thus, is more useful and universal. This flexibility allows the model to be used as an integral block/module of a larger OFDM system model that encompasses all the other features (i.e. a model for a particular OFDM standard) — Table 2.2 puts this thesis contribution in context with similar prior works in the literature;

2. To provide indicative performance assessment analyses of OFDM-based wireless networks in indoor environments using the derived analytical model. In those environments, internal and external interfering sources are considered. Two architecturally different indoor environments are considered in this thesis. The channel models for these environments are modelled using real RF propagation measurements from two previous measurements campaigns conducted at The University of Auckland. The analyses also identify the implications on system deployment strategies; and

3. To provide performance comparisons between OFDM and DS-SS networks under identical environmental conditions. Understanding the OFDM interference mechanisms and comparing them to the well-understood DS-SS interference mechanisms is important when

   (a) An existing DS-SS network is to be replaced/upgraded by an OFDM-based network. Differences in performance levels might result in the redeployment of the network's base stations.

   (b) A new OFDM network is deployed. Could the well-understood DS-SS error rate expressions be used to model an OFDM system performance with acceptable levels of accuracy?

These research outcomes (analytical models, indicative performance assessment studies, and comparison with DS-SS systems) provide radio engineers and system planners a detailed understanding of the behaviour of OFDM wireless networks in the presence of co-channel interference (through theory and results) along with the tools needed to acquire such an understanding. This enables the deployment and system optimisation of OFDM wireless networks.

2.6 Summary

In this chapter, a major limitation on the performance of wireless communication systems is identified — interference, particularly co-channel interference. The presence of co-channel interference also restricts

Table 2.2: Thesis contributions in context with similar prior work. $h(t)$ is the channel impulse response.

Work	Year	Desired System	Interference	Interference Modulation	FEC Code & Interleaving	Channel	Additional Notes
[45]	2006	BPSK-OFDM	Multiple NBIs (tones)	None	None	AWGN	Mitigation techniques included. Analysis in Chapter 6 is an extension of this work.
[65]	2007	M-ary QAM MB-OFDM	Multiple NBIs (tones)	None	Convolutional codes with interleaving	AWGN + correlated Rayleigh fading	Mitigation techniques included.
[66]	2009	QPSK-OFDM	Single NBI (Gaussian energy)	None	Binary linear block codes	AWGN + $h(t)$	Spectral leakage not considered.
[47]	2009	BPSK, QPSK MB-OFDM	Single WiMAX (SC and OFDM)	BPSK, QPSK	Bit interleaved modulation	AWGN + $h(t)$ + single tap channel for interference	Filter bank model for OFDM. Laplace transform & Gauss Chebyshev rule for BER calculation. Mitigation techniques considered.
[67]	2010	QPSK, 64QAM WiMAX OFDM	Single MB-OFDM	QPSK, 64QAM	Reed-Solomon (outer) + punctured convolutional code (inner)	AWGN + Rayleigh fading	Inversion theorem and characteristic functions are used to derive closed-form BER. Measurements conducted.
Thesis	*2011*	*Square M-ary QAM OFDM*	*Multiple NBIs (tones) + multiple OFDMIs*	*None for NBIs & square Z-ary QAM for OFDMIs*	*None — can be easily extended to include FEC.*	*AWGN + effective SIR (i.e. independent of channel model)*	*Same-type OFDMI. Rapid algorithm with high accuracy included.*

the usability of the radio spectrum and thus wireless communication systems have to share the spectrum to coexist harmoniously. Techniques and methods used to share the radio spectrum include frequency re-use (also known as the cellular concept) that allows the usage of the same radio spectrum simultaneously at non-adjacent geographic locations called cells. Multiple access techniques (including FDMA, TDMA and CDMA) are used to share the spectrum within the cell between users.

Many of the current wireless systems and standards employ OFDM as their physical layer air interface technology which are a special type of FDM. The popularity of OFDM is one of the key motivations for the research presented in this thesis.

There are three major research objectives for this thesis: the development of raw analytical error rate expressions for OFDM systems in the presence of multiple narrowband and OFDM interferers; the performance assessment of OFDM-based wireless networks in indoor environments with internal and external interfering sources; and a performance comparison between OFDM and DS-SS systems. The principles, architecture and implementation of OFDM along with its advantages and challenges are presented in Chapter 3.

Chapter 3

OFDM Fundamentals

3.1 Introduction

In Chapter 2, the history and development of multi-carrier communication systems (such as OFDM) was discussed. The popularity of OFDM as a physical layer air interface for a variety of modern WCSs both in licensed and unlicensed spectrum has made it the focus of the research presented in this thesis.

This chapter provides a foundation for the technical principles of OFDM that are needed in the latter chapters of this thesis (Chapters 6–9). In Section §3.2, the principles of OFDM are presented: mathematical concepts describing OFDM signals in both time and frequency domains, carrier orthogonality and traditional implementation on hardware. Section §3.3 extends this by introducing the fundamental principles of implementing OFDM digitally as well as synchronisation techniques for OFDM systems.

3.2 What is OFDM?

As mentioned in Section §2.2.2, OFDM can be regarded as a special case of FDM. The only difference between the two multiplexing schemes is that in OFDM the sub-channels (also called subcarriers) have overlapping spectra. Fig. 3.1 shows the frequency spectra of a communication system using FDM (Fig. 3.1a) and OFDM (Fig. 3.1b) multiplexing schemes. The subcarriers' spectra overlap in OFDM saving bandwidth relative to an equivalent FDM system. To prevent the subcarriers from interfering with each other (i.e. inter-carrier interference (ICI[1])), OFDM subcarriers have to be mutually *orthogonal*. The principles of subcarrier orthogonality are discussed in Section §3.2.2.

3.2.1 OFDM Signals in the Time and Frequency Domains

A baseband OFDM signal, $s\left(t\right)$, can be represented as the superposition of N subcarriers each with its own amplitude, A_k, frequency, f_k, and phase, ϕ_k [39, p. 638], [18, p. 353]

[1]Also known as multiple access interference (MAI), or multi-user interference (MUI).

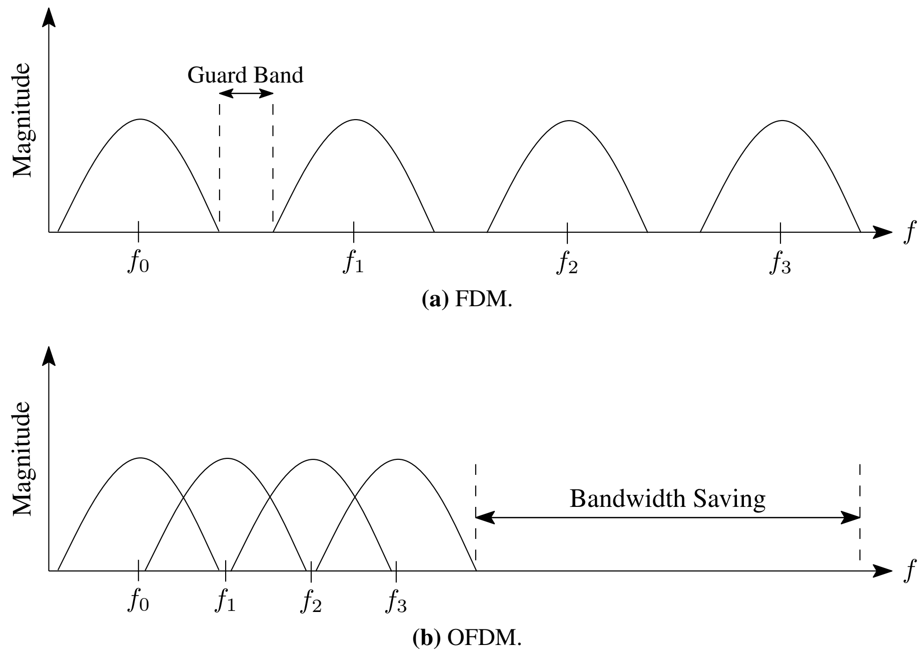

Figure 3.1: FDM and OFDM multiplexing techniques (adapted from [68, p. 5]). OFDM spectrum overlap is feasible when the subcarriers are mutually orthogonal resulting in ICI-free performance.

$$\begin{aligned} s(t) &= \sum_{k=0}^{N-1} s_k(t) \\ &= \sum_{k=0}^{N-1} A_k \cos(2\pi f_k t + \phi_k), \qquad 0 \leq t \leq T \end{aligned} \tag{3.1}$$

where T is the symbol period. Fig. 3.2 shows typical OFDM signals in the time domain with Quadrature Phase Shift Keying (QPSK) and 16QAM signal mapping schemes. The time domain amplitudes of the OFDM signals are normalised to the maximum amplitude of an individual subcarrier. It is observed in Fig. 3.2, that the amplitudes of the OFDM subcarriers sometimes add up constructively resulting in a relatively high composite amplitude value (close to seven times the maximum amplitude of an individual subcarrier in this example). This phenomenon means that the OFDM signal has a high *peak-to-average power ratio* (PAPR) which can have a detrimental effect on the transmission of OFDM signals as discussed in Section §3.3.3.

Fig. 3.3 illustrates the spectrum of an OFDM signal normalised to the maximum amplitude of an individual subcarrier[2]. While the spectra of the individual subcarriers overlap (as in Fig. 3.3a) at the ith subcarrier frequency, f_i, the amplitudes of all subcarriers with frequencies $f_k \neq f_i$ are zero. These nulls are a direct consequence of mutual subcarrier orthogonality and ensure that while the spectra of the subcarriers overlap, no ICI takes place.

[2]The sinc shape of the subcarriers' spectra is a result of windowing the time-domain signal with a rectangular pulse window function.

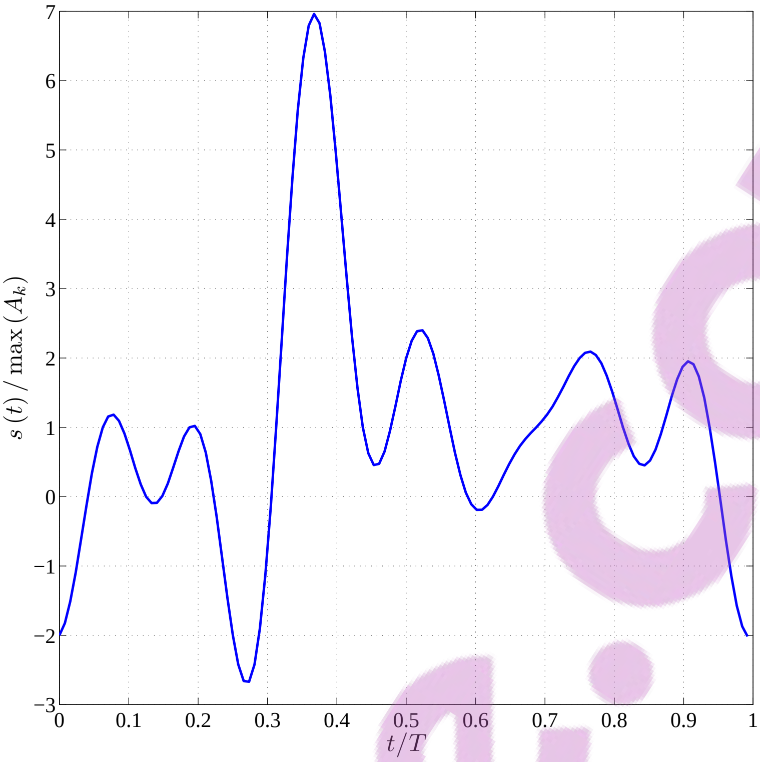

(a) Example of a QPSK-mapped OFDM signal.

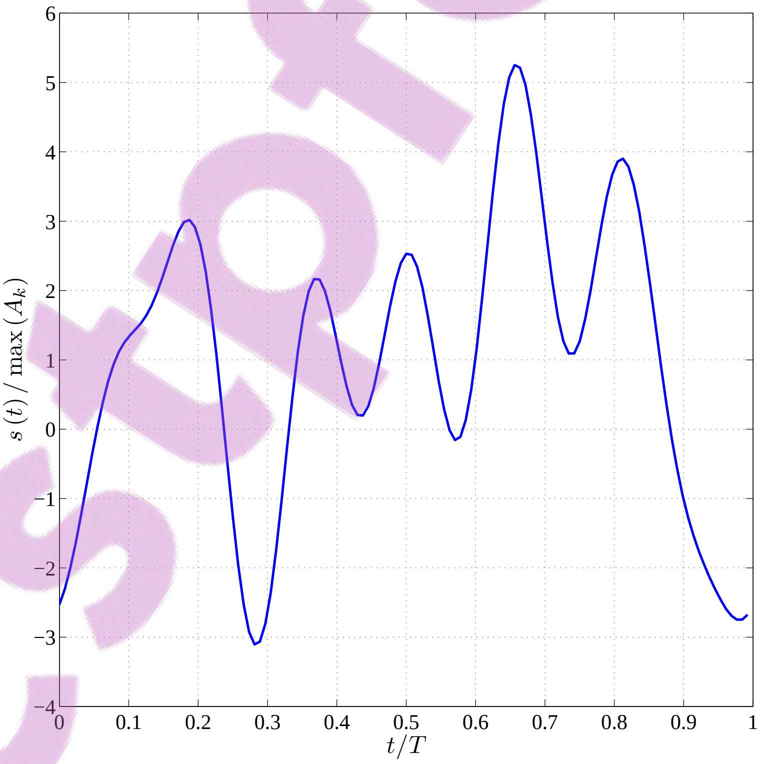

(b) Example of a 16QAM-mapped OFDM signal.

Figure 3.2: Examples of baseband OFDM signals in the time domain with eight subcarriers. The amplitudes are normalised to the maximum amplitude of an individual subcarrier. The subcarriers add like phasors to produce a resultant signal given by the waveforms shown here. There are no particular patterns related to the signal mapping scheme used in either plots.

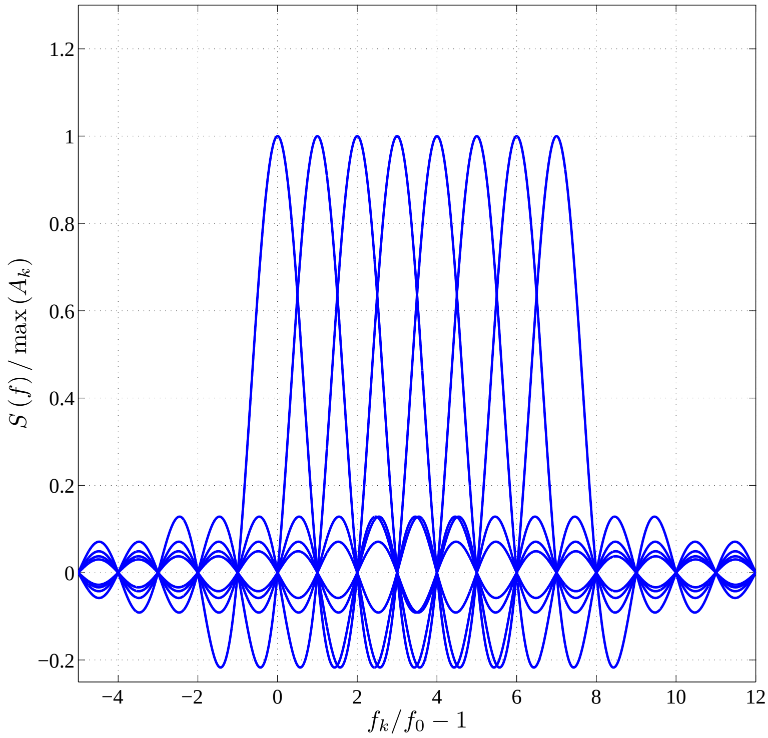

(a) Spectrum of individual OFDM subcarriers. Note that all subcarriers with frequencies $f \neq f_k$ have nulls at f_k because of subcarrier orthogonality, which ensures ICI-free performance.

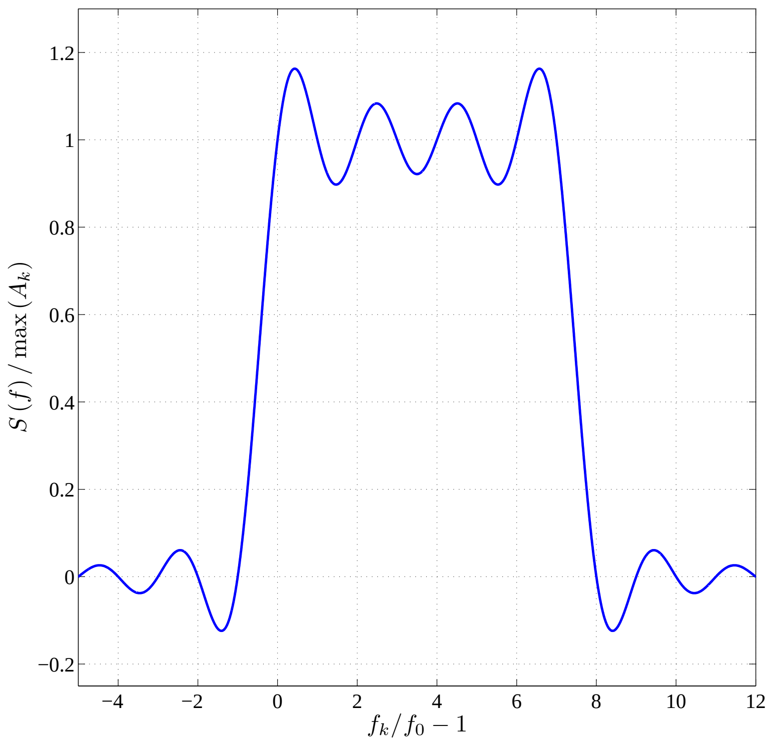

(b) Composite spectrum of OFDM signal.

Figure 3.3: Baseband OFDM signal in the frequency domain with eight subcarriers. f_0 is the frequency of the first subcarrier.

3.2.2 Orthogonality

Fundamentally, two functions, $\varphi_i(t)$ and $\varphi_j(t)$, will be orthogonal to each other over the time interval $0 \leq t \leq T$, if they satisfy the condition [11, p. 311]

$$\int_0^T \varphi_i(t)\,\varphi_j(t)\,dt = \begin{cases} C & i = j \\ 0 & i \neq j, \end{cases} \tag{3.2}$$

where C is a constant. For OFDM subcarriers to be mutually orthogonal, it is sufficient to define f_k to be in integer multiples of the the symbol rate, $R_s = 1/T$, and spaced in frequency by R_s [39, p. 638], i.e.

$$\begin{aligned} f_k &= kR_s \\ &= \frac{k}{T} \qquad k = 0, 1, 2, \ldots N-1. \end{aligned} \tag{3.3}$$

Applying the orthogonality condition in (3.2) to two OFDM subcarriers defined in (3.1) with frequencies set according to (3.3), yields

$$\int_0^T s_i(t)\,s_j(t)\,dt = \int_0^T A_i \cos(2\pi f_i t + \phi_i)\,A_j \cos(2\pi f_j t + \phi_j)\,dt$$

$$= \begin{cases} A_0^2 T \cos^2(\phi_0) & i = j = 0 \\ \frac{1}{2} A_i^2 T & i = j \neq 0 \\ 0 & i \neq j. \end{cases}$$

Therefore, setting the subcarriers' frequencies according to (3.3) will ensure orthogonality between the subcarriers and allow spectrum overlap to take place without the risk of ICI. However, there are external factors that can compromise the orthogonality of the subcarriers, such as inter-symbol interference (ISI). ISI is a phenomenon that takes place in wireless environments and is caused by multipath signal propagation (multipath propagation is discussed in Section §4.3.1).

3.2.3 Inter-Symbol Interference and its Mitigation

In a wireless environment, a receiver would receive multiple versions of the transmitted signal[3]: a direct signal or a line-of-sight (LOS) component (if there is a LOS path) and multiple indirect or non-line-of-sight (NLOS) components. These NLOS components exist due to the presence of objects and obstacles in the environment, which cause the transmitted signal to reflect, refract, and/or diffract of their surfaces/edges. Multiple copies (also called echoes) of the transmitted signal will arrive at the receiver's antenna at different times (due to the different path lengths they have travelled) and with different strengths (due to the attenuation effects of the distances travelled and the properties of the obstacles they

[3] In a free-space or fixed point-to-point (with directional antennas) situation, the receiver would receive just one signal.

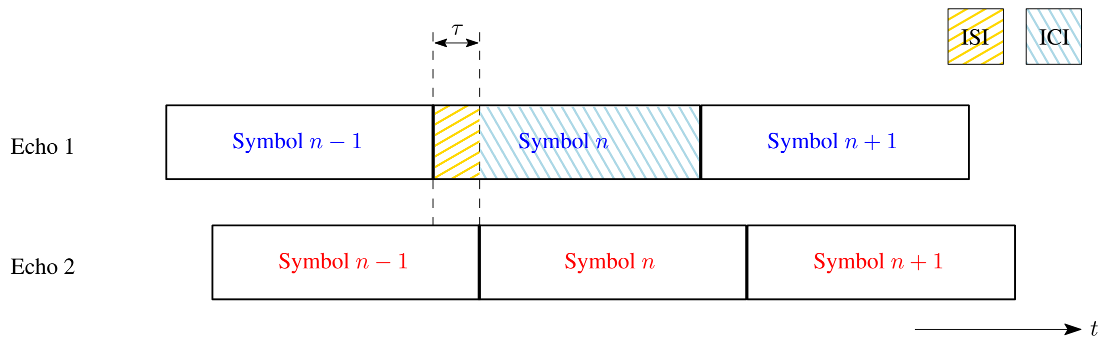

Figure 3.4: Two copies of the transmitted signal arrive at different times, causing ISI. τ is the relative delay between the two echos.

encountered in their paths[4]). This means that several copies of the transmitted signal will arrive at the receiver with different time delays.

As seen in Fig. 3.4, due to the relative delay between the copies of the transmitted signal (i.e. echoes 1 and 2), Echo 2's Symbol $n-1$ is overlapping with the Echo 1's Symbol n. This is direct interference and is labelled as ISI. The two echoes will add as phasors causing amplitude fluctuations. These time delays create phase offsets which cause the nulls in the signals' spectra to no longer align with each other, causing ICI (between Echo 1's Symbol n and Echo 2's Symbol n). Therefore, for an OFDM system, ISI poses two problems: the first of which is that ISI causes direct interference with the received data. The second is that the presence of ISI degrades subcarrier orthogonality causing ICI as well, meaning poorer performance or outages depending on the severity of the situation.

The question now arises as to how ISI might be avoided. It should be noted that OFDM systems, by their very architecture, are naturally resistant to ISI. This is because an OFDM system with N subcarriers occupying a bandwidth of B Hz will have a symbol period N times longer than a single-carrier transmission system with the same bandwidth. The time delays are governed by the *channel impulse response*, $h\,(t)$, which has a finite length. So, by making the symbol period considerably longer than the length of the channel impulse response or channel delay spread (defined in Chapter 4), the effects of ISI are minimised.

However, if a *guard interval* (GI) (of appropriate length and does not contain OFDM data), is inserted at the start of the OFDM symbol, ISI can be removed completely. Therefore, the OFDM symbol period becomes $T = T_g + T_s$, where T_g is the length of the GI and T_s is the duration of the OFDM data. Fig. 3.5 shows two OFDM signal echos with GIs. To ensure that ISI is removed completely, T_g must be longer than the length of $h\,(t)$ [39, p. 672]. By making T_g longer than the length of $h\,(t)$, $\tau \leq T_g$ will always be true. This arrangement, ensures that the ISI would always occur during the GI of the desired symbol, and since the GI does not contain any data, the effect of ISI becomes harmless as illustrated by Fig. 3.5. However, GIs do not remove the ICI generated by the delayed arrival of the echos; the channel equaliser at the receiver is used to ameliorate the effects of ICI. The overhead of having GIs reduces the efficiency of the OFDM system, since without GIs $T_s = T$ but with GIs $T_s < T$, meaning slower data rates.

Most OFDM systems in practice, though, do not use blank GIs; instead, they use a *cyclic prefix* (CP) [39, p. 672]. A CP is a GI that contains the last T_g data samples of the OFDM symbol data as illustrated by

[4]Signal propagation is discussed further in Chapter 4.

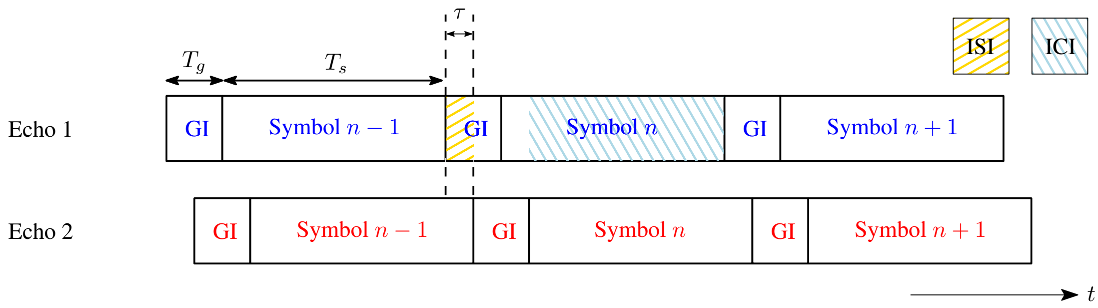

Figure 3.5: OFDM symbols with guard intervals.

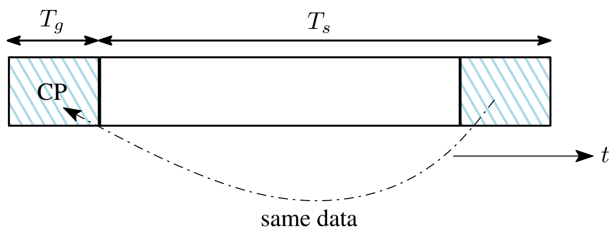

Figure 3.6: OFDM symbol with a cyclic prefix.

Fig. 3.6. CPs remove ISI just as efficiently as blank GIs but have other benefits to the OFDM system that are discussed later in Section §3.3.

3.2.4 Generating and Receiving OFDM Signals

In practical wireless systems, a baseband OFDM signal is upconverted to radio frequency (RF) and all the subcarrier frequencies will be centred around the RF carrier frequency, f_c, according to [39, p. 644]

$$f_k = f_c - \frac{N-1}{2T} + \frac{k}{T} \qquad k = 0, 1, 2, \ldots N-1.$$

Therefore, the bandpass OFDM signal, $s_{\mathrm{BP}}(t)$, can be expressed as

$$s_{\mathrm{BP}}(t) = \sum_{k=0}^{N-1} A_k \cos\left[2\pi\left(f_c - \frac{N-1}{2T} + \frac{k}{T}\right)t + \phi_k\right] \qquad 0 \le t \le T.$$

It should be noted that the subcarriers are not required to be mutually orthogonal in the RF bands, since demodulation is performed at baseband [39, p. 644]. One method of constructing an OFDM modulator and demodulator (modem) is to use discrete oscillators, multipliers and correlators [32–35]. Fig. 3.7 shows the core stages of an analogue OFDM modem. At the transmitter (Fig. 3.7a), the serial data *bit* stream is first split into N parallel streams by a 1:N serial-to-parallel converter, then the parallel data are mapped according the desired modulation/mapping scheme[5] (e.g. BPSK, QPSK, 16QAM, etc.) in the mapper block. The mapped *symbols* are denoted by

$$D_k = A_k e^{j\phi_k}, \tag{3.4}$$

[5]Modulation refers to the process of upconversion and sometimes to data mapping. Throughout this thesis, the term “modulation” will be used interchangeably with signal mapping schemes (e.g. BPSK, QPSK, etc.). That is, the statements “the signal is BPSK-modulated” and “the signal is BPSK-mapped” have the same meaning.

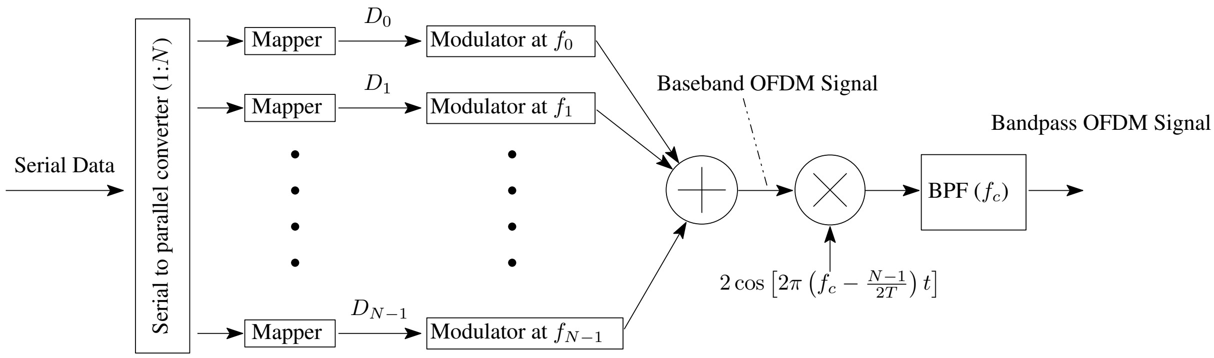

(a) Transmitter/Modulator.

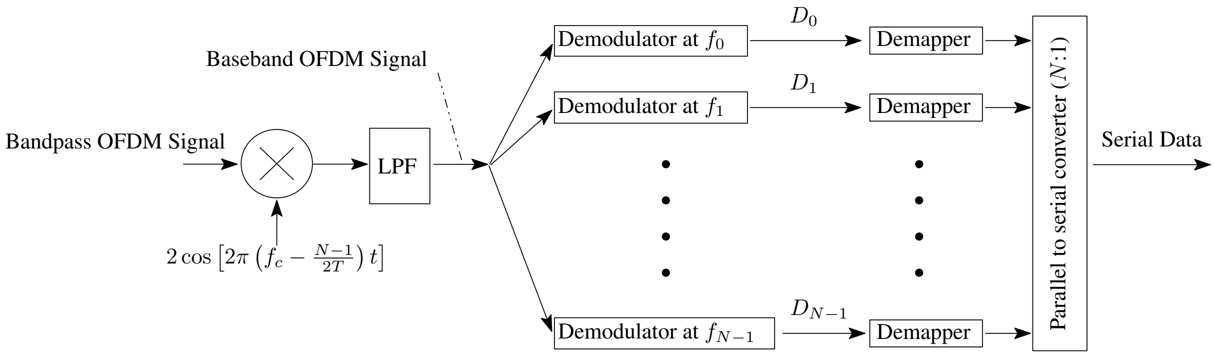

(b) Receiver/Demodulator.

Figure 3.7: Basic analogue OFDM modem (Adapted from [39, p. 650]).

where A_k and ϕ_k are determined by the mapping scheme used for the kth subcarrier. One of the features of OFDM systems is that different subcarriers can have different mapping schemes and are, therefore, independent of each other [69–72]. The mapped symbols are then modulated at their designated frequencies according to the expression in (3.3). The modulated subcarriers are then added together and upconverted to the RF band. The bandpass signal is then filtered using a bandpass filter (BPF), whose centre frequency is the RF carrier frequency, f_c, to remove the undesired harmonics that were created as a result of the upconversion process. The bandpass OFDM signal is then transmitted into the channel.

At the receiver (Fig. 3.7b), the reverse process of what happens in the transmitter takes place. The bandpass OFDM signal is down-converted to baseband, then the undesired harmonics are filtered out by a lowpass filter (LPF). The baseband OFDM signal is then demodulated at each subcarrier frequency, each demodulator consists of local oscillators, multipliers, integrators and threshold detectors. The data for each subcarrier is then demapped according the mapping scheme used for that subcarrier. The demapped data bits are then passed through an N:1 parallel-to-serial converter.

However, analogue OFDM modems have significant limitations. For instance, when N is large, the number of components for the transmitter and receiver will be large as well, which can be impractical to implement. The main practical issue raised in [32–35] is the inclusion of filters in the modulator and demodulator to maintain subcarrier orthogonality. For the filters to maintain subcarrier orthogonality, the filters' frequency responses must meet strict requirements [39, p. 651]. Implementing an OFDM modem using oscillators, multipliers and correlators is deemed too complex and impractical and thus analogue modems are not in use today. The next section will discuss how OFDM modems are implemented in modern communication systems.

3.3 Implementation of OFDM in Modern Communication Systems

3.3.1 OFDM Digital Modem

In 1971, Weinstein and Ebert [36] proposed a method of implementing a *discrete* OFDM modem. However, it was not until the mid 1990s that advances in digital signal processing (DSP) techniques allowed the implementation of the discrete modem in the *digital* domain [73, p. 23]. Recall the expression for baseband OFDM signals in the time domain, Equation (3.1):

$$\begin{aligned} s(t) &= \sum_{k=0}^{N-1} A_k \cos\left(2\pi f_k t + \phi_k\right) \\ &= \sum_{k=0}^{N-1} \Re\left\{A_k e^{j(2\pi f_k t + \phi_k)}\right\} \\ &= \Re\left\{\sum_{k=0}^{N-1} A_k e^{j\phi_k} e^{j2\pi \frac{k}{T} t}\right\} \\ &= \Re\left\{\sum_{k=0}^{N-1} D_k e^{j2\pi \frac{k}{T} t}\right\} \qquad 0 \le t \le T, \end{aligned} \tag{3.5}$$

where $\Re\{\cdot\}$ denotes the real component. Accordingly, the bandpass OFDM signal can be written as

$$s_{\text{BP}}(t) = \Re\left\{\left(\sum_{k=0}^{N-1} D_k e^{j2\pi \frac{k}{T} t}\right) e^{j2\pi\left(f_c - \frac{N-1}{2T}\right)t}\right\} \qquad 0 \le t \le T, \tag{3.6}$$

and the complex envelope of (3.6), $\widetilde{s}(t)$, is given by

$$\widetilde{s}(t) = \sum_{k=0}^{N-1} D_k e^{j2\pi \frac{k}{T} t} \qquad 0 \le t \le T. \tag{3.7}$$

Therefore, the baseband time domain OFDM signal given in (3.5) is the real part of the complex envelope of the bandpass OFDM signal, i.e. $s(t) = \Re\{\widetilde{s}(t)\}$. However, if $\widetilde{s}(t)$ is sampled with a period of $\Delta t = T/N$, and a normalising factor of $1/N$ is applied [39, p. 651], the sampled baseband OFDM signal, s_n, becomes

$$s_n = \frac{1}{N} \sum_{k=0}^{N-1} D_k e^{j2\pi n \frac{k}{N}} \qquad n = 0, 1, 2, \ldots N-1, \tag{3.8}$$

where n is the time domain sample index. The expression in (3.8) is an inverse discrete Fourier transform (IDFT), and this can be used to generate samples of the complex envelope of an OFDM signal [31,36,37]. At the receiver, the data symbols, D_k, can be recovered by using the discrete Fourier transform (DFT), i.e.

$$D_k = \sum_{n=0}^{N-1} s_n e^{-j2\pi n \frac{k}{N}} \qquad k = 0, 1, 2, \ldots N-1. \tag{3.9}$$

The DFT and its inverse operations are performed using the fast Fourier transform (FFT) and inverse FFT (IFFT) [39, p. 652]. The use of the IFFT/FFT pair greatly reduces the complexity of the OFDM modem. A block diagram of an OFDM system implementation using IFFT/FFT is shown in Fig. 3.8.

At the transmitter (Fig. 3.8a), the serial data bit stream is passed through a 1:$N-K$ serial-to-parallel converter, where K is the number of *virtual* subcarriers (subcarriers that are set to zero, i.e. carry no data) that are used for *spectral blanking*. Spectral blanking is needed for two reasons: the first is to reduce the risk of *aliasing*[6] [37], and the second is to allow the use of non-ideal lowpass filters in the digital-to-analogue converter (DAC) to obtain distortion-less analogue signals [39, p. 656].

After the serial data bit stream is passed through the 1:$N-K$ serial-to-parallel converter, the data streams are mapped according to the mapping scheme of each subcarrier. K virtual subcarriers are then added to the mapped symbols and all N parallel streams are passed thorough an N-point IFFT block (e.g. an 802.11a/g WLAN has $N = 64$ and $K = 12$ [21, 23]). A cyclic prefix is then added to the output of the IFFT (N modulated subcarriers) and then converted into a serial stream via an N:1 parallel-to-serial converter. The serial stream is then split into real and imaginary components, $\Re\{s_n\}$ and $\Im\{s_n\}$, respectively. The data in $\Re\{s_n\}$ and $\Im\{s_n\}$, respectively, represent the data in the *in-phase* (I-) and *quadrature* (Q-) channels. The I- and Q-data are then passed through a DAC, upconverted into an intermediate frequency (f_{IF}), added and upconverted to the RF frequency (f_c). The bandpass OFDM signal is then passed through a BPF (centred at f_c) before being transmitted into the channel.

At the receiver (Fig. 3.8b), the bandpass OFDM signal is downconverted to an intermediate frequency (f_{IF}) then passed through a BPF centred at f_{IF}. The signal is then split into its I- and Q-channels, downconverted to baseband, filtered and then passed through an analogue-to-digital converter (ADC). The digital I and Q data are added together and the CP is removed. The data is then passed through a 1:N serial-to-parallel converter before passing through an N-point FFT block. The virtual subcarriers are then removed and the parallel streams of symbols are demapped according to the mapping scheme for each subcarrier. The demapped bits are then passed through an $N-K$:1 parallel-to-serial converter.

The use of the IDFT at the transmitter means that each subcarrier will have an integer number of samples in the time domain. This feature allows the CP to provide limited protection against time offsets. As mentioned in Section §3.2.3, the OFDM symbol period, T, is given by $T = T_s + T_g$ where T_s is the period of the OFDM data (and is equal to the period of the IDFT) and T_g is the period of the CP. The CP is essentially the last T_g samples of T_s. To demodulate the data correctly, the receiver only requires

[6]The aliasing issue arises from the fact that the baseband OFDM signal in (3.5) is sampled at a rate of $\Delta t = T/N$ as in (3.8); but the double sideband bandwidth of (3.5) is $2N/T$ [39, p. 641]. Therefore, to avoid aliasing, the sampling rate should be greater than or equal to $2N/T$ [37]. One simple solution is to double the number of samples to $2N$ by *padding* the data with N zeros and using a $2N$-point IDFT at the transmitter and an N-point DFT at the receiver [37]. However, this method is wasteful of bandwidth and is replaced by another approach that uses an N-point IDFT at the transmitter *twice* to generate the real and imaginary components and an N-point DFT at the receiver twice to demodulate the data [37, 38]. While this approach does not waste bandwidth, it doubles the processing time. It was later proposed in [74] that shifting the DFT pair index range from $[0, N-1]$ to $[-N/2, N/2-1]$ will change the double sideband bandwidth of the baseband OFDM signal to $(N+2)/T$, which asymptotically satisfies the Nyquist rate as $N \to \infty$, since the sampling rate is N/T for a signal with double sideband bandwidth of $(N+2)/T$. However, for convenience, the indexing of the IDFT/DFT pair will be labelled as $[0, N-1]$ throughout this thesis with the exception of Fig. 3.8.

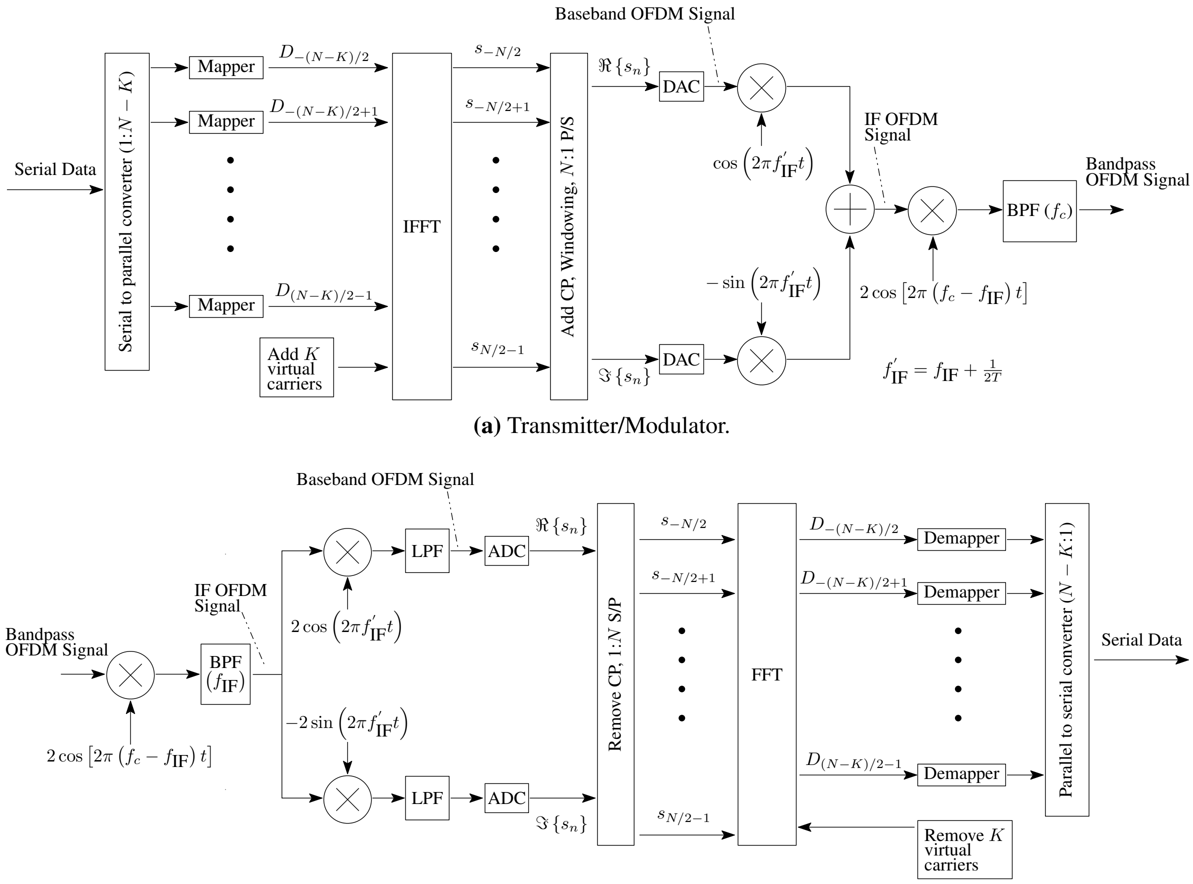

(a) Transmitter/Modulator.

(b) Receiver/Demodulator.

Figure 3.8: Digital OFDM modem using IFFT/FFT implementation (adapted from [39, p. 659]).

T_s samples and the remaining T_g samples are redundant. However, when there is a time offset, τ, that is less, in duration, than T_g, the DFT at the receiver will take the first T_s samples (i.e. samples τ to $\tau + T_s$) and it will still demodulate the data correctly due to the cyclic nature of the guard interval. Since a CP is used and not a blank GI, the time offset will cause a phase offset to all subcarriers, which can be corrected by the channel equaliser. For example, if the OFDM data set was $[D_0, D_1, D_2, D_3]$, i.e. $T_s = 4$, and the cyclic duration was two samples, i.e. $T_g = 2$, then the transmitted OFDM symbol will be $[D_2, D_3, D_0, D_1, D_2, D_3]$ which will have a duration $T = T_s + T_g = 6$ samples; assume there was time offset of one sample, i.e. $\tau = 1$, then the DFT will take the first T_s samples after the delay, i.e. $[D_3, D_0, D_1, D_2]$, which contains all the data but with a phase offset of one sample. Identifying when the OFDM data starts and correcting for frequency and phase offsets requires the implementation of a synchronisation algorithm.

3.3.2 Synchronisation

A major issue in the implementation of any digital communication system, whether it is wired or wireless, is knowing when the transmitted data has arrived. Since the receiver does not have prior knowledge of whether data is present, detecting the arrival of transmitted data is critically important. Detecting the presence of data and identifying the start time of the frame (sometimes called packet) is known in the literature as *frame synchronisation* or *time synchronisation* [73, p. 129]. Ideally, once the data frame is detected and the start time of the data symbol is known, the receiver can then proceed to perform its other functions, such as demodulation and demapping. In reality, though, the transmitted signals experience frequency and phase offsets. These frequency and phase offsets could (if uncorrected) degrade subcarrier orthogonality, which, in turn, would cause ICI and poor system performance. Frequency offsets can be caused by imperfect local oscillators at the transmitter and receiver, which will not generate exactly the same frequencies due to noise and other electrical and mechanical properties of the materials used to make the oscillators [75, Ch. 10]. Phase offsets can be caused by timing errors (or offsets) in the frame synchroniser (an example of which is given towards the end of Section §3.3.1). Phase offsets are also caused by the distance the transmitted signal has travelled to get to the receiver, and is given by [76, p. 11]

$$\phi = \frac{2\pi f d}{c},$$

where c is the speed of light, f is the frequency of the carrier and d is the distance travelled (or path length). Additional phase offsets are introduced by multipath fading (see Chapter 4). Estimating and correcting for frequency and phase offsets is referred to in the literature as *frequency synchronisation* [73, p. 129]. Minimising synchronisation errors (both time and frequency) is of extra importance for OFDM systems since they can degrade subcarrier orthogonality.

There are several established algorithms for achieving synchronisation in OFDM systems, but these algorithms have different limitations and levels of performance. Fortunately, some of the synchronisation algorithms provide a performance that is close to perfect. Therefore, to allow performance assessments which are independent from the synchronisation algorithm, throughout this thesis, *perfect* time and frequency synchronisation with desired OFDM transmission is assumed.

As mentioned in Chapter 2, OFDM is used in broadcast systems, e.g. DAB and DVB, and packet switched networks, e.g. WLANs. In broadcast systems, data is continuously being transmitted and, as a result, the receiver can take a relatively long time to establish frame synchronisation and then switch to tracking mode[7] [77]. However, in WLAN systems, data is not continuously being transmitted and therefore, packet detection and frame synchronisation must be performed rapidly to avoid data loss [78, p. 48][8]. Synchronisation algorithms used for single-carrier systems cannot be used for OFDM systems due to the complex characteristics of the baseband OFDM waveforms [39, p. 754] . Fortunately, an advantage of using IDFT/DFT pair in an OFDM system is that many synchronisation functions can be performed in the time or frequency domains [78, p. 48]. Frame synchronisation for OFDM systems is most commonly achieved through *correlation*. Practical OFDM systems include additional information in their transmitted packets to enable frame synchronisation such as cyclic prefixes in addition to pilot symbols and preambles. Since these overheads are needed to establish frame synchronisation, most OFDM systems have incorporated these features to facilitate frequency synchronisation as well [39, p. 755].

In addition to its important role in removing ISI and limited protection against phase/timing offsets, the cyclic prefix (CP) can also be used for packet detection as well as frequency and phase offsets estimation and correction [79–84]. The fact that the CP is an exact copy of the last T_g samples of the OFDM data

[7] Correcting for short term deviations [73, p. 129].

[8] OFDM systems are assumed to be packet switched networks in this thesis.

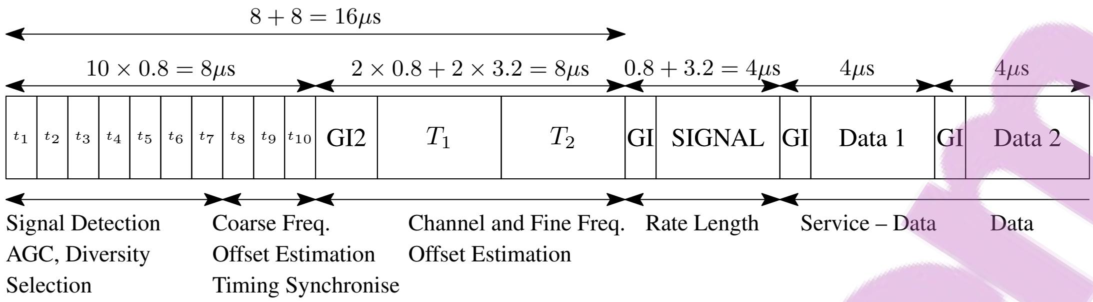

Figure 3.9: IEEE 802.11a packet structure (adapted from [21]). The two 8μs symbols are used for packet detection, symbol timing and frequency offset estimation. t_1 to t_{10} denote repetition of a short training symbol and T_1 and T_2 are two identical parts of a long training symbol with GI2 as its cyclic prefix (twice the duration of the data CP). For the IEEE 802.11a standard, $T_g = 0.8\mu$s and $T_s = 3.2\mu$s giving a symbol period of 4μs.

frame (Fig. 3.6), allows the receiver to estimate the symbol timing by correlating the most recent T_g time samples with another T_g samples that are T_s samples older; i.e. if the correlation window starts at time t_0, then the receiver would correlate samples $[t_0, \dots, t_0 + T_g - 1]$ with $[t_0 + T_s, \dots, t_0 + T_s + T_g - 1]$. When t_0 lines up with the start of the CP, the two sample sets will be exact copies of each other and the correlation output would produce a maximum value, which is proportional to the signal's energy in that correlation window. When there is a frequency offset present, the output of the correlator can also be used to estimate the frequency offset through joint maximum likelihood estimators (MLE) as in [83, 84]. Since CPs are already used in an OFDM frame to remove ISI, the biggest advantage of using them for synchronisation is that no additional symbols are needed to perform synchronisation tasks. However, using CPs for synchronisation also has its drawbacks: the maximum value for the output of the correlator is proportional to the energy of the CP and that changes significantly from symbol to symbol due to the randomness of the data. When the number of subcarriers N, is small, there will be many undesired sidelobes that are of comparable values to the peak value of the correlator due to the randomness of the data. CPs can only be used to estimate the symbol timing and not the start of the frame/packet [39, p. 763], which means it can be used for tracking a continuous OFDM transmission once the packet has been detected via a more reliable method.

One of the most reliable methods for OFDM synchronisation is the use of pilot (or training) symbols. There are many algorithms developed in the literature that use pilot symbols for OFDM synchronisation, e.g. [85–99]. The principle of some of algorithms (e.g. [87]) is almost identical to synchronisation using CPs: instead of correlating a CP with its copy, the correlation is performed between two (or more) special pilot symbols, either both present in the packet or one in the packet and one at the receiver. Unlike CPs, the pilot symbols have excellent auto-correlation and cross-correlation properties (e.g. maximum length sequences, MLSs). The disadvantage of pilot symbols is the additional overhead they impose on the OFDM signal. Synchronisation using pilot symbols can be performed either in the time or frequency domain, depending on the algorithm. The pilot symbols added to the OFDM packet are sometimes called *preambles* since they precede the CP and OFDM data; an example of a preamble is the IEEE 802.11a packet structure that is shown in Fig. 3.9.

3.3.3 Performance Issues

OFDM, by its very architecture, presents certain challenges that single-carrier transmission systems do not have to face. As mentioned in Section §3.3.2, OFDM systems are more sensitive to synchronisation errors than single-carrier transmission systems. This extra sensitivity to synchronisation errors arises from the fact that the OFDM subcarriers have to be mutually orthogonal to maintain an ICI-free performance, and synchronisation errors (both timing and frequency offsets) degrade subcarrier orthogonality. The additional susceptibility to synchronisation errors is a disadvantage for OFDM systems when compared with single-carrier transmission systems.

As mentioned in Section §3.2.1, the time domain OFDM signal can have a high peak-to-average power ratio (PAPR). This is because OFDM signals are comprised of N modulated signals (with different frequencies) added together in the time domain (as in Equation (3.1)), the result of which can be seen in Fig. 3.2 for $N = 8$. The N modulated signals produce a time-varying sum, the envelope of which can have a very high PAPR when the signals add up constructively. The high PAPR causes two problems for OFDM systems: the first is that it causes the signal to have a large dynamic range, which requires the DAC to have a large number of bits to accurately represent the signal. The second is the power amplifier has to have a large back-off and operate at a very low average power level (which is very inefficient) to accommodate the high peaks in its amplification range [39, p. 693]. Therefore, methods for removing the high PAPR and/or mitigating its effects are widely used in OFDM systems. These methods include peak cancellation with a complementary signal, clipping the signal above a certain threshold, special coding techniques and amplifier linearisation [39, Ch. 13]. Throughout this thesis, the effects of high PAPR are assumed to be mitigated.

3.4 Summary

In this chapter, the basic principles of OFDM have been discussed. OFDM can be considered as a special case of FDM with the spectra of its subcarriers overlapping. The spectra overlap is feasible when the OFDM subcarriers are mutually orthogonal. Modern OFDM modems are implemented digitally using the IFFT/FFT pair which has several benefits such as reducing system complexity and enabling synchronisation functions to be performed in either the time or fequency domains. OFDM systems are more sensitive to synchronisation errors than single-carrier communication systems since synchronisation errors degarde subcarrier orthogonality. OFDM signals have high PAPR which requires added complexity to mitigate its effects. Throughout this thesis, perfect synchronisation with desired OFDM transmission is assumed and the effects of high PAPR are assumed to have been mitigated.

In Chapter 4, the discussion will address how signals are affected during their journey from the transmitter to the receiver through the *channel*.

Chapter 4

Channel Characterisation

4.1 Introduction

As discussed in Chapter 2, a communication system has three generic components: a transmitter (Tx), a receiver (Rx) and a channel. In Chapter 3, the transmitter and receiver architectures and implementation of a generic OFDM system were discussed. In this chapter, the discussion is focused on the channel that links the transmitter and the receiver. In wired systems, the channel is, by definition, in a form of a wire/cable, e.g. an optical fibre. However, the emphasis of this research is on wireless applications, hence the channel discussed in this chapter is the *radio channel*. This chapter presents the fundamental principles of radio channels which provides an understanding of the channel models used in the latter chapters of this thesis. Understanding how the radio channel affects transmitted signals and modelling these effects to a sufficient degree of accuracy is essential for designing wireless systems with acceptable performance.

Section §4.2 discusses the fundamental principles of radio wave propagation. The important features and phenomena that are used to characterise radio channels are discussed in Section §4.3. Details of the specific radio channel models used in this thesis are discussed in Section §4.4.

4.2 Fundamentals of Radio Wave Propagation

A signal transmitted via a radio channel can reach the receiver via several propagation mechanisms (illustrated in Fig. 4.1), namely:

1. *Transmission*—transmitted signals travel via the shortest path to the receiver (usually a straight line). This direct transmission path can be

   (a) Unobstructed: unobstructed direct transmission occurs when there is a line-of-sight (LOS) between the transmitting and receiving antennas. The received signal from this path is called a LOS component.

   (b) Obstructed: when the direct path between the transmitting and receiving antennas is obstructed (e.g. by walls, furniture, etc.), the transmitted signal travels *through* the obstacle(s) and is attenuated as a consequence[1]. The received signal from this path is called a non-line-of-sight (NLOS) component.

2. *Reflection*— takes place when the transmitted signal (an electromagnetic wave) hits a surface that is dimensionally large relative to the wavelength, λ, of the transmitted signal. The electrical properties of the surface determine how much reflection and transmission take place, e.g. if the signal hits a perfect conductor, total reflection would occur [5, pp. 114–125]. Reflections normally take place on the surfaces of buildings, walls, furniture, etc.

3. *Diffraction*— takes place when the transmitted signal hits a surface that has a sharp edge, e.g. the corner of a wall. Even though there is no LOS between the transmitter and the receiver, the sharp edge creates secondary waves that are present behind the obstacle thus *bending* the wave around the obstacle [5, pp. 126–135].

4. *Scattering*— takes place when the transmitted signal hits an object that is dimensionally small relative to the wavelength of the transmitted signal, and where the number of obstacles per unit volume is large [5, pp. 135–138]. Rough surfaces, small objects and other channel irregularities will produce scattered waves/signals.

In a cluttered environment (such as an indoor environment), there are theoretically a number of paths a transmitted signal could take before arriving at the receiver, since the signal can be reflected, diffracted and scattered multiple times before arriving at the receiver. The arrival of multiple copies of the transmitted signal at the receiver at different times and with different strengths is an important characteristic of the radio channel and is called *multipath*.

4.3 Radio Channel Characterisation

The physical geometry of the radio channel by its very nature is complex and looks random/arbitrary, and factors such as the number of obstacles, type of obstacle, motion of receiver and/or transmitter, etc. can have a significant impact on transmitted signals. In the context of this thesis, there are four main features of the radio channel that must be considered, namely: *multipath fading*, *shadowing*, *path loss* and *noise*. Understanding and accurately modelling these features is of paramount importance when designing wireless systems.

4.3.1 Multipath Fading

At the receiving antenna, echos of the transmitted signal arrive at different times and with different strengths and add as phasors. When the echos add destructively, the resultant signal is a *fade*. This fading due to multipath is appropriately called *multipath fading* or small-scale fading since the fades occur roughly every half a wavelength [5, p. 211]. Fig. 4.2 shows a typical received signal in a multipath environment as a function of receiver location. The profile of the signal strength in a multipath environment

[1] The amount of attenuation experienced by a transmitted signal passing through an object is dependent on the electrical properties of the object, the signal's angle of arrival and the frequency of the transmitted signal.

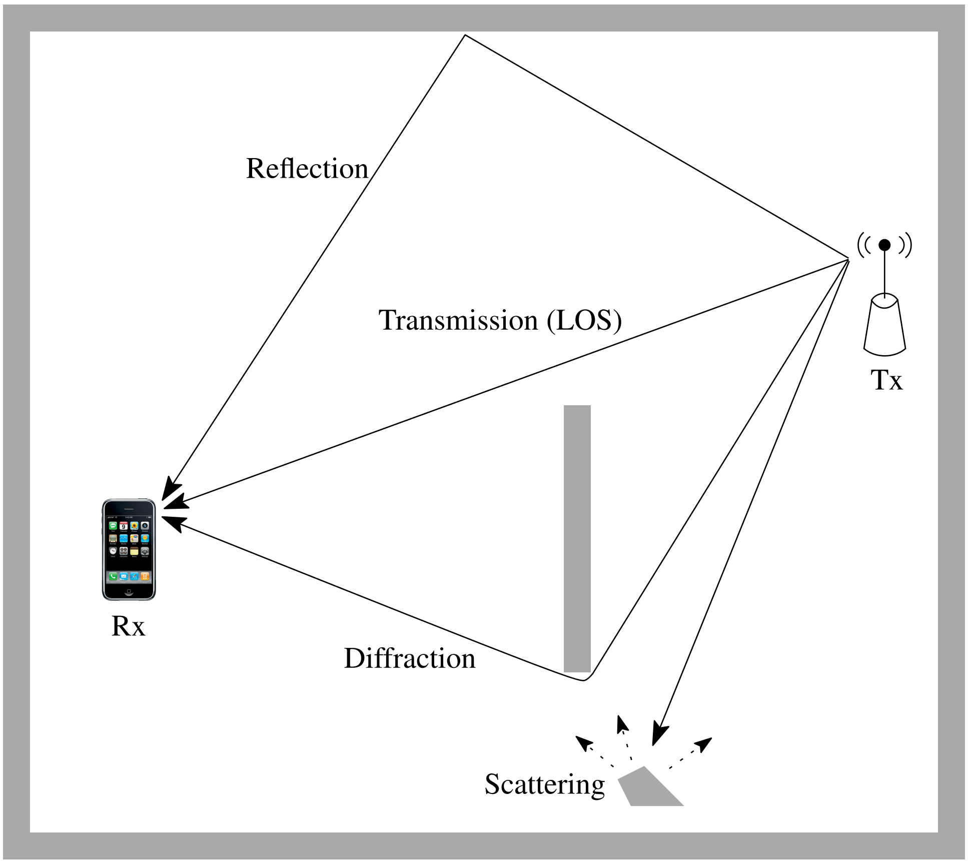

Figure 4.1: Fundamental radio wave propagation mechanisms.

(such as the one shown in Fig. 4.2) is called the *fading profile/envelope*. The spatial or temporal average of the received signal strength is called the *local mean* (shown as red dashed line in Fig. 4.2). Fig. 4.2 shows that while the local mean changes relatively slowly, the instantaneous signal strength fluctuates dramatically due the phasor addition of the echoes. Deep fades (such as the ones shown in Fig. 4.2) can be several orders of magnitude weaker in strength than the local mean and this can have an important effect on wireless systems. For example, if in a cellular system, a mobile receiver is located at a deep fade, then the mobile receiver will most likely experience an outage.

If the radio channel is static, then the fading profile (such as the one shown in Fig. 4.2) will not change with time. Even so, identifying the fade locations deterministically is a very challenging, but unnecessary, mathematical exercise. However, radio channels are constantly changing due to motion of the transmitter, receiver and/or obstacles in the environment. This motion causes the fading profile to be time-variant and the rate of which it changes depends on the velocity of the objects in the environment. In all but the most trivial of cases, modelling the electromagnetic fields deterministically in a time-varying channel is impractical and instead, statistical models are used.

4.3.1.1 Narrowband characterisation

In the late 1960s, Clarke [100] proposed a model that considers the arrival of N_p horizontal-travelling vertically-polarised plane waves (with a uniformly distributed angle of arrival) at the receiving, isotropic, antenna. Clarke's model also assumes that there is no dominant component (usually a LOS component)

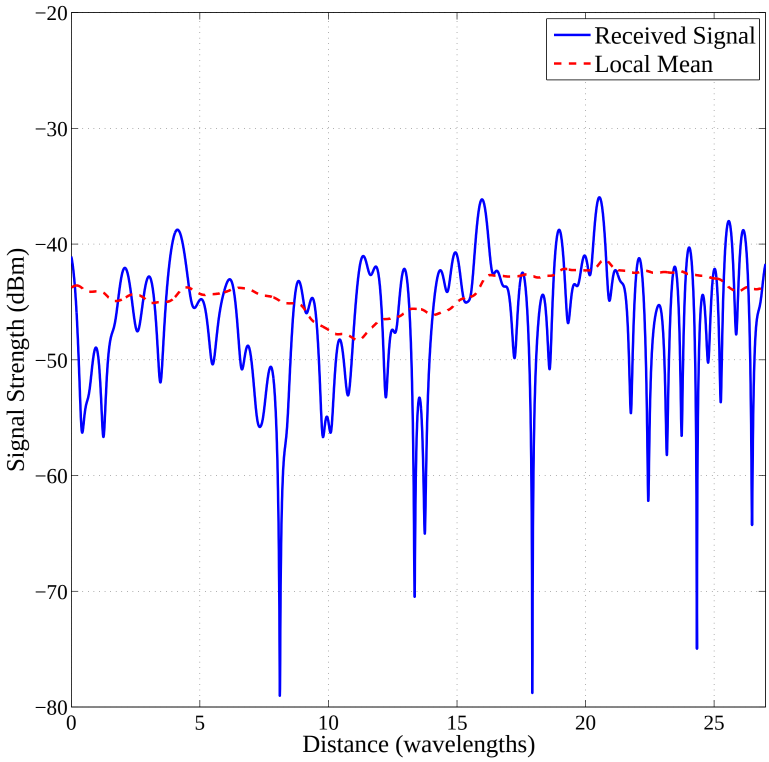

Figure 4.2: An example of a typical received signal in a multipath environment as a function of location. The distance shown on the x-axis is not the transmitter–receiver separation distance, but a distance moved by the receiver.

present. What Clarke showed in his model is that the fading envelope (in volts) resulting from the multipath environment follows a *Rayleigh* distribution. This means that amplitude fluctuations of the fading envelope with no dominant component can be reasonably accurately modelled using the Rayleigh probability density function (pdf). Therefore, the pdf of the fading envelope, υ (in volts), is given by

$$p(\upsilon) = \begin{cases} \frac{\upsilon}{\varpi}\exp\left[\frac{-\upsilon^2}{2\varpi}\right] & \upsilon \geq 0 \\ 0 & \text{otherwise,} \end{cases} \tag{4.1}$$

where ϖ is the time/spatial-average power of the received signal (in watts) or, simply, the local mean. Sometimes it is more convenient to describe signals in terms of their power. The distribution of the received *power* can be derived by making the variable substitution $w = \upsilon^2$ which produces an exponential pdf given by[2]

$$p(w) = \begin{cases} \frac{1}{2\varpi}\exp\left[-\frac{w}{2\varpi}\right] & w \geq 0 \\ 0 & \text{otherwise.} \end{cases} \tag{4.2}$$

An example of an environment where Rayleigh fading would occur in is an indoor office floor where a WLAN is operational and the receiving antenna is in a different room from the base station[3].

[2]In this context $\varpi = \bar{\upsilon^2}$.

[3]Most likely several rooms away to ensure no dominant component is present.

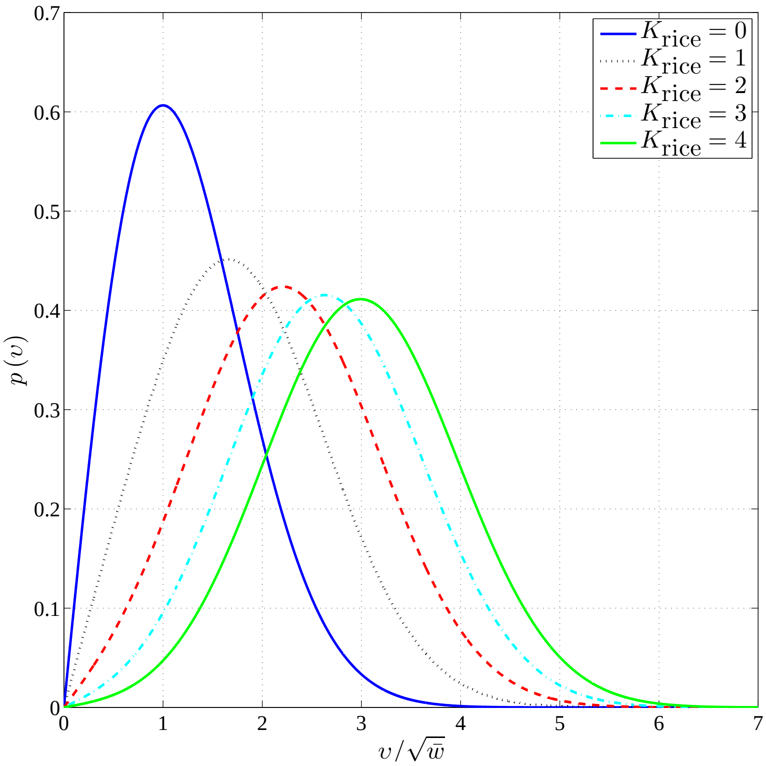

Figure 4.3: Rician pdfs with different K_{rice} values. The Rayleigh pdf is given when $K_{\text{rice}} = 0$. $\bar{w} = 1$ watt.

However, when a dominant component (usually a LOS component) is included in the model, the *Rician* (sometimes spelled Ricean) distribution is used to characterise the fading envelope according to [5, p. 213]

$$p(v) = \begin{cases} \frac{v}{\bar{w}} \exp\left[\frac{-\left(v^2+A^2\right)}{2\bar{w}}\right] I_0\left(\frac{Av}{\bar{w}}\right) & v \geq 0,\ A \geq 0 \\ 0 & \text{otherwise,} \end{cases} \tag{4.3}$$

where A is the peak amplitude (in volts) of the dominant component, and $I_0(\cdot)$ is the zeroth order modified Bessel function of the first kind. Usually, the Rician distribution is characterised by the K_{rice} factor given by

$$K_{\text{rice}} = \frac{A^2}{2\bar{w}}.$$

So, when there is no dominant component (i.e. $A = 0$), $K_{\text{rice}} = 0$ and the Rician pdf in (4.3) reduces to Rayleigh as in (4.1). Therefore, a Rayleigh distribution is a Rician distribution with $K_{\text{rice}} = 0$. Fig. 4.3 illustrates Rician pdfs with different K_{rice} values. An example of an environment where Rician fading would take place would be an outdoor cellular environment, where the receiving antenna (the mobile device) is in close proximity to the cellular base station.

4.3.1.2 Wideband characterisation

Multipath fading takes place when the echoes of the transmitted signal at the receiving antenna add as phasors. The phase of the qth echo, ϕ_q, is determined by its *electrical* path length, such that $\phi_q = \kappa d_q$, where d_q is the physical path length (in metres) travelled by the qth echo and $\kappa = 2\pi/\lambda$ is the wave number (in radians/metre) [76, p. 11]. It should be noted that the wave number, κ, can be written as

$$\kappa = \frac{2\pi}{\lambda} = \frac{2\pi f}{c}, \tag{4.4}$$

where c is the speed of light and f is the frequency of the transmitted signal. Therefore, the phase of the qth echo (and consequently the fading profile) is a function of the receiver's spatial location (which determines the physical path length) *and* the transmitted signal's frequency. For a narrowband signal that contains a single frequency component (a tone), the fading profile is a one-dimensional function of receiver location, as shown in Fig. 4.2. However, OFDM signals contain N subcarriers each with its own frequency as discussed in Chapter 3. Also, these N frequency components of the transmitted OFDM signal are allocated over a *wide* bandwidth, e.g. 10 MHz for some WiMAX profiles [8], 20 MHz for IEEE 802.11g WLAN standard [23] and 40 MHz for some IEEE 802.11n WLAN profiles [24]. Since OFDM signals are wideband, the individual OFDM subcarriers will experience different fading profiles even when the receiver is stationary. This type of fading is called *frequency selective* fading [39, p. 804]. Fig. 4.4 illustrates the frequency selective fading experienced by a 20 MHz signal.

The *type* of fading the transmitted signal experiences is dependent on the signal's properties (e.g. bandwidth) and the radio channel's characteristics (e.g. delay spread and coherence bandwidth) [5, p. 205]. The channel is characterised by its impulse response of which important properties of the channel can be extracted such as the mean excess delay, $\bar{\tau}$, and delay spread, σ_τ. $\bar{\tau}$ and σ_τ are calculated according to [101]

$$\bar{\tau} = \frac{\sum_{q=1}^{Q} \tau_q P\left(\tau_q\right)}{\sum_{q=1}^{Q} P\left(\tau_q\right)} - \tau_0, \tag{4.5}$$

$$\sigma_\tau = \sqrt{\frac{\sum_{q=1}^{Q} \left(\tau_q - \bar{\tau} - \tau_0\right)^2 P\left(\tau_q\right)}{\sum_{q=1}^{Q} P\left(\tau_q\right)}}, \tag{4.6}$$

where τ_0 is the arrival delay of the shortest path (usually the LOS component), τ_q is the qth echo arrival delay, and $P\left(\tau_q\right)$ is the power of the qth echo. The multipath environment and motion within it (i.e. Doppler spread) along with the transmitted signal's properties produce four types of fading channels, namely [5, pp. 205–210], [39, pp. 803–823]:

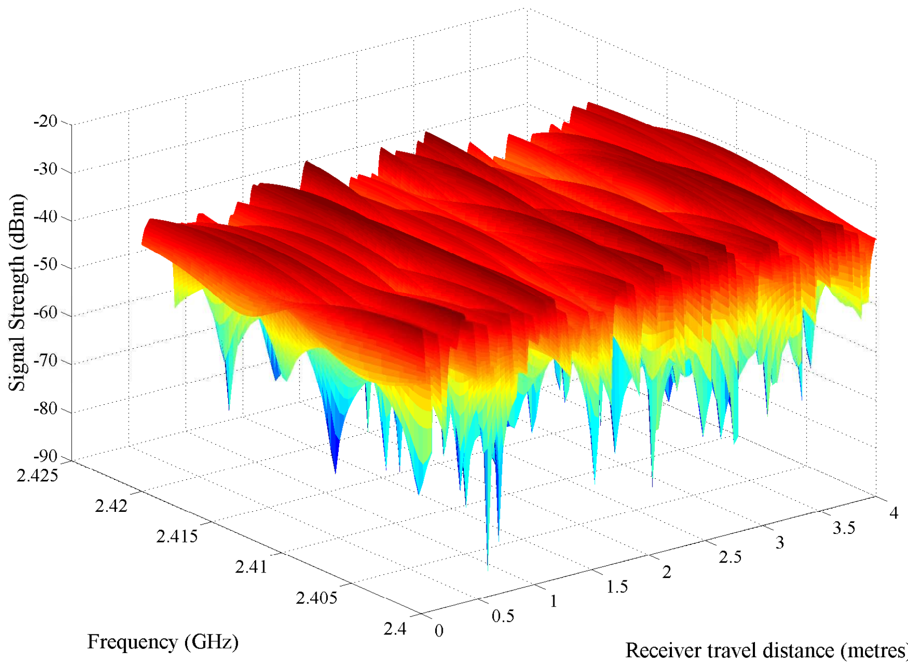

(a) Fading envelope as a function of receiver location and transmitted signal's frequency. The distances shown are not the transmitter–receiver separation distance, but the distance travelled by the receiver from the start location to the end location.

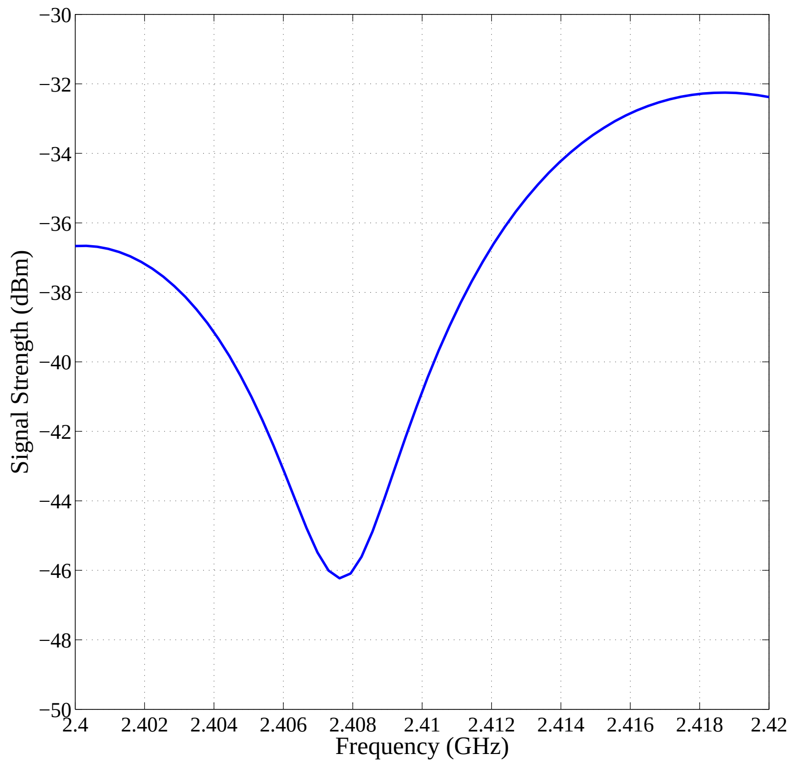

(b) Fading envelope as a function of transmitted signal's frequency (transmitter and receiver are stationary).

Figure 4.4: An example of frequency selective fading experienced by a 20 MHz wideband signal.

1. *Frequency flat slow fading*: when the radio channel has a constant gain and linear phase response over a coherence bandwidth, B_c, that is larger than the bandwidth of the transmitted signal, B, frequency *flat* fading occurs. Frequency flat fading means that the transmitted signal's amplitude changes according to the multipath fading but its spectrum is preserved. That is, all frequency components of the signal experience the same amplitude fluctuations and the channel is considered *narrowband* since B is narrow relative to B_c. The velocity of the transmitter, receiver and/or obstacles in the environment determine how fast the channel impulse response, $h(t)$, changes. If $h(t)$ changes at a rate that is slower than the transmitted baseband signal, then *slow* fading occurs. That is, the Doppler spread of the channel, B_d, is much smaller than B. The slowness and flatness of the fading are two independent properties. To summarise, the transmitted signal experiences a frequency flat slow fading when:

    - $B \ll B_c$ (alternatively, $T \gg \sigma_\tau$) which makes the fading flat; and
    - $B \gg B_d$ (alternatively, $T \ll T_c$, where T_c is the channel coherence time) which makes the fading slow.

2. *Frequency selective slow fading*: When B is greater than B_c, *frequency selective* fading occurs. In other words, the delay spread is greater than the signal's symbol period, meaning that multiple faded and time delayed copies of the transmitted signal are included in the received signal, which is also known as *inter-symbol interference* (ISI) (as discussed in Section §3.2.3). As discussed earlier, frequency selective fading means that different frequency components will experience different amplitude fluctuations and the channel is considered *wideband*. Therefore, the transmitted signal undergoes frequency selective slow fading when:

    - $B > B_c$ (alternatively, $T < \sigma_\tau$) which makes the fading frequency selective; and
    - $B \gg B_d$ (alternatively, $T \ll T_c$) which makes the fading slow.

3. *Frequency flat fast fading*: occurs when:

    - $B \ll B_c$ (alternatively, $T \gg \sigma_\tau$) which makes the fading flat; and
    - $B < B_d$ (alternatively, $T > T_c$) which makes the fading fast.

4. *Frequency selective fast fading*: occurs when:

    - $B > B_c$ (alternatively, $T < \sigma_\tau$) which makes the fading frequency selective; and
    - $B < B_d$ (alternatively, $T > T_c$) which makes the fading fast.

The type of multipath fading channel that is adopted in this thesis (further explained in Section §4.4) is frequency selective slow fading.

4.3.2 Shadowing

Changes in the local mean of the fading envelope occur over medium range distances (in the order of 10λ) and are usually caused when the receiver is shadowed by significant environmental obstacles

Table 4.1: Path loss exponent and standard deviation for different indoor wireless environments [5, p. 162].

Building	Frequency (GHz)	Path loss exponent, n_p	σ (dB)
Retail store	0.914	2.2	8.7
Grocery store	0.914	1.8	5.2
Office, hard partition	1.500	3.0	7.0
Office, soft partition	0.900	2.4	9.6
Office, soft partition	1.900	2.6	14.1
Textile/Chemical factory	1.300	2.0	3.0
Textile/Chemical factory	4.000	2.1	7.0
Metal working	1.300	1.6	5.8
Indoor street	0.900	3.0	7.0

(such as concrete walls, lift shafts, stairwells, buildings etc.). These local mean fluctuations are called *shadowing* [76, p. 23]. It has been experimentally determined that the effects of shadowing can be modelled statistically using the log-normal distribution [76, p. 24], [5, p. 139]. The log-normal pdf of the *average* received signal power, $\bar{w}$ (mW), is given by [10, pp. 232–233]

$$p(\bar{w}) = \frac{10}{\bar{w}\ln(10)\,\sigma\sqrt{2\pi}} \exp\left[\frac{-\left(10\log_{10}(\bar{w}) - \bar{M}\right)^2}{2\sigma^2}\right], \tag{4.7}$$

where $\bar{M}$ is the area mean (in dBm) and σ (dB) is the standard deviation from the area mean[4]. Typical values of σ in wireless environments are shown in Table 4.1. If the signal is expressed in volts, then the pdf, $p(\upsilon)$, is also log-normally distributed such that [102, p. 22]

$$p(\upsilon) = \frac{20}{\upsilon\ln(10)\,\sigma\sqrt{2\pi}} \exp\left[\frac{-\left(20\log_{10}(\upsilon) - \bar{M}\right)^2}{2\sigma^2}\right]. \tag{4.8}$$

To model the effects of multipath fading and shadowing together, the *Suzuki* distribution is used [103], that is, a power signal that has an exponential pdf (Equation (4.2)) with a mean that is log-normally distributed (Equation (4.7)) will have a pdf given by

$$p(w) = \frac{10}{\ln(10)\,\sigma\sqrt{2\pi}} \int_0^\infty \frac{1}{\bar{w}^2} \exp\left[\frac{-\left(10\log_{10}(\bar{w}) - \bar{M}\right)^2}{2\sigma^2}\right] \exp\left[-\frac{w}{\bar{w}}\right] d\bar{w}. \tag{4.9}$$

The area mean, $\bar{M}$, is determined by factors such as the transmitter–receiver separation distance, antennas, frequency, etc. and when normalised to the transmitted power of the signal it is called *path loss*.

4.3.3 Path loss

The simplest form/model of a radio channel is the Friis *free space* environment, in which there are no obstacles obstructing the path between the transmitter and the receiver. This model is used for satellite

[4]When a random variable is log-normally distributed, it means that the log of the variable has a normal/Gaussian distribution; i.e. if $\bar{W}$ is the average received power in dBm, then $p(\bar{W}) = \frac{1}{\sigma\sqrt{2\pi}} \exp\left[\frac{-\left(\bar{W}-\bar{M}\right)^2}{2\sigma^2}\right]$.

communications and microwave point-to-point systems. It should be noted that even in a free space environment, the transmitted signal's power is attenuated as it travels from the transmitting antenna to the receiving antenna. The Friis free space equation accounts for the spatial divergence due to the propagation of the signal's energy in equal amounts in all directions (isotropic radiation) and predicts the amount of path loss, L_p, as

$$L_p = \frac{P_r}{P_t} = \frac{G_t G_r \lambda^2}{(4\pi d)^2 L_s}, \tag{4.10}$$

where P_t and P_r are, respectively, the transmitted and received powers, G_t and G_r are, respectively, the transmitter and receiver antenna gains, λ is the wavelength, d is the transmitter–receiver separation distance, and L_s is a miscellaneous system loss factor that is not related to propagation ($L_s \geq 1$), e.g. cable losses.

Fig. 4.5 shows the effect of path loss on a 2.4 GHz signal in a free space environment with $G_t = G_r = 1$ and $L_s = 1$ as a function of the transmitter–receiver separation distance (measured in wavelengths). From Fig. 4.5, it is observed that by the time the transmitted signal has travelled 80 wavelengths it has only one millionth (-60 dB) of the original transmitted power (e.g. for a 2.4 GHz signal $80\lambda = 10$ metres). Clearly, path loss is an important feature of the radio channel since there is nothing obstructing the path between the transmitter and receiver and yet there is significant attenuation. One way of mitigating the effects of path loss is minimising system losses (L_s) through the use of better cables and connectors and maximising the gains of the transmitter and receiver antennas (G_t and G_r) by using different antenna designs and configurations, e.g. directional antennas at the base station.

It is important to note from Equation (4.10) that $L_p \propto 1/d^{n_p}$, where n_p is the *path loss exponent* ($n_p = 2$ for a free space channel). However, most practical radio channels cannot be classified as free space due to the presence of obstacles (including the ground). It has been observed in the literature that the value of the path loss exponent is directly related to the channel conditions, e.g. $n_p = 3$ for a hard partitioned office [5, p. 162]; meaning that the transmitted signal would be attenuated more rapidly than it would in a free space environment. Table 4.1 gives experimentally measured path loss exponent values for different indoor wireless environments. While a higher path loss exponent value means more severe attenuation and thus a problem for desired receivers, it also means that interference from other signals is reduced. This is because the transmitted interfering signals will also be attenuated more quickly and therefore, more wireless systems can coexist with each other in a relatively small area (depending on the frequencies used).

4.3.4 Noise

There are many types of noise that affect a system, such as shot noise and thermal noise [11, pp. 58–64]. Of particular importance in this thesis is thermal noise. Thermal noise is the electrical noise generated by the random motion of electrons in a conductor. The available thermal noise power, P_{TN} (in watts), is given by [11, p. 61]

$$P_{TN} = k_b T_k B, \tag{4.11}$$

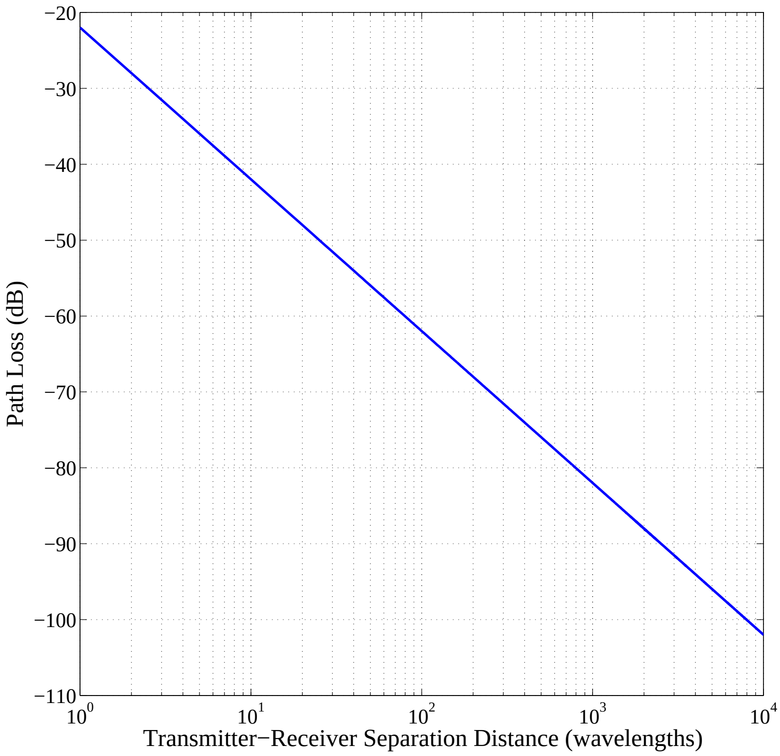

Figure 4.5: Path loss of a 2.4 GHz carrier in a free space environment with unity gain for the transmitter and receiver antennas. The slope of the line is determined by the path loss exponent, n_p.

where $k_b = 1.38 \times 10^{-23}$ joules per degree Kelvin is Boltzmann's constant, T_k is the temperature in degrees Kelvin and B is the bandwidth of the signal in Hz. For example, a 20 MHz signal at 20°C would experience a thermal noise power level of -101 dBm.

When thermal noise has equal power across all frequencies, it is called *white* noise. White noise is characterised by its power spectral density, $S_W(f) = N_0/2$ (Watts/Hz). N_0 is normally referenced to the receiver's input stage and is given by

$$N_0 = k_b T_e,$$

where T_e is the equivalent noise temperature of the receiver [11, p. 61]. White noise is random and has a Gaussian distribution, hence it is usually referred to in the literature as *additive white Gaussian noise* (AWGN). The pdf for AWGN is given by [39, p. 6]

$$P_{\text{AWGN}}(r) = \frac{1}{\sqrt{\pi N_0}} e^{-r^2/N_0}, \tag{4.12}$$

and it has a mean of zero and variance, $\sigma^2 = N_0/2$. An important parameter in any communication system is the signal-to-noise ratio (SNR), which is defined as the ratio of the signal's power to the noise power. Throughout this thesis, SNR will be used interchangeably with E_s/N_0, where E_s is the energy of the transmitted mapped *symbol*. Sometimes, it is important to characterise the SNR in terms of the energy-per-bit, E_b, such that

$$\text{SNR} = \frac{E_s}{N_0} = \frac{E_b}{N_0} \times b, \tag{4.13}$$

where b is the number of bits per symbol (e.g. there are two bits per QPSK symbol and six bits per 64QAM symbol).

4.4 Channel Models in Thesis

All channel models used in this thesis include AWGN as a channel impairment. The strength of the noise is characterised by the energy-per-bit-to-noise-ratio, E_b/N_0.

The channel is assumed to be linear and time-invariant (i.e. the maximum packet duration, T, is much shorter than the channel coherence time, T_c) and a cyclic prefix is used to remove the effects of ISI. The fading is assumed to be slow and the OFDM system models used in this thesis allow for frequency selectivity[5]. That is, transmitted OFDM signals experience *frequency selective slow fading*.

There are four ways to model the effects of the radio channel on OFDM signals: the first is to use various statistical tools (such as the ones described in this chapter). Statistical tools are relatively easy to implement and provide a wide range of environmental settings that can be used, but are restricted to the set of assumptions they are founded on. The second way is to use computational electromagnetic modelling techniques such as the finite-difference time-domain (FDTD) method [104, 105] — these can be computationally very intensive depending on the resolution and the environmental details of the simulation setup [106, pp. 34–36]. The third method is *mechanistic* modelling techniques that are based on the principal electromagnetics theory but take into account just the predominant components — these significantly reduce the computational overhead whilst maintaining acceptable accuracy levels [107, Sec. V]. The fourth method is to *measure* the radio channel; while this method is usually time consuming and location specific, it provides an accurate account of the channel characteristics without any assumptions. In this thesis, real channel measurements were used to model the effects of the radio channel on OFDM signals. Postgraduate students at the Department of Electrical and Computer Engineering conducted, over the years, *experimental measurements* in two different real, indoor environments at The University of Auckland. The OFDM system models developed in this thesis are general enough that they accommodate *both* statistical modelling of the radio channel and real channel measurements.

The measurements setup, architectures of the two environments and deployment scenarios are discussed in Chapter 5.

4.5 Summary

Understanding and accurately modelling the radio channel effects on transmitted signals are crucial when designing wireless communication systems that have optimum performance. In this chapter, radio wave propagation mechanisms and the effects of the radio channel on transmitted signals are discussed. Multipath fading, shadowing, path loss and noise occur in radio channels and have detrimental effects on transmitted signals. Shadowing, multipath fading and noise are usually modelled using statistical methods since the radio channel is too random to model deterministically.

[5]The models also allow for frequency flat fading. This can be achieved by setting the attenuation coefficients for all subcarriers to be identical.

In this thesis, OFDM signals are assumed to experience no ISI due to their long symbol duration and the presence of a cyclic prefix. The OFDM system models developed in this thesis assume the fading is slow and frequency selective. Experimental measurements were conducted in two different, real, indoor environments at The University of Auckland and provide the necessary channel characterisation information.

The discussion in Chapter 5 includes the experimental setup, building architectures and deployment scenarios that are used to analyse the performance of OFDM-based wireless systems in the latter chapters of this thesis.

Chapter 5

OFDM and Indoor Environments — Investigation Overview

5.1 Introduction

In Chapter 3, the basic principles of generic OFDM systems have been discussed, including how OFDM signals are generated, modulated, received and demodulated. In Chapter 4, this discussion was extended to consider how the radio channel can be characterised and its effects on OFDM signals. As shown in Section §4.4, statistical tools are not used in this thesis to model the effects of the radio channel on OFDM signals. Instead, real RF measurements were taken in two test environments at The University of Auckland that provide the necessary channel information (i.e. path loss estimates) for indoor OFDM-based wireless networks.

This chapter is divided into two parts: the first part (Section §5.2) discusses the environmental considerations used in this thesis that provide realistic channel information in two different indoor test environments. The second part (Section §5.3) gives an overview of the research philosophy adopted in this thesis and links the material presented thus far in the thesis, and those in Chapters 6-9.

5.2 Environmental Considerations

The main focus of the research presented in this thesis is the performance assessment of OFDM-based wireless networks in *indoor* environments. Since the 1990s, postgraduate students in the Department of Electrical and Computer Engineering (ECE) at The University of Auckland have conducted numerous narrowband RF propagation measurement campaigns (at a range of frequencies) which have been used to construct path loss databases. Two of those propagation databases are used in this thesis to provide the environmental characterisation for OFDM-based wireless networks (an example of such a network is an IEEE 802.11g WLAN).

A brief discussion of the measurement setup, data output and relevance to this thesis is presented in Section §5.2.1. Descriptions and building architectures of two test environments along with transmitter and receiver locations within each test environment are presented in Sections §5.2.2 and §5.2.3.

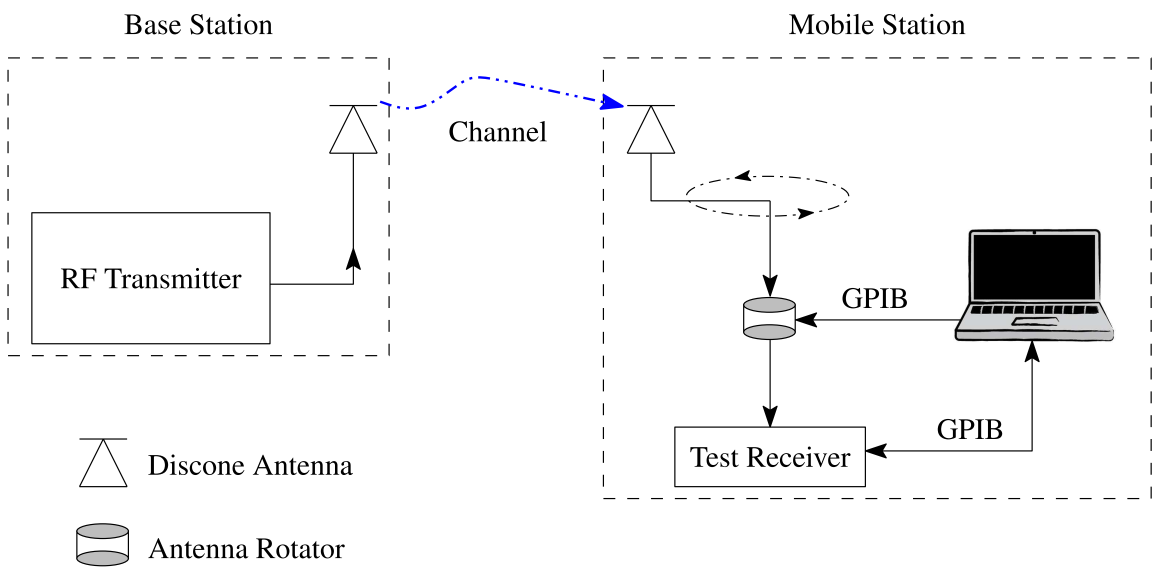

Figure 5.1: Illustration of the narrowband measurement setup used in [108].

5.2.1 Channel Modelling

The effects of the radio channel on OFDM signals were identified via RF propagation measurement campaigns in two different indoor test environments as conducted by Wong [15] in 2004 and Yang [108] in 2009. An overview of the measurement setup of these two campaigns is presented here. Both measurement campaigns used very similar experimental equipment configurations to measure narrowband path loss. Fig. 5.1 shows a simplified illustration of the narrowband measurement setup used in the 2009 campaign [108]. The setup consists of two components: a *transmitter* (also referred to as *Base Station* (BS)) and a *receiver* (also referred to as *Mobile Station* (MS)).

The Base Station (BS)

The base station comprises an RF transmitter, a feeder cable and a transmitting antenna. The RF transmitter produces a continuous wave (CW) signal in the 1.8 GHz band, and frequencies of 1.885 GHz and 1.88 GHz were used in [15] and [108] respectively[1]. Although this band is slightly different to that utilised by the IEEE 802.11g/n systems, it is sufficiently close for the values of measured path loss to be representative and to allow indicative trends to be explored. From the RF transmitter, this CW signal passes through the feeder cable to the transmitting antenna (discone) which was mounted on a 1.8 m mast. Fig. 5.2a shows the BS setup used by Yang in 2009 [108].

The Mobile Station (MS)

The mobile station comprises a receiving antenna (a half-wavelength folded dipole was used in [15] and a discone in [108]), a feeder cable, an antenna rotator, a test receiver and a laptop. The receiving antenna was mounted on an arm (0.5 m long in [15] and 0.3 m long in [108]) that was rotated by a stepper

[1]These experiments were necessarily constrained to the 1.8 GHz frequency band since there were no services using that band in central Auckland at the time and a radio license was obtained to operate at that frequency band.

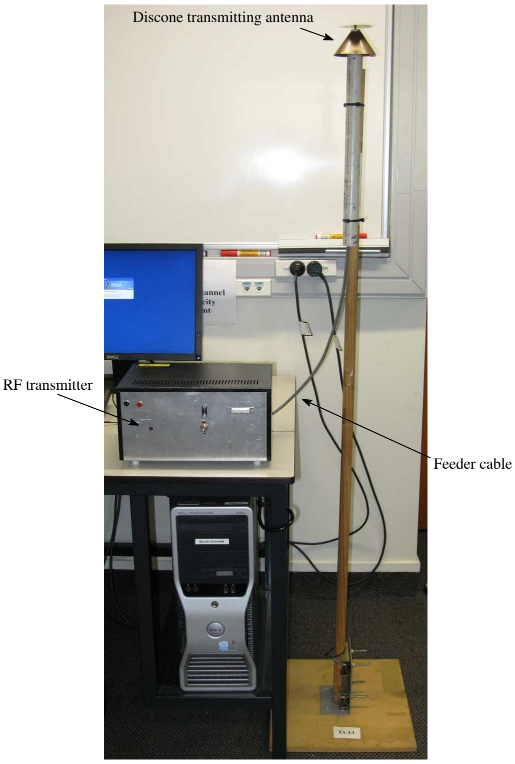

(a) Base station setup.

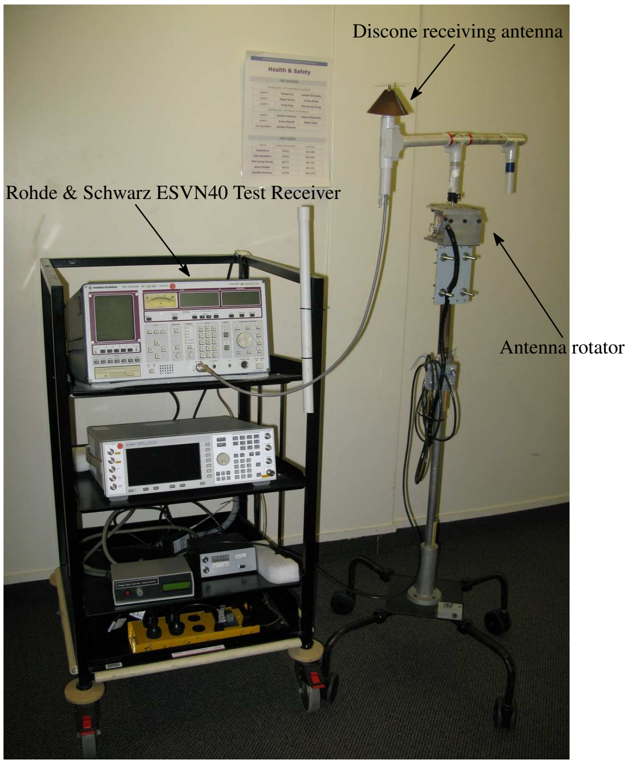

(b) Mobile station setup.

Figure 5.2: Measurement setup used by Yang [108].

motor over a full circle in 360 evenly spaced steps. A test receiver (Rohde & Schwarz ESVN40) that is connected to the receiving antenna by a feeder cable measures the instantaneous received signal strength (RSS) at each arm position (i.e. 360 measurements per rotation). A laptop computer controls the test receiver and the antenna rotator via a GPIB[2] interface. Fig. 5.2b shows the MS setup used by Yang in 2009.

The Measurement Process

In a test environment, a number of potential BS and MS locations are identified. Propagation measurements were performed simultaneously for multiple BSs at the identified locations in the test environment[3]. The advantage of this method is two fold: firstly, it significantly reduces the data collection time and secondly, it ensures the radio channel has not changed appreciably when measuring path loss data for each BS. At the identified MS locations, a set of instantaneous RSS measurements take place by rotating the receiving antenna in a full circle in 360 evenly spaced steps. At each step, the test receiver measures the instantaneous RSS from each BS by sequentially scanning the list of frequencies used by the BSs deployed. The instantaneous RSS measurements are recorded by the laptop and then averaged (with respect to linear units, i.e. watts) to remove the effects of multipath fading for that MS location. Therefore, for each permutation of BS and MS locations, a single *averaged* RSS value is recorded that takes into account the effects of path loss and shadowing on the transmitted signal.

[2]General purpose interface bus.
[3]The BSs are differentiated by being assigned different frequencies (spaced 400 kHz apart) in the 1.8 GHz frequency band.

These averaged RSS values are used in this thesis to give the *signal-to-interference ratios* (SIR) at each location in the test environment. The SIR is defined as the ratio of the desired signal's power to the total interference power and is an important parameter in most communication systems. In this thesis, two test environments were measured and these are discussed in Sections §5.2.2 and §5.2.3.

5.2.2 Test Environment A — The Science Building

The first test environment considered in this thesis is The Science Building at The University of Auckland, hereafter referred to as *Test Environment A*. The Science Building is a multistorey building consisting of nine levels (a basement, a ground floor and seven floors above) and is constructed from steel-reinforced concrete. Fig. 5.3 shows exterior and interior images of The Science Building[4]. The Science Building is surrounded by several buildings in close proximity (not shown in Fig. 5.3), of similar structural characteristics, specifically to its south (behind The Science Building in Fig. 5.3a) and west (to the right of The Science Building in Fig. 5.3a). Due to the close proximity of these neighbouring buildings and the fact that The Science Building has many glass windows on its exterior, RF signal reflections from these neighbouring buildings are likely contributors to the overall RSS within The Science Building. Floors on The Science Building are 15m $\times$ 70m and are made up of several offices, laboratories, storage areas, two stairwells and an elevator shaft. Rooms on each floor are surrounded by glass windows on their sides and separated from each other by walls constructed of a mixture of wood and plasterboard. Floors are separated from each other by steel-reinforced concrete floors/ceilings.

Base stations were deployed on levels 1–3 of The Science Building at three different locations on each floor as illustrated by Fig. 5.4. Mobile stations, on the other hand, were deployed only on level 3 of The Science Building at 52 different locations. The floor plan of level 3 and the BS and MS locations are shown in Fig. 5.5.

5.2.3 Test Environment B — The Engineering Tower

The second test environment considered in this thesis is The Engineering Tower at The University of Auckland, hereafter referred to as *Test Environment B*. As shown in Fig. 5.6, the Engineering Tower is a 12-storey building (the first three floors are underground, and level 4 is at ground level as seen in Fig. 5.6) that is constructed from similar materials to The Science Building (i.e. steel-reinforced concrete). RF propagation measurements were taken in The Engineering Tower by Wong [15] in 2004 on the eighth floor and by Yang [108] in 2009 on the sixth floor. The exterior of the building essentially consists of glass windows with "decorative" concrete slabs projecting out between floors. There are no buildings immediately adjacent to the eighth floor; however, there are buildings on the western and eastern sides of the building up to the level of the sixth floor. The floors of The Engineering Tower are 18.5m $\times$ 18.5m and have very similar layout, i.e. each floor contains a central services core surrounded by a internal corridor with fixed-partition offices between this corridor and the external wall. The central core is constructed from steel-reinforced concrete and accommodates lifts, stairwell and other building services. The offices are partitioned with a mixture of timber and plasterboard walls.

[4]The ECE Department is located on levels 1–3 of The Science Building and is the reason why the RF propagation measurements taken by Yang [108] in level 3 (indicated by the red rectangle in Fig. 5.3a) were performed.

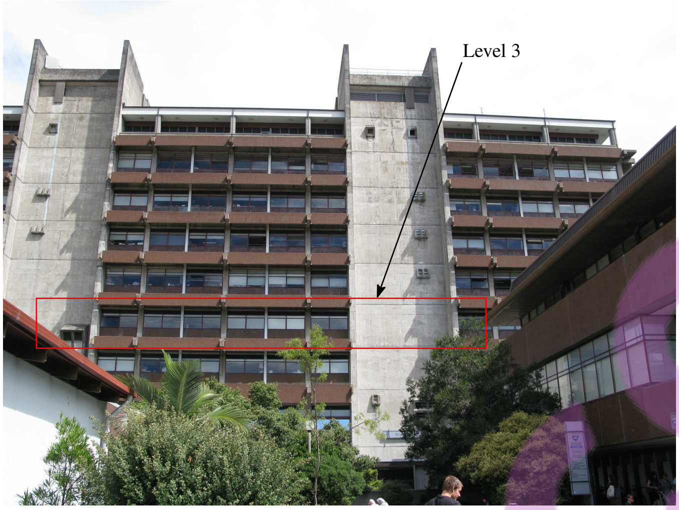

(a) The exterior of The Science Building at The University of Auckland. The RF propagation measurements were taken in level 3 of this building.

(b) Typical indoor office environment on level 3 of The Science Building.

(c) The long corridor on level 3 of The Science Building.

Figure 5.3: Test Environment A: Exterior and interior images of The Science Building at The University of Auckland.

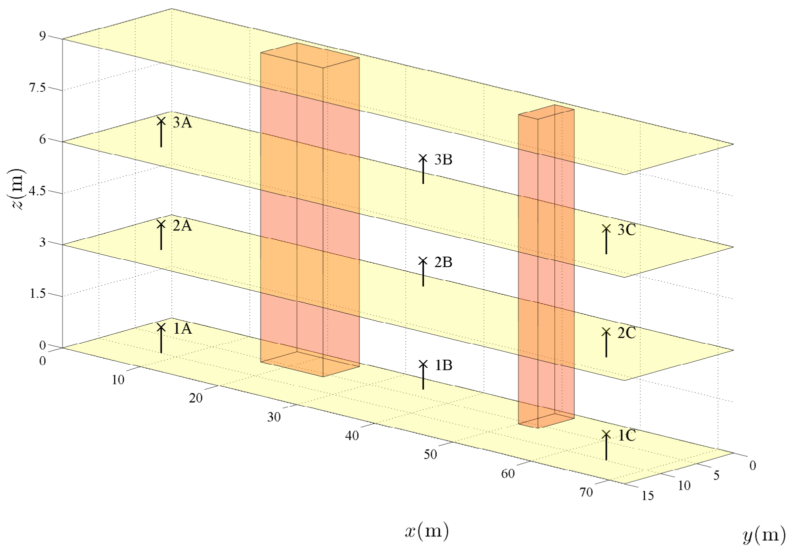

(a) 3D view.

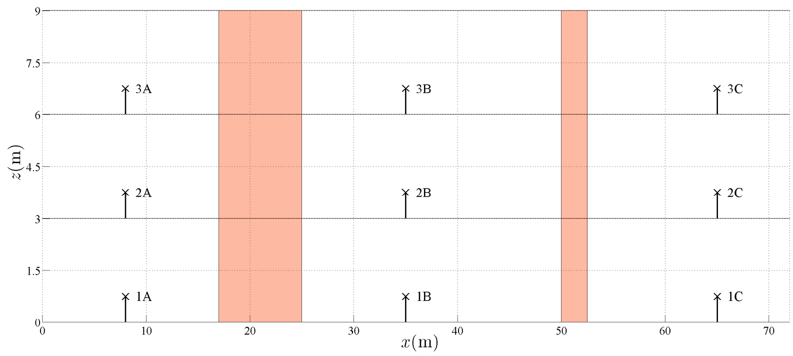

(b) Side view.

Figure 5.4: Illustration of base station deployment locations within floors 1–3 of The Science Building. Base stations are labelled according to their location using the notation yx, in which y refers to the floor (1, 2 or 3), and x being one of three (A, B or C) horizontal locations. Base stations which share a common alphabetical suffix are vertically aligned. The shaded columns represent the elevator shaft and the two stairwells. The x and y-axes are to scale but the z-axis is not.

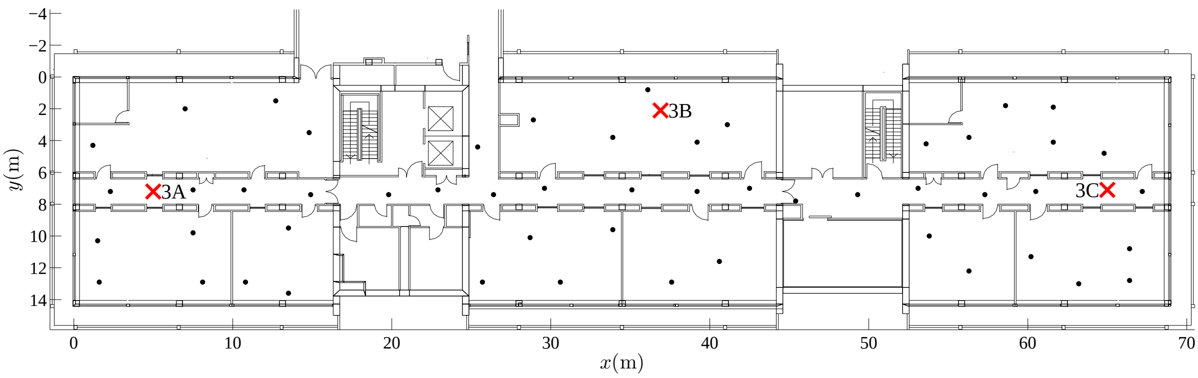

Figure 5.5: Floor plan of level 3 of The Science Building. Base station locations are indicated by $\times$ and mobile station locations are indicated by $\bullet$.

Figure 5.6: Exterior view of the School of Engineering Tower.

During the measurement campaign conducted by Yang in 2009, 11 BSs were deployed inside The Engineering Tower (levels 5–10). Two BSs were deployed on each floor between level 5 and level 9 and one BS was deployed on level 10 as illustrated by Fig 5.7. Odd numbered BSs share a common vertical alignment, as do the even numbered BSs. The RF measurements were taken on level 6. The floor plan for level 6 of The Engineering Tower along with MS and BS locations are shown in Fig 5.9a.

Wong's 2004 measurement campaign [15] involved deploying two indoor BSs on the eighth floor of The Engineering Tower and an additional four BSs outside The Engineering Tower on the rooftops of two neighbouring building (their height equivalent to the sixth floor of The Engineering Tower) as illustrated by Fig. 5.8. The floor plan for level 8 of The Engineering Tower along with MS and BS locations are shown in Fig 5.9b.

At this stage, all the background material needed to understand the performance assessment of OFDM in the presence of interference has been presented. Section §5.3 provides an overview of the investigation plan into the assessment of OFDM-based networks in the presence of interference.

5.3 Investigation Plan

The main focus of the research presented in this thesis is the performance assessment of OFDM-based wireless networks in the presence of interference in indoor environments. In this section, the research philosophy adopted in this thesis is discussed. Fig. 5.10 provides an illustration of the investigation plan adopted in this thesis. The plan shows how the information presented in the next four chapters of this thesis are connected.

The next stage in the investigation starts with the performance assessment of OFDM in the presence of single-carrier narrowband interferers (NBIs), which is presented in Chapter 6. Numerical and analytical

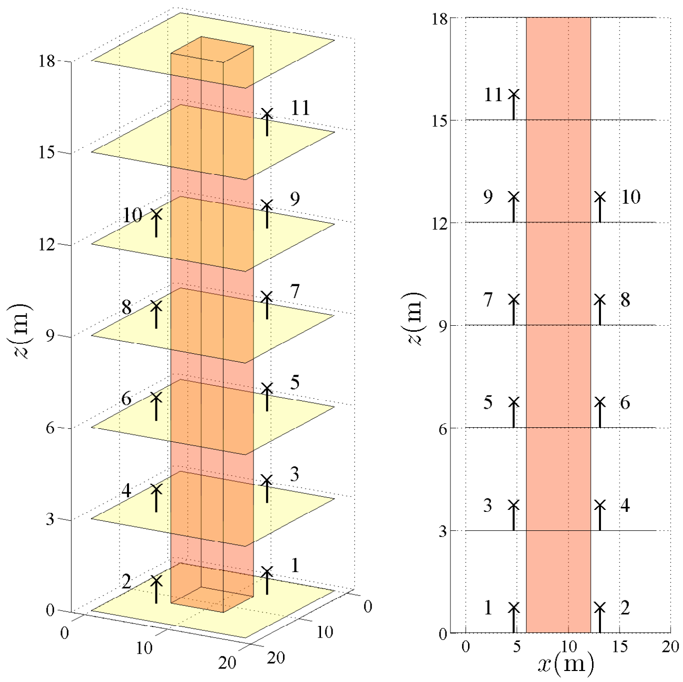

(a) 3D view. **(b)** Side view.

Figure 5.7: Illustration of base station deployment within floors 5–10 of The Engineering Tower (Yang's measurement campaign [108]). Odd numbered base stations are vertically aligned and, similarly, even numbered base stations are vertically aligned as well. The shaded column represent the elevator and stairwell shaft (central core). z-axis is not to scale.

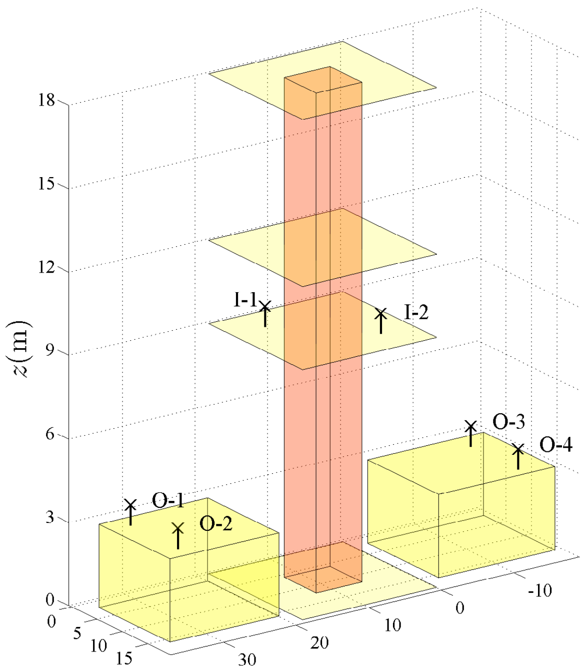

Figure 5.8: Illustration of base station deployment of The Engineering Tower (Wong's measurement campaign [15]). There are two indoor BSs (I-1 and I-2) that are located on the 8th floor of The Engineering Tower and four outdoor BSs (O-1 – O-4) that are located on the roofs of the building adjacent to The Engineering Tower (same height as level 6 of The Engineering Tower). z-axis is not to scale.

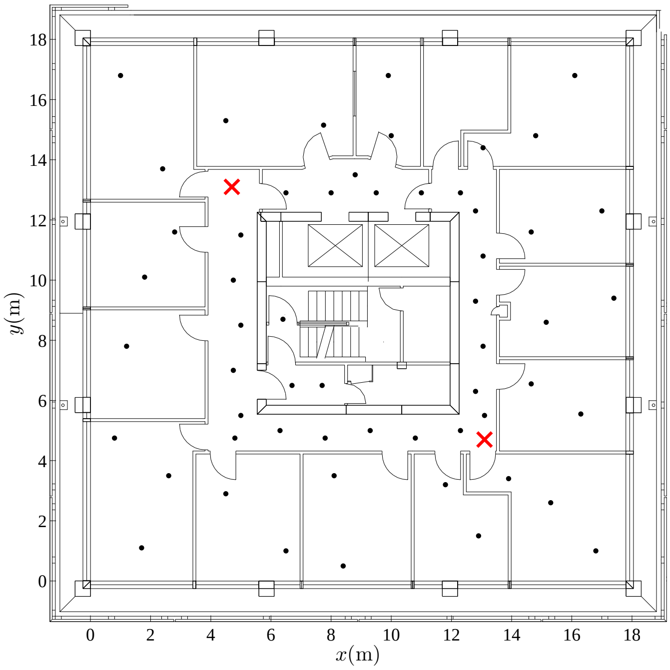

(a) Floor plan of the sixth floor of The Engineering Tower.

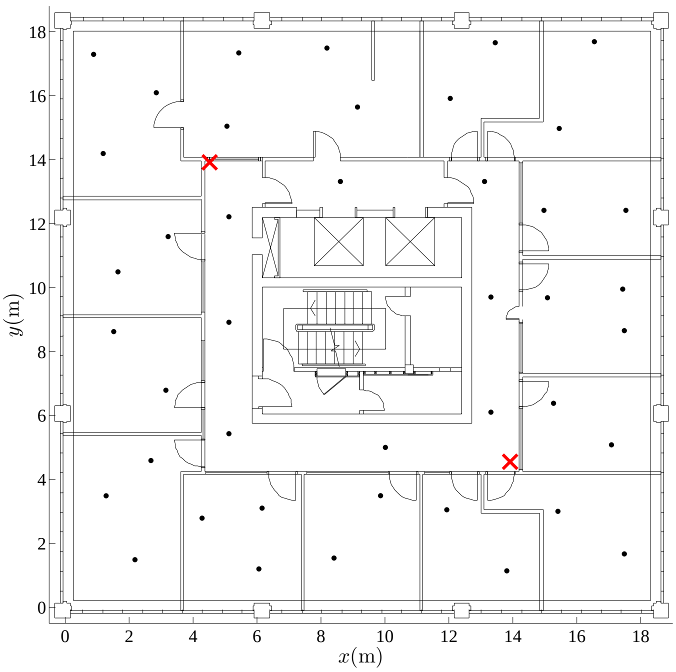

(b) Floor plan of the eighth floor of The Engineering Tower.

Figure 5.9: Floor plans of levels 6 and 8 of The School of Engineering Tower. Base station locations are indicated by $\times$ and mobile station locations are indicated by $\bullet$.

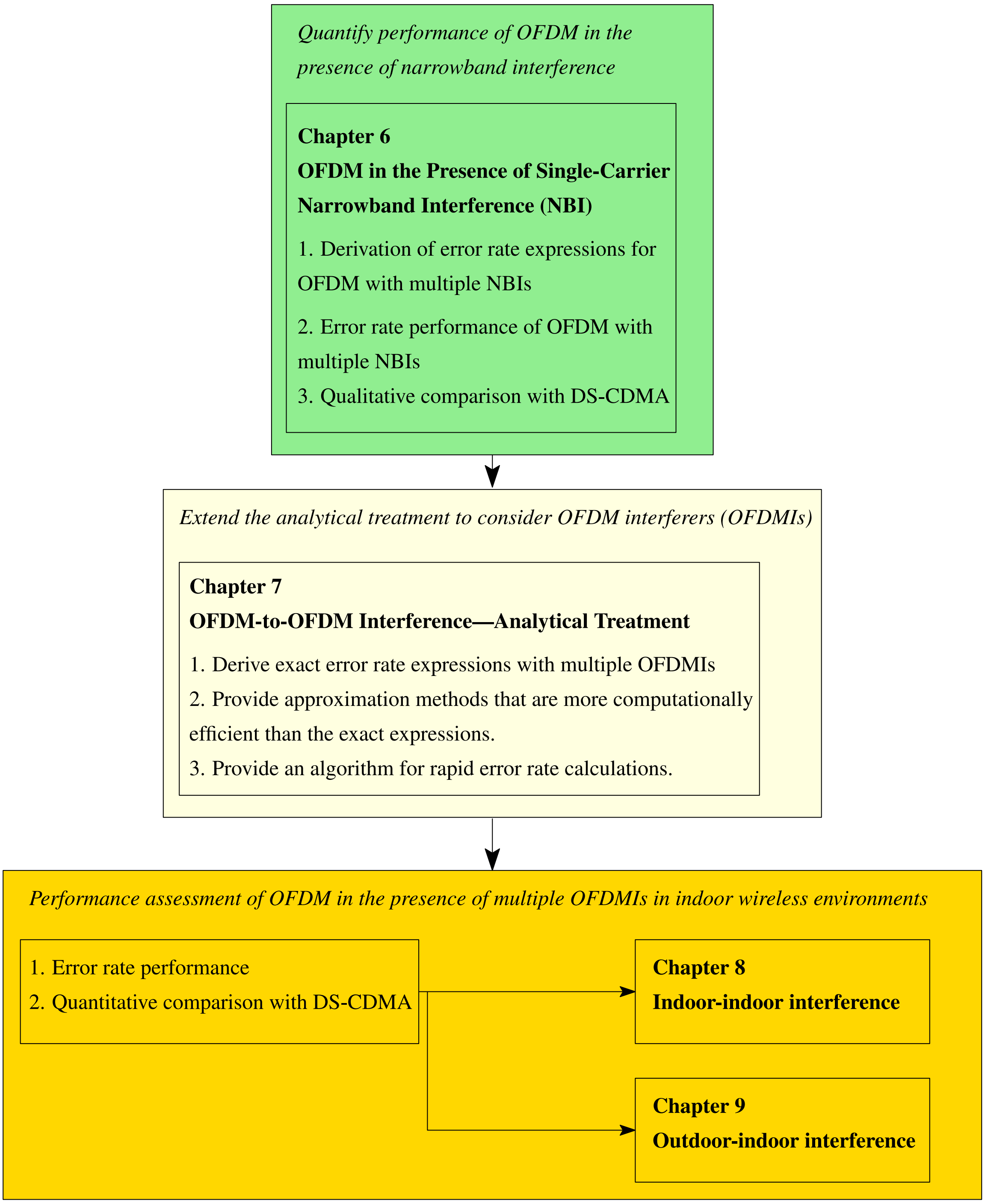

Figure 5.10: Investigation overview of OFDM interference analysis in indoor wireless environments presented in this thesis.

OFDM models are developed in Chapter 6 using the information provided in Chapters 3 to 5. Firstly, error rate expressions for OFDM in the presence of multiple NBIs are derived from the analytical OFDM model. Secondly, the results from these analytical expressions are validated against the numerical model results. Thirdly, an investigation into the general performance of OFDM in the presence of multiple NBIs is presented and general patterns and trends are outlined.

The investigation continues in Chapter 7 by extending the analytical error rate expressions derived in Chapter 6 to consider OFDM interferers (OFDMIs). Exact analytical expressions for error rate performance of OFDM in the presence multiple OFDMIs are derived. Also, several approximation methods that are more computationally efficient than the exact expressions are presented along with their benefits and drawbacks. The results obtained from the analytical error rate expressions (exact and approximations) are compared against the results produced by Monte Carlo numerical models.

The performance assessment of OFDM in the presence of multiple OFDMIs are presented in Chapter 8 for indoor-to-indoor scenarios and in Chapter 9 for outdoor-to-indoor scenarios. Test Environments A and B are used for the analysis in Chapter 8[5] and only Test Environment B is used in Chapter 9[6]. The structure of the investigation in Chapters 8 and 9 is similar to that in Chapter 6 where performance assessment patterns and trends are outlined. Lastly, the OFDM results are compared with DS-CDMA systems under identical environmental conditions. The aim of the comparison with DS-CDMA systems is to find out how similar are the performance patterns of OFDM and DS-CDMA systems in the presence of interference. The feasibility of using DS-CDMA models and interference patterns (already well established in the literature) to give insight into OFDM system performance is explored.

5.4 Summary

The effects of the radio channel on OFDM signals will be investigated in this thesis using measurements performed in two different indoor test environments. In this chapter, the RF propagation measurements configuration has been discussed as well as textual and visual descriptions of the architectures of the two test environments and their respective BS & MS deployment locations. The measurement campaigns provided path loss databases that are used throughout this thesis to estimate signal-to-interference ratios at specific locations within each test environment.

The overview of the investigation into the performance of OFDM in the presence of interference is laid out. The investigation begins in Chapter 6 by considering the presence of multiple single-carrier narrowband interferers and is then extended to consider OFDM interferers in Chapters 7-9.

[5]For Test Environment B, only Y. Yang's database (i.e. sixth floor measurements database) is used since it includes measurement data from BSs that are on several floors within the building.

[6]Only A. Wong's database (i.e. eighth floor measurements database) is used since it includes measurement data from BSs that are *outside* the building.

Chapter 6

OFDM in the Presence of Single-Carrier Narrowband Interference

6.1 Introduction

The investigation of OFDM performance in the presence of interference begins by considering single-carrier narrowband interference (NBI) sources, i.e. tones. OFDM systems that operate in the license-exempt bands (e.g. IEEE 802.11a/g/n WLANs) are especially vulnerable to interference from single-carrier NBI sources. Interference from systems such as cordless phones and garage door openers can be modelled as individual single-carrier NBIs.

Two metrics used to assess the performance of a communication system are the *error rate* and *probability of error*. The error rate is a measure of how often an error occurs when detecting a stream of received message data points (hence it is a rate). When used for mapped symbols, the error rate is called *symbol error rate* (SER) and *bit error rate* (BER) for unmapped data bits. The probability of error is a measure of the likelihood of making an error in the detection of a received message data point. The *probability of symbol error*, P_s, is defined as the probability of the receiver detecting a mapped symbol erroneously (likewise, the the *probability of bit error*, P_b is defined as the probability of the receiver detecting an unmapped data bit erroneously). The error rate and the probability of error metrics are different from each other but they essentially quantify the same entity, the likelihood of making an error at the receiver. Throughout this thesis the SER and P_s are used interchangeably and similarly, for the BER and P_b.

Analytical BER expressions for M-ary QAM systems in the presence of AWGN are given in [109]. Also, analytical BER expressions for OFDM systems in the presence of narrowband interference have been presented in [45, 65, 66], see Table 2.2. In [45], an analytical expression for the BER of BPSK-OFDM in the presence of multiple NBIs is derived along with mitigation techniques. In [66], an expression of the BER for QPSK-OFDM in the presence of narrowband interference is given. The authors of [65] present analytical BER expressions for Multiband OFDM (MB-OFDM) over quasi-static fading channels with OFDM models that include convolutional encoding and bit-interleaving techniques. However, the focus in this thesis is not on MB-OFDM or the effects of coding and interleaving techniques on error rates.

In this chapter, analytical expressions for the SER and BER of M-ary QAM-OFDM in the presence of multiple NBIs are derived (Section §6.2), and can be used for AWGN channels, and flat- & frequency-selective fading channels. These expressions do not include data encoding or interleaving techniques and are derived and presented here as an intermediate step for modelling *OFDM* interferers (OFDMIs) later in the thesis (Chapter 7). The expressions are validated numerically, and their accuracy for different QAM levels demonstrated in Section §6.3. The performance of OFDM in the presence of single and multiple NBIs is presented in Section §6.4 along with qualitative comparison with DS-SS systems. The concept of extending the analytical models presented in this chapter to consider OFDM interferers are discussed in Section §6.5.

6.2 Error Rate Calculations

6.2.1 Post-DFT Signal

The SER and BER expressions are derived for the signals at the final stage of the receiver, i.e. after the DFT (Fig. 3.8b). Therefore, before deriving the SER and BER, an expression for the received signal after it has passed through the DFT is derived first[1]. A received, sampled, baseband OFDM signal, r_n, in the presence of J NBIs can be represented as [45]

$$r_n = c\left(\tau;\, nT\right) \star s\left(nT - \tau_s\right) e^{j[2\pi\nu(nT-\tau_s)+\theta]} + \sum_{i=1}^{J} \beta_i e^{j[2\pi\zeta_i n+\phi_i]} + \eta\left(nT\right), \tag{6.1}$$

where $c\left(\tau;\, nT\right)$ is the doubly dispersive complex fading channel impulse response, T is the symbol period, n is the time domain sample index, $s\left(t\right)$ is the transmitted OFDM signal with N subcarriers, τ_s, ν and θ are, respectively, the time, frequency and phase offsets at the receiver relative to the transmitter, β_i, ζ_i and ϕ_i are, respectively, the amplitude-, normalised frequency- and phase of the ith narrowband interferer, η is complex AWGN with bandwidth $\frac{1}{T}$, and $\star$ is the convolution operator[2].

As discussed in Chapter 4, the channel is assumed to be linear and time invariant and a cyclic prefix is used to remove the effects of ISI. As discussed in Chapter 3, the data for the desired OFDM system is assumed to be uncoded and perfect synchronisation (time and frequency) with desired OFDM transmission is also assumed. The system is assumed to be single-input single-output (SISO) and the QAM constellation is assumed to be square. Applying these assumptions and approximations, r_n becomes

$$r_n = s_n + \sum_{i=1}^{J} \beta_i e^{j[2\pi\zeta_i n+\phi_i]} + \eta_n, \tag{6.2}$$

where s_n is the *desired* OFDM signal at the input of the receiver given by

$$s_n = \frac{1}{N} \sum_{k=0}^{N-1} a_k D_k e^{j2\pi n \frac{k}{N}}, \tag{6.3}$$

[1]This subsection is essentially an extensive review of [45, Sec. II].

[2]N, J, β_i and ζ_i are equivalent to L, N, b_i and $\xi_i T$ in [45], respectively.

where a_k is the channel gain for the kth frequency bin[3] and D_k is the complex envelope of the kth modulated data symbol defined in Equation (3.4). At the receiver, r_n is passed through an N-point DFT. The post-DFT received signal at the kth bin, R_k, is given by

$$R_k = D_k + I_k + H_k, \tag{6.4}$$

where H_k is the post-DFT equivalent of η_n and has a Gaussian pdf given by Equation (4.12). The post-DFT interference component, I_k, is given by

$$\begin{aligned} I_k &= \sum_{n=0}^{N-1} \sum_{i=1}^{J} \beta_i e^{j[2\pi\zeta_i n + \phi_i]} e^{-j2\pi n \frac{k}{N}}, \\ &= \sum_{i=1}^{J} \beta_i \Psi_k \left(\zeta_i, \phi_i\right), \end{aligned}$$

where

$$\Psi_k \left(\zeta_i, \phi_i\right) = \sum_{n=0}^{N-1} e^{j\left[2\pi n\left(\zeta_i - \frac{k}{N}\right) + \phi_i\right]}, \tag{6.5}$$

is the *spectral leakage* component . To simplify this expression, the geometric series expansion given by [110, p 10]

$$\sum_{n=0}^{N-1} a^n = \begin{cases} \frac{1-a^N}{1-a} & a \neq 1 \\ N & a = 1, \end{cases} \tag{6.6}$$

is used to give

$$\begin{aligned} \Psi_k \left(\zeta_i, \phi_i\right) &= e^{j\phi_i} \frac{1 - e^{j\left[2\pi N\left(\zeta_i - \frac{k}{N}\right)\right]}}{1 - e^{j\left[2\pi\left(\zeta_i - \frac{k}{N}\right)\right]}} \\ &= e^{j\phi_i} \frac{e^{j\left[\pi N\left(\zeta_i - \frac{k}{N}\right)\right]}}{e^{j\left[\pi\left(\zeta_i - \frac{k}{N}\right)\right]}} \frac{\left\{e^{j\left[\pi N\left(\zeta_i - \frac{k}{N}\right)\right]} - e^{-j\left[\pi N\left(\zeta_i - \frac{k}{N}\right)\right]}\right\}}{\left\{e^{j\left[\pi\left(\zeta_i - \frac{k}{N}\right)\right]} - e^{-j\left[\pi\left(\zeta_i - \frac{k}{N}\right)\right]}\right\}}. \end{aligned}$$

Using Euler's formula [110, p 71], $\Psi_k \left(\zeta_i, \phi_i\right)$ becomes

$$\begin{aligned} \Psi_k \left(\zeta_i, \phi_i\right) &= \frac{\sin\left[\pi N\left(\zeta_i - \frac{k}{N}\right)\right]}{\sin\left[\pi\left(\zeta_i - \frac{k}{N}\right)\right]} e^{j\left[\pi N\left(\zeta_i - \frac{k}{N}\right) - \pi\left(\zeta_i - \frac{k}{N}\right)\right]} e^{j\phi_i} \\ &= \frac{\sin\left[\pi N\left(\zeta_i - \frac{k}{N}\right)\right]}{\sin\left[\pi\left(\zeta_i - \frac{k}{N}\right)\right]} e^{j\left[\pi(N-1)\left(\zeta_i - \frac{k}{N}\right) + \phi_i\right]}. \end{aligned} \tag{6.7}$$

Therefore, I_k is given by

[3] Only the *effective* SINR at the kth frequency bin is considered in this thesis, meaning all received signal levels are normalised to a_k — thus, a_k is dropped from subsequent expressions.

$$I_k = \sum_{i=1}^{J} \beta_i \frac{\sin\left[\pi N\left(\zeta_i - \frac{k}{N}\right)\right]}{\sin\left[\pi\left(\zeta_i - \frac{k}{N}\right)\right]} e^{j\left[\pi(N-1)\left(\zeta_i - \frac{k}{N}\right)+\phi_i\right]}, \tag{6.8}$$

which represents, essentially, a weighted sum of the amplitudes of the NBIs.

6.2.2 Probability of Symbol Error, P_s

A square or rectangular QAM constellation can be treated as two *independent* amplitude modulated signals (i.e. ASK[4]) on quadrature carriers [39, p. 464], [109]. For a square QAM constellation with M points, both in-phase (I-) and quadrature (Q-) carriers will have $\sqrt{M}$ discrete amplitudes. Therefore, an M-ary QAM symbol is only detected correctly when *both* $\sqrt{M}$-ary ASK symbols are detected correctly [39, p. 464].

Let P_s^I and P_s^Q denote, respectively, the probability of making a symbol error in the I- and Q-channels. As mentioned in Section §6.2.1, H_k has a Gaussian pdf (given by Equation (4.12)) in both the I- and Q-channels and they are assumed to be independent of each other. Therefore, the probability of symbol error, P_s, is given by

$$\begin{aligned} P_s &= 1 - \left(1 - P_s^I\right)\left(1 - P_s^Q\right) \\ &= P_s^I + P_s^Q - P_s^I P_s^Q. \end{aligned} \tag{6.9}$$

In [109], the BER for an M-ary QAM signal is derived. However, the only channel impairment considered is AWGN. In this chapter, the additional effects of multiple NBIs on the SER and BER of an M-ary QAM-OFDM signal are considered. Considering the I-channel for a $\sqrt{M}$-ary ASK mapping: there are $\sqrt{M}-2$ message points with a decision boundary on each side (“middle” message points) and two message points with only one decision boundary on one of their sides (“edge” message points). For example, for a 64QAM mapping scheme (i.e. $M = 64$), there are six middle message points and two edge message points in the I-channel as well as in the Q-channel. However, the effect of the two edge points on the error rate performance is equivalent, mathematically, to *one* middle point, therefore, for each channel, an equivalent of $\sqrt{M} - 1$ middle message points are considered (e.g. seven equivalent middle points each for the I- and Q-channels when $M = 64$). Fig. 6.1 illustrates the concept of middle and edge points on a 64QAM constellation.

Recall the expression for the received signal after the DFT in the kth frequency bin, R_k (Equation (6.4)). Detection errors are caused by the presence of noise, H_k, and interference, I_k. Since H_k is a random variable with a zero mean Gaussian pdf, its presence transforms R_k into a Gaussian random variable with mean of D_k in signal space. The effect of I_k on R_k is that it offsets the mean of R_k by I_k. Therefore, R_k is a Gaussian random variable in signal space with mean $\mu = D_k + I_k$ and variance $\sigma^2 = N_0/2$. A symbol detection error occurs when R_k is detected *outside* the decision boundaries. Fig. 6.2 illustrates the pdf for a middle message point (i.e. with two decision boundaries) for a given superposition of multiple NBIs in the in-phase channel. The shaded areas represent the probability of symbol error in the I-channel, P_s^I (the concepts are identical for the Q-channel).

[4]Amplitude shift keying.

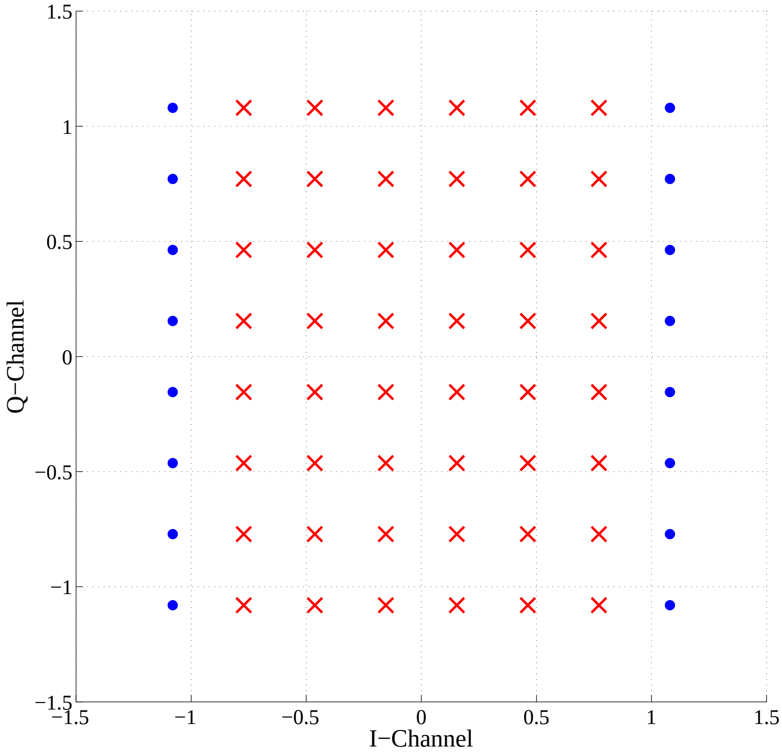

(a) Middle and edge points when considering the I-channel for a 64QAM constellation.

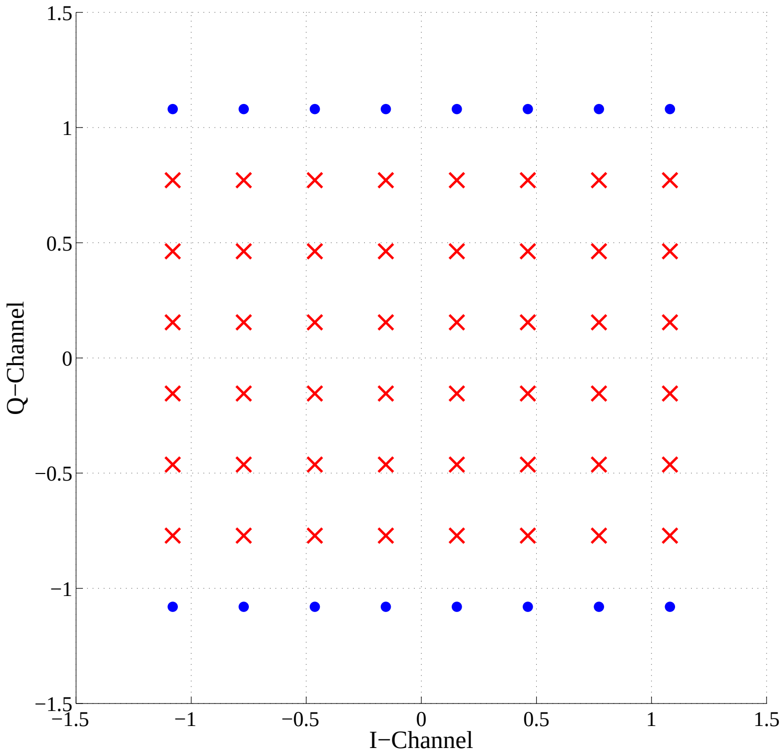

(b) Middle and edge points when considering the Q-channel for a 64QAM constellation.

Figure 6.1: 64QAM constellation illustrating the concept of middle and edge points. Middle points are indicated by $\times$ and edge points are indicated by $\bullet$.

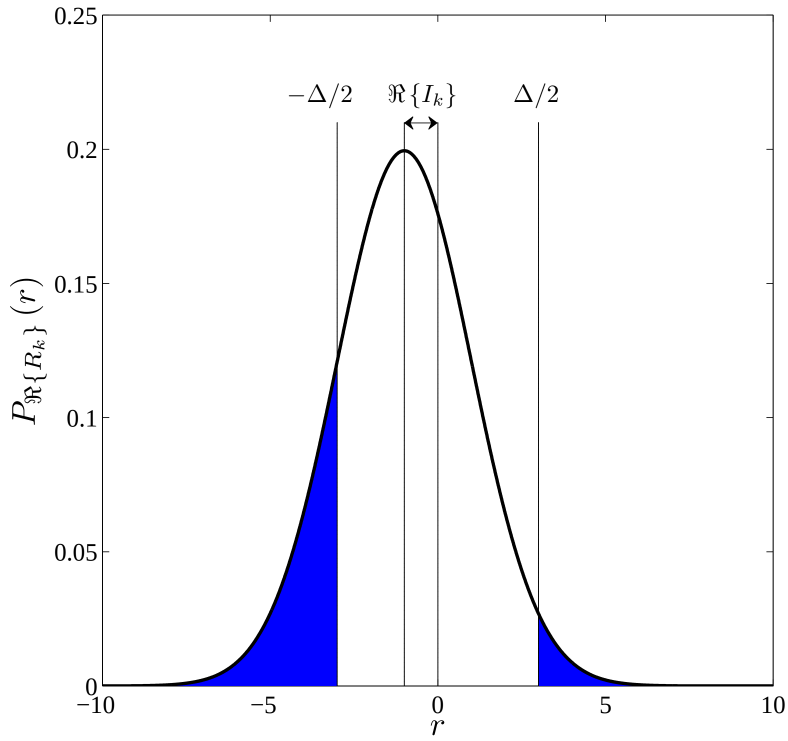

Figure 6.2: Pdf illustration of $\Re\{R_k\}$ for an ASK middle message point (I-channel). The shaded areas represent P_s^I. The x-axis is centered around $\Re\{D_k\}$, i.e. $r = 0 = \Re\{D_k\}$. $\Delta = 6$ in this illustration.

Since there are an equivalent of $\sqrt{M}-1$ middle points out of a total $\sqrt{M}$ message points in the I-channel, the conditional probability of symbol error in the in-phase channel, P_s^I, can be derived as

$$\begin{aligned} P_s^I &= \frac{\sqrt{M}-1}{\sqrt{M}} \frac{1}{\sqrt{\pi N_0}} \left\{ \int_{\frac{\Delta}{2}}^{\infty} \exp\left[\frac{-\left(r+\Re\{I_k\}\right)^2}{N_0}\right] dr + \int_{-\infty}^{-\frac{\Delta}{2}} \exp\left[\frac{-\left(r+\Re\{I_k\}\right)^2}{N_0}\right] dr \right\} \\ &= \frac{\sqrt{M}-1}{2\sqrt{M}} \left\{ \text{erfc}\left[\frac{\frac{\Delta}{2}+\Re\{I_k\}}{\sqrt{N_0}}\right] + \text{erfc}\left[\frac{\frac{\Delta}{2}-\Re\{I_k\}}{\sqrt{N_0}}\right] \right\}, \end{aligned} \tag{6.10}$$

where Δ is the signal space separation distance between adjacent signal levels as well as the decision thresholds, $\Re\{\cdot\}$ denotes the real component, and

$$\text{erfc}(x) \triangleq \frac{2}{\sqrt{\pi}} \int_x^{\infty} e^{-t^2} dt, \tag{6.11}$$

is the complementary error function [110, p 297]. The expression in (6.10) is more meaningful if Δ is expressed in terms of the average symbol or bit energy. For square M-ary QAM constellations with bipolar symmetric signals, Δ is given by [39, p. 464] (for the derivation see Appendix A)

$$\frac{\Delta}{2} = \sqrt{\frac{3E_b \log_2(M)}{2(M-1)}}, \tag{6.12}$$

where E_b is the average energy-per-bit. Therefore, the conditional probability of symbol error in the in-phase channel can be written as

$$P_s^I = \frac{\sqrt{M}-1}{2\sqrt{M}}\left\{\text{erfc}\left[\sqrt{\frac{3\log_2(M)}{2(M-1)}\frac{E_b}{N_0}} + \frac{\Re\{I_k\}}{\sqrt{N_0}}\right] + \text{erfc}\left[\sqrt{\frac{3\log_2(M)}{2(M-1)}\frac{E_b}{N_0}} - \frac{\Re\{I_k\}}{\sqrt{N_0}}\right]\right\}. \tag{6.13}$$

Similarly, P_s^Q can be derived as

$$P_s^Q = \frac{\sqrt{M}-1}{2\sqrt{M}}\left\{\text{erfc}\left[\sqrt{\frac{3\log_2(M)}{2(M-1)}\frac{E_b}{N_0}} + \frac{\Im\{I_k\}}{\sqrt{N_0}}\right] + \text{erfc}\left[\sqrt{\frac{3\log_2(M)}{2(M-1)}\frac{E_b}{N_0}} - \frac{\Im\{I_k\}}{\sqrt{N_0}}\right]\right\}, \tag{6.14}$$

where $\Im\{\cdot\}$ denotes the imaginary component. The interference components in (6.13) and (6.14) can be expressed as

$$\frac{\Re\{I_k\}}{\sqrt{N_0}} = \sum_{i=1}^{J}\sqrt{\gamma_i}\,\Re\{\Psi_k(\zeta_i,\phi_i)\}, \tag{6.15}$$

$$\frac{\Im\{I_k\}}{\sqrt{N_0}} = \sum_{i=1}^{J}\sqrt{\gamma_i}\,\Im\{\Psi_k(\zeta_i,\phi_i)\}, \tag{6.16}$$

where $\gamma_i = \beta_i^2/N_0$ is the *interference-to-noise ratio* (INR) of the ith NBI. Therefore, the expressions in (6.13) and (6.14) are denoted as $P_s^I\left(\frac{E_b}{N_0},\gamma \mid k,\zeta,\phi\right)$ and $P_s^Q\left(\frac{E_b}{N_0},\gamma \mid k,\zeta,\phi\right)$ respectively, and the total SER as $P_s\left(\frac{E_b}{N_0},\gamma \mid k,\zeta,\phi\right)$. The SER for all frequency bins is obtained by averaging across all $N-K$ *occupied* bins, i.e.

$$P_s\left(\frac{E_b}{N_0},\gamma \mid \zeta,\phi\right) = \frac{1}{N-K}\sum_{k=0}^{N-K-1} P_s\left(\frac{E_b}{N_0},\gamma \mid k,\zeta,\phi\right), \tag{6.17}$$

where K is the number of subcarriers set to zero for spectral blanking. In the multiple access case, i.e. OFDMA, the uth user occupying $\boldsymbol{f}^u = \boldsymbol{k}^u/N$ frequency bins, where $\boldsymbol{k}^u$ is a vector of size v containing the indicies of the frequencies occupied by the uth user, will have a SER of

$$P_s^u\left(\frac{E_b}{N_0},\gamma \mid \zeta,\phi\right) = \frac{1}{v}\sum_{\forall k\in\boldsymbol{k}^u} P_s\left(\frac{E_b}{N_0},\gamma \mid k,\zeta,\phi\right). \tag{6.18}$$

The mean SER for all possible values of $\zeta \sim U\,[0,1]$ and $\phi \sim U\,[-\pi,\pi]$ is obtained by averaging over the pdfs of ζ and ϕ giving

$$\begin{aligned} P_s\left(\frac{E_b}{N_0},\gamma\right) &= \iint\limits_{\zeta\phi} P_s\left(\frac{E_b}{N_0},\gamma \mid \zeta,\phi\right) p_\zeta(\zeta)\, p_\phi(\phi)\, d\phi d\zeta \\ &= \frac{1}{2\pi}\int_0^1\int_{-\pi}^{\pi} P_s\left(\frac{E_b}{N_0},\gamma \mid \zeta,\phi\right) d\phi d\zeta. \end{aligned} \tag{6.19}$$

6.2.3 Probability of Bit Error, P_b

The relationship between the probability of bit error, P_b, the probability of bit error in the I-channel, P_b^I, and the probability of bit error in the Q-channel, P_b^Q is different from that between P_s, P_s^I and P_s^Q. This is because the bits carried by the two channels (I and Q) are *independent* of each other and Gray coding is assumed. Thus, P_b is given by

$$P_b = \frac{1}{2}\left(P_b^I + P_b^Q\right). \tag{6.20}$$

Calculating P_b^I and P_b^Q is slightly more complicated than calculating their symbol error counterparts. This is because of the Gray coding used, which means when a received symbol is detected erroneously (more than one decision boundary away), it is not straightforward to determine how many data *bits* were detected erroneously. The number of data bits per mapped symbol is determined by the QAM level used according to

$$b = \log_2(M). \tag{6.21}$$

Gray coding ensures that adjacent message points in the QAM constellation have just *one* bit difference between them. This is used to ensure that detection errors resulting from crossing one decision boundary would result in $1/b$ data bits being detected erroneously. Fig. 6.3 shows a 16QAM constellation using Gray coding. In [109], analytical P_b expressions for an M-ary QAM system in the presence of AWGN are derived. The analysis presented in [109] is extended here to consider the effect of multiple NBIs on P_b. However, the principles of deriving P_b here are the same as in [109] and will be repeated here for convenience.

As mentioned earlier, a QAM signal can be considered as two independent amplitude modulated signals on quadrature carriers (I and Q). Taking the 16QAM constellation shown in Fig. 6.3 as an example, the data bits in the QAM signal can be represented as $x_0x_1y_0y_1$, where the bits represented by x are carried by the I-carrier and the bits represented by y are carried by the Q-carrier. Considering the I-channel (the same principles apply for the Q-channel), the axes Q, q_1 and q_2 are the decision boundaries, as shown in Fig. 6.3b. The estimate of data bit x_0, $\hat{x}_0$, is determined according to the location of the received message point in signal space relative to the Q-axis. Therefore, $\hat{x}_0 = \mathrm{B}|_Q$, where $\mathrm{B}|_a$ is the data bit decision result (0 or 1) that is found by a hard decision based on the axis a. The second data bit estimation is determined by the axes q_1 and q_2 according to $\hat{x}_1 = \mathrm{B}|_{q_1} \oplus \mathrm{B}|_{q_2}$, where $\oplus$ is the logical *exclusive OR* operator[5]. In [109], it is assumed that a bit error is most likely caused by a noise magnitude exceeding $\Delta/2$ and the probability of the noise magnitude exceeding $3\Delta/2$ is insignificant. Thus, the decision statistic about axis q_1 is considered independent of that of axis q_2. Therefore, $P_Q = P_{q_1} = P_{q_2}$, where P_a is the probability of error corresponding to the decision based on the a-axis. Also, $P(x_0) = P_Q$ and $P(x_1) \cong P_{q_1} + P_{q_2} = 2P_Q$, where $P(x_i)$ is the probability of error given that x_i was transmitted. Similarly for the Q-channel, $P(y_0) = P_Q$ and $P(y_1) \cong 2P_Q$. Therefore, P_b for 16QAM with equi-probable symbols is given by

[5] It is impossible for $\mathrm{B}|_{q_1} = 0$ and $\mathrm{B}|_{q_1} = 1$ to be true simultaneously.

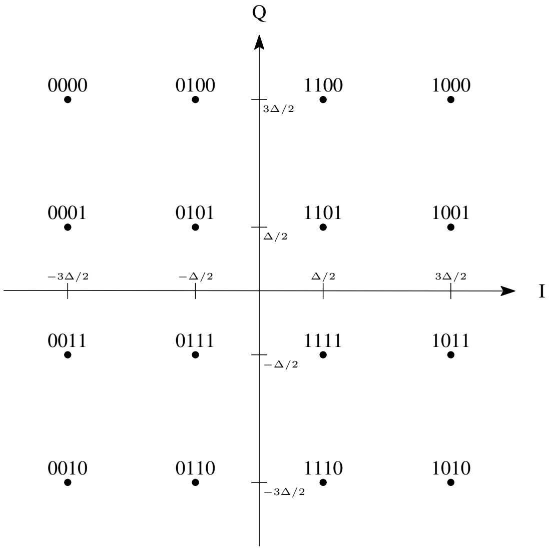

(a) 16QAM constellation with Gray coding.

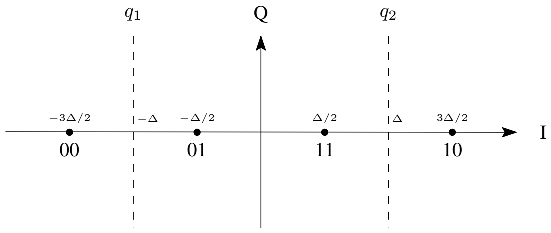

(b) I-channel of a Gray coded 16QAM constellation.

Figure 6.3: Gray coding illustration for a 16QAM constellation (adapted from [109]).

$$P_{b,16\text{QAM}} = \frac{1}{2}\left(1+2\right)P_Q.$$

For a generic M-ary QAM signal, it can be shown that [109]

$$\begin{aligned} P_b &\cong \frac{1}{\log_2\left(\sqrt{M}\right)}\left(1+2+4+\cdots+2^{\log_2\left(\sqrt{M}-1\right)}\right)P_Q \\ &= \frac{2}{\log_2\left(M\right)}\left(\sqrt{M}-1\right)P_Q. \end{aligned} \tag{6.22}$$

To find P_Q, first consider the message points on the left hand side of the Q-axis in Fig. 6.3b (i.e. points “00” and “01”). A bit error would occur if the received message is estimated to be on the right hand side of the Q-axis when either of the left hand side message points was transmitted. For the message points “00” and “01” in the presence of just AWGN, P_Q becomes

$$P_{Q,00} = \text{erfc}\left[\frac{\Delta/2}{\sqrt{N_0}}\right]$$

$$P_{Q,01} = \text{erfc}\left[\frac{3\Delta/2}{\sqrt{N_0}}\right].$$

Given the symmetry around the Q-axis (i.e. $P_{Q,11} = P_{Q,01}$ and $P_{Q,10} = P_{Q,00}$) and the fact that P_Q is the average of all the individual probabilities of error, P_Q in the presence of AWGN becomes

$$P_Q = \frac{1}{\sqrt{M}}\sum_{m=1}^{\sqrt{M}/2}\text{erfc}\left[\frac{(2m-1)\frac{\Delta}{2}}{\sqrt{N_0}}\right].$$

Therefore, P_b in the presence of AWGN[6] is given by [109][7]

$$P_b\left(\frac{E_b}{N_0}\right) \approx \varsigma_M \sum_{m=1}^{\sqrt{M}/2} \operatorname{erfc}\left[(2m-1)\,\varrho_M\sqrt{\frac{E_b}{N_0}}\right], \tag{6.23}$$

where

$$\varsigma_M = \frac{2}{\log_2(M)}\left(1-\frac{1}{\sqrt{M}}\right), \tag{6.24}$$

and

$$\varrho_M = \sqrt{\frac{3\log_2(M)}{2(M-1)}}. \tag{6.25}$$

However, when multiple NBIs are present as well as AWGN, the probability of bit error in the I-channel, P_b^I, becomes

$$\begin{aligned} P_b^I\left(\frac{E_b}{N_0},\gamma \mid k,\zeta,\phi\right) \;\approx\; & \frac{\varsigma_M}{2}\sum_{m=1}^{\sqrt{M}/2}\left\{\operatorname{erfc}\left[(2m-1)\,\varrho_M\sqrt{\frac{E_b}{N_0}}+\sum_{i=1}^{J}\sqrt{\gamma_i}\,\Re\left\{\Psi_k(\zeta_i,\phi_i)\right\}\right]+\right. \\ & \left.\operatorname{erfc}\left[(2m-1)\,\varrho_M\sqrt{\frac{E_b}{N_0}}-\sum_{i=1}^{J}\sqrt{\gamma_i}\,\Re\left\{\Psi_k(\zeta_i,\phi_i)\right\}\right]\right\}. \end{aligned} \tag{6.26}$$

Similarly, for the Q-channel

$$\begin{aligned} P_b^Q\left(\frac{E_b}{N_0},\gamma \mid k,\zeta,\phi\right) \;\approx\; & \frac{\varsigma_M}{2}\sum_{m=1}^{\sqrt{M}/2}\left\{\operatorname{erfc}\left[(2m-1)\,\varrho_M\sqrt{\frac{E_b}{N_0}}+\sum_{i=1}^{J}\sqrt{\gamma_i}\,\Im\left\{\Psi_k(\zeta_i,\phi_i)\right\}\right]+\right. \\ & \left.\operatorname{erfc}\left[(2m-1)\,\varrho_M\sqrt{\frac{E_b}{N_0}}-\sum_{i=1}^{J}\sqrt{\gamma_i}\,\Im\left\{\Psi_k(\zeta_i,\phi_i)\right\}\right]\right\}, \end{aligned} \tag{6.27}$$

and $P_b\left(\frac{E_b}{N_0},\gamma \mid k,\zeta,\phi\right)$ is related to $P_b^I\left(\frac{E_b}{N_0},\gamma \mid k,\zeta,\phi\right)$ and $P_b^Q\left(\frac{E_b}{N_0},\gamma \mid k,\zeta,\phi\right)$ according to Equation (6.20). The expressions for $P_b\left(\frac{E_b}{N_0},\gamma \mid \zeta,\phi\right)$, $P_b^u\left(\frac{E_b}{N_0},\gamma \mid \zeta,\phi\right)$ and $P_b\left(\frac{E_b}{N_0},\gamma\right)$ are obtained in the same manner as Equations (6.17)-(6.19), respectively.

6.2.4 Normalised Frequency Offset, α

The term α is used in this thesis to describe the relative frequency offset between the NBI and a desired OFDM subcarrier. The normalised, sampled *desired* subcarrier frequencies, f_k, are given by

---

[6] In the presence of just AWGN, $P_b^I = P_b^Q = P_b$.

[7] In [109], the P_b expression uses the Q-function defined as $Q(x) \triangleq \frac{1}{\sqrt{2\pi}}\int_x^\infty \exp\left(-t^2/2\right)dt$. The Q-function and $\operatorname{erfc}(\cdot)$ are inter-related according to $Q(x) = \frac{1}{2}\operatorname{erfc}\left(x/\sqrt{2}\right)$ and $\operatorname{erfc}(x) = 2Q\left(\sqrt{2}x\right)$.

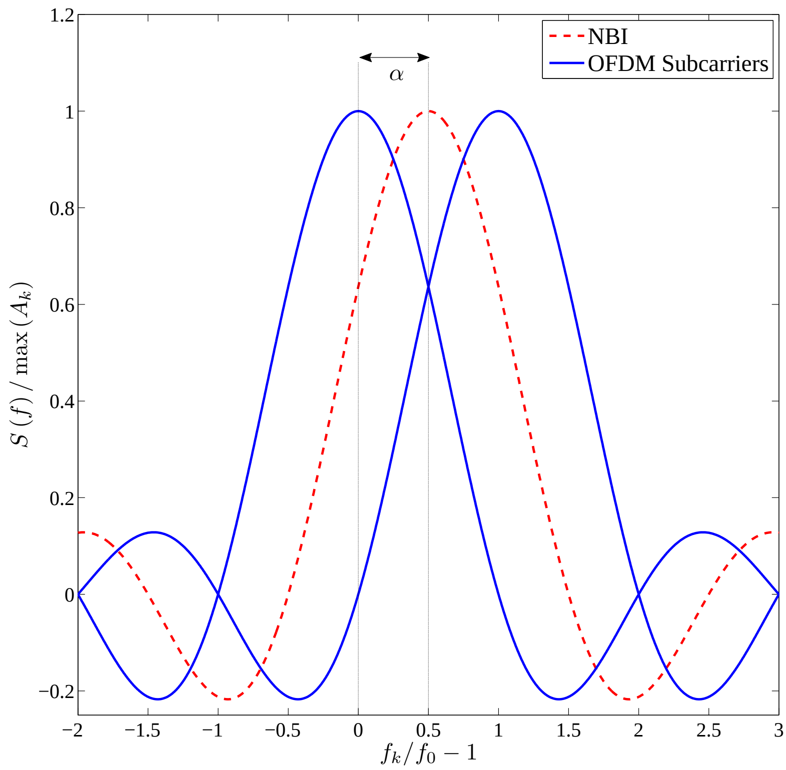

Figure 6.4: Illustration of the normalised frequency offset, α, between a narrowband interfering carrier and two OFDM subcarriers. In this example the narrowband carrier is halfway between the two OFDM subcarriers, i.e. $\alpha = 0.5$.

$$f_k = \frac{k}{N} \qquad k = 0, 1, 2, \ldots N - 1,$$

and the normalised ith *interfering* carrier frequency is given by

$$\zeta_i = \frac{k + \alpha_i}{N} \qquad k = 0, 1, 2, \ldots N - 1, \tag{6.28}$$

where $\alpha_i \in [0,1]$ is the normalised frequency offset. For example, $\alpha = 0$ means the NBI's frequency is identical to that of one the subcarriers, and $\alpha = 0.5$ means the NBI has a frequency exactly halfway between two OFDM subcarriers as illustrated in Fig. 6.4.

6.3 Analytical Models' Validity

The error rate expressions derived in Section §6.2 are validated against a Monte Carlo numerical model[8]. The results obtained from this model are labelled P_s^{MC} and P_b^{MC} for the SER and BER respectively. Fig. 6.5 shows the SER and BER performance of M-ary QAM OFDM in the presence of a single NBI normalised to the results obtained by the Monte Carlo numerical model as a function of E_b/N_0. Considering the P_s performance first (Fig. 6.5a), the results from the analytical model closely match those

[8]Details of the Monte Carlo numerical model are presented in Appendix B.

Table 6.1: Peak and mean percentage deviation between analytical and Monte Carlo values for P_s and P_b in Fig. 6.5.

	P_s/P_s^{MC}		P_b/P_b^{MC}	
	Mean % deviation	Peak % deviation	Mean % deviation	Peak % deviation
$M = 2$	1%	3.3%	1%	3.3%
$M = 4$	0.94%	2.87%	0.92%	2.84%
$M = 16$	0.87%	2.91%	9.8%	22.43%
$M = 64$	0.82%	3.55%	15.5%	82.62%

obtained from the numerical model for all QAM levels[9]. The mean and peak percentage deviation between the analytical and numerical results presented in Fig. 6.5 are shown in Table 6.1. This difference has been observed to reduce as the number of trials in the Monte Carlo method is increased, and can thus be attributed to the inherent resolution of the Monte Carlo method. The reason for this consistent high accuracy for SER values is that once a received message point is estimated to be outside *any* decision boundary, a symbol error occurs and this is easily calculated according to the P_s expressions in Section §6.2.2. Fig. 6.5a is the only figure showing the accuracy of the SER expressions in this chapter because all other scenarios give very similar plots.

The accuracy of the BER expressions, on the other hand, are not as consistent as their SER counterparts. This is because of the Gray coding (as explained in Section §6.2.3). Considering the accuracy of the analytical BER expressions as a function of E_b/N_0 (Fig. 6.5b and Table 6.1), it is observed that for BPSK and QPSK signal mapping schemes, there is close agreement between the analytical and numerical P_b values. However, for higher QAM levels (i.e. $M \geq 16$), there are significant discrepancies between the analytical and numerical P_b values, especially for high E_b/N_0 values. These discrepancies between the analytical and numerical values can be explained by examining the scenario parameters: In Fig. 6.5, the OFDM system is in the presence of a single NBI (i.e. $J = 1$) with SIR = 15 dB, $\alpha = 0$ and $\phi = 0$. The α and ϕ values ensure that there is no spectral leakage from that interferer, i.e. $\Psi_k(\zeta, \phi) = N$ for the affected OFDM subcarrier and $\Psi_k(\zeta, \phi) = 0$ for all other OFDM subcarriers. This means that *all* the interferer's energy is directed at the in-phase component of *one* subcarrier. For $M \geq 16$ an SIR value of 15 dB is considered to be a high level of interference, which means there is enough interference power to make the received message point cross more than one decision boundary in signal space. The reason for the discrepancies is that the P_b expressions derived in Section 6.2.3 *assume* that the likelihood of crossing a decision boundary more than $3\Delta/2$ is insignificant. This assumption is perfectly reasonable when considering only AWGN or low QAM levels (i.e. $M < 16$) since the noise is characterised by a Gaussian pdf and is very unlikely for its magnitude to exceed $3\Delta/2$ and for low QAM levels there is only one decision boundary to cross in the I- and Q-channels (no decision boundary in the Q-channel for BPSK). From Fig. 6.5b the discrepancies between the analytical and numerical BER values for $M \geq 16$ become more significant as E_b/N_0 increases. This is because when E_b/N_0 is low (i.e. high levels of noise), the probability that the noise will offset the effects of the interference is higher than when the noise is weak.

[9]For BPSK (i.e. $M = 2$), $P_s = P_b$.

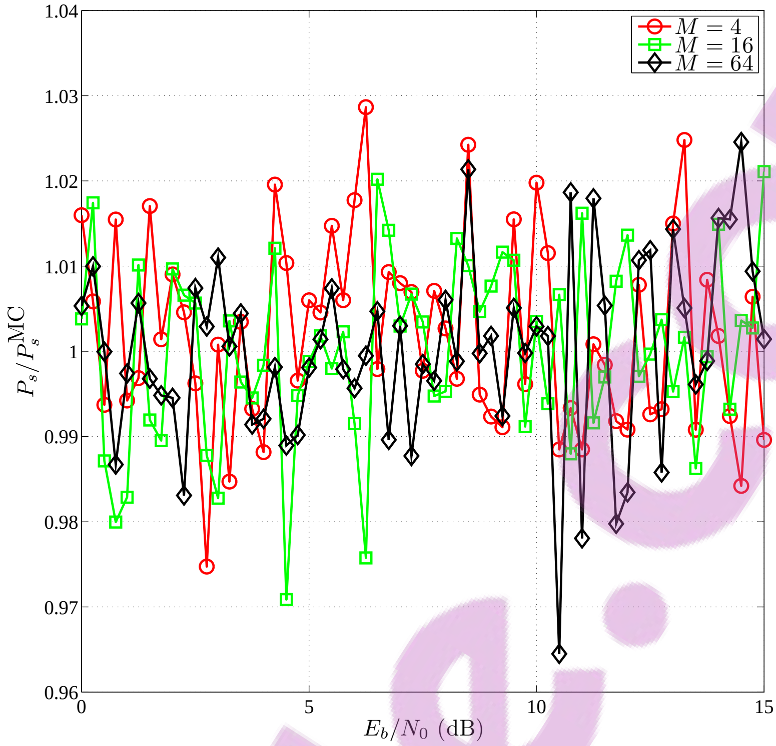

(a) P_s/P_s^{MC}.

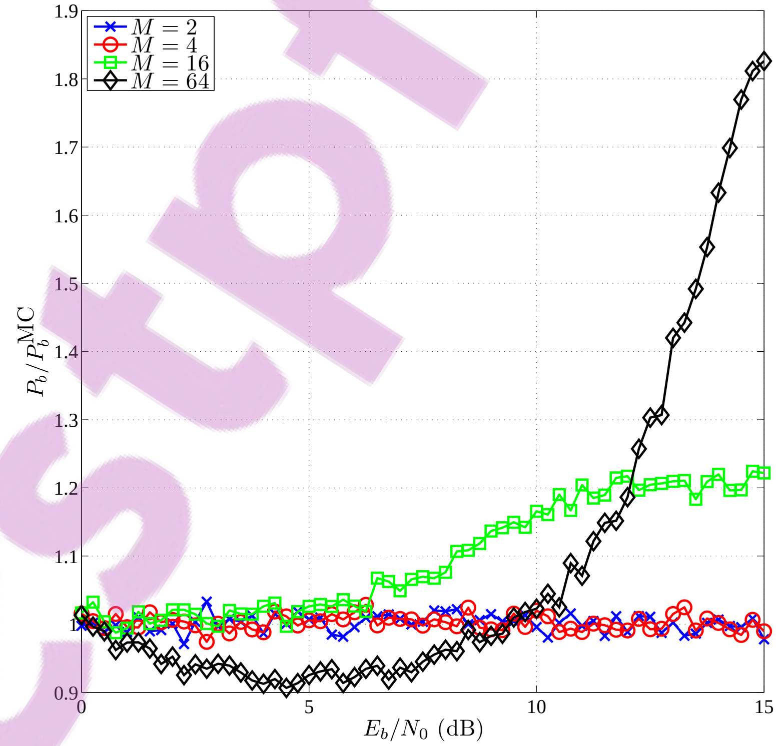

(b) P_b/P_b^{MC}.

Figure 6.5: P_s and P_b versus E_b/N_0 performance of OFDM in the presence of a single NBI normalised to the results obtained by the Monte Carlo numerical model. SIR $= 15$ dB, $\alpha = 0$, $\phi = 0$ and $J = 1$.

Table 6.2: Peak and mean percentage deviation between analytical and Monte Carlo values for P_b in Fig. 6.6.

	SIR = 15 dB		SIR = 20 dB	
	Mean % deviation	Peak % deviation	Mean % deviation	Peak % deviation
$M = 4$	0.82%	2.6%	N/A	
$M = 16$	10.2%	20.53%	0.71%	2.02%
$M = 64$	27.22%	83.23%	12.03%	56.03%

Table 6.3: Peak and mean percentage deviation between analytical and numerical values for P_b in Fig. 6.7.

	Mean % deviation	Peak % deviation
$M = 4$	0.87%	2.23%
$M = 16$	9.05%	18.9%
$M = 64$	18.7%	28%

However, when there *is* spectral leakage, the accuracy of the analytical BER expressions for $M \geq 16$ improves dramatically. Fig. 6.6 shows BER performance of M-ary QAM OFDM[10] in the presence of a single NBI normalised to the results obtained by the Monte Carlo numerical model as a function of α[11]. The accuracy of the analytical BER expressions for the QPSK signal mapping is unaffected by α, but for $M \geq 16$, there is significant accuracy improvement with $\alpha \neq 0$ values. This improvement in accuracy is due to the fact that the interferer's energy is no longer focused on the I-channel of a single OFDM subcarrier. Instead, the interferer's energy is smeared across the entire OFDM spectrum in both the I- and Q-channels. However, even when there is spectral leakage, there are still considerable discrepancies between the analytical and numerical BER values when the SIR is 15 dB (Fig. 6.6a). This is because the interference power is still strong enough to cause multiple crossings of decision boundaries. But when the SIR is increased to 20 dB (Fig. 6.6b), the accuracy for the analytical expressions improves considerably as seen in Fig. 6.6b and Table 6.2. For $M = 16$, the accuracy of the analytical BER expressions become dependent only on the resolution of the Monte Carlo numerical method, i.e. the numerical results would asymptote to the analytical BER values. The accuracy for $M = 64$ improves significantly but there are still discrepancies with the numerical results and that is because the interference power is still strong enough to cause multiple crossings of decision boundaries.

Fig. 6.7 shows BER performance of M-ary QAM OFDM in the presence of six NBIs normalised to the results obtained by the Monte Carlo numerical model as a function of the SIR. Each NBI has an equal share of the total interference power (i.e. $1/J$th of the total interference power[12]) and has a different α value. As previously seen, the analytical BER values for QPSK match very well with their numerical counterparts across all SIR values as shown in Fig. 6.7 and Table 6.3. As the SIR increases, the accuracy for the analytical BER expressions for $M \geq 16$ improves considerably.

To summarise, the analytical SER and BER expressions derived in Section §6.2.2 and §6.2.3 have been validated against a Monte Carlo numerical model. The SER expressions are seen to be valid and accurate. The BER expressions are valid, accurate for BPSK and QPSK signal mapping schemes and can be used

[10] BPSK performance is not shown since $P_b = P_s$ and that is always very accurate.

[11] α values are shown from 0 to 0.5 since there is symmetry around $\alpha = 0.5$ when $\phi = 0$, e.g. results for $\alpha = 0.7$ are identical to those with $\alpha = 0.3$.

[12] With this arrangement, the signal-to-ith-interference ratio, SIR_i, is given by $\mathrm{SIR}_i = \mathrm{SIR} \times J$.

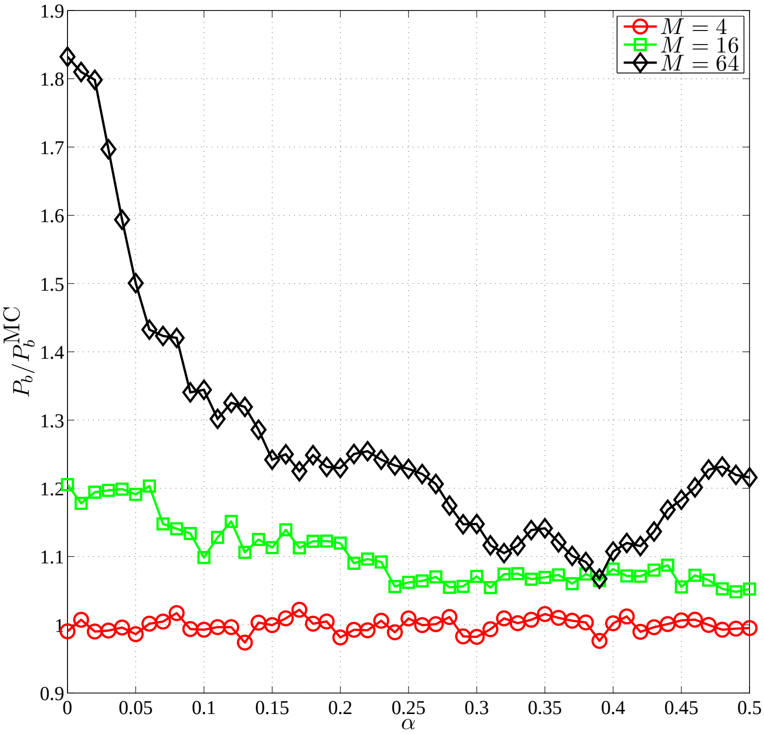

(a) SIR $= 15$ dB.

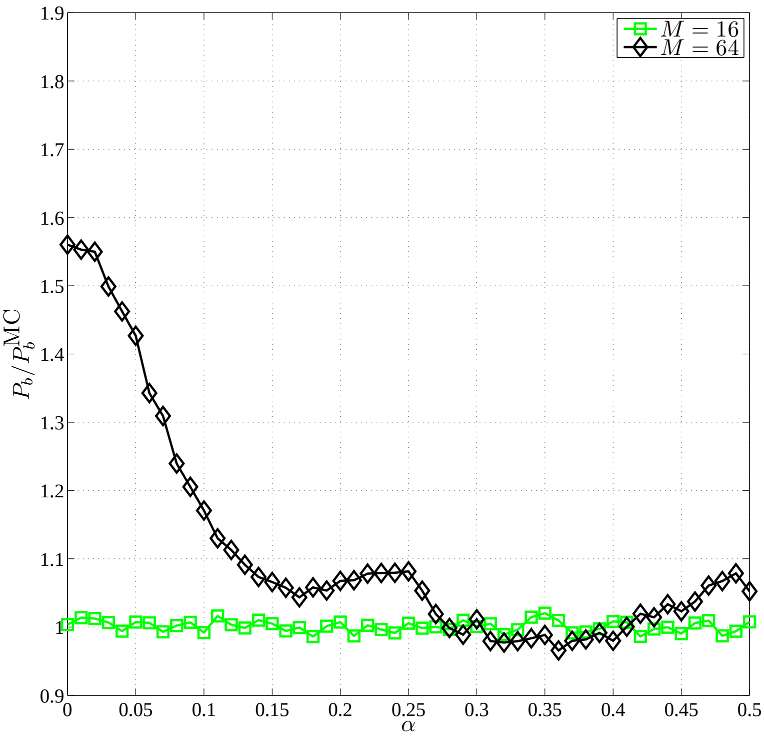

(b) SIR $= 20$ dB.

Figure 6.6: P_b versus α performance of OFDM in the presence of a single NBI normalised to the results obtained by the Monte Carlo numerical model. $E_b/N_0 = 15$ dB and $\phi = 0$.

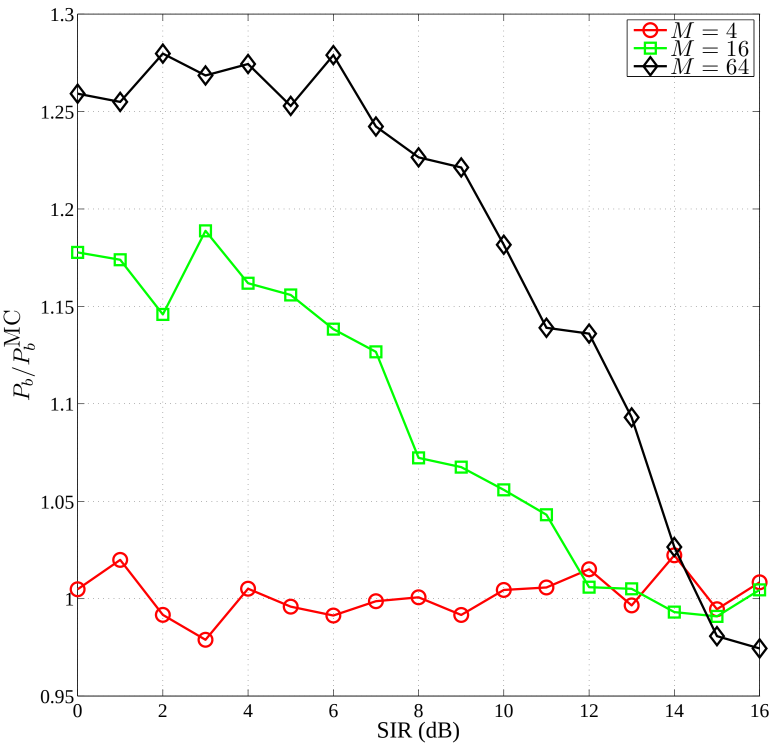

Figure 6.7: P_b versus SIR performance of OFDM in the presence of six NBIs normalised to the results obtained by the Monte Carlo numerical model. $E_b/N_0 = 15$ dB, $\alpha = [0,0.1,0.2,0.3,0.4,0.5]$, $\phi = 0\ \forall i$ and $J = 6$.

for any scenario for those mapping schemes. However, for higher QAM levels (i.e. $M \geq 16$), the accuracy of the BER expressions vary dramatically depending on the scenario parameters. The analytical BER expressions will *not* give accurate results if the following conditions apply simultaneously:

1. $M \geq 16$;
2. Low signal-to-interference-and-noise ratio (SINR), i.e. high levels of interference and noise; and
3. Low amounts of spectral leakage.

However, that does not mean the P_b expressions cannot be used for $M \geq 16$, since in practice, $M \geq 16$ will not be used anyway for low SINR conditions. This means that when the appropriate channel conditions allow the use of higher QAM levels, the analytical P_b expressions derived in Section §6.2.3 can be used with confidence.

6.4 Error Rate Performance Assessment

6.4.1 Single Narrowband Interferer

As identified by the analytical error rate expressions, there are several factors that influence the error rate performance of an OFDM system in the presence of narrowband interference. One key influencing factor is the interference spectral leakage produced by the DFT at the receiver, $\Psi_k(\zeta, \phi)$, which is a function of the interferer's frequency, ζ (and consequently α), and phase offset, ϕ. Fig. 6.8 illustrates the impact of α and ϕ on the BER performance of a QPSK-OFDM system. It is clear from Fig. 6.8 that the BER pattern repeats every $\pi/2$ radians and thus it would be sufficient to consider $\phi \in [-\pi/4, \pi/4]$ radians. Also, when $\phi = x\pi/4$ where x is an integer number, the BER has even symmetry around $\alpha = 0.5$, i.e. $\xi(\alpha) = \xi(-\alpha) = \xi(1-\alpha) = \xi(\alpha-1)$, where $\xi(\alpha)$ is the error rate expression as a function of α. Throughout this chapter ϕ is set to zero and $\alpha \in$ [0,0.5] without loss of generality.

Fig. 6.9a shows the probability of bit error performance for a QPSK-OFDM system in the presence of a single NBI as a function of E_b/N_0 and α. The presence of a single NBI with a modest SIR of 15 dB has a significant impact on P_b, since for QPSK systems in the presence of just AWGN, P_b would be equivalent to the ideal BPSK case, i.e. $P_b = \frac{1}{2}\text{erfc}\left(\sqrt{E_b/N_0}\right)$. It is clear from Fig. 6.9a that a plateau is reached for high SNRs where the effect of the interference is dominant. Similar patterns for P_s and P_b have been observed for 16- and 64QAM-OFDM systems, however that is not the case with uni-dimensional modulation schemes (i.e. no quadrature component) such as BPSK. The behaviour of P_b for BPSK-OFDM in the presence of NBI is shown in [45, Fig. 1]. The plateau levels can be explained by considering the limiting case where $E_b/N_0 \to \infty$. P_b is observed to asymptote to 3.9×10^{-3} when $\alpha = 0$ due to there being no spectral leakage, and only *one* subcarrier is affected by the NBI. For $M = 4$, $K = 0$, $J = 1$ (as in Fig. 6.9a), and $\alpha = 0$, P_b for the affected subcarrier reduces to

$$P_b = \frac{1}{8}\left\{\text{erfc}\left[\sqrt{\frac{E_b}{N_0}}\left(1-\sqrt{\frac{2N}{\text{SIR}}}\right)\right] + \text{erfc}\left[\sqrt{\frac{E_b}{N_0}}\left(1+\sqrt{\frac{2N}{\text{SIR}}}\right)\right]\right\}, \tag{6.29}$$

and zero for all other subcarriers. When $E_b/N_0 \to \infty$,

$$\lim_{E_b/N_0\to\infty} P_b = \begin{cases} 0 & \text{SIR} > 2N \\ 0.25 & \text{SIR} < 2N. \end{cases} \tag{6.30}$$

If, for $N = 64$, the SIR is greater than 21 dB, the interference will not influence the probability of bit error and since the SIR in Fig. 6.9a is 15 dB, $P_b = 0.25/64 \approx 3.9 \times 10^{-3}$ as observed in Fig. 6.9a. For cases where $\alpha \neq 0$, the expression is more complicated

$$\begin{aligned}\lim_{E_b/N_0\to\infty} P_b \quad = \quad & \frac{1}{8N}\sum_{k=0}^{N-1}\text{erfc}\left[\sqrt{\frac{E_b}{N_0}}\left(1-\Re\left\{\Psi_k(\zeta)\right\}\sqrt{\frac{2}{N\times\text{SIR}}}\right)\right] + \\ & \text{erfc}\left[\sqrt{\frac{E_b}{N_0}}\left(1-\Im\left\{\Psi_k(\zeta)\right\}\sqrt{\frac{2}{N\times\text{SIR}}}\right)\right],\end{aligned} \tag{6.31}$$

which, for the parameters in Fig. 6.9a, will have three discrete values

$$\lim_{E_b/N_0\to\infty} P_b = \begin{cases} 0 & \text{SIR} > \frac{2[\Re\{\Psi_k(\zeta)\}]^2}{N} \wedge \text{SIR} > \frac{2[\Im\{\Psi_k(\zeta)\}]^2}{N} \\ 3.9\times10^{-3} & \text{SIR} > \frac{2[\Re\{\Psi_k(\zeta)\}]^2}{N} \oplus \text{SIR} > \frac{2[\Im\{\Psi_k(\zeta)\}]^2}{N} \\ 7.8\times10^{-3} & \text{otherwise,} \end{cases} \tag{6.32}$$

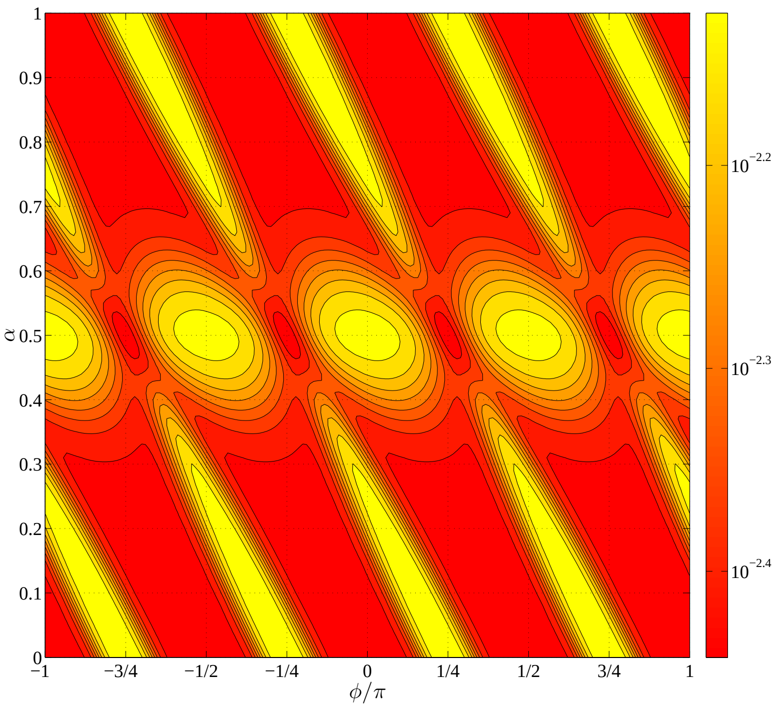

Figure 6.8: Probability of bit error performance of QPSK-OFDM in the presence of a single NBI as a function of α and ϕ. SIR = 15 dB, $E_b/N_0 = 15$ dB, $N = 64$, and $K = 0$.

where $\wedge$ and $\oplus$ are the logical *AND* and *exclusive OR* operators, respectively. It should be noted that, since the SIR in Fig. 6.9a is 15 dB, the conditions for P_b to be zero are not met, which explains the two values for the plateau; and that for increasing E_b/N_0 the transitional regions between the plateau levels become increasingly abrupt, i.e. P_b will truly be discrete as in (6.32). Fig. 6.9b shows the BER curves for 16QAM-OFDM for the same conditions as in Fig. 6.9a. Similar analyses can be performed for any other QAM level. Depending on the QAM level, SIR and α there are several plateaus the BER value could take when the system performance is considered *interference limited* (i.e. the noise level is considered negligible) as shown in Fig. 6.10.

6.4.2 Multiple Narrowband Interferers

The analytical error rate expressions can be used to quantify the performance of OFDM systems in the presence of multiple NBIs. There are several factors influencing the error rate performance including SNR, SIR, M, J, α_i and ϕ_i. When $J > 1$ (i.e. multiple interferers), there is a large number of parameter permutations since α and ϕ are particular to each interferer. In this section, results are shown for a particular set of parameters and can be easily extended to include any other set of parameter values.

The error rate performance sensitivity to spectral leakage is further illustrated when considering multiple narrowband interferers. Consider the scenario where the total interference power is fixed (i.e. constant SIR), J is fixed, but one of the NBIs has a larger share of the total interference power than the others and the frequency offset of each interferer, α_i, changes. Fig. 6.11 shows the BER performance of QPSK-OFDM in the presence of four NBIs normalised to the BER performance in the presence of a single NBI with equivalent total interference power. The different lines in Fig. 6.11 represent different percentage

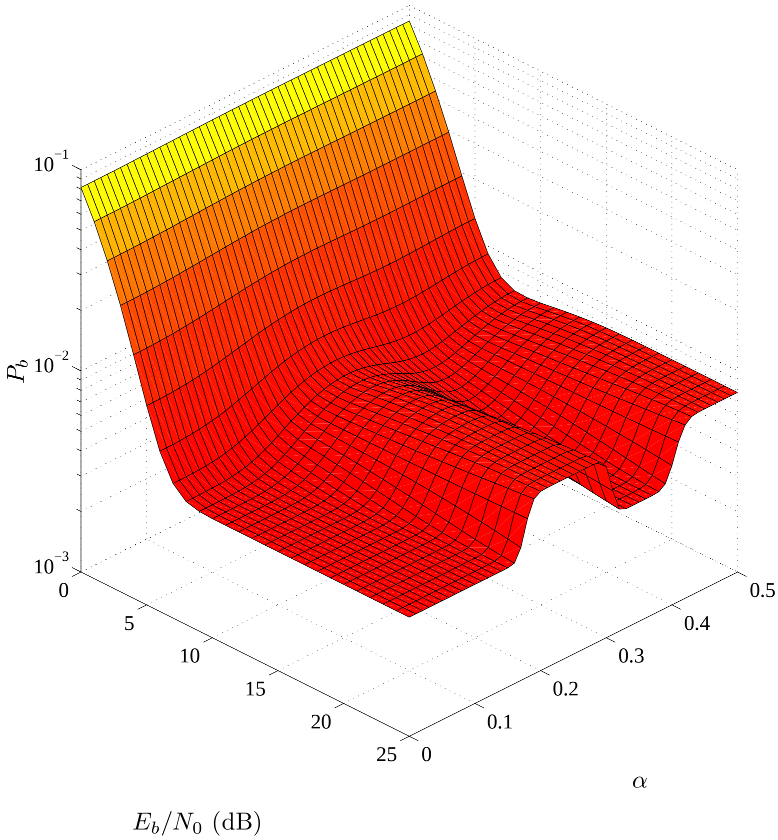

(a) QPSK-OFDM.

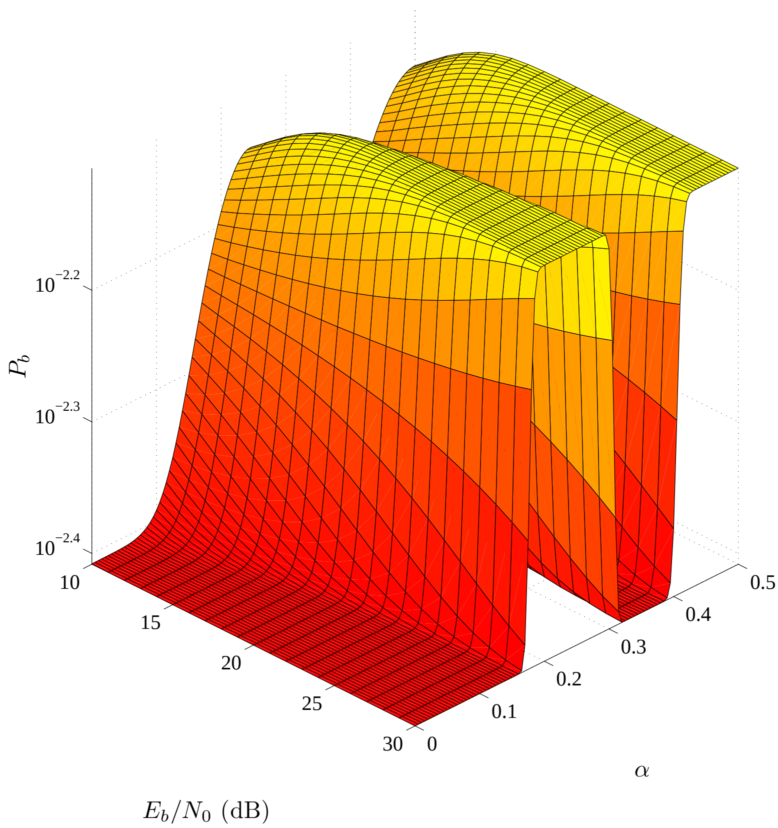

(b) 16QAM-OFDM.

Figure 6.9: Probability of bit error of OFDM in the presence of a single NBI. SIR $= 15$ dB, $N = 64$, $K = 0$, and $\phi = 0$.

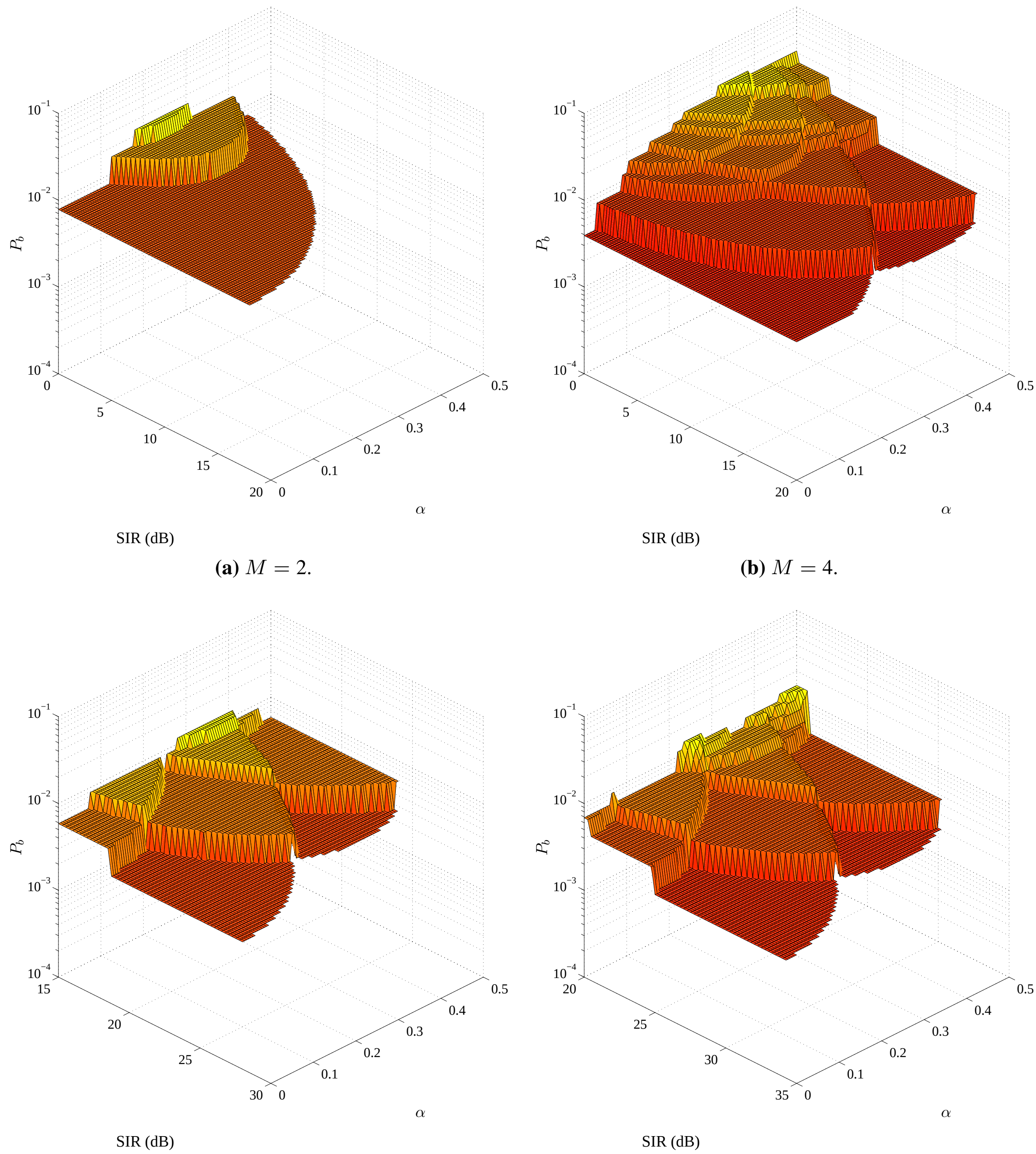

(a) $M = 2$.

(b) $M = 4$.

(c) $M = 16$.

(d) $M = 64$.

Figure 6.10: BER performance of M-ary QAM OFDM in the presence of a single NBI as a function of the SIR and α. $E_b/N_0 = 100$ dB, $N = 64$, $K = 0$, and $\phi = 0$. BER values that are less than 10^{-15} are not shown in the plots.

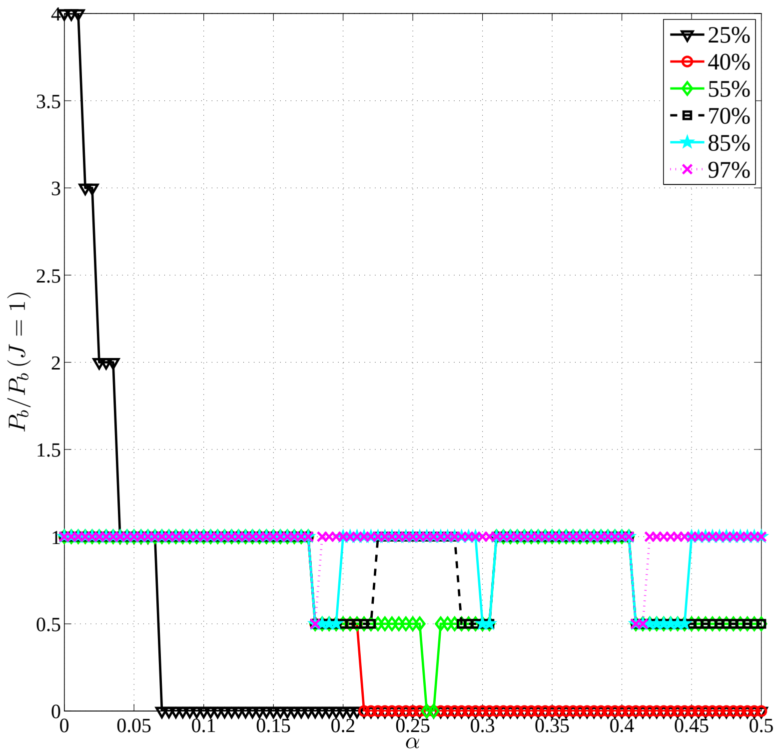

Figure 6.11: BER performance of QPSK-OFDM in the presence of four NBIs normalised to the BER performance of a single NBI with equivalent SIR value. Total SIR $=$ 15 dB, $E_b/N_0 = 100$ dB, $\phi_i = 0\,\forall i$ and $\alpha_i = \alpha\,\forall i$. Each line represents the performance when there is a dominant NBI with the indicated percentage share of the total interference power. The other three NBIs have an equal share of the remaining interference power.

shares of the dominant NBI of the total interference power (the other three NBIs have an equal share of the remaining interference power, e.g. when the dominant NBI has 55% of the total interference power, the other three NBIs each have 15% of the total interference power). It is clear from Fig. 6.11 that a constant QAM level and SIR are *not* sufficient to provide a constant error rate performance. The error rate performance is affected by both the amount of spectral leakage produced by the interfering signals after passing through the DFT at the receiver *and* the power distribution of the interfering signals.

This error rate behaviour is not typical among other communication systems, such as DS-SS systems (this is discussed further in Section §6.4.3). The error rate expressions derived in this chapter can be used to produce practical results as demonstrated by the following case study.

Case Study

Consider Test Environment A (Section §5.2.2) as a case study. Let BS 3C be the OFDM transmitter and all other BSs in the test environment (Fig. 5.4) as interfering narrowband transmitters. Four interference scenarios are considered: Scenario I in which no interferers are active; Scenario II in which only those interferers on the same floor as the desired base station are considered active (i.e. 3A and 3B); Scenario III in which all interferers (i.e. 3A, 3B, 2A, 2B, 2C, 1A, 1B and 1C) are considered active; and Scenario IV in which the interferers on the first floor are inactive (i.e. 1A, 1B and 1C). From an engineering perspective, it is necessary to determine which locations on the third floor the system can provide coverage for $P_b \leq \epsilon$ (where ϵ is a certain threshold dependent on the system requirements) using BPSK, QPSK, 16QAM and 64QAM.

Fig. 6.12 shows the distribution of maximum achievable QAM levels on the third floor of Test Environment A for Scenarios I-III. For all the scenarios, $\epsilon = 10^{-3}$, $\alpha = [0.2,0.5,0.1,0.3,0,0.4,0.35,0]$, and $\phi = 0 \; \forall i$. For a system with 20 MHz bandwidth at 20°C, the noise floor is calculated to be -101 dBm [11, p. 61].

The influence of narrowband interference on the performance of M-ary QAM-OFDM is significant, as can be seen in Fig. 6.12. For Scenario I (Fig. 6.12a) the performance is limited by the path loss (which determines the SNR). A drop of just 3.5 dB in the received signal level is enough to degrade the achievable QAM level from 64QAM to 16QAM. The system performance across the floor degrades dramatically in Scenario II (Fig. 6.12b) compared with the performance in Scenario I due to the close proximity of the active NBIs at 3A and 3B. For Scenario III (Fig. 6.12c), further performance degradation is observed but it is not as drastic as that in Scenario II. This is because the other NBIs are on different floors and therefore contribute much weaker levels of interference. This observation is confirmed by Scenario IV, where the NBIs on the first floor are inactive; the QAM level distribution did not change compared with Scenario III. Table 6.4 shows the percentage of the floor that can be operated at different QAM levels[13].

The results obtained demonstrate that the location of the NBIs in an environment, coupled with the physical obstacles in that environment with which the propagating fields interact, can significantly influence the SIR at a particular location and hence the performance of OFDM systems. This type of information assists engineers and system designers to compensate for the effects of the environment and optimise the performance of the OFDM system. The example shown in Fig. 6.12 demonstrates how the model for interference derived herein, together with propagation data, can be used to produce results of practical significance.

6.4.3 Comparison with DS-SS Systems

As discussed in Chapter 2, DS-SS systems are architecturally very different from OFDM systems. The architectural differences between the two systems are reflected in their error rate performance in the presence of interference. The effects of narrowband interference (or jammers) on DS-SS systems and jamming rejection techniques are well studied in the literature (e.g. [111–119]).

As mentioned in [45], error rate expressions for DS-SS systems in the presence of narrowband interference (such as [111, Eq. (27)] and [116, Eq. (17)]) average the noise and interference terms across frequencies *inside* the error function while the expressions derived herein average them *outside* the error function. In other words, the error rate expressions for DS-SS systems are influenced by the average interference power and therefore, the frequency, phase and number of NBIs are of no particular importance. This is clearly not the case for OFDM systems as demonstrated in Sections §6.4.1 and §6.4.2, where the interferer's frequency and phase determine the amount of spectral leakage produced by the DFT at the receiver. The amount of spectral leakage along with the interference power determine the error rate performance for OFDM systems.

[13]The percentages are inclusive of each other, i.e. 31% of the floor can achieve BPSK modulation but that includes locations where higher QAM levels are achievable, but 10% of the floor can achieve BPSK as the *best* modulation scheme, etc.

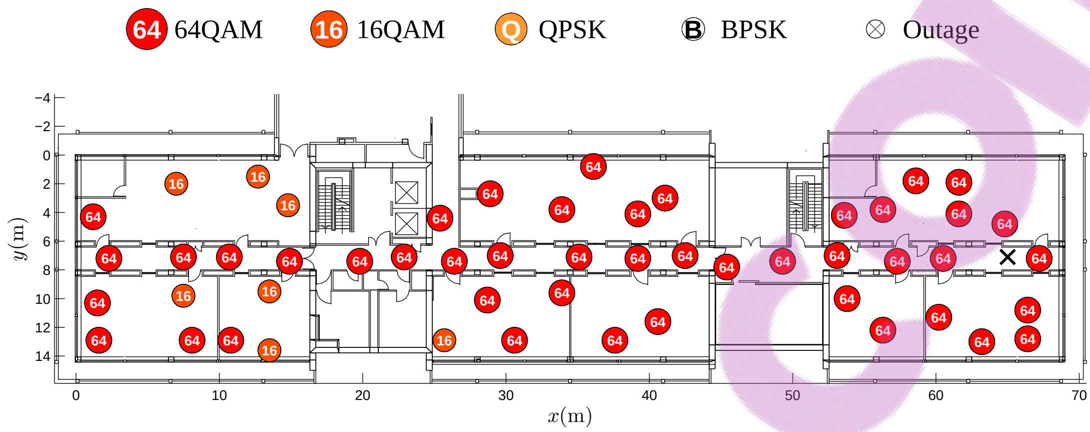

(a) Scenario I: All NBIs are inactive.

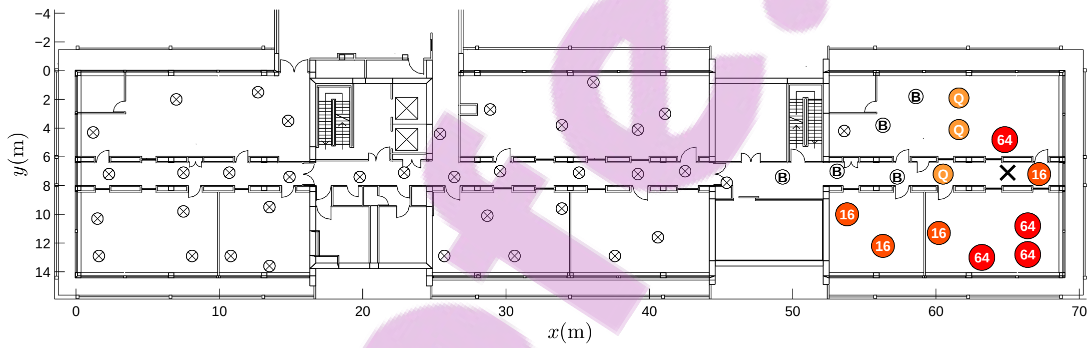

(b) Scenario II: 3A and 3B are active.

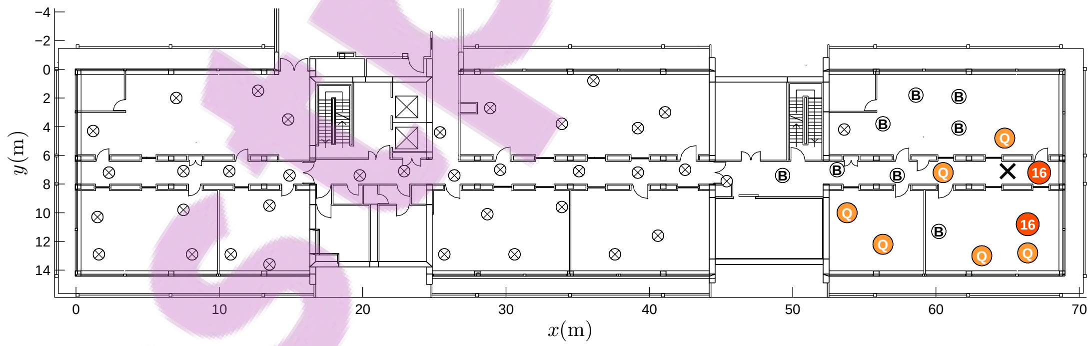

(c) Scenario III: All NBIs are active.

Figure 6.12: Distribution of maximum achievable QAM levels across the third floor of Test Environment A ($\epsilon = 10^{-3}$). Note that any location in which 16QAM is achievable also includes QPSK and BPSK modulations, etc.

Table 6.4: Best achievable QAM level percentage coverage for the third floor in Test Environment A.

	Percentage of locations for which indicated QAM levels were achieved				
Interference Scenario	64QAM	16QAM	QPSK	BPSK	Outage
Scenario I: All NBIs are inactive	86%	14%	0%	0%	0%
Scenario II: 3A & 3B are active	8%	8%	6%	9%	69%
Scenario III: All NBIs are active	0%	4%	12%	15%	69%
Scenario IV: 1A, 1B & 1C are inactive	0%	4%	12%	15%	69%

A more quantitative comparison between OFDM and DS-SS error rate performance is presented in Chapters 8 & 9 where each system suffers from "same-system" interference, i.e. OFDM-to-OFDM and DS-SS to DS-SS interference scenarios.

6.5 OFDM Interference as a Superposition of Single-Carrier NBIs

One of the main objectives of this chapter is to present the narrowband interference models as a stepping stone for modelling OFDM interferers (OFDMIs). Since the radio channel is linear, an OFDM signal can be considered as a superposition of narrowband subcarriers [47,66]. Therefore, the error rate expressions derived in this chapter can be used, with modifications, to model the effects of OFDMIs on M-ary QAM OFDM systems.

To model an OFDMI, the *data modulation* of the *interfering* subcarriers has to be included in the model. The derivation of error rate expressions of M-ary QAM OFDM in the presence of multiple Z-ary[14] QAM OFDMIs is presented in Chapter 7 with performance assessments presented in Chapters 8 and 9.

6.6 Summary

In this chapter, analytical symbol and bit error rate expressions of M-ary QAM OFDM in the presence of multiple NBIs are derived. The analytical expressions are validated against a Monte Carlo numerical model and results show close agreement between the analytical and numerical results. There are, however, inaccuracies for the BER expressions when considering high QAM levels ($M \geq 16$) and low SINR values. These inaccuracies are a result of the Gray coding used for mapping the data bits. In practice, though, high QAM mapping schemes are not used when the channel conditions are poor, i.e. low SINR values.

The error rate performance of OFDM systems suffering from narrowband interference is sensitive to the frequency and phase offset of the interfering signals. The NBIs' frequencies and phase offsets determine how much spectral leakage is produced after the DFT at the receiver. The spectral leakage coupled with the interference power and the OFDM QAM level determine the error rate performance. Unlike DS-SS systems, the total interference power is not sufficient to give an accurate indication of the OFDM

[14] To avoid confusion between the desired OFDM QAM level and the interfering OFDM QAM level, throughout this thesis Z is used to indicate the *interfering* OFDM QAM level.

error rate performance in the case of multiple NBIs. This is due to fluctuations in the amount of spectral leakage which spreads the interference power across the entire OFDM spectrum and signal space (DS-SS systems *always* spread the energy of the interference across their spectrum).

OFDM interferers can be modelled as a superposition of *mapped* narrowband subcarriers due to the linearity of the radio channel. The derivation of error rate expressions of M-ary QAM OFDM in the presence of multiple Z-ary QAM OFDMIs is presented in Chapter 7.

Chapter 7

OFDM-to-OFDM Interference — Analytical Treatment

7.1 Introduction

OFDM-based wireless systems, like any other wireless system, can be detrimentally affected by interference. Interference can come from a variety of sources, especially if the system operates in license-exempt bands (e.g. ISM band). The focus of this chapter (and Chapters 8 & 9) is to study the effects of interference from same-type systems, e.g. two or more 802.11g networks, or two or more WiMAX systems. These same-type interference situations could occur in places where the receiver can detect two or more networks but the networks cannot detect each other, and are therefore unable to mitigate the effects of interference via MAC layer protocols. These kinds of situations often take place in cluttered environments where there is large path loss, such as indoor environments. The ability to estimate the error rate performance precisely without relying on time-consuming Monte Carlo numerical methods is crucial if error rate calculations are required intensively in the system planning process.

Interference analyses for OFDM systems have traditionally considered the interference to be narrowband, e.g. [45, 66, 120]. Although an OFDM interferer can be modelled as a superposition of narrowband carriers [66], the models and expressions presented in [45,66,120] do not consider the modulation of the *interfering* system. The authors of [47] have considered the interference effects of WiMAX on multiband (MB)-OFDM systems (see Table 2.2); modulation of the interfering WiMAX system was considered and analytical expressions for the BER derived. However, the analysis in [47] considers only BPSK and QPSK modulation for the desired and interfering systems and just a single interferer. The authors of [67] have considered the reverse problem studied in [47], where coded and uncoded WiMAX systems are impaired by a single MB-OFDM. The study in [67] produced a closed form analytical BER expression that is obtained by computing the MB-OFDM characteristic function without using numerical integration methods.

In Section §7.2 exact analytical error expressions of a generic M-ary QAM OFDM system in the presence of multiple generic Z-ary QAM OFDMIs of the same system type as the desired system are derived. Approximations to the exact analytical expressions that are more computationally efficient are presented in Section §7.3. Finally, an algorithm for rapid error rate estimation is proposed in Section §7.4.

7.2 Error Rate Calculations

Similar to Chapter 6, the error rate calculations are performed on the received signal after it passes through the DFT at the receiver. Thus, the analysis begins by formulating the post-DFT received signal.

7.2.1 Post-DFT Signal

Using the same system assumptions described in Section §6.2.1, a received, sampled, baseband OFDM symbol, r_n, in the presence of J OFDMIs is represented as

$$r_n = \frac{1}{N}\sum_{k=0}^{N-1} a_k D_k e^{j2\pi n \frac{k}{N}} + \eta_n + \sum_{i=1}^{J} \Gamma_{n,i}, \tag{7.1}$$

where $\Gamma_{n,i}$ is the ith OFDM interferer, and is given by

$$\Gamma_{n,i} = \frac{1}{G_i}\sum_{\ell=-\infty}^{\infty}\sum_{g=0}^{G_i-1} D_{i,g}^{(\ell)}\beta_{i,g}e^{j[2\pi\zeta_{i,g}n+\phi_i]}. \tag{7.2}$$

The ith OFDM interferer has G_i subcarriers each with $\beta_{i,g}$, $\zeta_{i,g}$, and ϕ_i, respectively, as the amplitude, normalised frequency, and constant phase offset relative to the desired OFDM transmission. $D_{i,g}^{(\ell)}$ is the ith OFDMI's modulated data for the gth subcarrier of the ℓth time-domain symbol. Throughout this thesis, all OFDM systems (both desired and interfering) are assumed to be of the same type (e.g. all WiMAX) since those scenarios result in maximum frequency band alignment which causes maximum interference levels. This assumption results in the following: $G_i = N\ \forall i$, and a maximum of *two* interfering time-domain symbols per OFDMI are present in the DFT window at the receiver as illustrated by Fig. 7.1. Therefore,

$$\Gamma_{n,i} = \Gamma_{n,i}^{(1)} + \Gamma_{n,i}^{(2)}, \tag{7.3}$$

where

$$\Gamma_{n,i}^{(1)} = \frac{1}{N}\sum_{g=0}^{N-1} D_{i,g}^{(1)}\beta_{i,g}e^{j[\phi_i+2\pi(n+[N-\tau_i])(g+\alpha_i)/N]}, \tag{7.4}$$

$$\Gamma_{n,i}^{(2)} = \frac{1}{N}\sum_{g=0}^{N-1} D_{i,g}^{(2)}\beta_{i,g}e^{j[\phi_i+2\pi(n-\tau_i)(g+\alpha_i)/N]}, \tag{7.5}$$

$\tau_i = 0,1,2,\ldots,N-1$, and α_i are, respectively, the time and frequency offsets between the ith OFDMI and the desired OFDM transmission, and $n = 0$ is the time when the DFT window starts. At the receiver, r_n is passed through an N-point DFT. The post-DFT interference component at the kth frequency bin, I_k, is given by

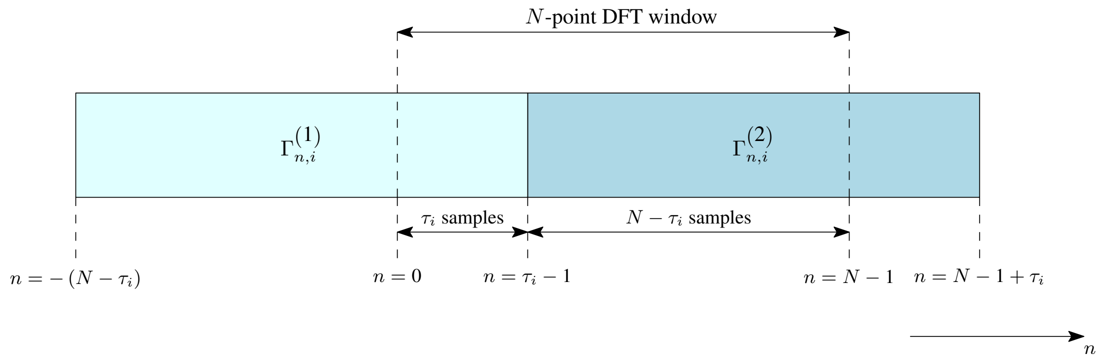

Figure 7.1: The timing misalignment between the ith interfering transmission and the desired transmissions, τ_i, causes *two* interfering time-domain symbols to pass through the DFT at the receiver. When $\tau_i = 0$, only one interfering time-domain symbol passes through the DFT, namely, $\Gamma^{(2)}_{n,i}$.

$$\begin{aligned} I_k &= \sum_{i=1}^{J}\left\{\sum_{n=0}^{\tau_i-1}\Gamma^{(1)}_{n,i}e^{-j2\pi kn/N}+\sum_{n=\tau_i}^{N-1}\Gamma^{(2)}_{n,i}e^{-j2\pi kn/N}\right\} \\ &= \sum_{i=1}^{J}\sum_{g=0}^{N-1}\left\{\frac{\beta_{i,g}}{N}\left[D^{(1)}_{i,g}\Psi^{(1)}_{i,g}(\alpha,\tau,\phi)+D^{(2)}_{i,g}\Psi^{(2)}_{i,g}(\alpha,\tau,\phi)\right]\right\}, \end{aligned} \tag{7.6}$$

where

$$\Psi^{(1)}_{i,g}(\alpha,\tau,\phi) = \frac{\sin\left[\pi\tau_i(g+\alpha_i-k)/N\right]}{\sin\left[\pi(g+\alpha_i-k)/N\right]}e^{j[\phi_i+\pi\{(g+\alpha_i)(2N-\tau_i-1)-k(\tau_i-1)\}/N]}, \tag{7.7}$$

$$\begin{aligned} \Psi^{(2)}_{i,g}(\alpha,\tau,\phi) &= \frac{e^{j[\phi_i-2\pi\tau_i(g+\alpha_i)/N]}}{\sin\left[\pi(g+\alpha_i-k)/N\right]}\Big\{\sin\left[\pi(g+\alpha_i-k)\right]e^{j\pi(g+\alpha_i-k)(N-1)/N} \\ &\quad -\sin\left[\pi\tau_i(g+\alpha_i-k)/N\right]e^{j\pi(g+\alpha_i-k)(\tau_i-1)/N}\Big\}, \end{aligned} \tag{7.8}$$

are the complex spectral leakage terms for $\Gamma^{(1)}_{n,i}$ and $\Gamma^{(2)}_{n,i}$, respectively. Derivations of $\Psi^{(1)}_{i,g}(\alpha,\tau,\phi)$ and $\Psi^{(2)}_{i,g}(\alpha,\tau,\phi)$ are presented in Appendix C. $D^{(1)}_{i,g}$ and $D^{(2)}_{i,g}$ are random variables and in this thesis, it is assumed, without loss of generality, that both have the *same* QAM level, Z_i, of the ith OFDMI[1]. This means that I_k is a sum of $2 \times N \times J$ random variables and is thus a random variable itself with a pdf given by the convolution of the individual pdfs of its terms [121, p. 47]. As discussed in Section §6.2.1, the post-DFT received signal at the kth bin, R_k, is given by

$$R_k = D_k + I_k + H_k, \tag{6.4}$$

[1]In practice, though, individual subcarriers can have different QAM levels. In that case $D^{(\ell)}_{i,g}$ would have a QAM level given by $Z^{(\ell)}_{i,g}$.

that has a pdf given by the convolution of the pdfs of I_k and H_k[2]. The error rate expressions are derived using the pdf of R_k.

7.2.2 Probability Density Function of R_k

The pdf of R_k, $P_{R_k}(r)$, in the I- and Q-channels are considered independent of each other and are derived separately. H_k has a Gaussian pdf (given by Equation (4.12)) in both the I- and Q-channels, which are assumed to be independent of each other. The *original* locations of the interfering message points, $L_{i,g}^{(\ell)}(x,y)$, in signal space (where ℓ can be either 1 or 2) with bipolar symmetric ASK signals are given by

$$L_{i,g}^{(\ell)}(x,y) = \beta_{i,g}\left[\left(2x_{i,g}^{(\ell)} - 1 - \sqrt{Z_i}\right) + j\left(2y_{i,g}^{(\ell)} - 1 - \sqrt{Z_i}\right)\right], \tag{7.9}$$

where $x_{i,g}^{(\ell)} = 1,2,\ldots,\sqrt{Z_i}$ and $y_{i,g}^{(\ell)} = 1,2,\ldots,\sqrt{Z_i}$. However, due to the spectral leakage produced by the DFT, the *actual* locations of the interfering message points, $l_{i,g}^{(\ell)}(x,y)$, in signal space are scaled and rotated according to

$$l_{i,g}^{(\ell)}(x,y) = \frac{1}{N}\Psi_{i,g}^{(\ell)}(\alpha,\tau,\phi)\, L_{i,g}^{(\ell)}(x,y)\,. \tag{7.10}$$

Since $P_{R_k}(r)$ in the I- and Q-channels are derived separately, only the projections of $l_{i,g}^{(\ell)}(x,y)$ on the I- and Q-channels are of interest. The projection of $l_{i,g}^{(\ell)}(x,y)$ on the I- and Q-channels are, respectively, given by

$$\begin{aligned}
\Re\left\{l_{i,g}^{(\ell)}(x,y)\right\} &= \Re\left\{L_{i,g}^{(\ell)}(x,y)\right\}\Re\left\{\frac{\Psi_{i,g}^{(\ell)}(\alpha,\tau,\phi)}{N}\right\} - \Im\left\{L_{i,g}^{(\ell)}(x,y)\right\}\Im\left\{\frac{\Psi_{i,g}^{(\ell)}(\alpha,\tau,\phi)}{N}\right\} \\
&= \frac{1}{N}\beta_{i,g}\left|\Psi_{i,g}^{(\ell)}(\alpha,\tau,\phi)\right|\left\{\left(2x_{i,g}^{(\ell)} - 1 - \sqrt{Z_i}\right)\cos\left[\varphi_{i,g}^{(\ell)}(\alpha,\tau,\phi)\right]\right. \\
&\quad \left. - \left(2y_{i,g}^{(\ell)} - 1 - \sqrt{Z_i}\right)\sin\left[\varphi_{i,g}^{(\ell)}(\alpha,\tau,\phi)\right]\right\} \\
&= \frac{1}{N}\beta_{i,g}\left|\Psi_{i,g}^{(\ell)}(\alpha,\tau,\phi)\right|\Omega_{i,g,I}^{(\ell)}(x,y,\alpha,\tau,\phi)\,,
\end{aligned} \tag{7.11}$$

and

$$\begin{aligned}
\Im\left\{l_{i,g}^{(\ell)}(x,y)\right\} &= \Re\left\{L_{i,g}^{(\ell)}(x,y)\right\}\Im\left\{\frac{\Psi_{i,g}^{(\ell)}(\alpha,\tau,\phi)}{N}\right\} + \Im\left\{L_{i,g}^{(\ell)}(x,y)\right\}\Re\left\{\frac{\Psi_{i,g}^{(\ell)}(\alpha,\tau,\phi)}{N}\right\} \\
&= \frac{1}{N}\beta_{i,g}\left|\Psi_{i,g}^{(\ell)}(\alpha,\tau,\phi)\right|\left\{\left(2x_{i,g}^{(\ell)} - 1 - \sqrt{Z_i}\right)\sin\left[\varphi_{i,g}^{(\ell)}(\alpha,\tau,\phi)\right]\right. \\
&\quad \left. + \left(2y_{i,g}^{(\ell)} - 1 - \sqrt{Z_i}\right)\cos\left[\varphi_{i,g}^{(\ell)}(\alpha,\tau,\phi)\right]\right\} \\
&= \frac{1}{N}\beta_{i,g}\left|\Psi_{i,g}^{(\ell)}(\alpha,\tau,\phi)\right|\Omega_{i,g,Q}^{(\ell)}(x,y,\alpha,\tau,\phi)\,,
\end{aligned} \tag{7.12}$$

where

$$\varphi_{i,g}^{(\ell)}(\alpha,\tau,\phi) \triangleq \angle\left\{\Psi_{i,g}^{(\ell)}(\alpha,\tau,\phi)\right\}, \tag{7.13}$$

[2] $D_{i,g}^{(\ell)}$ is the modulated data on the *interfering* subcarriers and is not to be confused with D_k, which is the modulated data on the *desired* subcarrier at the kth bin.

and $\angle\{\cdot\}$ denotes the complex argument. From the expressions in (7.11) and (7.12), the pdf of the gth subcarrier of $\Gamma_{n,i}^{(\ell)}$ in the I- and Q-channels can be shown to be

$$P_{\Gamma}^{I}[r|i,g,\ell] = \frac{1}{Z_i}\sum_{x_{i,g}^{(\ell)}=1}^{\sqrt{Z_i}}\sum_{y_{i,g}^{(\ell)}=1}^{\sqrt{Z_i}}\delta\left[r-\frac{1}{N}\beta_{i,g}\left|\Psi_{i,g}^{(\ell)}(\alpha,\tau,\phi)\right|\Omega_{i,g,I}^{(\ell)}(x,y,\alpha,\tau,\phi)\right], \quad (7.14)$$

$$P_{\Gamma}^{Q}[r|i,g,\ell] = \frac{1}{Z_i}\sum_{x_{i,g}^{(\ell)}=1}^{\sqrt{Z_i}}\sum_{y_{i,g}^{(\ell)}=1}^{\sqrt{Z_i}}\delta\left[r-\frac{1}{N}\beta_{i,g}\left|\Psi_{i,g}^{(\ell)}(\alpha,\tau,\phi)\right|\Omega_{i,g,Q}^{(\ell)}(x,y,\alpha,\tau,\phi)\right], \quad (7.15)$$

where $\delta[\cdot]$ is the *Kronecker* delta function defined as [122, p. 191]

$$\delta[n] \triangleq \begin{cases} 1 & n=0 \\ 0 & \text{otherwise.} \end{cases} \quad (7.16)$$

Therefore, the pdf of the gth subcarrier of the ith OFDMI in the I-channel (identical principles apply to the Q-channel) is given by convolving $P_{\Gamma}^{I}[r|i,g,\ell=1]$ with $P_{\Gamma}^{I}[r|i,g,\ell=2]$ such that

$$\begin{aligned} P_{I_k}^{I}[r|i,g] = {} & Z_i^{-2}\sum_{\ell=1}^{2}\sum_{x_{i,g}^{(\ell)}=1}^{\sqrt{Z_i}}\sum_{y_{i,g}^{(\ell)}=1}^{\sqrt{Z_i}}\delta\Bigg[r-\frac{1}{N}\beta_{i,g}\times \\ & \left\{\left|\Psi_{i,g}^{(1)}(\alpha,\tau,\phi)\right|\Omega_{i,g,I}^{(1)}(x,y,\alpha,\tau,\phi)+\left|\Psi_{i,g}^{(2)}(\alpha,\tau,\phi)\right|\Omega_{i,g,I}^{(2)}(x,y,\alpha,\tau,\phi)\right\}\Bigg]. \end{aligned}$$

Using the properties of convolution and Fourier transforms, the complete pdf of I_k in the I-channel, $P_{I_k}^{I}[r]$, for J interferers is[3]

$$\begin{aligned} P_{I_k}^{I}[r] &= \mathcal{F}^{-1}\left\{\prod_{i=1}^{J}\prod_{g=0}^{N-1}\mathcal{F}\left\{P_{I_k}^{I}[r|i,g]\right\}\right\} \\ &= \left(\prod_{w=1}^{J}Z_w^{-2N}\right)\sum_{i=1}^{J}\sum_{g=0}^{N-1}\sum_{\ell=1}^{2}\sum_{x_{i,g}^{(\ell)}=1}^{\sqrt{Z_i}}\sum_{y_{i,g}^{(\ell)}=1}^{\sqrt{Z_i}}\delta\Bigg[r-\frac{1}{N}\times \\ & \qquad \sum_{d=1}^{J}\sum_{p=0}^{N-1}\sum_{q=1}^{2}\left\{\beta_d\left|\Psi_{d,p}^{(q)}(\alpha,\tau,\phi)\right|\Omega_{d,p,I}^{(q)}(x,y,\alpha,\tau,\phi)\right\}\Bigg], \end{aligned} \quad (7.17)$$

where $\mathcal{F}\{\cdot\}$ and $\mathcal{F}^{-1}\{\cdot\}$ are, respectively, the Fourier and inverse Fourier transforms. The pdf of R_k in the I-channel, $P_{R_k}^{I}(r)$, is obtained by convolving (7.17) with the pdf of H_k (given by Equation (4.12)). The expression in (7.17) is essentially a weighted train of delta functions at locations given by the interfe-

[3] Derivation in Appendix D.

rence parameters. Therefore, the convolution of (7.17) with (4.12) results in a weighted sum of Gaussian pdfs centred around the locations of the delta functions, such that

$$\begin{aligned} P_{R_k}^I(r) &= \frac{1}{\sqrt{\pi N_0}}\left(\prod_{w=1}^{J} Z_w^{-2N}\right)\sum_{i=1}^{J}\sum_{g=0}^{N-1}\sum_{\ell=1}^{2}\sum_{x_{i,g}^{(\ell)}=1}^{\sqrt{Z_i}}\sum_{y_{i,g}^{(\ell)}=1}^{\sqrt{Z_i}} \exp\left[-\frac{1}{N_0}\times\right. \\ &\left.\left(r-\sum_{d=1}^{J}\sum_{p=0}^{N-1}\sum_{q=1}^{2}\left\{\frac{\beta_d}{N}\left|\Psi_{d,p}^{(q)}(\alpha,\tau,\phi)\right|\Omega_{d,p,I}^{(q)}(x,y,\alpha,\tau,\phi)\right\}\right)^2\right]. \qquad (7.18)\end{aligned}$$

Similarly, the pdf of I_k in the Q-channel, $P_{R_k}^Q(r)$, is given by

$$\begin{aligned} P_{R_k}^Q(r) &= \frac{1}{\sqrt{\pi N_0}}\left(\prod_{w=1}^{J} Z_w^{-2N}\right)\sum_{i=1}^{J}\sum_{g=0}^{N-1}\sum_{\ell=1}^{2}\sum_{x_{i,g}^{(\ell)}=1}^{\sqrt{Z_i}}\sum_{y_{i,g}^{(\ell)}=1}^{\sqrt{Z_i}} \exp\left[-\frac{1}{N_0}\times\right. \\ &\left.\left(r-\sum_{d=1}^{J}\sum_{p=0}^{N-1}\sum_{q=1}^{2}\left\{\frac{\beta_d}{N}\left|\Psi_{d,p}^{(q)}(\alpha,\tau,\phi)\right|\Omega_{d,p,Q}^{(q)}(x,y,\alpha,\tau,\phi)\right\}\right)^2\right]. \qquad (7.19)\end{aligned}$$

The expressions in (7.18) and (7.19) are used to derive the probabilities of symbol and bit error for an M-ary QAM OFDM system in the presence of multiple Z-ary QAM OFDMIs.

7.2.3 Probability of Symbol Error, P_s

The relationship between P_s, P_s^I and P_s^Q is given by (6.9). Since (7.18) is symmetrical around zero, P_s^I can be derived as

$$P_s^I = 2\times\frac{\sqrt{M}-1}{\sqrt{M}}\int_{\frac{\Delta}{2}}^{\infty} P_{R_k}^I(r)\,dr,$$

where Δ is given by (6.12). Using the definition of the complementary error function in (6.11) and a change of variables, P_s^I becomes

$$\begin{aligned} P_s^I &= \frac{\sqrt{M}-1}{\sqrt{M}}\left(\prod_{w=1}^{J} Z_w^{-2N}\right)\sum_{i=1}^{J}\sum_{g=0}^{N-1}\sum_{\ell=1}^{2}\sum_{x_{i,g}^{(\ell)}=1}^{\sqrt{Z_i}}\sum_{y_{i,g}^{(\ell)}=1}^{\sqrt{Z_i}} \operatorname{erfc}\left[\varrho_M\sqrt{\frac{E_b}{N_0}}-\right. \\ &\left.\sum_{d=1}^{J}\sum_{p=0}^{N-1}\sum_{q=1}^{2}\left\{\frac{\sqrt{\gamma_d}}{N}\left|\Psi_{d,p}^{(q)}(\alpha,\tau,\phi)\right|\Omega_{d,p,I}^{(q)}(x,y,\alpha,\tau,\phi)\right\}\right] \\ &= P_s^I\left(\frac{E_b}{N_0},\gamma\mid k,\alpha,\tau,\phi\right), \qquad (7.20)\end{aligned}$$

where ϱ_M is given by (6.25), and $\gamma_d = \beta_d^2/N_0$ is the INR of the dth OFDMI at the kth frequency bin. For the Q-channel, $P_s^Q\left(\frac{E_b}{N_0},\gamma\mid k,\alpha,\tau,\phi\right)$ is identical to $P_s^I\left(\frac{E_b}{N_0},\gamma\mid k,\alpha,\tau,\phi\right)$ in (7.20) but with $\Omega_{d,p,I}^{(q)}(x, y, \alpha, \tau, \phi)$ replaced with $\Omega_{d,p,Q}^{(q)}(x, y, \alpha, \tau, \phi)$. The average probability of symbol error, $P_s\left(\frac{E_b}{N_0}, \gamma \mid \alpha, \tau, \phi\right)$, is obtained by averaging across all $N - K$ occupied bins, i.e.

$$P_s^I\left(\frac{E_b}{N_0}, \gamma \mid \alpha, \tau, \phi\right) = \frac{1}{N-K}\sum_{k=0}^{N-K-1} P_s^I\left(\frac{E_b}{N_0}, \gamma \mid k, \alpha, \tau, \phi\right). \tag{7.21}$$

In the multiple access case, i.e. OFDMA, the uth user occupying $\boldsymbol{f}^u = \boldsymbol{k}^u/N$ frequency bins will have a SER of

$$P_s^u\left(\frac{E_b}{N_0}, \gamma \mid \alpha, \tau, \phi\right) = \frac{1}{v}\sum_{\forall k \in \boldsymbol{k}^u} P_s\left(\frac{E_b}{N_0}, \gamma \mid k, \alpha, \tau, \phi\right), \tag{7.22}$$

where $\boldsymbol{k}^u$ is a vector of size v containing the indicies of the frequencies occupied by the uth user.

7.2.4 Probability of Bit Error, P_b

The relationship between P_b, P_b^I and P_b^Q is given by (6.20). As in the probability of symbol error case, the analysis begins by considering the I-channel first then extending it to include the Q-channel. Given $P_{R_k}^I(r)$ in (7.18) with its symmetry around zero and using the same principles in Section §6.2.3, P_b^I can be shown to be

$$\begin{aligned} P_b^I\left(\frac{E_b}{N_0}, \gamma \mid k, \alpha, \tau, \phi\right) \approx\; & \varsigma_M \left(\prod_{w=1}^{J} Z_w^{-2N}\right) \times \\ & \sum_{i=1}^{J}\sum_{g=0}^{N-1}\sum_{\ell=1}^{2}\sum_{m=1}^{\sqrt{M}/2}\sum_{x_{i,g}^{(\ell)}=1}^{\sqrt{Z_i}}\sum_{y_{i,g}^{(\ell)}=1}^{\sqrt{Z_i}} \operatorname{erfc}\left[(2m-1)\,\varrho_M\sqrt{\frac{E_b}{N_0}} - \right. \\ & \left. \sum_{d=1}^{J}\sum_{p=0}^{N-1}\sum_{q=1}^{2}\left\{\frac{\sqrt{\gamma_d}}{N}\left|\Psi_{d,p}^{(q)}(\alpha, \tau, \phi)\right|\Omega_{d,p,I}^{(q)}(x, y, \alpha, \tau, \phi)\right\}\right], \end{aligned} \tag{7.23}$$

where ς_M is given by Equation (6.24). For the Q-channel, P_b^Q is identical to P_b^I in (7.23) but with $\Omega_{d,p,I}^{(q)}(x, y, \alpha, \tau, \phi)$ replaced with $\Omega_{d,p,Q}^{(q)}(x, y, \alpha, \tau, \phi)$. The expressions for $P_b\left(\frac{E_b}{N_0}, \gamma \mid \alpha, \tau, \phi\right)$ and $P_b^u\left(\frac{E_b}{N_0}, \gamma \mid \alpha, \tau, \phi\right)$ are obtained in the same manner as (7.21) and (7.22), respectively.

7.2.5 BPSK Signal Mapping

The expressions in (7.20) and (7.23) and their Q-channel equivalents assume $M > 2$ and $Z_i > 2\,\forall i$, i.e. the expressions need modifications when either the desired or interfering signal(s) are BPSK modulated. When the desired signal mapping is set to BPSK (i.e. $M = 2$), the following changes must take place to obtain correct analytical results:

1. $P_b = P_s$ since there is only one data bit per symbol (i.e. $b = 1$);
2. $P_b^Q = 0$ since no data bits are carried by the Q-channel; and

3. M is replaced by 4 (that is, BPSK is identical to QPSK in one dimension). This results in $\varsigma_M = \frac{1}{2}$ and $\varrho_M = 1$.

When the ith OFDMI uses BPSK signal mapping (i.e. $Z_i = 2$), the following changes must take place to obtain correct analytical results:

1. Z_i is replaced with 4; and
2. $y_{i,g}^{(\ell)} = 0\,\forall g, \forall \ell$ since the ith interferer does not have any data carried by the Q-channel.

7.2.6 Computational Feasibility

While the expressions for P_s^I and P_b^I in (7.20) and (7.23) and their Q-channel equivalents are exact, evaluating them is not a simple task. Computation of the expression in (7.20) requires $\prod_{i=1}^{J} Z_i^{2N}$ iterations because of the nested summations. So, for a simple scenario where $N = 64$, $J = 1$ and $Z = 4$, the number of iterations required to compute (7.20) is $4^{128} \approx 1.16 \times 10^{77}$, which would take a single 3 GHz CPU chip approximately 1.22×10^{57} *millennia* to compute and is, therefore, computationally infeasible. This observation suggests that engineers would be better off using Monte Carlo numerical methods than exact analytical expressions.

However, a better alternative would be to derive approximations to the exact expressions to reduce the computational complexity while, at the same time, maintaining an acceptable level of accuracy.

7.3 Approximations to the Exact Error Rate Expressions

The computational complexity of the exact analytical expressions arise mainly from the presence of spectral leakage, i.e. $\Psi_{i,g}^{(1)}(\alpha, \tau, \phi)$ and $\Psi_{i,g}^{(2)}(\alpha, \tau, \phi)$. Spectral leakage means that *every* interfering subcarrier will have a weighted component at the kth frequency bin. Spectral leakage is caused by frequency and time offsets between the interfering and desired signals, i.e. α and τ, respectively. It should be noted that for an OFDMI with N subcarriers, if $\alpha \neq 0$ and $\tau = 0$ there will be N components present at the kth frequency bin. However, when $\tau \neq 0$ there will be $2N$ components present at the kth bin regardless of the value of α (see Appendix C). That is because with a timing misalignment, *two* interfering symbols will be present in the DFT window (Fig. 7.1).

There are several approaches that can be taken to approximate the exact analytical expressions for P_s and P_b. These approaches vary in complexity and accuracy and are addressed in this section.

7.3.1 Typical Accuracy of Crystal Oscillators

When considering OFDM systems of the same type (e.g. all IEEE 802.11g WLANs) as is the case throughout this thesis, the typical accuracy of crystal oscillators can be used to simplify the spectral leakage terms. The accuracy of a 10 MHz crystal oscillator at -140 dBc (noise power in 1 Hz bandwidth at f_m Hz offset from carrier per carrier signal power [75, p. 100]) is $f_m = \pm 10$ Hz [75, p. 390]. Therefore, operating at 2.4 GHz, the frequency offset error will be $f_m = \pm 2.4$ kHz. For an 802.11g/n system that has a carrier bandwidth of 312.5 kHz, the maximum percentage offset is approximately $\pm 0.8\%$ (i.e. $|\alpha| \leq 0.008$). For all intents and purposes, it can be assumed that the desired and interfering subcarriers are perfectly aligned, i.e. $\alpha_i = 0 \, \forall i$.

While the assumption of no frequency offsets between desired an interfering OFDM signals will reduce the complexity of $\Psi^{(1)}_{i,g}(\alpha, \tau, \phi)$ and $\Psi^{(2)}_{i,g}(\alpha, \tau, \phi)$ (see Appendix C), it will have *no* impact on the number of iterations needed to compute the error rate expressions (provided that $\tau_i \neq 0$). However, the assumption becomes useful when considering the case of $\tau_i = 0$, as explained in Section §7.3.3.

7.3.2 Subcarrier Selectivity

The number of interfering subcarriers, N, is a major factor in the computational complexity of the analytical expressions. However, depending on the values of α and τ, the nearest interfering subcarriers to the kth frequency bin have the majority of the interference energy. Fig. 7.2 shows the energy contributions of the interfering subcarriers at the kth bin with different τ, α and ϕ values. Table 7.1 shows the energy contributions of the nearest v interfering subcarriers to the kth frequency bin, E_v, for the cases shown in Fig. 7.2. Typically, the nearest five subcarriers will account for more than 90% of the total interference energy.

Therefore, one approach is to consider *only* the nearest v interfering subcarriers to the kth frequency bin. This would reduce the computational complexity from $\prod_{i=1}^{J} Z_i^{2N}$ to $\prod_{i=1}^{J} Z_i^{2v}$ iterations that are needed to compute (7.20). The drawback is, of course, that since the majority of interfering subcarriers are not included (however small their energy contributions are), the accuracy of the results is compromised. To compensate for the missing subcarriers, a *scaling factor*, s_f, can be introduced and multiplied by $\left|\Psi^{(q)}_{d,p}(\alpha, \tau, \phi)\right|$ in the expressions. An *approximate* scaling factor that can be considered is given by

$$s_f = 2 - E_v, \tag{7.24}$$

where

$$E_v = \frac{1}{N^2} \sum_{g \in v} \sum_{\ell=1}^{2} \left|\Psi^{(\ell)}_{i,g}(\alpha, \tau, \phi)\right|^2,$$

is the energy *contribution* of the selected v subcarriers. It should be noted that

$$\frac{1}{N^2} \sum_{g=0}^{N-1} \sum_{\ell=1}^{2} \left|\Psi^{(\ell)}_{i,g}(\alpha, \tau, \phi)\right|^2 \equiv 1. \tag{7.25}$$

The accuracy of the *full* analytical expressions are shown in Fig. 7.3a where a scaled down scenario ($N = 4$) is chosen for feasible computational complexity. It is clear from Fig. 7.3a that the full analytical expressions match very closely with the results obtained from the Monte Carlo method. The effectiveness of the subcarrier selectivity approach is demonstrated in Figs. 7.3b and 7.4 against the results obtained from the Monte Carlo method. In Fig. 7.3b, selecting only the nearest five interfering subcarriers (out of a total $N = 64$) to the desired frequency bin without using a scaling factor results in significant deviation

Table 7.1: Energy contributions of the nearest v interfering subcarriers to the kth frequency bin, E_v, for the scenarios in Fig. 7.2.

	Fig. 7.2a	Fig. 7.2b	Fig. 7.2c	Fig. 7.2d	Fig. 7.2e	Fig. 7.2f
E_v,$v = 4$	0.9010	0.8964	0.8799	0.9346	0.9027	1
E_v,$v = 6$	0.9335	0.9369	0.9092	0.9563	0.9324	1
E_v,$v = 8$	0.9503	0.9485	0.9337	0.9674	0.9501	1
E_v,$v = 10$	0.9604	0.9595	0.9528	0.9741	0.9605	1

from the Monte Carlo results. However, when the scaling factor defined in (7.24) is used, the accuracy of the approximation improves significantly, with marginal deviation at high E_b/N_0 values. The methods for calculating the lower and upper bounds are described in Sections §7.3.3 and §7.3.4 respectively.

The accuracy of the subcarrier selectivity approximation method is further improved when considering the parameters used in Fig. 7.4. The fact that $\tau = 0$ in Fig. 7.4 reduces the computation time by a factor of a square root, which enables the inclusion of the nearest eight interfering subcarriers to the desired frequency bin (out of a total $N = 128$). While the subcarrier selectivity approximation method provides accuracy levels that can be considered good (very good in the case of Fig. 7.4), it is computationally infeasible when considering multiple interferers (i.e. $J > 1$). Therefore, more computationally efficient approximation methods are needed to enable analytical estimation of error rate performance of OFDM systems in the presence of multiple OFDMIs.

7.3.3 The Lower Bound

The lower bound to the error rate performance (i.e. best case scenario) is achieved when there is no spectral leakage, i.e. when $\tau_i = 0\,\forall i$ *and* $\alpha_i = 0\,\forall i$. While the assumption of perfect frequency alignment between desired and interfering signals is reasonable (as discussed in Section §7.3.1) when considering same-type system interference, perfect time synchronisation between desired and interfering signals is possible, but unlikely. Setting $\tau_i = 0\,\forall i$ and $\alpha_i = 0\,\forall i$ would reduce the computational complexity of (7.20) from $\prod_{i=1}^{J} Z_i^{2N}$ to $\prod_{i=1}^{J} Z_i$ iterations, which is considerable. The lower bound expressions for P_s^I and P_b^I are, respectively, given by

$$P_s^I\left(\frac{E_b}{N_0}, \gamma \mid k, \phi\right) = \frac{\sqrt{M}-1}{\sqrt{M}}\left(\prod_{w=1}^{J} Z_w^{-1}\right)\sum_{i=1}^{J}\sum_{x_{i,}=1}^{\sqrt{Z_i}}\sum_{y_{i,}=1}^{\sqrt{Z_i}} \mathrm{erfc}\left[\varrho_M\sqrt{\frac{E_b}{N_0}} - \sum_{d=1}^{J}\sqrt{\gamma_d}\,\Phi_{d,I}\left(x, y, \phi\right)\right], \tag{7.26}$$

and

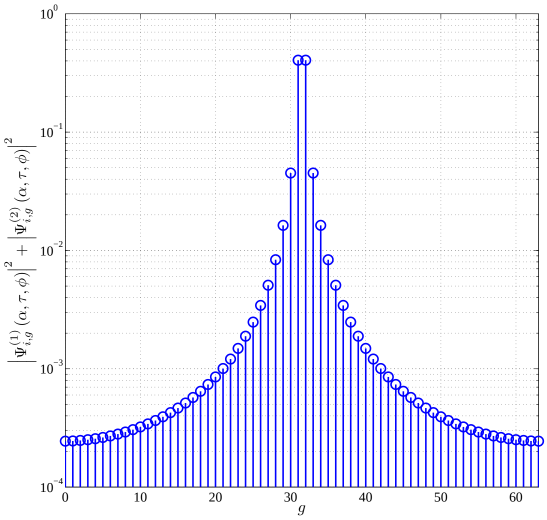

(a) $N = 64$, $\tau = 32$, $\alpha = 0.5$, $\phi = 0$ and $k = 32$.

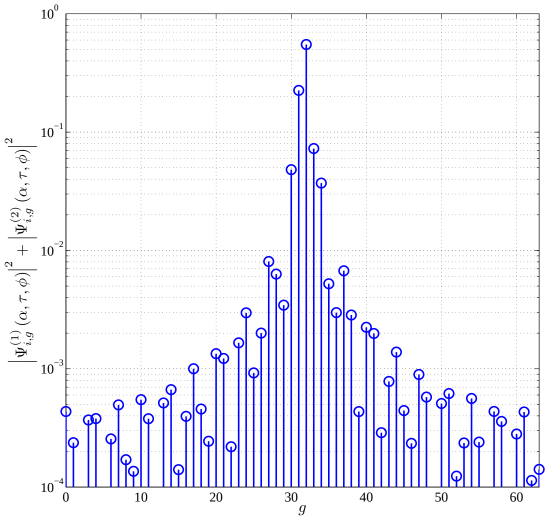

(b) $N = 64$, $\tau = 19$, $\alpha = 0.2$, $\phi = \pi/4$ and $k = 32$.

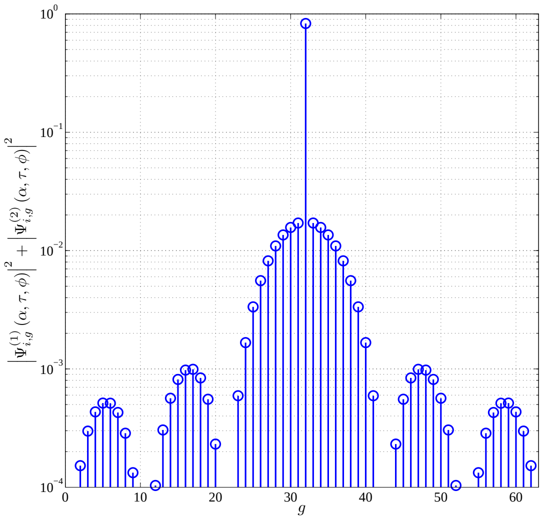

(c) $N = 64$, $\tau = 6$, $\alpha = 0$, $\phi = \pi/6$ and $k = 32$.

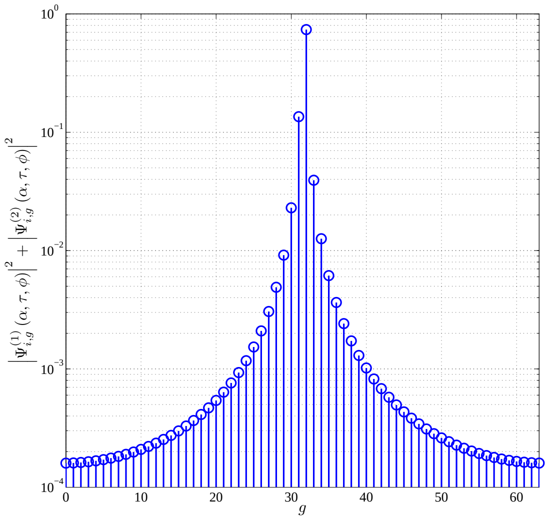

(d) $N = 64$, $\tau = 0$, $\alpha = 0.3$, $\phi = \pi/12$ and $k = 32$.

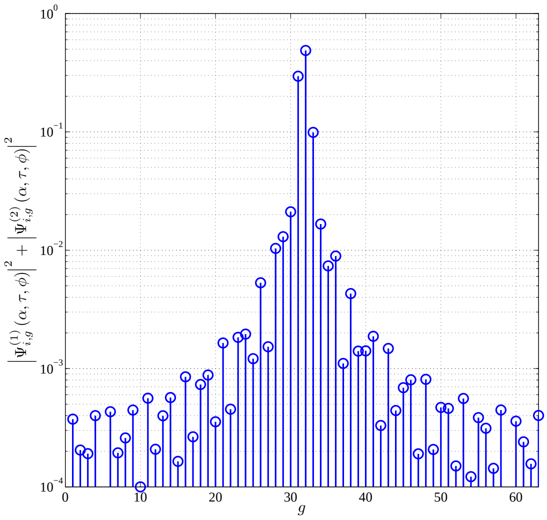

(e) $N = 64$, $\tau = 26$, $\alpha = 0.1$, $\phi = 0$ and $k = 32$.

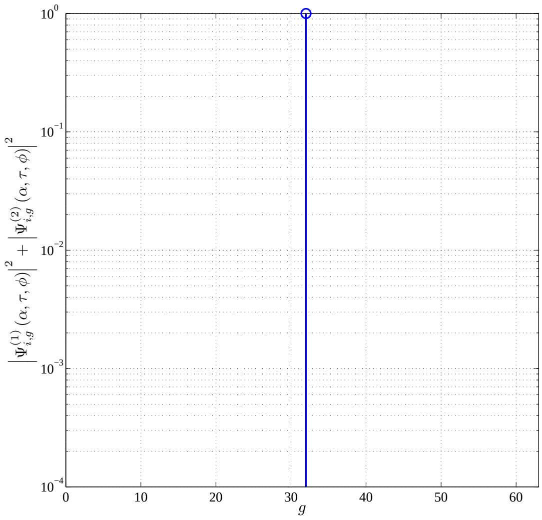

(f) $N = 64$, $\tau = 0$, $\alpha = 0$, $\phi = 0$ and $k = 32$. No spectral leakage.

Figure 7.2: Typical energy distribution (shown on a logarithmic scale) of the ith OFDMI's subcarriers at the kth frequency bin as a function of τ_i, α_i and ϕ_i.

$$P_b^I\left(\frac{E_b}{N_0},\gamma \mid k,\phi\right) \approx \varsigma_M\left(\prod_{w=1}^{J} Z_w^{-1}\right)\sum_{i=1}^{J}\sum_{m=1}^{\sqrt{M}/2}\sum_{x_i,=1}^{\sqrt{Z_i}}\sum_{y_i,=1}^{\sqrt{Z_i}} \operatorname{erfc}\left[(2m-1)\,\varrho_M\sqrt{\frac{E_b}{N_0}}- \sum_{d=1}^{J}\sqrt{\gamma_d}\Phi_{d,I}\left(x,y,\phi\right)\right], \tag{7.27}$$

where

$$\Phi_{d,I}\left(x,y,\phi\right) = \left(2x_d - 1 - \sqrt{Z_d}\right)\cos\left(\phi_d\right) - \left(2y_d - 1 - \sqrt{Z_d}\right)\sin\left(\phi_d\right).$$

The expressions for P_s^Q and P_b^Q are identical to (7.26) and (7.27), respectively, but with $\Phi_{d,I}\left(x,y,\phi\right)$ replaced by

$$\Phi_{d,Q}\left(x,y,\phi\right) = \left(2x_d - 1 - \sqrt{Z_d}\right)\sin\left(\phi_d\right) + \left(2y_d - 1 - \sqrt{Z_d}\right)\cos\left(\phi_d\right).$$

7.3.4 The Upper Bound

The upper bound to the error rate performance (i.e. worst case scenario) is obtained using the *central limit theorem* (CLT). The CLT states that the distribution of the sum of a large number of independent random variables (i.r.v.'s) converges to a Gaussian distribution regardless of the distributions of the individual i.r.v.'s [123, p. 278]. Convergence in distribution means that the cumulative density function (cdf) of the sum of i.r.v.'s converges point-wise to the cdf of a Gaussian distribution [124, p. 249].

Given that I_k is the sum of $2NJ$ i.r.v.'s each with a pdf given by (7.14) and (7.15) for the I- and Q-channels respectively, and that $2NJ$ is typically large, the CLT could be applied to find an *approximate* pdf for I_k that follows a Gaussian distribution. According to the CLT, the mean and variance of the sum of i.r.v.'s (I_k in this case) are, respectively, given by

$$\mu_I = \sum_{i=1}^{J}\sum_{g=0}^{N-1}\sum_{\ell=1}^{2}\mu_{i,g,\ell,I}, \tag{7.28}$$

$$\sigma_I^2 = \sum_{i=1}^{J}\sum_{g=0}^{N-1}\sum_{\ell=1}^{2}\sigma_{i,g,\ell,I}^2, \tag{7.29}$$

where $\mu_{i,g,\ell,I}$ and $\sigma_{i,g,\ell,I}^2$ are, respectively, the mean and variance of (7.14)[4]. Given that (7.14) is symmetrical around zero, $\mu_{i,g,\ell,I} = 0\,\forall i, \forall g, \forall \ell$ and consequently $\mu_I = 0$ (similarly, $\mu_Q = 0$). It can be shown that the variances of (7.14) and (7.15) are, respectively, given by[5]

$$\sigma_{i,g,\ell,I}^2 = \frac{(Z_i - 1)}{3N^2}\beta_i^2\left|\Psi_{i,g}^{(\ell)}\left(\alpha,\tau,\phi\right)\right|^2\Lambda_{i,g,I}^{(\ell)}, \tag{7.30}$$

[4]The same principles apply for the Q-channel.

[5]Derivation in Appendix E.

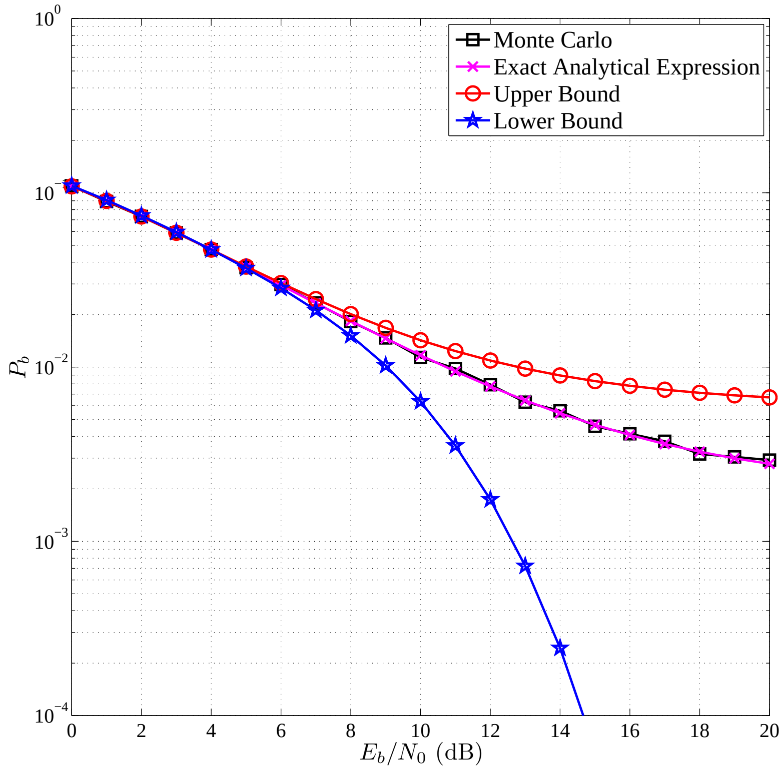

(a) $N = 4$.

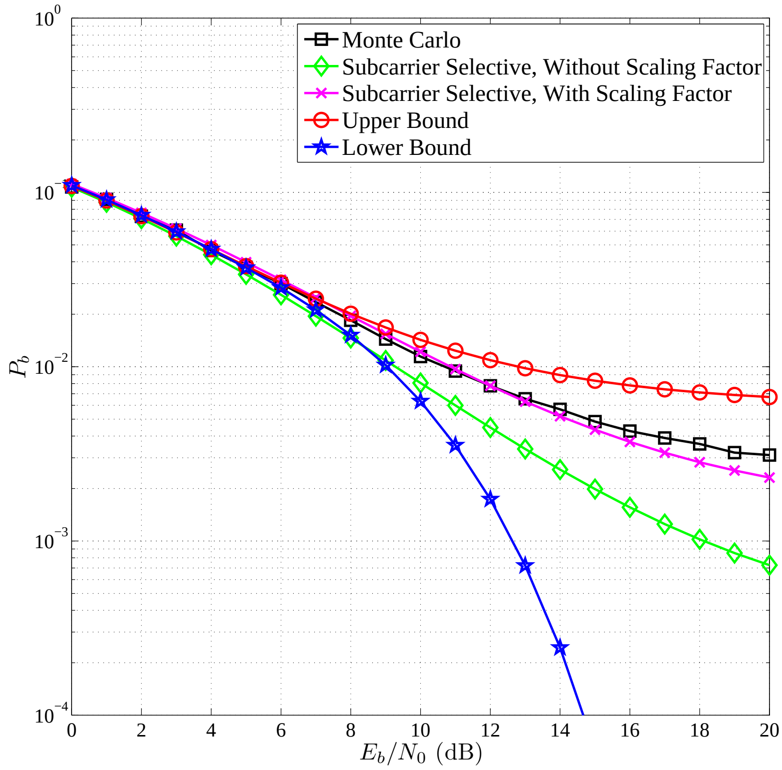

(b) $N = 64$.

Figure 7.3: P_b performance comparison of QPSK OFDM in the presence of a single QPSK OFDMI using the Monte Carlo Method and the analytical approximation methods described in Section §7.3. SIR $= 8$ dB, $\tau = 13$, $\alpha = 0.3$, and $\phi = \pi/4$. The subcarrier selective method uses $\upsilon = 5$ and the scaling factor is defined in (7.24).

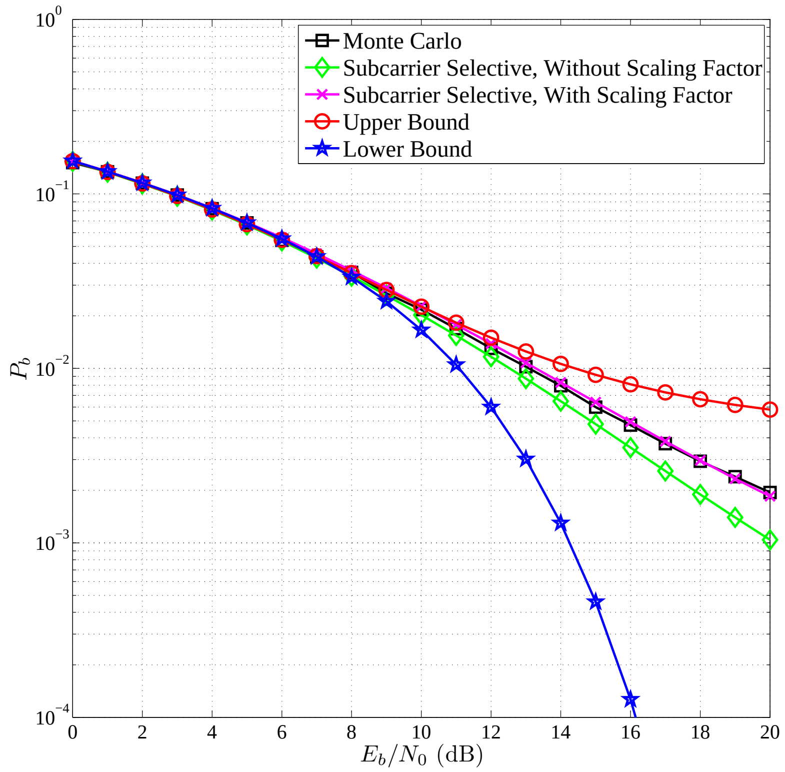

Figure 7.4: P_b performance comparison of 16QAM OFDM in the presence of a single QPSK OFDMI using the Monte Carlo Method and the analytical approximation methods described in Section §7.3. SIR $= 15$ dB, $N = 128$, $\tau = 0$, $\alpha = 0.4$, and $\phi = 0$. The subcarrier selective method uses $\upsilon = 8$ and the scaling factor is defined in (7.24).

$$\sigma^2_{i,g,\ell,Q} = \frac{(Z_i - 1)}{3N^2}\beta_i^2 \left|\Psi^{(\ell)}_{i,g}(\alpha,\tau,\phi)\right|^2 \Lambda^{(\ell)}_{i,g,Q}, \tag{7.31}$$

where

$$\Lambda^{(\ell)}_{i,g,I} = \begin{cases} \cos^2\left[\varphi^{(\ell)}_{i,g}(\alpha,\tau,\phi)\right] & Z_i = 2 \\ 1 & \text{otherwise,} \end{cases} \tag{7.32}$$

and

$$\Lambda^{(\ell)}_{i,g,Q} = \begin{cases} \sin^2\left[\varphi^{(\ell)}_{i,g}(\alpha,\tau,\phi)\right] & Z_i = 2 \\ 1 & \text{otherwise.} \end{cases} \tag{7.33}$$

Therefore, given the expression in (7.25), the variances for I_k in the I- and Q-channels are, respectively, given by

$$\begin{aligned}
\sigma_I^2 &= \frac{1}{3N^2}\sum_{i=1}^{J}\beta_i^2\left(Z_i-1\right)\sum_{g=0}^{N-1}\sum_{\ell=1}^{2}\left\{\left|\Psi_{i,g}^{(\ell)}\left(\alpha,\tau,\phi\right)\right|^2\Lambda_{i,g,I}^{(\ell)}\right\} \\
&= \frac{1}{3}\sum_{i=1}^{J}\beta_i^2\left(Z_i-1\right)\Upsilon_{i,g,I}^{(\ell)} \qquad (7.34)\\
&= \begin{cases} \dfrac{1}{3N^2}\displaystyle\sum_{i=1}^{J}\beta_i^2\left(Z_i-1\right)\sum_{g=0}^{N-1}\sum_{\ell=1}^{2}\left\{\left|\Psi_{i,g}^{(\ell)}\left(\alpha,\tau,\phi\right)\right|^2\cos^2\left[\varphi_{i,g}^{(\ell)}\left(\alpha,\tau,\phi\right)\right]\right\} & Z_i=2\\ \dfrac{1}{3}\displaystyle\sum_{i=1}^{J}\beta_i^2\left(Z_i-1\right) & \text{otherwise,}\end{cases}
\end{aligned}$$

and

$$\begin{aligned}
\sigma_Q^2 &= \frac{1}{3N^2}\sum_{i=1}^{J}\beta_i^2\left(Z_i-1\right)\sum_{g=0}^{N-1}\sum_{\ell=1}^{2}\left\{\left|\Psi_{i,g}^{(\ell)}\left(\alpha,\tau,\phi\right)\right|^2\Lambda_{i,g,Q}^{(\ell)}\right\} \\
&= \frac{1}{3}\sum_{i=1}^{J}\beta_i^2\left(Z_i-1\right)\Upsilon_{i,g,Q}^{(\ell)} \qquad (7.35)\\
&= \begin{cases} \dfrac{1}{3N^2}\displaystyle\sum_{i=1}^{J}\beta_i^2\left(Z_i-1\right)\sum_{g=0}^{N-1}\sum_{\ell=1}^{2}\left\{\left|\Psi_{i,g}^{(\ell)}\left(\alpha,\tau,\phi\right)\right|^2\sin^2\left[\varphi_{i,g}^{(\ell)}\left(\alpha,\tau,\phi\right)\right]\right\} & Z_i=2\\ \dfrac{1}{3}\displaystyle\sum_{i=1}^{J}\beta_i^2\left(Z_i-1\right) & \text{otherwise.}\end{cases}
\end{aligned}$$

Therefore, for a large number of random components (i.e. $2NJ$) and with a mean of zero and a variance given by (7.34), $P_{I_k}^{I}\left(r\right)$ can be approximated to be

$$P_{I_k}^{I}\left(r\right)\approx\frac{1}{\sqrt{2\pi\sigma_I^2}}e^{-r^2/\left(2\sigma_I^2\right)}, \qquad (7.36)$$

and consequently, the pdf of R_k in the I-channel is given by

$$P_{R_k}^{I}\left(r\right)\approx\frac{1}{\sqrt{\pi\left(N_0+2\sigma_I^2\right)}}e^{-r^2/\left(N_0+2\sigma_I^2\right)}. \qquad (7.37)$$

Given (7.37) and using the same steps in Section §7.2, the upper bound expressions for P_s^I and P_b^I for M-ary QAM OFDM in the presence of J OFDMIs can be shown to be

$$P_s^I\left(\frac{E_b}{N_0},\gamma\mid k\right)\approx\frac{\sqrt{M}-1}{\sqrt{M}}\operatorname{erfc}\left[\varrho_M\left\{\frac{N_0}{E_b}+\frac{2\log_2\left(M\right)}{3}\sum_{i=1}^{J}\frac{\left(Z_i-1\right)\Upsilon_{i,g,I}^{(\ell)}}{\mathrm{SIR}_{k,i}}\right\}^{-\frac{1}{2}}\right], \qquad (7.38)$$

$$P_b^I\left(\frac{E_b}{N_0},\gamma \mid k\right) \approx \varsigma_M \sum_{m=1}^{\sqrt{M}/2} \operatorname{erfc}\left[(2m-1)\,\varrho_M \left\{\frac{N_0}{E_b} + \frac{2\log_2(M)}{3}\sum_{i=1}^{J}\frac{(Z_i-1)\,\Upsilon_{i,g,I}^{(\ell)}}{\mathrm{SIR}_{k,i}}\right\}^{-\frac{1}{2}}\right], \tag{7.39}$$

where $\mathrm{SIR}_{k,i} = E_s/\beta_i^2$ is the signal-to-interference ratio of the ith interferer in the kth bin. The upper bound expressions for P_s^Q and P_b^Q are identical to those in (7.38) and (7.39), respectively, with $\Upsilon_{i,g,I}^{(\ell)}$ replaced by $\Upsilon_{i,g,Q}^{(\ell)}$. It should be noted that with the exception of BPSK interference, the upper bound expressions are independent of τ, α and ϕ. Also, the computational time needed to evaluate the upper bound expressions is in the order of a fraction of a second.

It is clear from Figs. 7.3b and 7.4, that despite the presence of $2N$ and N random variables, respectively, the upper bound results do not provide a close match to the Monte Carlo results. While spectral leakage ensures the presence of at least N random variables ($2N$ when $\tau \neq 0$), the magnitude of the vast majority of these random variables is very small compared to the nearest interfering subcarriers as illustrated in Fig. 7.2. Effectively, this is equivalent to just having v strong components added together (as opposed to N components), which results in a distribution that is *not* Gaussian. It should be noted that in both Figs. 7.3b and 7.4 the upper bound approximation provides a closer fit to the Monte Carlo results than the lower bound. The strength of the upper bound approximation is enhanced when multiple interferers are considered as illustrated in Fig. 7.5, i.e. when there are $2NJ$ random variables present with $\sum_{i=1}^{J} v_i$ strong components.

Based on the results in Figs. 7.3 – 7.5, the following observations can be made regarding the lower and upper bound approximation methods:

1. In all cases, the upper bound provides a closer fit to the Monte Carlo results than the lower bound;
2. As the number of interferers increases, the upper bound accuracy improves;
3. The accuracy of the upper bound improves as the SINR gets smaller; and
4. The upper bound is more computationally efficient than the lower bound.

Given the exact expressions with their computational infeasibility and the approximation methods with their respective limitations, an algorithm is needed to provide an easy and fast way to estimate the error rate performance with acceptable accuracy levels.

7.4 Proposed Algorithm for Rapid Error Rate Estimation

Based on the computational complexity and accuracy of the full analytical model and the various approximation methods discussed in Section §7.3, the following algorithm is proposed when estimating the error rate performance of M-ary QAM OFDM systems in the presence of OFDM interference:

1. When there is only one interferer, the *subcarrier selectivity* approximation method with a scaling factor is the method of choice. The number of included subcarriers, v, is chosen based on the available computational power;

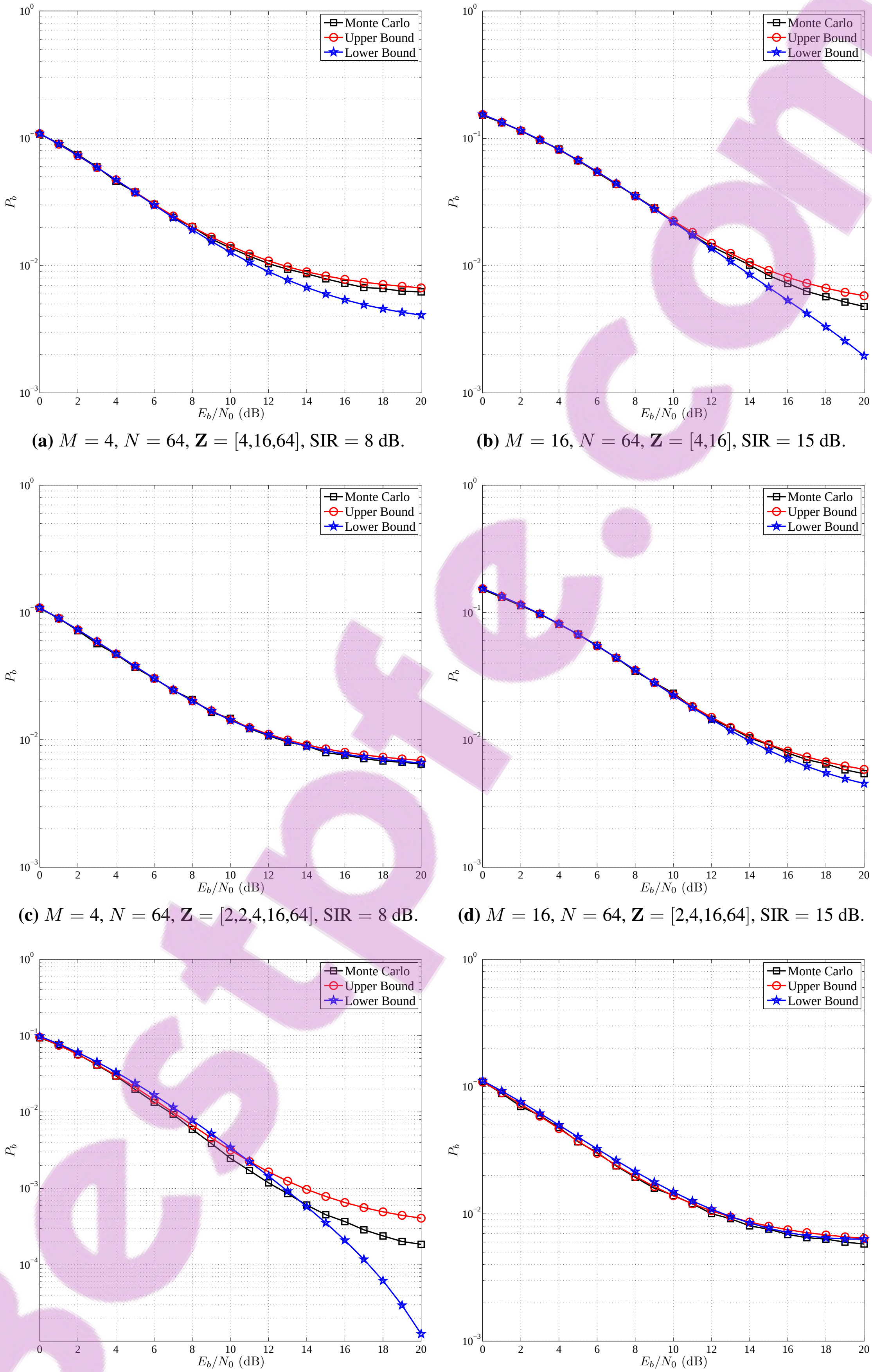

(a) $M = 4$, $N = 64$, $\mathbf{Z} = [4,16,64]$, SIR $= 8$ dB.

(b) $M = 16$, $N = 64$, $\mathbf{Z} = [4,16]$, SIR $= 15$ dB.

(c) $M = 4$, $N = 64$, $\mathbf{Z} = [2,2,4,16,64]$, SIR $= 8$ dB.

(d) $M = 16$, $N = 64$, $\mathbf{Z} = [2,4,16,64]$, SIR $= 15$ dB.

(e) $M = 2$, $N = 64$, $\mathbf{Z} = [2,4,16,4]$, SIR $= 8$ dB.

(f) $M = 2$, $N = 64$, $\mathbf{Z} = [2,4,16,4]$, SIR $= 5$ dB.

Figure 7.5: P_b performance comparison of M-ary QAM OFDM in the presence of J OFDMIs. Each interferer has $1/J$th of the total interference power. $\tau \sim U[0, N-1]$, $\alpha \sim U[0,1]$, and $\phi \sim U[0, 2\pi]$.

2. In the case of multiple interferers, the *upper bound* is the best available option for the following reasons:

   (a) It provides the closest fit to the Monte Carlo results;

   (b) It is computationally efficient; and

   (c) It provides the results for the worst case error rate performance. Therefore, its results are meaningful to system engineers when designing and planning OFDM-based wireless networks.

Throughout Chapters 8 and 9 this algorithm is used for estimating the error rate performance. While the approximation methods do not provide *exact* results, they do provide estimations with acceptable accuracy and are significantly faster and more convenient than Monte Carlo methods[6].

7.5 Application to OFDMA

Orthogonal Frequency Division Multiple Access (OFDMA) is a multiple access scheme used by modern WCSs (e.g. LTE and LTE Advanced) to provide wireless services to multiple users that operate on a network using OFDM as a PHY transmission protocol. In OFDMA, each user is allocated a set of subcarriers (they don't have to be in a contiguous spectrum) for a time slot. The subcarrier allocation for each user may differ from one time slot to the next depending on the algorithm used by the system to allocate the subcarriers.

The raw error rate expressions derived in Chapters 6 and 7 can be directly applied to OFDMA systems — prior knowledge of the user's allocated subcarriers is needed to average the individual error rates for those allocated subcarriers according to equation (6.18) for the NBIs case and equation (7.22) for the OFDMIs case (and their equivalent Q-channel and BER expressions).

7.6 Forward Error Correction Coding and Interleaving

Most (if not all) commercial OFDM systems use a form of forward error correction (FEC) coding scheme with interleaving techniques to improve (sometimes substantially) their error rate performances. However, there are several types of FEC codes (e.g. Reed-Solomon, convolutional, turbo, etc.) and they differ in the way they enhance the raw error rate performance . Also, once the raw error rates are given (as in this thesis), it is relatively straight forward to calculate the corrected/refined error rates by substituting the raw error rate values into the expressions specific to the FEC scheme in use as in [66, p. 244] and [67, p. 6]. Furthermore, the corrected error rates and the raw error rates are related to each other in a monotonic relationship and a raw error rate threshold will correspond to a refined/corrected threshold. Therefore, FEC codes are not included in the the analyses presented in this thesis to ensure they are *independent* of the FEC coding scheme and thus, transportable across different platforms and standards.

[6]Depending on the resolution of the Monte Carlo model and the scenario parameters, the duration of the Monte Carlo simulations take anywhere between a few seconds and several days which is orders of magnitude longer than the analytical approximation methods selected for the algorithm.

It should also be noted that the results presented in Chapters 6–9 of this thesis are *indicative* since no FEC scheme or interleaving techniques were used, and the performance *trends* are of particular importance.

7.7 Summary

Analytical error rate expressions for a generic M-ary QAM OFDM in the presence of multiple generic Z-ary QAM OFDMIs have been derived in this chapter. While the full analytical expressions are exact, they are computationally infeasible, thus several approximation methods have been developed that differ in computational complexity and accuracy. The proposed algorithm for rapid error rate estimation used in this thesis is a hybrid of two approximation methods: a scaled down version of the full analytical expressions is used when considering a single interferer with a scaling factor included to compensate for underestimation. The central limit theorem is used to calculate the upper bound and is used when considering multiple interferers.

Performance assessments of OFDM systems in the presence of multiple OFDMIs are presented in Chapter 8 for indoor-to-indoor interference scenarios and Chapter 9 for outdoor-to-indoor interference scenarios.

Chapter 8

OFDM-to-OFDM Interference Performance Assessment — Indoor Environments

8.1 Introduction

In Chapter 7, a computationally efficient algorithm for calculating error rate performance of OFDM systems in the presence of multiple OFDMIs was presented. The algorithm uses approximations to the analytical expressions for the error rate performance and has been shown to provide fast and sufficiently accurate estimations. Using this algorithm and the path loss databases for Test Environments A & B (presented in Chapter 5), a performance assessment is presented in this chapter for OFDM-to-OFDM interference scenarios in indoor environments. The OFDM results are then compared with DS-SS results under identical environmental conditions. This comparison enables the investigation into the feasibility of using DS-SS system planning strategies for OFDM systems.

Section §8.2 presents general error rate performance trends[1] using the upper bound expressions derived in Section §7.3.4. Case studies that use path loss databases for Test Environments A & B are presented in Section §8.3 followed by the comparison with DS-SS systems in Section §8.4.

8.2 General Performance Trends

The error rate performance of OFDM systems depend on both the desired and interfering QAM levels, M and $\mathbf{Z}$ respectively. Fig. 8.1 illustrates the effect of changing M on the probability of bit error, P_b, performance as a function of E_b/N_0 (Fig. 8.1a) and SIR (Fig. 8.1b) while all other system parameters are held constant. It is observed from Fig. 8.1 that M has a profound impact on the P_b performance — both when the system is noise-limited (Fig. 8.1a) and interference-limited (Fig. 8.1b). The bit error performance improves significantly for a given SINR as the QAM level is reduced (the best performance is observed with BPSK mapping, $M = 2$). While a lower QAM level achieves a superior bit error

[1] Not specific to a test environment.

performance compared to a high QAM level, the downside is reduction of throughput, since the number of data bits per mapped symbol, b, is given by

$$b = \log_2 (M) . \tag{6.21}$$

It is important to note that the trend of changing M on the bit error performance is universal and not case-specific with the individual parameter values determining the actual change in P_b as a function of M. To determine the effect of the interference QAM levels, $\mathbf{Z}$, on the bit error performance, recall the upper bound expression in the I-channel (identical principals apply for Q-channel and the symbol error performance)

$$P_b^I \approx \varsigma_M \sum_{m=1}^{\sqrt{M}/2} \text{erfc} \left[(2m-1)\, \varrho_M \left\{ \frac{N_0}{E_b} + \frac{2\log_2(M)}{3} \sum_{i=1}^{J} \frac{(Z_i - 1)\, \Upsilon_{i,g,I}^{(\ell)}}{\text{SIR}_{k,i}} \right\}^{-\frac{1}{2}} \right], \tag{7.39}$$

where P_b^I is clearly a function of Z_i. However, the QAM constellations used (both for desired and interfering OFDM signals) ensure that the *mean energy* of the mapped symbols is normalised to one (i.e. the mean energy of $L_{i,g}^{(\ell)}(x,y)/\beta_{i,g}$ is normalised to one). Therefore, a normalising factor, n_i, is included in the expression for locations of the interfering message points, $l_{i,g}^{(\ell)}(x,y)$, in signal space such that

$$l_{i,g}^{(\ell)}(x,y) = \frac{1}{N} \Psi_{i,g}^{(\ell)}(\alpha,\tau,\phi)\, L_{i,g}^{(\ell)}(x,y) \times n_i, \tag{8.1}$$

where $L_{i,g}^{(\ell)}(x,y)$ is given by (7.9). This means that the expression in (7.39) has to be modified to include n_i according to

$$P_b^I = \varsigma_M \sum_{m=1}^{\sqrt{M}/2} \text{erfc} \left[(2m-1)\, \varrho_M \left\{ \frac{N_0}{E_b} + \frac{2\log_2(M)}{3} \sum_{i=1}^{J} \frac{(Z_i - 1)\, n_i^2 \Upsilon_{i,g,I}^{(\ell)}}{\text{SIR}_{k,i}} \right\}^{-\frac{1}{2}} \right]. \tag{8.2}$$

The mean energy of $L_{i,g}^{(\ell)}(x,y)/\beta_{i,g}$ is calculated using its variance and is given by[2]

$$\text{Var}\left(L_{i,g}^{(\ell)}(x,y)/\beta_{i,g}\right) = \frac{Z_i - 1}{3}. \tag{8.3}$$

Since n_i is applied to the I-channel in (8.2), it follows that

$$n_i^2 \times \frac{Z_i - 1}{3} = \frac{1}{2},$$

since the I-channel contains 50% of the QAM energy (for square QAM constellations and using the Pythagorean identity). Therefore[3],

[2]See Appendix E.

[3]Note that for BPSK mapping ($Z_i = 2$), $n_i^2 \times \frac{Z_i - 1}{3} = 1$, since BPSK has no energy in the Q-channel and Z_i is replaced by 4 since BPSK is equivalent to QPSK in one channel.

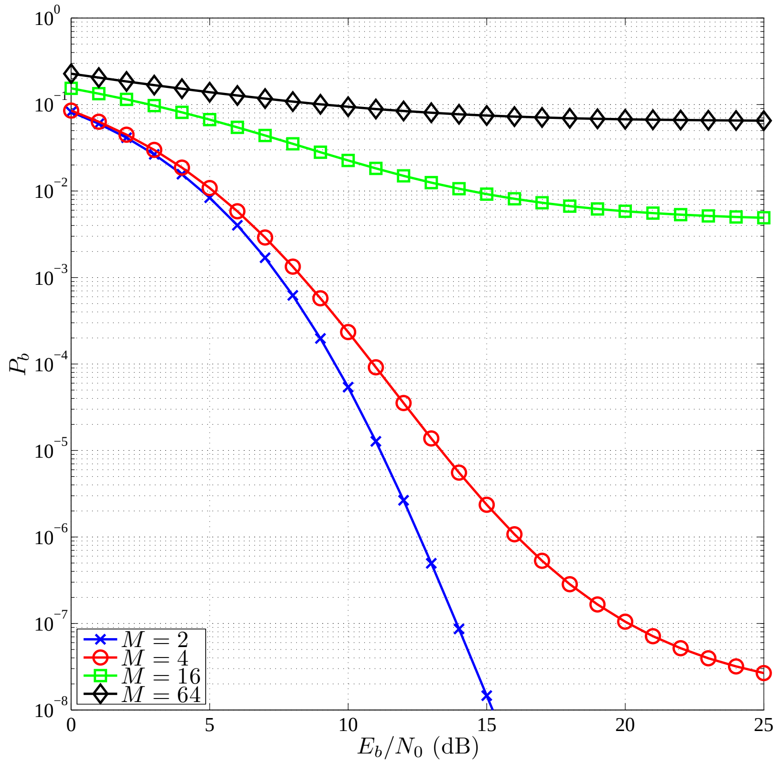

(a) SIR = 15 dB.

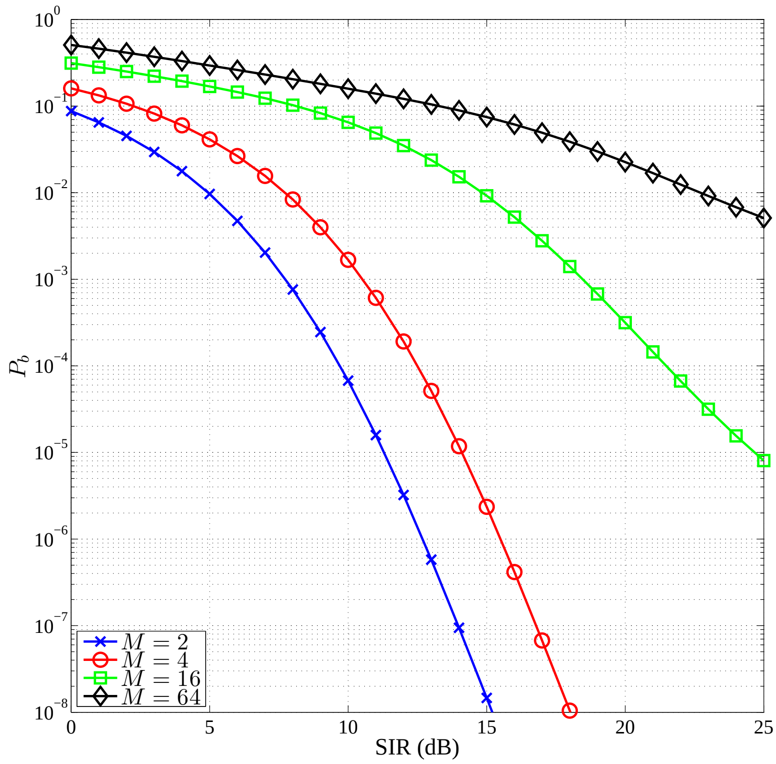

(b) $E_b/N_0 = 15$ dB.

Figure 8.1: Probability of bit error, P_b, performance of M-ary QAM OFDM in the presence of four OFDMIs with equal powers. $N = 64$, $\alpha = [0.2, 0.5, 0.35, 0]$, $\tau = [12, 49, 32, 14]$, $\phi = [0, \pi/6, \pi/3, \pi/2]$ radians and $\mathbf{Z} = [2, 4, 16, 64]$.

$$n_i = \sqrt{\frac{3}{2\left(Z_i - 1\right)}} \qquad (8.4)$$
$$= \begin{cases} 1 & Z_i = 2 \\ 1/\sqrt{2} & Z_i = 4 \\ 1/\sqrt{10} & Z_i = 16 \\ 1/\sqrt{42} & Z_i = 64. \end{cases}$$

For $Z_i > 2$, n_i has the effect of removing Z_i from the expression in (8.2) such that

$$P_b^I = \varsigma_M \sum_{m=1}^{\sqrt{M}/2} \operatorname{erfc}\left[\left(2m-1\right)\varrho_M \left(\frac{N_0}{E_b} + \log_2\left(M\right) \sum_{i=1}^{J} \begin{cases} \dfrac{2\Upsilon_{i,g,I}^{(\ell)}}{\mathrm{SIR}_{k,i}} & Z_i = 2 \\ \\ \dfrac{1}{\mathrm{SIR}_{k,i}} & Z_i > 2 \end{cases} \right)^{-\frac{1}{2}}\right], \qquad (8.5)$$

where $\Upsilon_{i,g,I}^{(\ell)}$ is defined in (7.34). It should be noted that

$$\sum_{i=1}^{J} \frac{1}{\mathrm{SIR}_{k,i}} = \sum_{i=1}^{J} \frac{\beta_{k,i}^2}{E_s}$$
$$= \frac{1}{E_s} \sum_{i=1}^{J} \beta_{k,i}^2$$
$$= \frac{1}{\mathrm{SIR}_k}, \qquad (8.6)$$

which is independent of J. This means that for $Z_i > 2\,\forall i$, the upper bound for the probability of bit error is given by

$$P_b^I = \varsigma_M \sum_{m=1}^{\sqrt{M}/2} \operatorname{erfc}\left[\left(2m-1\right)\varrho_M \left(\frac{N_0}{E_b} + \frac{\log_2\left(M\right)}{\mathrm{SIR}_k}\right)^{-\frac{1}{2}}\right], \qquad (8.7)$$

which is a function of the desired QAM level, M, the energy-per-bit-to-noise ratio, E_b/N_0, and the *overall* signal-to-interference ratio, SIR_k. While the presence of spectral leakage allows the use of the upper bound, the individual values for τ_i, α_i and ϕ_i become immaterial when $Z_i > 2$. Also, when $Z_i > 2\,\forall i$, the particular value of Z_i becomes unimportant as demonstrated by (8.7). Therefore, the particular values of τ_i, α_i and ϕ_i are important only when considering BPSK-OFDM interference sources. However, when there is no spectral leakage present (i.e. $\tau_i = 0\,\forall i$ and $\alpha_i = 0\,\forall i$), the parameters J, Z_i and ϕ_i influence the error rate performance significantly as demonstrated in Appendix F.

8.3 Case Studies

The analytical error rate expressions derived in Chapter 7 and Section §8.2 can be used as a tool for base station (BS) deployment studies in real environments. Select examples of such studies are presented in this section as case studies using the path loss databases for Test Environments A & B (discussed in Chapter 5). The path loss values for each BS in Test Environments A & B are shown in Appendix G. The case studies shown in this chapter aim to answer the question: *Given a multi-storey building environment with a single BS on each floor (that can be located anywhere on the floor), what BS deployment configuration provides optimum error rate performance?*

8.3.1 Test Environment A — The Science Building

Five base station deployment scenarios are considered for Test Environment A (TEA) and are summarised in Table 8.1. Scenario TEA-I is where all BSs (desired and interfering) are vertically aligned on the right end of the building. The error rate performance for scenario TEA-I is used as a benchmark for comparison purposes in this subsection. Scenario TEA-II is where a zigzag configuration is adopted, i.e. the locations of the BSs alternate between the sides of the building. Scenario TEA-III adopts a diagonal BS configuration in which BSs on different floors are placed on opposite sides of the building and a BS deployed at the centre of the building in the floor sandwiched between the other two BSs. Scenario TEA-IV is similar to scenario TEA-I but the the BSs are vertically aligned at the centre of the building. Scenario TEA-V is where the desired BS is at the centre of the building and the interfering BSs are on either side of the building.

For each scenario, the BER is calculated at each mobile station location for given values of M and $\mathbf{Z}$ using Yang's path loss database [108] and a noise floor of -101 dBm as calculated in Section §4.3.4. The $\log_{10}(\text{BER})$ values are then plotted on contour maps using MATLAB's *linear* interpolation algorithm. The plotting of $\log_{10}(\text{BER})$ values instead of BER values is to give a better visual resolution for the contour maps. The colour scale on the contour maps has a lower limit of -8, i.e. BER values less than or equal to 10^{-8} are coloured as dark blue[4].

All OFDM signals in all deployment scenarios are QPSK mapped[5]. As shown in Section §8.2, the particular value of Z_i becomes unimportant for the upper bound estimation when considering $Z_i > 2$. The error rate performance for scenario TEA-I is shown in Fig. 8.2. It is clear from Fig. 8.2 that scenario TEA-I provides a good BER coverage across the floor with the exception of one room on the top middle of the floor. The poor BER performance in that room is primarily due to the fact that the received signals from Tx 3C and 2C are of comparable power levels (see Appendix G). One possible reason for the signals from Tx 2C having similar power levels to those from Tx 3C in the top side of the floor is the presence of several buildings in close proximity to The Science Building, particularly to its top and right. RF signal reflections from these neighbouring buildings coupled with the fact that the entire exterior of the room of interest is covered with glass windows may have allowed signals from Tx 2C to arrive with comparable strengths to those from Tx 3C.

[4]The bottom-end colour for MATLAB's *jet* colour map.

[5]Results with different desired mapping schemes are shown in Appendix H.

Table 8.1: Base station deployment scenarios for Test Environment A.

	TEA-I	TEA-II	TEA-III	TEA-IV	TEA-V
Desired BS	3C	3C	3C	3B	3B
Active Interfering BSs	1C and 2C	1C and 2A	1A and 2B	1B and 2B	1C and 2A
Physical Depiction					

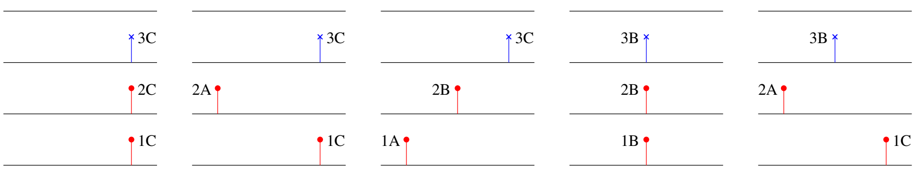

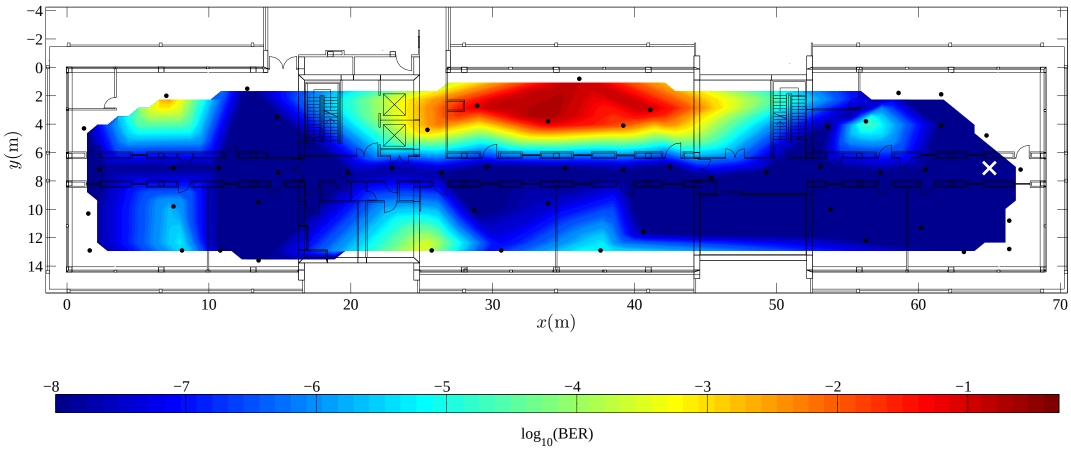

Figure 8.2: Contour map of $\log_{10}$ (BER) for scenario TEA-I. $M = 4$, $\mathbf{Z} = [4,4]$. Location of desired BS is indicated by a white $\times$.

The BER performance when the BS deployment configuration changes to that of scenario TEA-II is shown in Fig. 8.3. The raw BER performance is shown in Fig. 8.3a where most of the floor locations receive a good BER coverage. Expectedly, the BER performance at the left end of the floor is poor due to the close proximity of Tx 2A one floor below. Fig. 8.3b shows the BER performance of scenario TEA-II normalised to that of scenario TEA-I. The BER performance in the top middle side of the floor is improved significantly while the left side gets a much poorer BER performance relative to scenario TEA-I and the rest of the floor gets a comparable BER performance to that in scenario TEA-I.

The BER performance for deployment scenario TEA-III is shown in Fig. 8.4. Using the diagonal BS deployment configuration results in good BER performance in the right end of the building and most of the internal corridor while the rest of the floor has a poor BER performance as illustrated by Fig. 8.4a. Normalised BER results to scenario TEA-I are shown in Fig. 8.4b and it it clear that with the exception of one location on the floor, no BER improvements are gained through this BS deployment configuration. This suggests that the diagonal BS deployment configuration is inferior in terms of BER performance to the vertically aligned configuration of scenario TEA-I.

Using the BS deployment configuration in scenario TEA-IV results in the BER performance shown in Fig. 8.5. It is interesting to note that the inner part of the floor has a good BER performance while the sides of the floor have a poor BER performance as illustrated in Fig. 8.5a. Although the BSs in scenarios

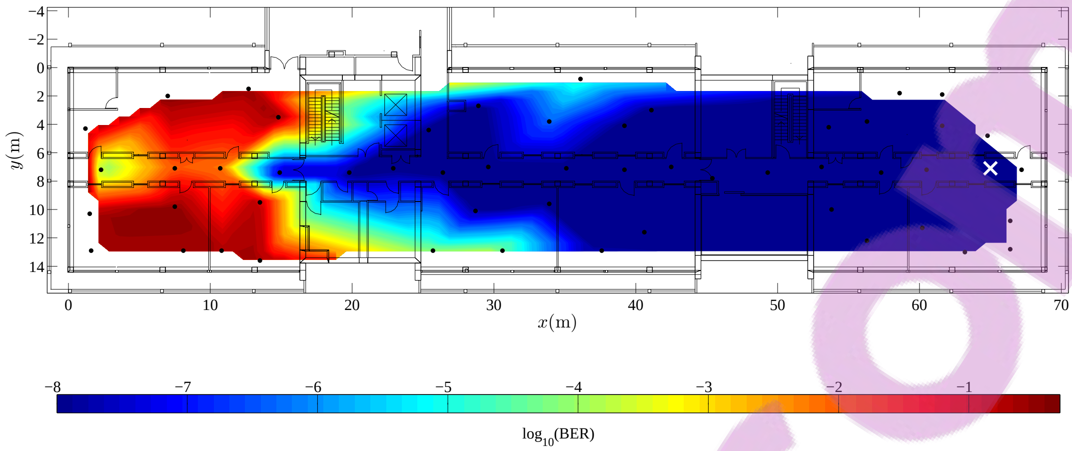

(a) $\log_{10}(\mathrm{BER}_{\mathrm{II}})$. Location of desired BS is indicated by a white $\times$.

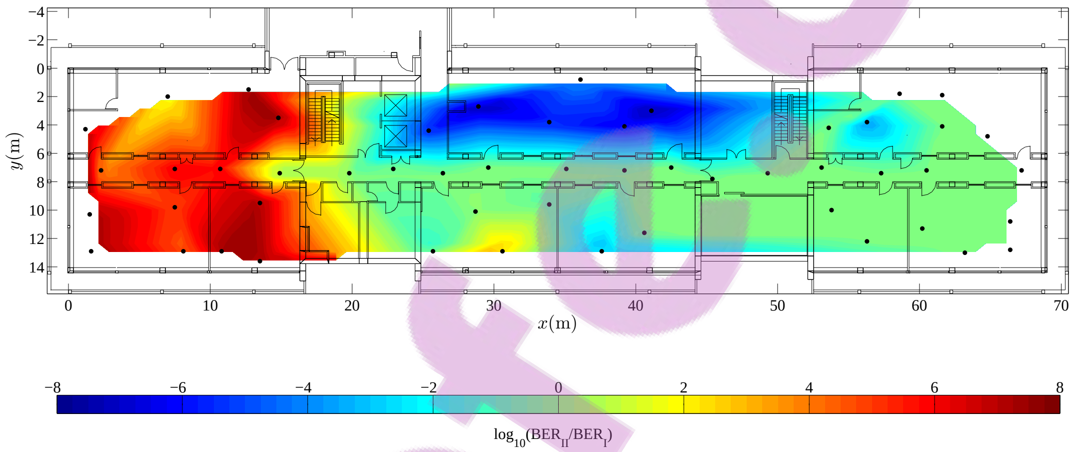

(b) $\log_{10}(\mathrm{BER}_{\mathrm{II}}/\mathrm{BER}_{\mathrm{I}})$.

Figure 8.3: Contour maps of BER performance for scenario TEA-II. $M = 4$, $\mathbf{Z} = [4,4]$.

TEA-I and TEA-IV are vertically aligned, the BER performance of scenario TEA-IV is much poorer on the sides of the floor relative to those of scenario TEA-I as shown in Fig. 8.5b.

The BER performance using the BS deployment configuration in scenario TEA-V is shown in Fig. 8.6. It is interesting to note that the BER performance is similar to that from scenario TEA-IV where the centre of the floor has a good BER performance and the sides of the floor having poor BER performance levels as seen in Fig. 8.6a. The BER performance of scenario TEA-V normalised to those obtained by scenarios TEA-I and TEA-IV are shown in Figs. 8.6b and 8.6c respectively. Based on the results shown in Figs. 8.2–8.6, the vertically aligned BS deployment configuration on the right side of the building (scenario TEA-I) provides the best BER performance across the floor[6]. Table 8.2 confirms this observation by showing the percentages of floor area that satisfy the condition $P_b \leq \epsilon$.

[6]Average BER performance across the floor for scenario TEA-I is 0.015. Second best average BER performance is 0.067 for scenario TEA-II.

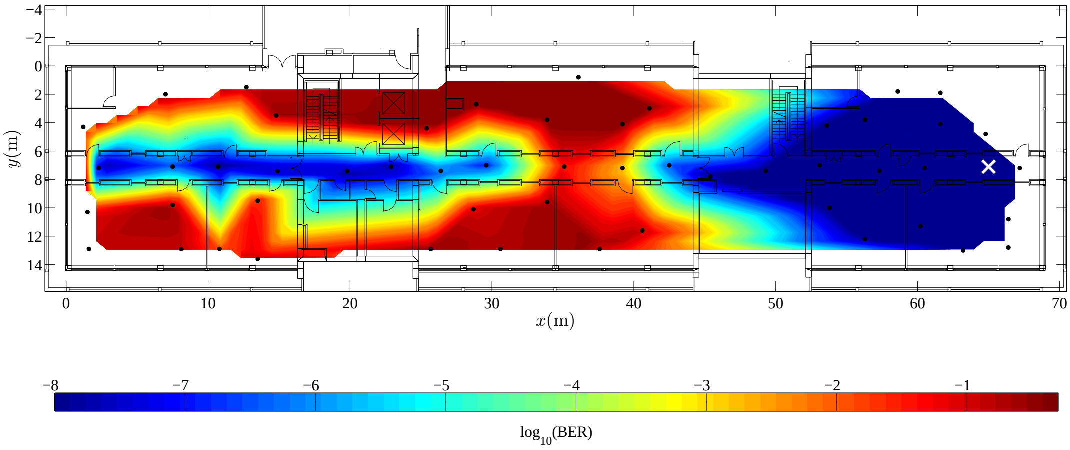

(a) $\log_{10}(\mathrm{BER_{III}})$. Location of desired BS is indicated by a white $\times$.

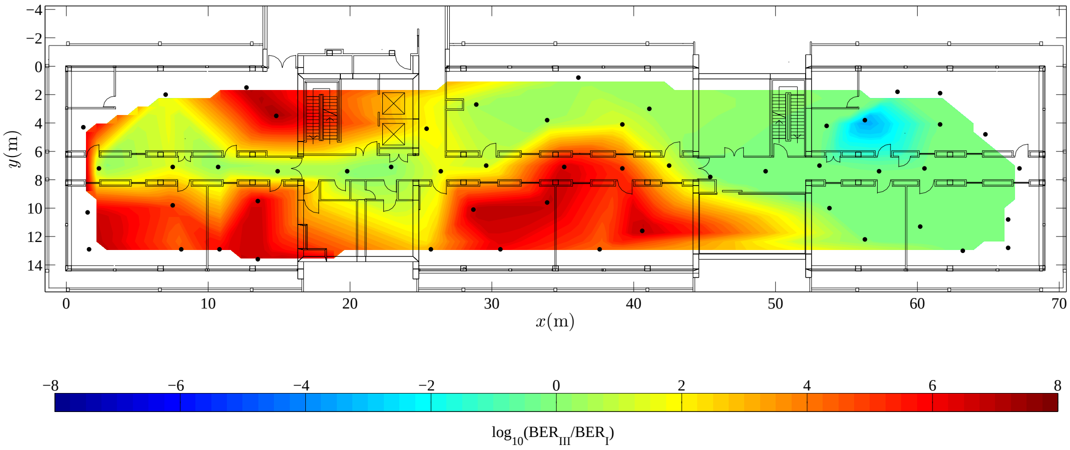

(b) $\log_{10}(\mathrm{BER_{III}}/\mathrm{BER_{I}})$.

Figure 8.4: Contour maps of BER performance for scenario TEA-III. $M = 4$, $\mathbf{Z} = [4,4]$.

Table 8.2: Percentage floor coverage for TEA when $P_b \leq \epsilon$.

	TEA-I	TEA-II	TEA-III	TEA-IV	TEA-V
$\epsilon = 10^{-6}$	76.92%	67.31%	51.92%	34.62%	42.31%
$\epsilon = 10^{-4}$	84.62%	73.08%	51.92%	36.54%	42.31%
$\epsilon = 10^{-2}$	90.38%	76.92%	53.85%	48.08%	44.23%

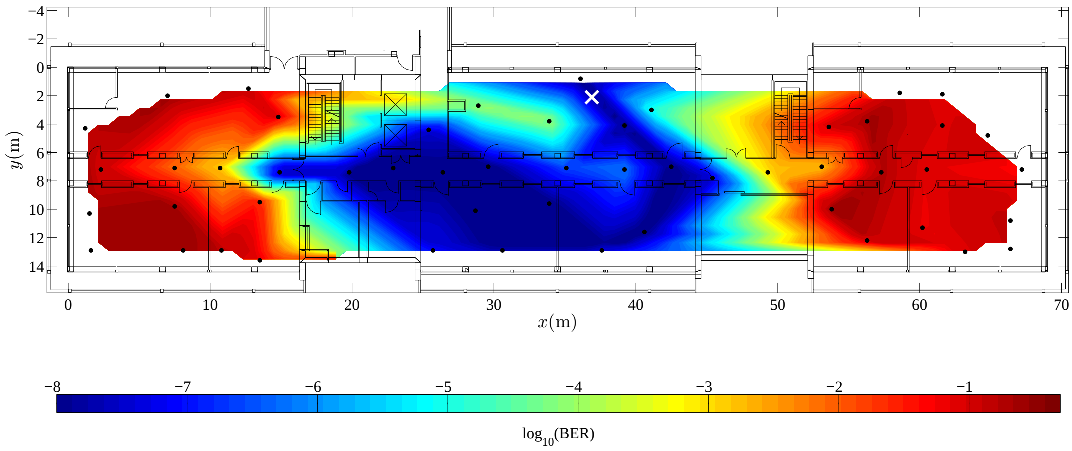

(a) $\log_{10}(\mathrm{BER_{IV}})$. Location of desired BS is indicated by a white $\times$.

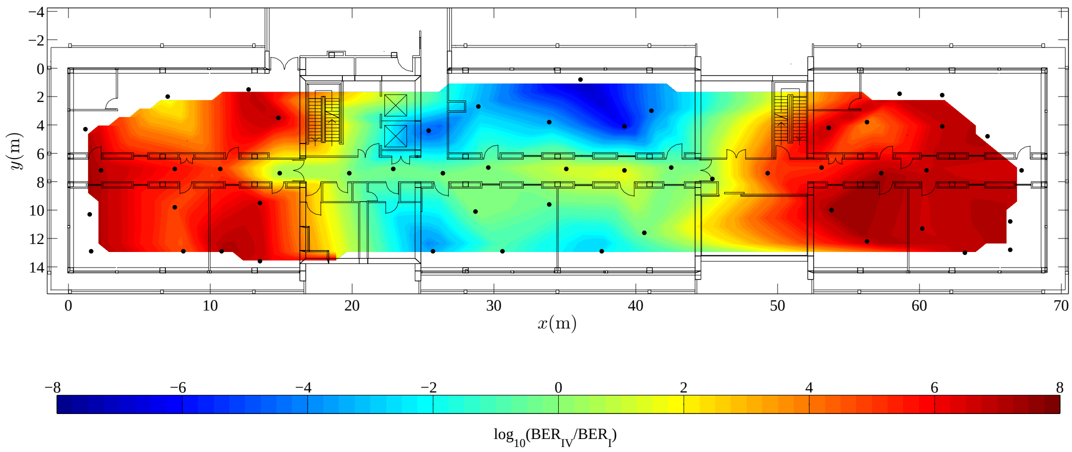

(b) $\log_{10}(\mathrm{BER_{IV}}/\mathrm{BER_{I}})$.

Figure 8.5: Contour maps of BER performance for scenario TEA-IV. $M = 4$, $\mathbf{Z} = [4,4]$.

8.3.2 Test Environment B — The Engineering Tower

Two base station deployment scenarios are considered for Test Environment B (TEB) and are summarised in Table 8.3. Scenario TEB-I is where all BSs (desired and interfering) are vertically aligned on one side of the building. The error rate performance for scenario TEB-I is used as a benchmark for comparison purposes in this subsection. Scenario TEB-II is where a zigzag configuration is adopted, i.e. the locations of the BSs alternate between either side of the building. The BER calculation process is identical to that for TEA. All OFDM signals in both deployment scenarios are QPSK mapped[7].

The BER performances using the BS deployment configurations in scenarios TEB-I and TEB-II are shown in Fig. 8.7. It is interesting to note that in *both* scenarios, the side of the building opposite to the desired BS has poor BER levels. Also, unlike TEA, the zigzag BS deployment configuration (TEB-II) provides a better BER performance across the floor relative to scenario TEB-I as illustrated by Fig. 8.7c and Table 8.4. This result shows that a certain BS deployment configuration is not guaranteed to provide the best error rate performance for every environment and the propagation conditions of the environment

[7]Results with different desired mapping schemes are shown in Appendix H.

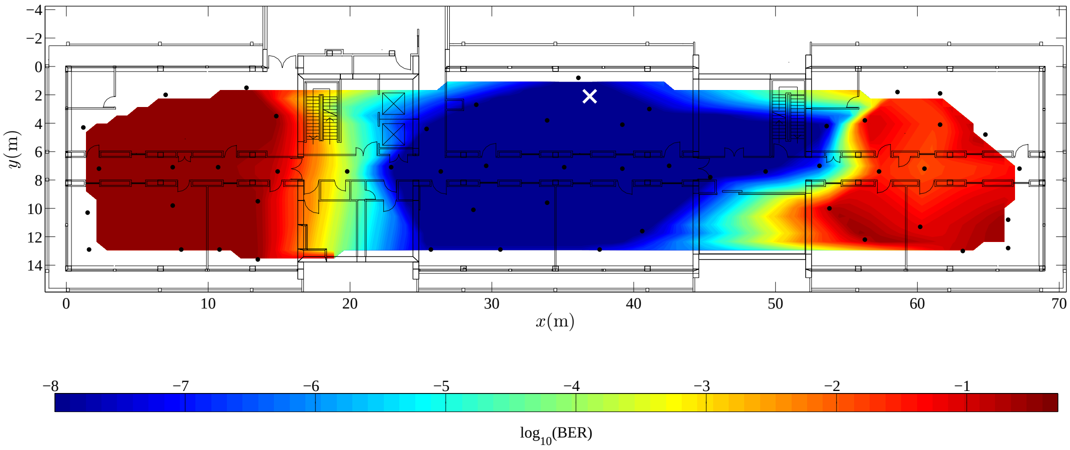

(a) $\log_{10}(\mathrm{BER}_{\mathrm{V}})$. Location of desired BS is indicated by a white $\times$.

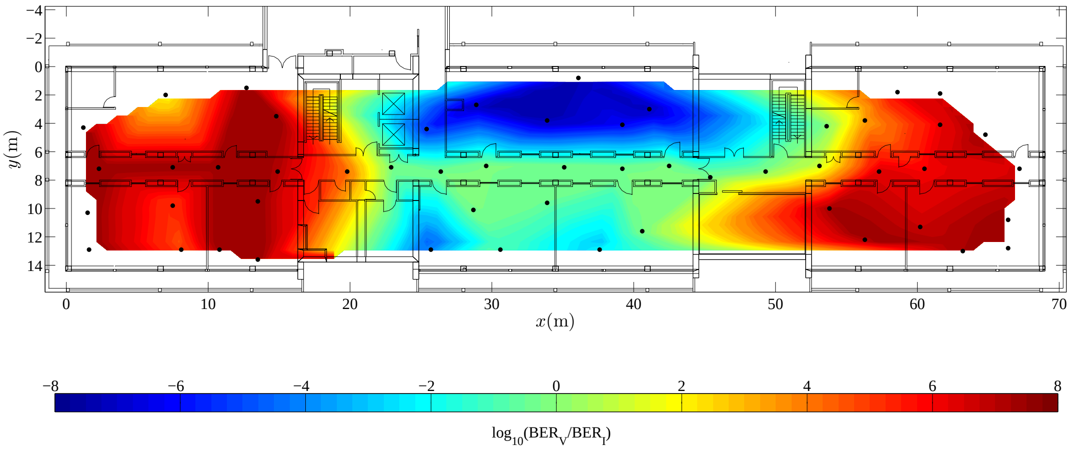

(b) $\log_{10}(\mathrm{BER}_{\mathrm{V}}/\mathrm{BER}_{\mathrm{I}})$.

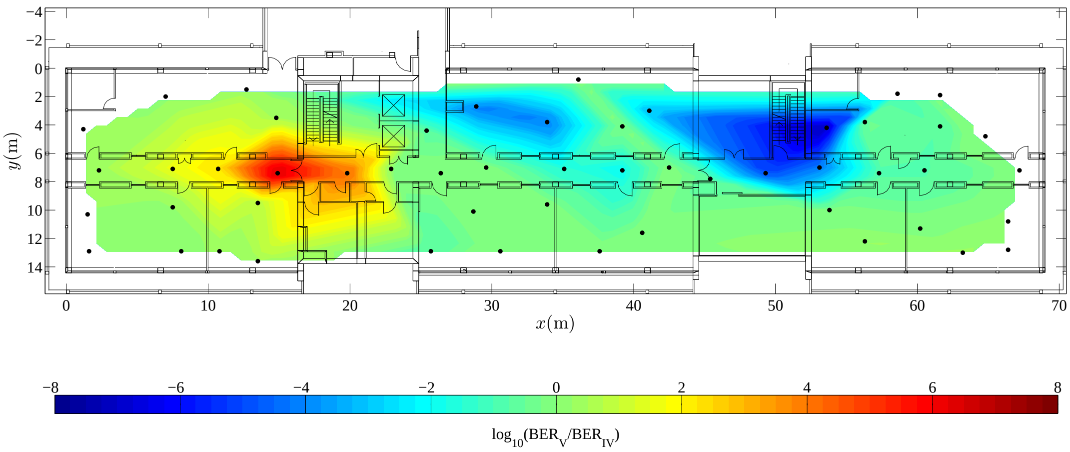

(c) $\log_{10}(\mathrm{BER}_{\mathrm{V}}/\mathrm{BER}_{\mathrm{IV}})$.

Figure 8.6: Contour maps of BER performance for scenario TEA-V. $M = 4$, $\mathbf{Z} = [4,4]$.

Table 8.3: Base station deployment scenarios for Test Environment B.

	TEB-I	TEB-II
Desired BS	4	4
Active Interfering BSs	2, 6, 8 and 10	1, 5, 8 and 9
Physical Depiction	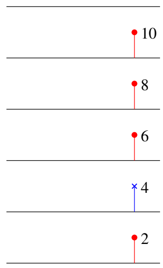	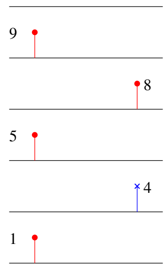

Table 8.4: Percentage floor coverage for TEB when $P_b \leq \epsilon$.

	TEB-I	TEB-II
$\epsilon = 10^{-6}$	10.71%	30.36%
$\epsilon = 10^{-4}$	12.50%	32.14%
$\epsilon = 10^{-2}$	39.29%	41.07%

itself are a key factor influencing the deployment strategy. Also, BER performances for the deployment scenarios for different values of M (shown in Appendix H) show that the deployment configurations with the most consistent BER performances are TEA-II, TEA-V and TEB-II. An alternative option for both test environments is to deploy a second BS on each floor that operates at an *adjacent* (but not overlapping) frequency band. The BS deployment configuration will be zigzag one such that for TEA, BSs 1A, 2C and 3A will use an adjacent frequency band to BSs 1C, 2A and 3C and for TEB, BSs 2, 3, 6, 7 and 10 will use an adjacent frequency band to BSs 1, 4, 5, 8 and 9.

These results show the usefulness and practical aspect of the analytical error rate expressions derived in this thesis. These expressions also allow a comparison between OFDM-based and DS-SS-based wireless networks performance in the presence of interference. One key question is: *if a DS-SS network already exists in an environment and it is to be replaced by an OFDM-based network, could the existing BS/antenna deployment be retained?*

8.4 Comparison with DS-SS Systems

As mentioned in Chapter 2, direct sequence-spread spectrum (DS-SS) is a popular physical layer air interface for wireless systems, e.g. IEEE 802.11b WLANs and 3G cellular systems. However, an increasing number of wireless systems are adopting OFDM as their physical layer air interface, which means that some existing DS-SS based wireless networks will be upgraded to OFDM-based ones. An important engineering exercise is whether this upgrade will necessitate a redeployment of the existing BSs[8]. The

[8]The analyses and results presented next are expanded from those in [125].

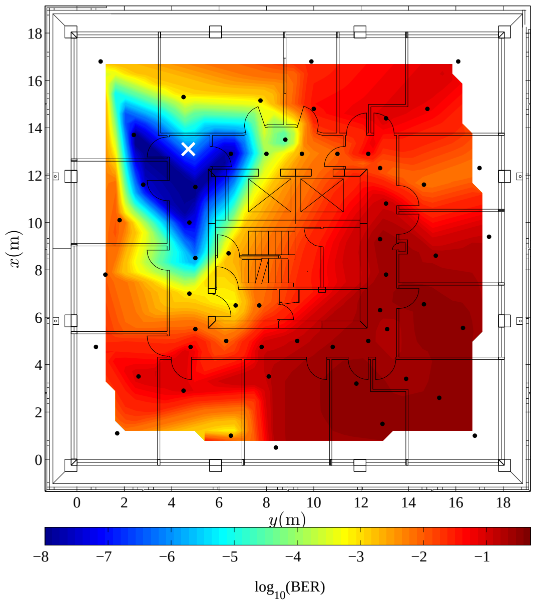

(a) $\log_{10}$ (BER) for Scenario TEB-I.

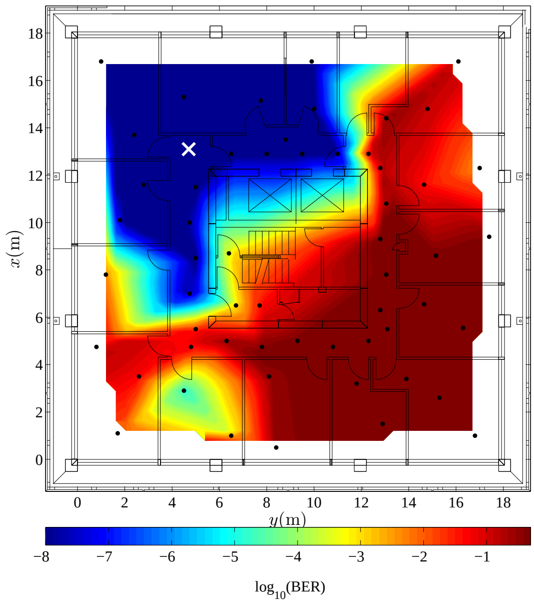

(b) $\log_{10}$ (BER) for Scenario TEB-II.

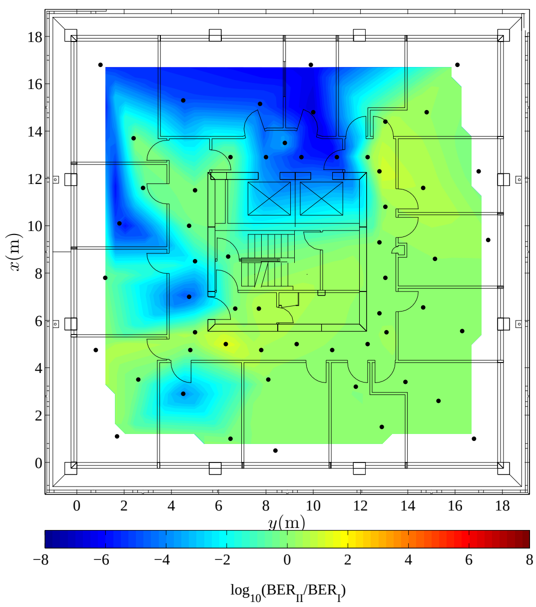

(c) $\log_{10}\left(\mathrm{BER_{II}}/\mathrm{BER_{I}}\right)$.

Figure 8.7: Contour maps of BER performance for scenario TEB-I and TEB-II. $M = 4$, $Z_i = 4\,\forall i$. Location of desired BS is indicated by a white $\times$.

downlink probability of bit error of a BPSK-mapped DS-SS system in the presence of AWGN and DS-SS interference (both intra-cell and inter-cell interference) is given by [14, pp. 14–19], [126]

$$P_b = \frac{1}{2}\text{erfc}\left[\left(\frac{N_0}{E_b} + \frac{2V}{3G_p}\left[U - 1 + \frac{1}{\text{SIR}}\right]\right)^{-\frac{1}{2}}\right], \tag{8.8}$$

where V is the voice activity factor[9] and is set to $\frac{1}{2}$, G_p is the processing gain and is set to 11 for a 2 Mbps IEEE 802.11b WLAN [22], U is the number of users connected to each DS-SS BS, and SIR is the ratio of the desired DS-SS signal's energy to the collective energy of the interfering *inter*-cell DS-SS signals.

Four BS deployment configuration scenarios are considered for the comparison between DS-SS and OFDM systems: TEA-I, TEA-II, TEB-I and TEB-II. To facilitate a "fair" comparison, all desired and interfering OFDM signals are BPSK-mapped since the expression in (8.8) assumes BPSK signal mapping for all DS-SS signals. Also, for each scenario, two cases are considered for DS-SS systems: one with just a single user connected to each BS (i.e. $U = 1$) and the other with ten users connected to each BS (i.e. $U = 10$). It should be noted that the error rate expressions derived for OFDM systems are for the kth frequency bin (which is allocated to a single user at a given time slot) and the orthogonality of the subcarriers ensures no inter-carrier interference (ICI) is present. The overall OFDM error rate value for the uth user is obtained by averaging the error rates for all the frequency bins allocated to the uth user (see Equation (7.22)). However, in DS-SS systems, signals are differentiated by semi-orthogonal spreading codes and added together [128]. This results in *intra*-cell interference (the equivalent to ICI in OFDM systems). Therefore, when multiple users are connected to a DS-SS BS, intra-cell interference is unavoidable and thus has to be taken into consideration (hence the two cases of $U = 1$ and $U = 10$).

Fig. 8.8 shows the BER performances for scenario TEA-I. Two things can be observed from Fig. 8.8, the first is that both DS-SS performances are almost uniform across the floor, unlike the OFDM case where there is a serious performance degradation in one of the rooms at the top middle of the building. The second thing is that the DS-SS performance degrades significantly when nine additional users are connected to each BS (a realistic scenario). The DS-SS performance can be improved markedly by increasing the processing gain, G_p, but at the expense of reduced data rate. Assuming no ICI for the OFDM case, the average BER for the 10-user DS-SS network is significantly higher than the OFDM network for the majority of the floor area.

BER performances for scenario TEA-II are shown in Fig. 8.9. The BER patterns for OFDM and DS-SS systems are similar but with different values. For the OFDM network, the majority of the floor area has a good BER performance with the left end of the floor experiencing significantly poorer BER performance due to the close proximity of BS 2A. The 10-user DS-SS network has a much poorer BER performance across most of the floor area compared to the OFDM network, but a better BER performance at the left end of the building. Based on the results from Figs. 8.8 and 8.9, the vertically aligned BS configuration (scenario TEA-I) provides a better BER performance than the zigzag configuration (scenario TEA-II) for *both* OFDM and DS-SS networks. This is also confirmed by Table 8.5 that shows the percentages of floor area that satisfy the condition $P_b \leq \epsilon$.

[9]In telephone channels, the voice activity is defined as the percentage of time during which voice is present [127, p. 12].

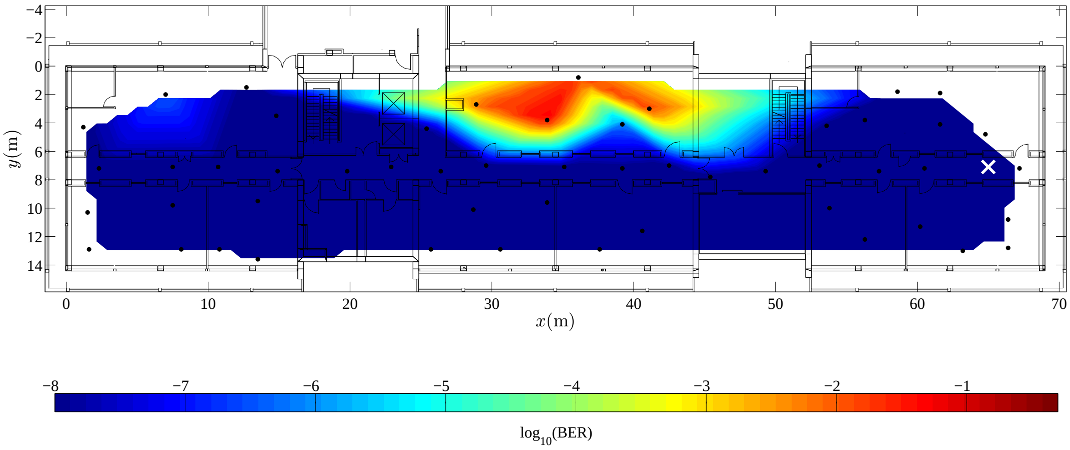

(a) OFDM-based networks.

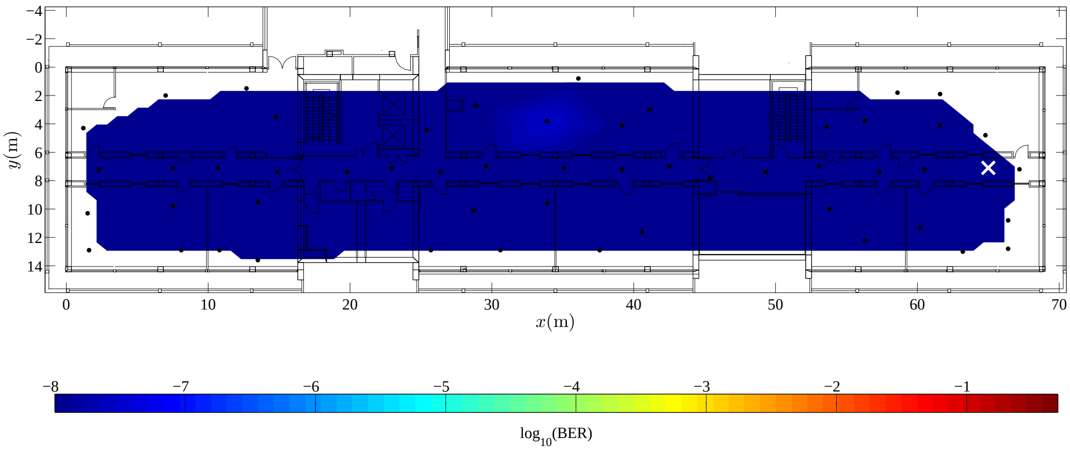

(b) DS-SS-based networks with $U = 1$.

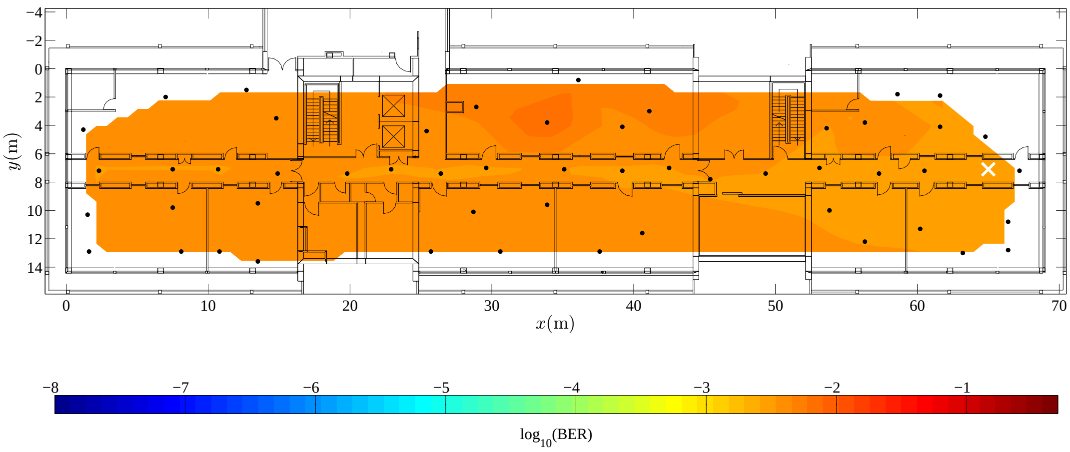

(c) DS-SS-based networks with $U = 10$.

Figure 8.8: Contour map of $\log_{10}$ (BER) for scenario TEA-I. $M = 2$, $\mathbf{Z} = [2{,}2]$. Location of desired BS is indicated by a white $\times$.

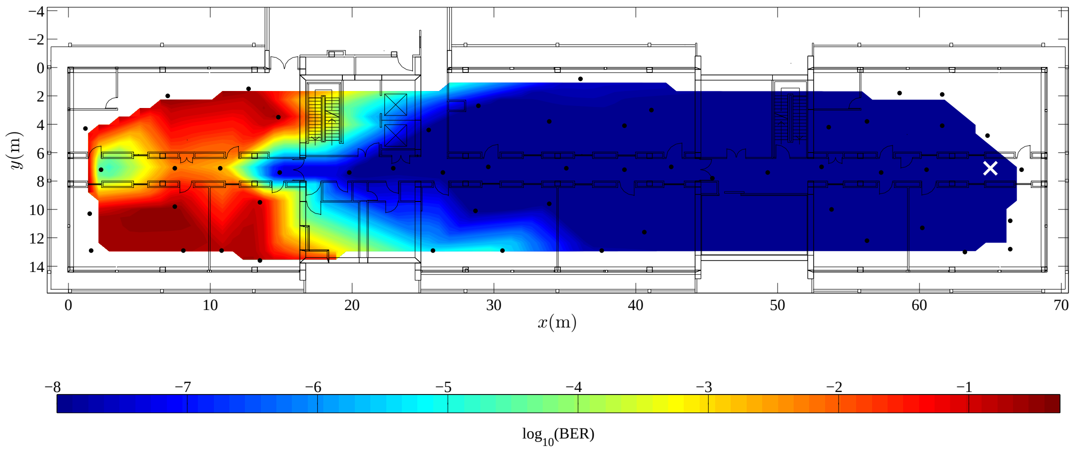

(a) OFDM-based networks.

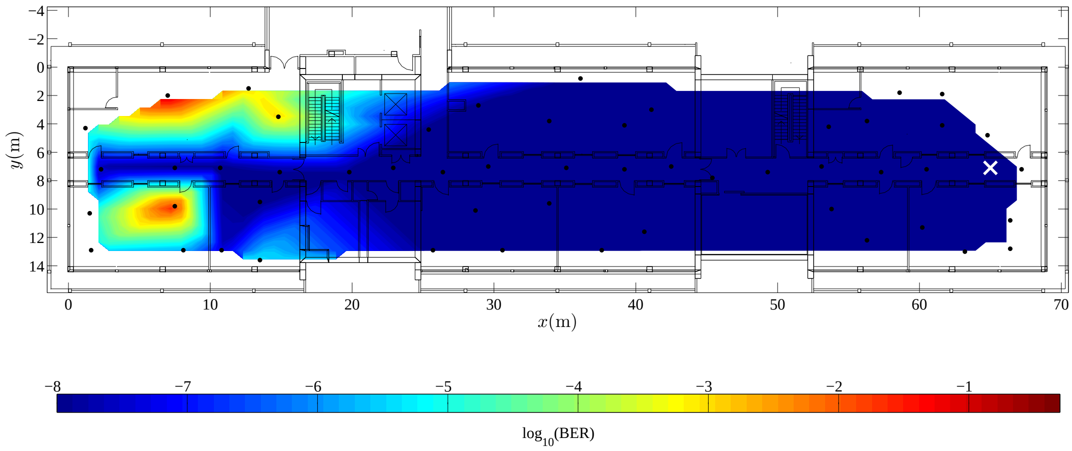

(b) DS-SS-based networks with $U = 1$.

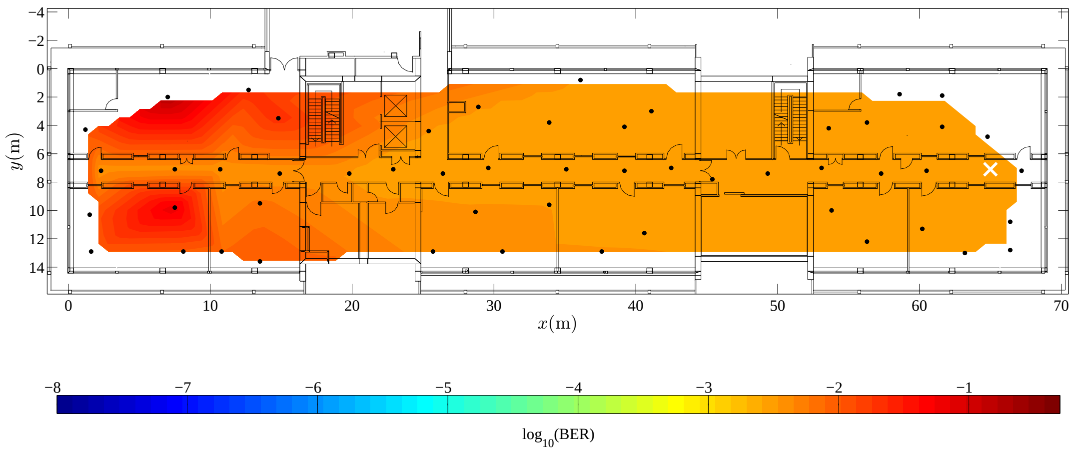

(c) DS-SS-based networks with $U = 10$.

Figure 8.9: Contour map of $\log_{10}(\text{BER})$ for scenario TEA-II. $M = 2$, $\mathbf{Z} = [2{,}2]$. Location of desired BS is indicated by a white $\times$.

Table 8.5: Percentage floor coverage for TEA when $P_b \leq \epsilon$.

	TEA-I			TEA-II		
	OFDM	DS-SS, $U = 1$	DS-SS, $U = 10$	OFDM	DS-SS, $U = 1$	DS-SS, $U = 10$
$\epsilon = 10^{-6}$	92.31%	100%	0%	69.23%	82.69%	0%
$\epsilon = 10^{-4}$	92.31%	100%	0%	75.00%	92.31%	0%
$\epsilon = 10^{-2}$	94.23%	100%	100%	78.85%	96.15%	84.62%

Table 8.6: Percentage floor coverage for TEB when $P_b \leq \epsilon$.

	TEB-I			TEB-II		
	OFDM	DS-SS, $U = 1$	DS-SS, $U = 10$	OFDM	DS-SS, $U = 1$	DS-SS, $U = 10$
$\epsilon = 10^{-6}$	12.50%	83.93%	0%	37.50%	60.71%	0%
$\epsilon = 10^{-4}$	21.43%	89.29%	0%	41.07%	62.50%	0%
$\epsilon = 10^{-2}$	46.43%	100%	87.50%	51.79%	67.86%	60.71%

Fig. 8.10 shows the BER performances for scenario TEB-I. It is interesting to note that the DS-SS networks (even the 10-user network) provide a more consistent BER performance across the floor than the OFDM network. The results for TEB-II are shown in Fig. 8.11 and demonstrate a marked improvement for the BER performance for the OFDM network compared with TEB-I and a significant BER performance degradation for the DS-SS networks. This is further illustrated by Table 8.6.

Based on the results from Figs. 8.10 and 8.11, the vertically aligned BS configuration (scenario TEB-I) provides a better BER performance for the DS-SS networks while the zigzag configuration (scenario TEB-II) provides a better BER performance for the OFDM network. This is interesting, since the need for BS redeployment is dependent on the *environment* itself as demonstrated by the results in Figs. 8.8–8.11 where a redeployment is unnecessary for TEA but necessary for TEB. It is also important to note that the error rate performance of DS-SS systems is limited by interference (both intra-cell and inter-cell), which can be mitigated with higher processing gains, G_p. Subcarrier orthogonality for OFDM systems ensures ICI-free error rate performance, and the absence of spectrum spreading makes OFDM systems more sensitive to external interference sources than DS-SS systems.

8.5 Summary

In this chapter, the effects of system parameters on the error rate performance of OFDM-based wireless networks are demonstrated along with OFDM-to-OFDM performance assessment in indoor environments. The error rate performance is sensitive to the desired QAM level, M, with higher QAM levels ($M > 4$) recommended to be used in good channel conditions (high SINR values). Due to the fact that transmitted QAM symbols have the same average energy regardless of the QAM level, the upper bound error rate performance becomes independent of **Z**, J, α_i, τ_i and ϕ_i when $Z_i > 2\,\forall i$. It is important to note that the presence of the spectral leakage allows the use of the upper bound approximation but the specific values of α_i, τ_i and ϕ_i become unimportant.

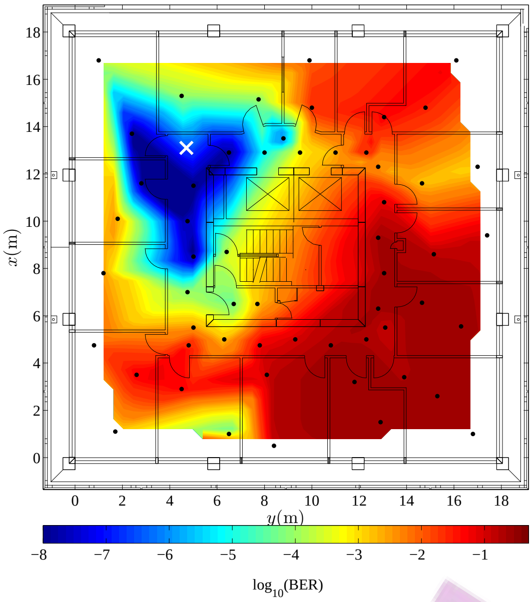

(a) OFDM-based networks.

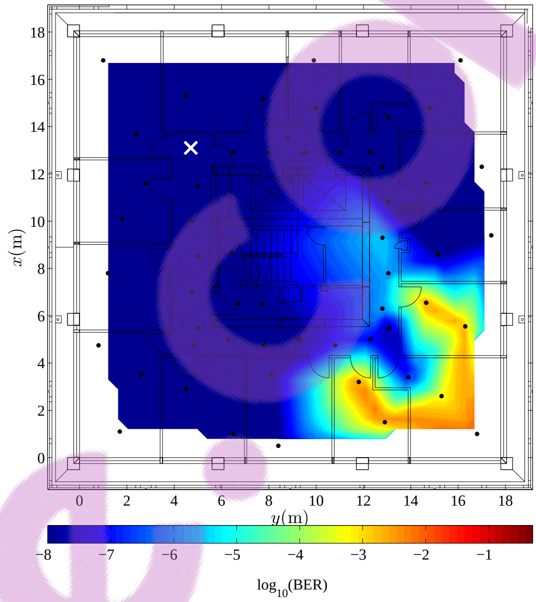

(b) DS-SS-based networks with $U = 1$.

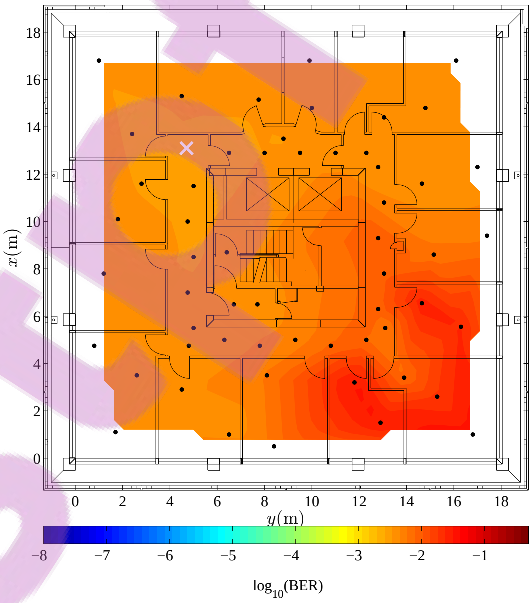

(c) DS-SS-based networks with $U = 10$.

Figure 8.10: Contour map of $\log_{10}$ (BER) for scenario TEB-I. $M = 2$, $Z_i = 2\,\forall i$. Location of desired BS is indicated by a white $\times$.

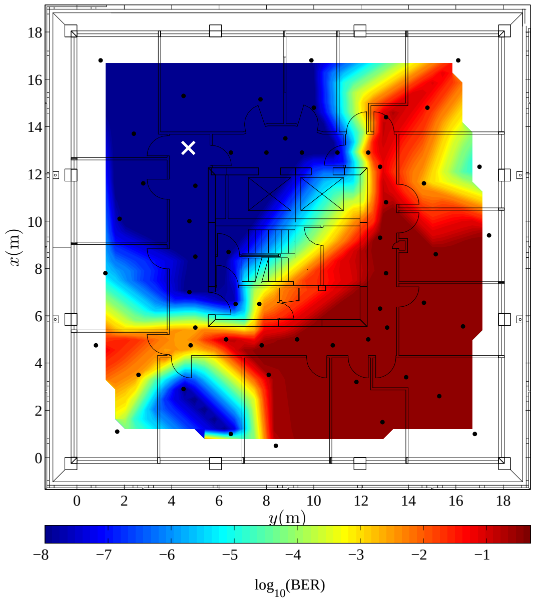

(a) OFDM-based networks.

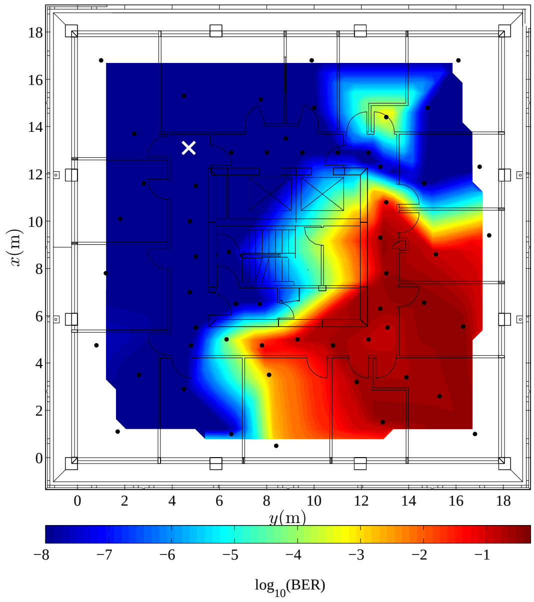

(b) DS-SS-based networks with $U = 1$.

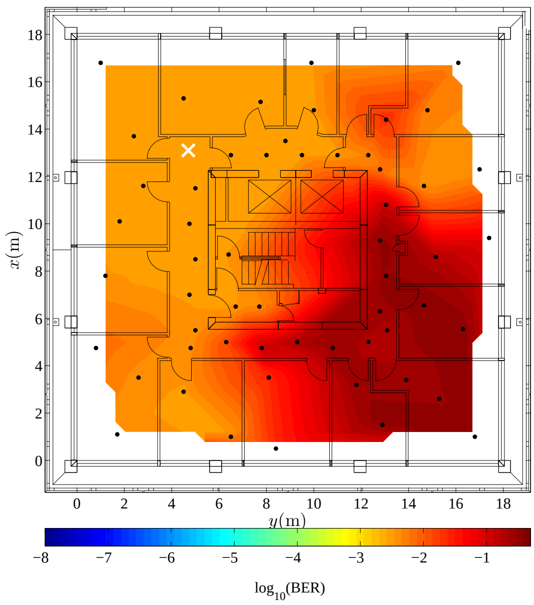

(c) DS-SS-based networks with $U = 10$.

Figure 8.11: Contour map of $\log_{10}(\mathrm{BER})$ for scenario TEB-II. $M = 2$, $Z_i = 2\,\forall i$. Location of desired BS is indicated by a white $\times$.

Case studies using real path loss measurement databases for The Science Building and The Engineering Tower at The University of Auckland are used to illustrate the usefulness of the analytical error rate expressions derived in this thesis. These studies demonstrate that a vertically aligned base station deployment configuration is best for The Science Building while a zigzag configuration is best for the The Engineering Tower.

A comparison with DS-SS systems under identical conditions show that the error rate patterns for OFDM and DS-SS networks depend on the environment itself. For the The Science Building both OFDM and DS-SS networks have similar error rate patterns and thus a base station redeployment is not required if a DS-SS network is to be replaced with an OFDM-based network. However, DS-SS and OFDM networks have opposite error rate patterns for The Engineering Tower and therefore a base station reassignment would be necessary if a DS-SS network were to be replaced by an OFDM-based network.

Performance assessments of OFDM systems in the presence of multiple OFDMIs are presented in Chapter 9 for outdoor-to-indoor interference scenarios.

Chapter 9

OFDM-to-OFDM Interference Performance Assessment — Indoor/Outdoor Environments

9.1 Introduction

In Chapter 8, the applicability of the analytical error rate expressions developed in Chapter 7 have been demonstrated on deployment scenarios where the interference comes from within the same environment, i.e. indoor-to-indoor interference. However, interference sources could also come from external sources, e.g. access points deployed within neighbouring buildings, street level WLAN hotspots, geographically co-located services such as WiMAX etc. In this chapter, the applicability of the analytical error rate expressions is demonstrated for deployment scenarios where there are external interfering sources present. Similar to Chapter 8, path loss measurements in a real environment are used to model the radio channel. For this chapter, the path loss database from Wong's measurements campaign [15] for The Engineering Tower is used[1].

Error rate performance assessment of OFDM systems in the presence of multiple OFDMIs for several case studies are presented in Section §9.2 followed by comparisons with DS-SS systems in Section §9.3.

9.2 Case Studies

Four base station deployment scenarios are considered in this chapter and are summarised in Table 9.1. In all scenarios Tx I-1 is considered to be the desired BS. Scenario I is where there are two external interfering BSs (O-1 and O-3) each located on one side of the building. As discussed in Chapter 5, Wong's measurements were conducted on the eighth floor of The Engineering Tower and the external BSs are at a height equivalent to the sixth floor (see Fig. 5.8). Scenario II considers two interfering BSs — one external (O-1) and one internal (I-2). Scenario III is similar to Scenario II but with BS O-1

[1]See Chapter 5 for details of the environment and Appendix G for path loss measurements.

Table 9.1: Base station deployment scenarios. The shaded area represents the building's central services core (containing lifts, stairwell, etc.)

Scenario	Base Stations		Physical Depiction
I	Desired BS	I-1	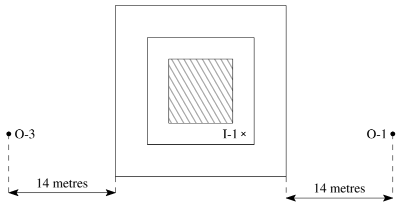
	Active Interfering BSs	O-1 and O-3	
II	Desired BS	I-1	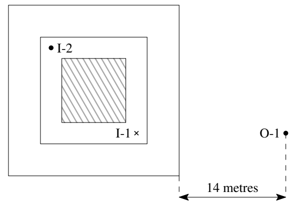
	Active Interfering BSs	I-2 and O-1	
III	Desired BS	I-1	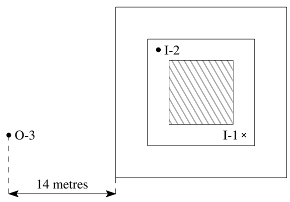
	Active Interfering BSs	I-2 and O-3	
IV	Desired BS	I-1	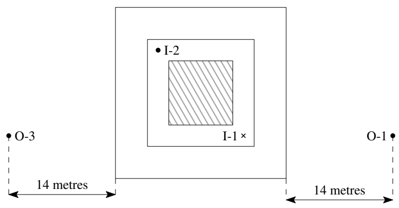
	Active Interfering BSs	I-2, O-1 and O-3	

replaced with BS O-3. Scenario IV is where there are three active interfering BSs, one internal (I-2) and two external (O-1 and O-3).

As in Chapter 8, all desired and interfering OFDM signal are QPSK mapped and the noise floor is at -101 dBm. Fig. 9.1 shows the BER performance across the eighth floor of The Engineering Tower for Scenario I. Unlike Yang's measurement campaign [108], no path loss measurements were taken *inside* the central services core in Wong's measurement campaign [15], hence there are no contour lines inside the central services core for the contour maps presented in this chapter.

It is observed from Fig. 9.1 that the presence of external interfering sources on either side of the building results in poor BER performances at the corner opposite to the desired BS location as well as some of

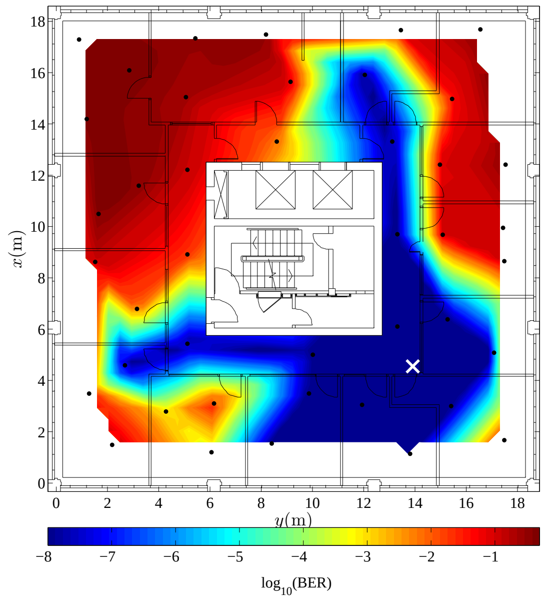

Figure 9.1: Contour maps of BER performance for Scenario I. $M = 4$, $Z_i = 4\,\forall i$. The location of the desired BS is indicated by a white $\times$.

the offices on the same side as the desired BS[2]. The BER result for Scenario I is used as a benchmark for comparison with the other scenarios.

Fig. 9.2 shows the error rate performance for Scenario II where Fig. 9.2a shows the raw BER performance and Fig. 9.2b shows the BER performance normalised to the BER performance of Scenario I. Based on the results from Fig. 9.2, the presence of the internal interfering source (I-2) has a detrimental effect on the error rate performance mainly on two opposite corners of the floor (indicated by the red and yellow patches in Fig. 9.2b). The fact that BS O-3 is inactive (compared to Scenario I) did not have an effect on the error rate performance due to the influence of the internal interference source, BS I-2.

The error rate performance for Scenario III is shown in Fig. 9.3 with the raw BER performance in Fig. 9.3a and the normalised BER to Scenario I in Fig. 9.3b. The placement of the external interferer (O-3) on the other side of the building (away from the desired BS) improves the BER performance on the side next to the desired BS as indicated by the blue patches in Fig. 9.3b. The detrimental effects of BSs I-2 and O-3 on the BER performance are similar to those in Scenario II. This suggests that the influence of the external interferer O-3 is minimal when BS I-2 is active.

Fig. 9.4 shows the error rate performance for Scenario IV where the raw BER performance is shown Fig. 9.4a and Fig. 9.4b shows the BER performance normalised to the BER performance of Scenario I. It is observed that the error rate performance for Scenario IV is very similar to that of Scenario II. Fig. 9.4c shows the BER performance normalised to the BER performance of Scenario II[3]. Based on Fig. 9.4c, only a handful of locations on one side of the building are influenced by the presence of BS O-3.

The results from Figs. 9.1–9.4 show that external interference sources can have a significant impact on the error rate performance of an OFDM-based wireless network even when there are no internal interference sources (Scenario I). The influence of the external interference can be masked by the presence of a strong

[2] Offices in The Engineering Tower have large glass exterior windows as seen in Fig. 5.6.

[3] The colour scale is different to emphasise the differences between Scenarios II and IV.

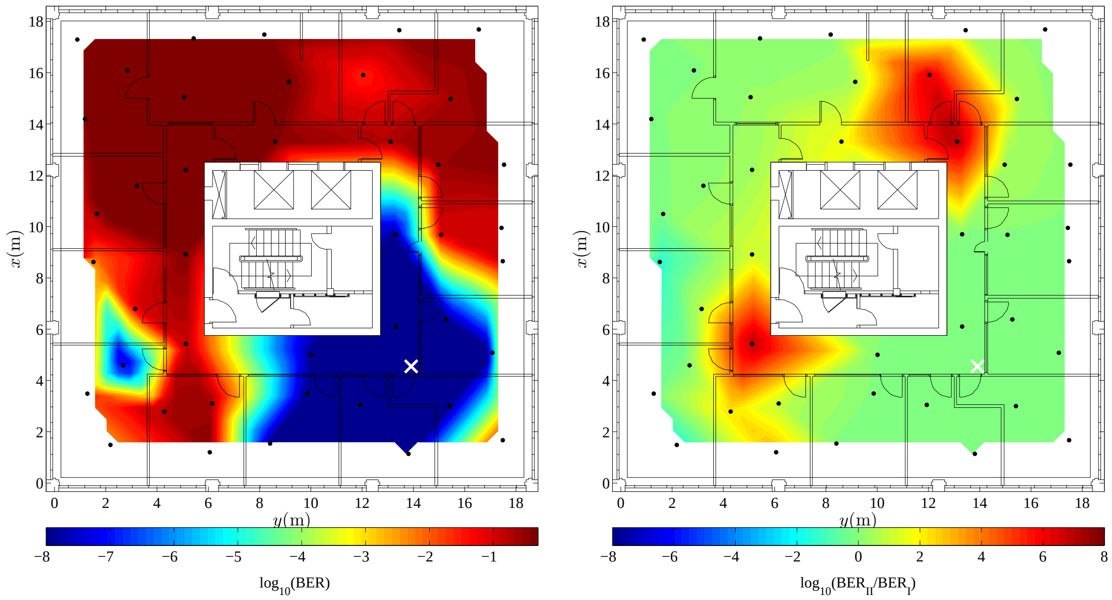

(a) $\log_{10}$ (BER) for Scenario II. **(b)** $\log_{10}$ ($\mathrm{BER_{II}}/\mathrm{BER_{I}}$).

Figure 9.2: Contour maps of BER performance for Scenario II. $M = 4$, $Z_i = 4\,\forall i$. The location of the desired BS is indicated by a white $\times$.

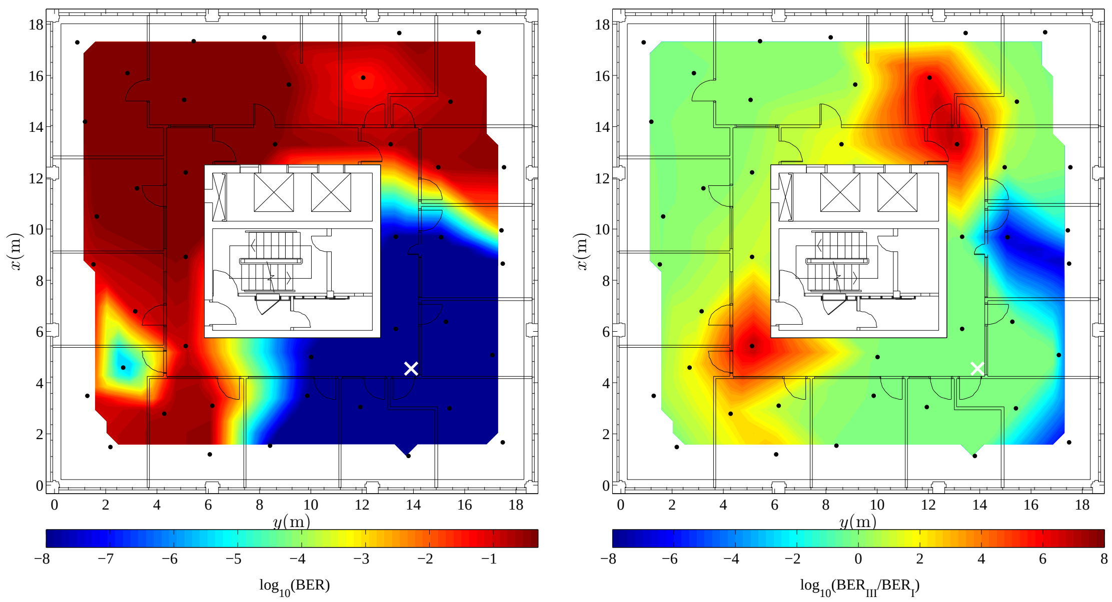

(a) $\log_{10}$ (BER) for Scenario III. **(b)** $\log_{10}$ ($\mathrm{BER_{III}}/\mathrm{BER_{I}}$).

Figure 9.3: Contour maps of BER performance for Scenario III. $M = 4$, $Z_i = 4\,\forall i$. The location of the desired BS is indicated by a white $\times$.

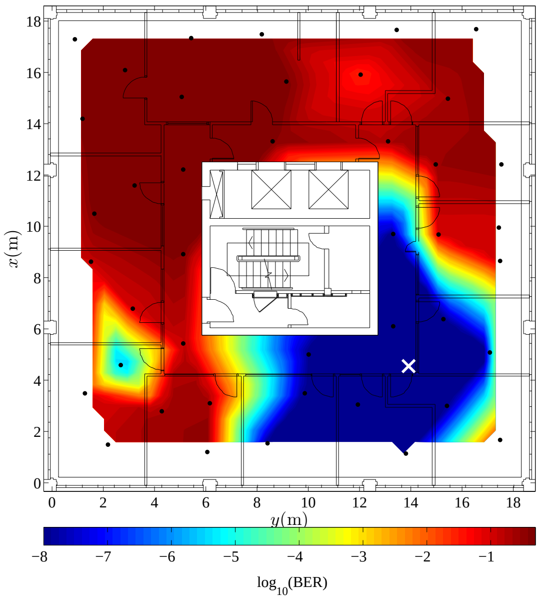

(a) $\log_{10}(\mathrm{BER})$ for Scenario IV.

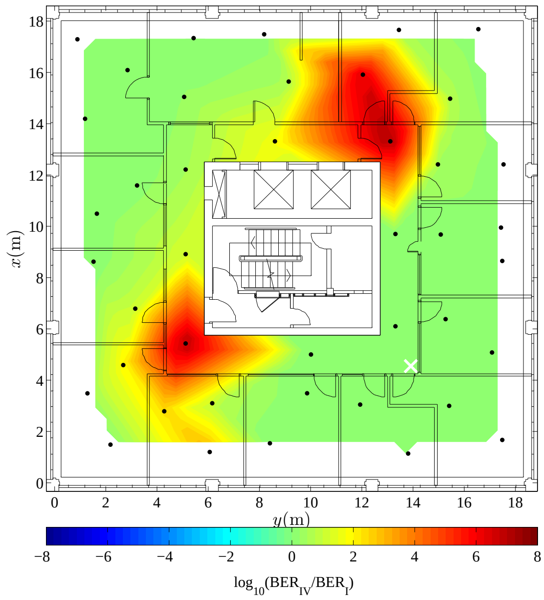

(b) $\log_{10}(\mathrm{BER_{IV}}/\mathrm{BER_{I}})$.

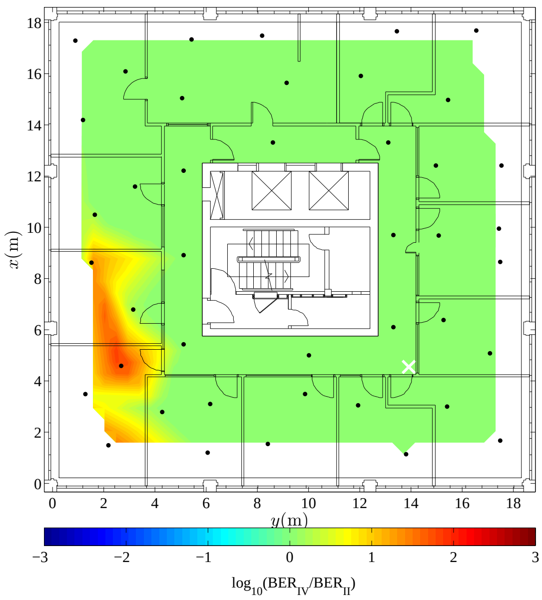

(c) $\log_{10}(\mathrm{BER_{IV}}/\mathrm{BER_{II}})$.

Figure 9.4: Contour maps of BER performance for Scenario IV. $M = 4$, $Z_i = 4\,\forall i$. The location of the desired BS is indicated by a white $\times$.

Table 9.2: Percentage floor area that satisfies $P_b \leq \epsilon$.

	Scenario I	Scenario II	Scenario III	Scenario IV
$\epsilon = 10^{-6}$	33.33%	26.19%	33.33%	26.19%
$\epsilon = 10^{-4}$	33.33%	26.19%	33.33%	26.19%
$\epsilon = 10^{-2}$	40.48%	30.95%	35.71%	26.19%

Table 9.3: Percentage floor area that satisfies $P_b \leq \epsilon$.

	Scenario I			Scenario IV		
	OFDM	DS-SS, $U = 1$	DS-SS, $U = 10$	OFDM	DS-SS, $U = 1$	DS-SS, $U = 10$
$\epsilon = 10^{-6}$	35.71%	78.57%	0%	26.19%	57.14%	0%
$\epsilon = 10^{-4}$	40.48%	83.33%	0%	28.57%	61.91%	0%
$\epsilon = 10^{-2}$	54.76%	85.71%	78.57%	30.95%	66.67%	57.14%

internal interferer (Scenarios II and IV). Table 9.2 shows the percentage area of the floor that that have BER values below a threshold, ϵ, for the Scenarios I–IV.

9.3 Comparison with DS-SS Systems

As in Chapter 8, the comparison with DS-SS systems is done under identical environmental conditions. Scenarios I and IV are considered for the comparison with DS-SS systems with all desired and interfering signals BPSK-mapped since the expression in (8.8) assumes BPSK signal mapping for all DS-SS signals. The DS-SS cases are considered with a single and ten users connected to each base station to illustrate the effect of intra-cell interference.

Fig. 9.5 shows the BER performances for Scenario I. It is clear from Figs. 9.5a and 9.5b that OFDM-based networks are more sensitive to the external interference sources than single-user DS-SS networks. When ten users are connected to each BS (Fig. 9.5c), the intra-cell interference degrades the BER performance across the entire floor area with the poorest BER performance regions matching those for the single-user DS-SS networks.

The BER performances for Scenario IV are shown in Fig. 9.6 whereby an internal interference source is active (BS I-2). The influence of the internal interferer is immediately visible for both OFDM and DS-SS networks. For the DS-SS networks, the poorest BER performances are obtained in the vicinity of the internal interferer while for the OFDM networks, significantly more locations on the floor experience very poor BER performances. This is due to the fact that OFDM systems, unlike DS-SS systems, do not spread the spectrum of the interfering signals and therefore, are more sensitive to fluctuations in the SIR than their DS-SS counterparts. Table 9.3 shows the percentage area of the floor that that have BER values below a threshold, ϵ, for the Scenarios I and IV.

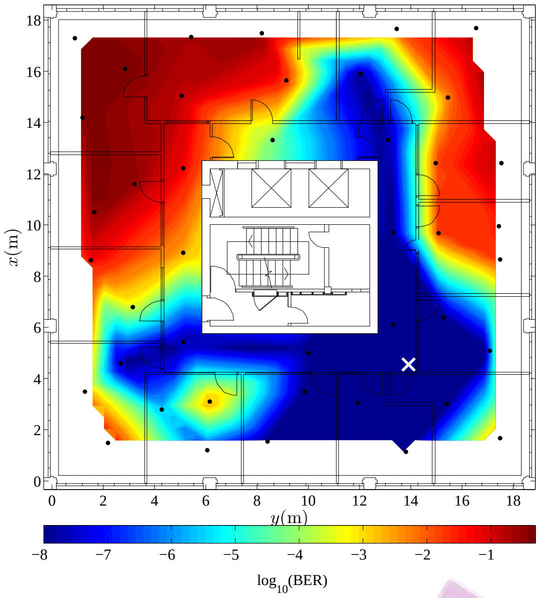

(a) OFDM-based networks.

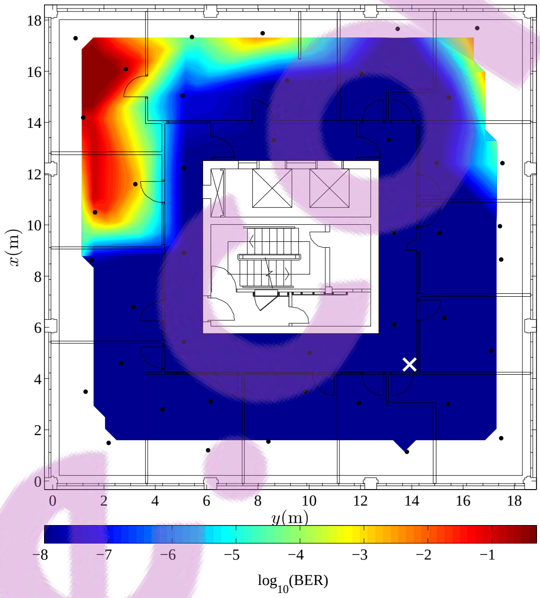

(b) DS-SS-based networks with $U = 1$.

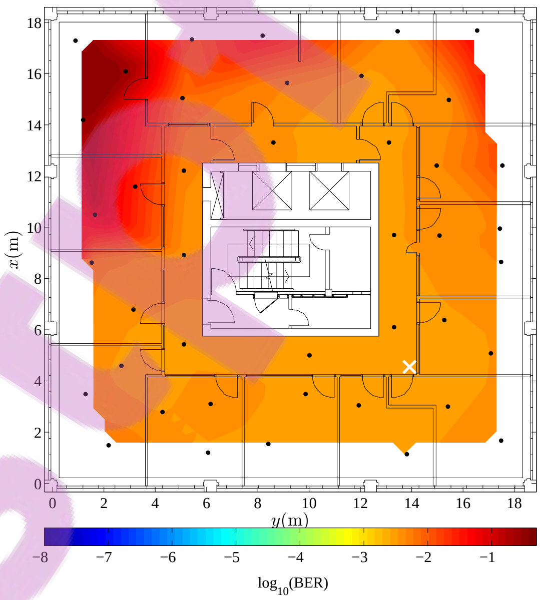

(c) DS-SS-based networks with $U = 10$.

Figure 9.5: Contour map of $\log_{10}(\text{BER})$ for Scenario I. $M = 2$, $Z_i = 2\,\forall i$. The location of the desired BS is indicated by a white $\times$.

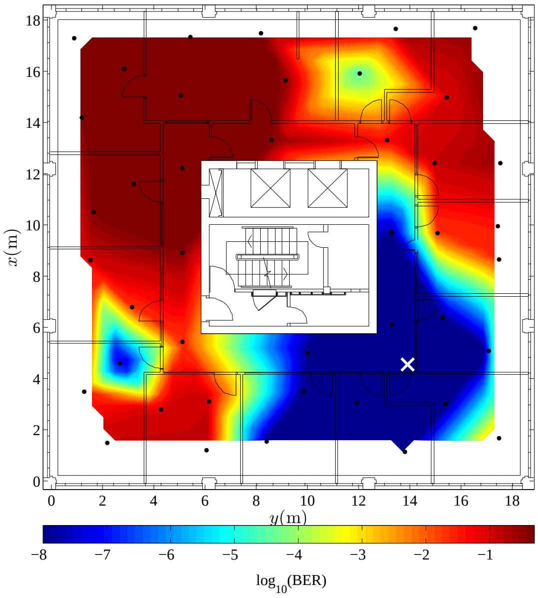

(a) OFDM-based networks.

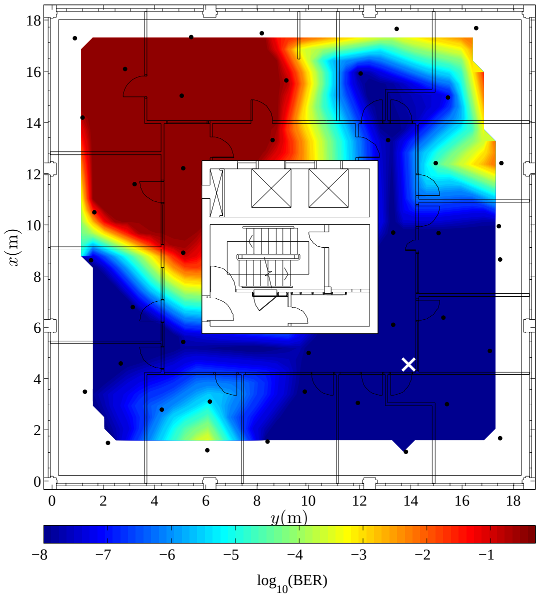

(b) DS-SS-based networks with $U = 1$.

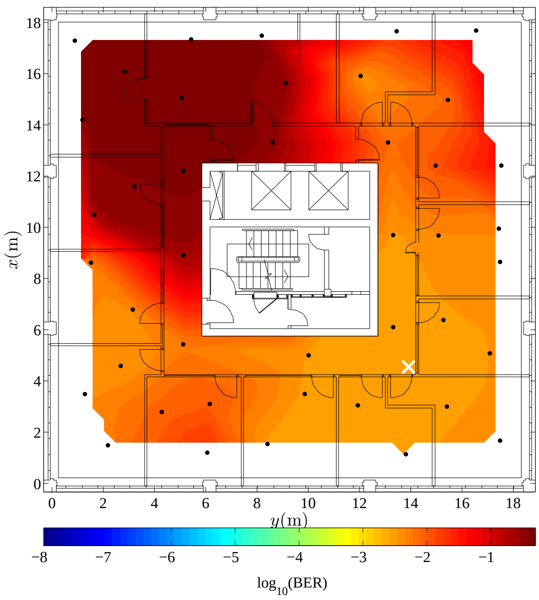

(c) DS-SS-based networks with $U = 10$.

Figure 9.6: Contour map of $\log_{10}(\text{BER})$ for Scenario IV. $M = 2$, $Z_i = 2\,\forall i$. The location of the desired BS is indicated by a white $\times$.

9.4 Summary

In this chapter, the analytical error rate expressions were used to show the effects of interference sources outside an environment on OFDM-based wireless networks. Results show that the presence of just external interferers several metres away from the test environment and at height equivalent to two floors below has a significant impact on the OFDM error rate performance. Results also show that when the external interferer is on the same side as an internal interferer, its influence on the error rate performance becomes minimal. Comparisons with DS-SS systems enforced the patterns observed in Chapter 8, where OFDM systems are more sensitive to SIR fluctuations than DS-SS systems due to the lack of spectrum spreading in OFDM systems. Also, DS-SS systems have error rate performances that are limited by the intra-cell interference as well as inter-cell interference and both can be mitigated with higher processing gains.

In practice, radio engineers tasked with replacing/upgrading DS-SS networks with OFDM-based ones need to be aware of such differences in performance and limitations between DS-SS and OFDM systems. In particular, OFDM systems' inability to combat interference using spectrum spreading techniques, emphasises the need to preserve subcarrier orthogonality (through synchronisation algorithms and ISI suppression techniques) to maintain ICI-free performance. Unlike DS-SS systems, as long as subcarrier orthogonality is preserved, OFDM systems can combat multiple access interference (MAI[4]) *without* the penalty of lowering data throughput. This allows radio engineers and system planners to focus on the presence of *inter*-cell interference and ways to avoid and/or cancel/mitigate its effects on OFDM-based wireless systems.

Throughout Chapters 8 and 9, the usefulness and applicability of the analytical error rate expressions derived in this thesis have been demonstrated. In Chapter 10, the significance of the analytical error rate expressions/models are put into context and future developments that would improve the capabilities of these models are discussed.

[4]Sometimes called multi-user interference (MUI), or intra-cell interference.

Chapter 10

Context and Future Developments

10.1 Introduction

The ubiquity of wireless systems in deployment coupled with the ever increasing number of these systems adopting OFDM as their air interface technology necessitate the development of fast and reliable tools that can quantify the impact of OFDM-to-OFDM interference. In Chapter 7, analytical expressions for OFDM error rate performance in the presence of same-type system interference were derived. While the full expressions are exact, they are not computationally feasible. Therefore, a computationally efficient algorithm that estimates the error rate performance with acceptable accuracy levels was developed using a hybrid of two approximation methods. Chapters 8 and 9 demonstrated the applicability and practical use of this algorithm in wireless systems design and deployment optimisation.

Section §10.2 demonstrates how the work presented in this thesis fits into the "big picture" of wireless systems design and how it can be utilised as an integral block of the design process. Several improvements on the current analytical work are suggested for future work in Section §10.3.

10.2 Wireless Systems Design and Optimisation

One of the major tasks of radio systems engineers is the design and optimisation of wireless systems in deployment. The design and optimisation process of any wireless system can be subdivided into three core stages, as shown in Fig. 10.1. The first is determining the system parameters: these parameters include (but are not limited to) antenna type, physical layer interface, modulation schemes, frequency range, bandwidth, number of carriers, deployment configuration etc. Once the system parameters are determined, the system performance can then be assessed in terms of error rates, outage probabilities or data throughputs, which are all inter-related. Based on the system performance, some parameters might be adjusted to improve the system performance. The base station deployment can then be optimised based on the system performance obtained for each deployment/configuration.

The system performance assessment process is shown in Fig. 10.2 and consists of several discrete stages/blocks. Given the system parameters, the first stage is quantifying the effect of the radio channel on the transmitted signals (desired and interfering alike), i.e. determining the channel impulse response

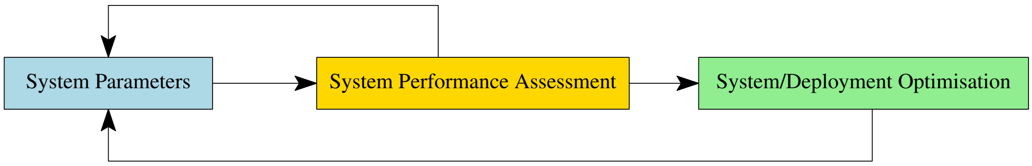

Figure 10.1: Communications system design and optimisation process.

for each received signal. This can be done in four different ways: the channel impulse response can be measured for a collection of transmitter-receiver locations (as was demonstrated in Chapter 5). While this method is laborious, time-consuming and environment-specific, there are no assumptions and/or simplifications of the radio channel. The second way of quantifying the channel impulse response is using computational electromagnetic modelling techniques such as the finite-difference time-domain (FDTD) method [104, 105]. Depending on the resolution and the environmental details of the simulation setup, the FDTD can be computationally very intensive [106, pp. 34–36]. The third method is to use *mechanistic* models that are based on the fundamental electromagnetics theory but consider only the dominant components; this allows channel estimations that have acceptable accuracy levels but with a significantly reduced computational overhead [107, Sec. V]. Other methods include simplistic channel modelling such as free space, Rayleigh fading etc. (see Chapter 4). While these methods provide fast channel estimations, they are based on a set of approximations/assumptions which (depending on the task at hand) could be inappropriate. The main objectives of channel estimation block are to

1. Quantify the desired transmission's resultant phase offset[1] (consequence of multipath fading and travelling); and

2. Quantify the *received* SINR, i.e. the SINR at the receiver's front end.

Since phase offsets are usually corrected by the synchroniser at the receiver, the received SINR is the main output of the channel estimation block. The synchronisation block at the receiver's front end is tasked with maintaining time- and frequency-domain synchronisation with the desired transmission. However, synchronisation errors (dependent on the channel conditions and the synchronisation algorithm) can change the received SINR, e.g. synchronisation errors in OFDM-based networks would result in ICI (which changes the SIR at each subcarrier frequency bin) [129, Ch. 5]. Estimating the synchronisation errors[2] (symbol timing offsets and carrier frequency offsets) can be achieved in one of three different ways: hardware testing/prototyping where a prototype of the system is implemented on hardware[3] and the performance of the synchronisation algorithm is tested under various channel conditions. The second approach is using Monte Carlo numerical methods to model the synchronisation algorithm and quantify its impact under different channel conditions. The third method is analytical modelling where the effects of the synchronisation algorithm are quantified mathematically and incorporated into the system model. The received SINR at the receiver's front end could change depending on the extent of the synchronisation errors and an *effective* SINR is obtained[4].

[1]If uncorrected for in the synchronisation block, phase offsets can cause bit errors.
[2]The effects and extent of these errors are dependent on the synchronisation algorithm used.
[3]This could be done on digital signal processors (DSPs) or field programmable gate arrays (FPGAs).
[4]Many system performance models assume perfect synchronisation with the desired transmission (as in this thesis) and therefore, the received SINR obtained from the channel model is the effective SINR.

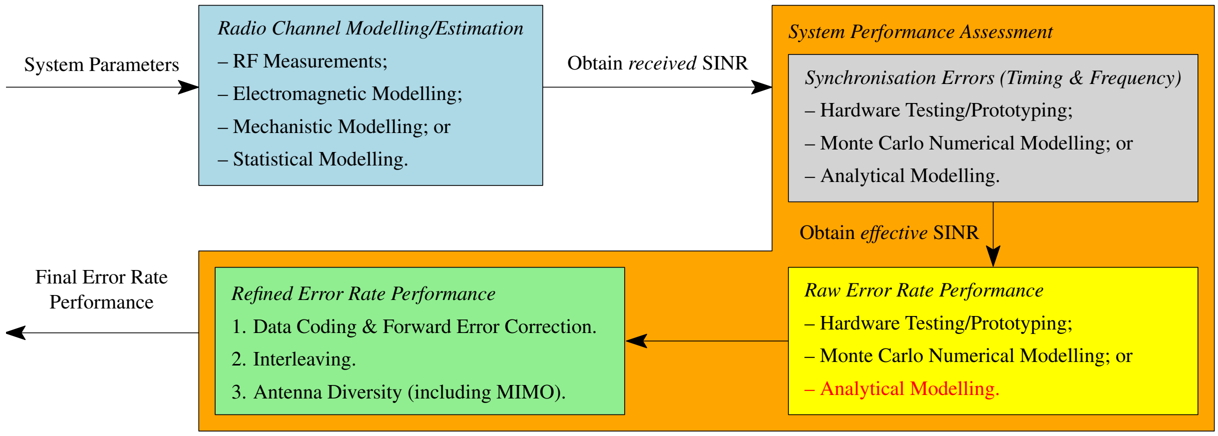

Figure 10.2: System performance assessment process. The main thesis contribution is highlighted in red text.

Once the effective SINR is obtained, the *raw* error rate performance can be be quantified via one of three methods: hardware testing/prototyping where the raw error rate performance is measured using a system prototype on hardware. Modelling the system using Monte Carlo numerical methods is a popular option due to its relative simplicity and versatility. However, depending on the resolution of the Monte Carlo model and the scenario parameters, the duration of Monte Carlo simulations could take anywhere between a few seconds and several days or longer. The third option is quantifying the raw error rate performance using analytical expressions that accurately capture the system behaviour in the presence of noise and interference. The main contribution of this thesis falls under the third category, whereby a fast, robust and sufficiently accurate analytical algorithm is developed that quantifies the raw error rate performance of OFDM-based networks in the presence of noise and multiple same-type OFDMIs.

Most, if not all, commercial wireless systems have features that improve their raw error rate performance. These features include data coding (forward error correction (FEC) codes), interleaving, antenna diversity, adaptive subcarrier allocation algorithms. The refined, or final, error rate performance is quantified once these features are taken into consideration. Quantifying the refined error rate performance carries with it two major challenges, namely:

1. The inclusion of additional features results in more complex system models that can be challenging to fully model analytically; and

2. Most of these features are algorithm-dependent. Therefore, it is challenging to come up with a model (especially analytical) that encompasses all possible performance outcomes.

The beauty of the raw error rate algorithm developed here is that it is independent of the channel, synchronisation algorithm, and all the additional enhancing features (coding, diversity, etc.) and can be used as a *module* inside a larger system model. However, the developed analytical model/algorithm is not "complete" and there are several features than can be incorporated to make it more comprehensive and useful.

10.3 Recommendations for Future Work

This thesis provides an *analytical* technique that enables fast and robust error rate performance assessment of OFDM-based wireless systems in the presence of interference, mainly same-type system interference. However, there are numerous ways that the work presented in this thesis can be extended and improved to provide a better and universal tool that enables a more comprehensive performance assessment of OFDM-based systems suffering from OFDM interference. The recommendations for future work are classified into two major categories: the first consists of improvement and refinement of the work presented here by making it universal and robust. The second category is the development of additional modules/tools that *complement* the work presented in this thesis to provide a more complete OFDM performance assessment tool.

10.3.1 General Model Refinements

The analytical model derived in this thesis is based on a set of assumptions and approximations that reduce its complexity. This section presents some recommendations for removing some of the main assumptions and approximations inherent in the analytical model. The removal of some of these assumptions and approximations would produce a more general analytical model (perhaps more complex) that can be used for scenarios and cases where the current model is inadequate.

QAM Constellations

When it comes to the QAM constellations used by the analytical model for the OFDM signals, there are two assumptions, namely:

- Square QAM constellations (apart from BPSK) for all desired and interfering OFDM signals; and
- The QAM levels of all interfering OFDM signals are known and constant across time and frequency.

While these assumptions are not critical to the performance assessment, removing them would enhance the usability of the analytical model. The square QAM constellations are not an unreasonable assumption since most wireless standards using OFDM adopt square QAM signal mapping (e.g. [8, 23]). However, allowing the QAM constellations to be rectangular (i.e. the number of signal points on the I-channel is not necessarily the same as the Q-channel) can be achieved with relative ease.

The second assumption can be removed by replacing Z_i with $Z_{i,g}^{(\ell)}$, which is the QAM level of the ℓth symbol of the gth subcarrier of the ith OFDM interferer. However, as seen in Section §8.2, the upper bound expression is insensitive to the particular value of Z (as long as it is not BPSK), and therefore, replacing Z_i with $Z_{i,g}^{(\ell)}$ is potentially a futile exercise for non-BPSK OFDMIs.

Random α, τ and ϕ

The frequency, time and phase offsets between the desired OFDM transmission and the ith OFDMI, α_i, τ_i and ϕ_i respectively, are assumed to be known/given. Also, τ_i is assumed to be an integer multiple of the time-domain sampling rate. A possible extension is to consider these parameters as random entities such that

- The normalised frequency offset, α_i is uniformly distributed between 0 and 1, i.e. $\alpha_i \sim U[0, 1]$;
- The time offset, τ_i is uniformly distributed between 0 and N, i.e. $\tau_i \sim U[0, N]$; and
- The phase offset, ϕ_i is uniformly distributed between 0 and 2π radians, i.e. $\phi_i \sim U[0, 2\pi]$.

However, as seen in Section §8.2, the upper bound expression is sensitive to the particular values of α_i, τ_i and ϕ_i only when the OFDMI is BPSK-mapped.

Partial Co-Channel Interference

The analytical model assumes that the OFDM interferers (while being of the same type as the desired system) are co-channel interferers, i.e. they use completely overlapping spectra. Most modern wireless standards (e.g. IEEE 802.11g WLANs [23]) have several full-bandwidth "channels" that can be used by the network. However, some of these channels partially overlap, which means that if two neighbouring wireless networks use partially overlapping channels then there will be interference (not as severe as co-channel interference). Therefore, the analytical model can be extended by considering partial co-channel interference and this would require modelling the bandpass filter's response at the receiver's front end.

General OFDM-to-OFDM Interference

One of the major assumptions of the analytical model is that *all* OFDM systems (desired and interfering) are of the same type, e.g. all are IEEE 802.11n WLANs or all are WiMAX. This assumption resulted in several simplifications (see Section §7.2.1), namely there are only two OFDM time-domain symbols present at the receiver's DFT window per OFDMI and the number of subcarriers and their frequency separation are identical to those of the desired system. Removing this assumption would have significant changes to the analytical model derived herein. The benefit of removing this assumption is to provide a tool that can analyse OFDM-to-OFDM interference across any OFDM standard/system.

10.3.2 Complementary Modules

As discussed in Section §10.2, evaluating the *true* performance of an OFDM-based wireless network requires several modules/blocks including the raw error rate estimation module (main thesis contribution). This section provides recommendations for additional modules that can be used to complement the work presented in this thesis to provide a more complete OFDM performance assessment tool.

OFDMA

The analytical model derived in this thesis is able to quantify the raw OFDM error rate performance at the subcarrier level. This can be used for single-user systems (OFDM) and multi-user systems (OFDMA) by averaging the raw error rates for the subcarriers allocated for a particular user (averaging across all subcarriers for the OFDM case). Therefore, a module that adaptively allocates resources to the users connected to the network across time and frequency (i.e. which subcarriers get allocated to which user at what time) can be used in conjunction with the analytical model to provide raw error rate performance assessment for OFDMA systems. There are several resource allocation algorithms and some are summarised in [19], [73, Ch. 6], and [129, pp. 143–151]. Another closely related module would be an adaptive modulation module whereby the desired QAM level changes according to instantaneous SINR.

Synchronisation

As mentioned in Section §3.3.2, OFDM systems are very sensitive to synchronisation errors. This is due to the fact that synchronisation errors can degrade subcarrier orthogonality and thus induce ICI. Therefore, a module that implements OFDM synchronisation and estimates the synchronisation errors can be used to provide the raw error rate module with the effective SINR and thus gives a better representation of commercial OFDM systems. There are many synchronisation algorithms in the literature that can be used by this module, some of which are summarised in [39, Ch. 14], [73, Ch. 5] and [129, Ch. 5].

High PAPR Mitigation

As mentioned in Section §3.3.3, multi-carrier transmission systems (such as OFDM) have a high peak-to-average power ratio (PAPR) that causes problems for the OFDM transmitter. However, there are several techniques that reduce or mitigate the effects of high PAPR and these are summarised in [39, Ch. 13] and [129, Ch. 7]. A module that utilises one or more of these techniques can be incorporated into the overall OFDM system model and the effects of this mitigation process can be included into the raw error rate module to provide a more accurate representation of a commercial OFDM system.

Uplink

Throughout this thesis all OFDM transmissions and system performances are considered for the downlink. However, if perfect synchronisation and perfect high PAPR mitigation are assumed, then there is no difference between OFDM uplink and downlink system performances. When non-ideal synchronisation is considered, OFDM uplink synchronisation is implemented differently than downlink synchronisation. In an OFDMA system, the mobile stations (MSs) will transmit their uplink data at different times. While each MS is allocated orthogonal subcarriers to all other MSs, the non-simultaneous arrival of the uplink signals at the base station (BS) would cause degradation of subcarrier orthogonality, causing ICI [129, p. 183]. Unlike downlink synchronisation, uplink synchronisation is performed in a closed loop since MSs typically are not capable of estimating propagation delays from the BS preamble. Therefore, if non-ideal synchronisation is considered, a separate module (perhaps a sub-module within the synchronisation module) that performs uplink synchronisation is used to estimate any synchronisation errors (and corresponding ICI) for uplink transmissions.

High PAPR is a particularly problematic issue with uplink transmissions since MSs have limited battery power and thus, the efficiency of the power amplifier becomes more critical than for downlink transmissions [129, p. 209]. One high PAPR reduction technique that is being adopted for 3GPP LTE uplink transmissions is DFT-spreading [129, p. 224], [130]. This technique reduces the PAPR of an OFDM signal to that of a single-carrier transmission by inserting a DFT *prior* to the IDFT in the transmitter[5] [129, pp. 241–250]. Therefore, for accurate representation of commercial *cellular* uplink transmission, a separate module that uses SC-FDMA transmission is needed.

Coding and Interleaving

Coding and interleaving schemes are used by most, if not all, commercial wireless systems to improve their raw error rate performance. In single-carrier systems, coding is used to combat time-domain burst errors while in OFDM systems, coding is mainly used to combat frequency-domain burst errors [39, p. 851]. In frequency-selective channels, several OFDM subcarriers can suffer from deep fades causing loss of data on those affected subcarriers. Thus, coding is used to spread the information across the subcarriers, and therefore, the correctly detected coded symbols on the strong subcarriers would assist in recovering the erroneous symbols on the faded subcarriers. OFDM systems use a variety of codes such as convolutional codes, Reed-Solomon (RS) codes, concatenated codes, turbo codes, and trellis coded modulation (TCM) [129, p. 142].

However, for frequency-flat channels, adjacent subcarriers will have similar fading patterns and therefore, if a large set of consecutive subcarriers suffer from deep fades, decoding errors will occur due to FEC code's inherent limited capability for error correction [39, p. 851]. Thus, interleaving is used to scramble consecutive coded symbols across the subcarriers[6]. At the receiver, there is a de-interleaver block immediately after the DFT that spreads consecutive faded symbols to several codewords containing isolated erroneous symbols that are then corrected by the coding scheme [39, p. 852]. A module quantifying the effects of coding and interleaving on the OFDM system performance can be used in conjunction with the raw error rate estimation block developed here.

Signal Diversity

Along with coding and interleaving, signal diversity techniques are used to combat poor channel conditions and improve the effective SINR. There are five main types of signal diversity techniques, namely [39, pp. 612–613]:

1. *Space* diversity can be achieved by utilising multiple receiving antennas. In a typical scattered environment, a separation distance of half a wavelength between adjacent receiver antennas would result in the received signals on the antennas experiencing uncorrelated fading patterns.

2. *Polarisation* diversity can be achieved by using receiver antennas with different polarisations since a scattering environment tends to depolarise a signal. For example, cellular MSs use vertical monopole and patch antennas to achieve this kind of diversity.

[5] If this extra DFT block is of the same size as the IDFT at the transmitter, the net effect is the OFDMA system becomes equivalent to a single-carrier FDMA (SC-FDMA) system. Usually the DFT has a smaller size than the IDFT with the "extra" subcarriers at the IDFT set to zero (zero padding), hence the name DFT-spreading.

[6] Interleaving can be performed at the bit level before mapping, or at the symbol level after mapping.

3. *Frequency* diversity is obtained by transmitting the same signal on multiple carriers such that each carrier experiences a different fading pattern. OFDM systems are inherently frequency-diverse since multiple subcarriers can be used to transmit the same data if need be.

4. *Time* diversity is when signals are transmitted at different time slots separated by at least the channel coherence time. Coding techniques for single-carrier transmission systems are an example of time diversity.

5. *Multipath* diversity is achieved when the energy of the multipath echoes of the transmitted signal are collected such that their weighted sum produces a stronger signal than just the first echo. A RAKE receiver is an example of a system that utilises multipath diversity.

Diversity *combining techniques* (e.g. selective combining, equal gain combining, and maximal ratio combining) are then used to mix/combine the received signals in such a way to optimise the SINR. One of the most popular and successful combination of diversity schemes that has emerged in the last decade or two is the multi-input multi-output (MIMO) wireless link. Many modern OFDM wireless systems use MIMO such as LTE, WiMAX and IEEE 802.11n WLAN to name a few. MIMO systems use multiple transmit and receive antennas with the signals cleverly combined using space-time coding and spatial multiplexing to enhance the channel capacity relative to a single-input single-output (SISO) link [39, pp. 616–627]. Therefore, a module that takes into account the diversity gains obtained by a MIMO link and estimates the received SINR is another candidate to work effectively with the raw error rate module developed in this thesis.

10.4 Summary

In this chapter, the main contribution of the thesis is put into context. The analytical model that is derived in this thesis is capable of quantifying the raw error rate performance of an OFDM system in the presence of noise and multiple same-type OFDM interferers. Because the analytical model is independent of the type of channel, synchronisation algorithm and coding scheme, it can be used as an integral block/module in a larger OFDM model that encompasses those other features (such as synchronisation, channel estimation and forward error correction coding).

Refinements to the current analytical model would improve its usability. These include non-square QAM constellations and general OFDM-to-OFDM interference where the OFDM systems do not have to be of the same type. The development of complementary modules that work in conjunction with the analytical model enable more realistic assessments of a commercial OFDM system performance.

Chapter 11

Conclusions

The rise of OFDM as a popular physical layer air interface technology among contemporary wireless communication systems is one of the major motivations for this research. As more OFDM-based wireless networks become operational (especially in the license-exempt bands), interference from neighbouring wireless systems becomes an issue. The research presented in this thesis is focused on *analytically* quantifying the performance of OFDM-based wireless systems in the presence of interference, both narrowband (in the form of tones) and wideband (in the form of same-type OFDM systems). Another research objective is comparing OFDM system performance with DS-CDMA system performance under identical environmental conditions. This comparison is important to radio systems engineers when replacing/upgrading existing DS-CDMA networks with OFDM-based networks, since it provides answers to questions like “Is a base station/antenna reassignment or redeployment necessary when replacing a DS-CDMA network with an OFDM one?”.

Analytical symbol and bit error rate expressions for a generic M-ary QAM OFDM in the presence of noise and multiple narrowband interferers have been developed. The symbol error rate expressions provide estimates that match very well with results obtained from Monte Carlo numerical methods. The same has been found for the bit error rate expressions for BPSK and QPSK mapped OFDM signals. However, for higher QAM levels (16QAM and higher), there are significant inaccuracies for the bit error rate expressions at low SINRs (i.e. poor channel conditions). These inaccuracies stem from the fact that Gray coding is used for signal mapping and the model’s inherent assumption that channel impairments causing message point detection to be more than one decision boundary away are very unlikely. This is not an issue in practice though, since high QAM mapping schemes are not used for poor channel conditions. Therefore, the analytical bit error rate expressions can be used with confidence to estimate OFDM performance in the presence of multiple narrowband interferers.

The frequency and phase offsets between a narrowband signal and the OFDM subcarriers cause spectral leakage at the receiver’s DFT output. The OFDM error rate performance is observed to be sensitive to the amount of spectral leakage present. This sensitivity to the spectral leakage means that, unlike DS-CDMA systems, the total interference power is not sufficient to provide an accurate indication of the error rate performance when multiple narrowband interferers are present.

The linearity of the radio channel enables the modelling of an interfering OFDM system as a superposition of mapped narrowband subcarriers. Thus, the analytical error rate expressions developed for assessing OFDM performance in the presence of narrowband interference are extended to model the presence of multiple same-type OFDM interferers (e.g. if the desired and interfering OFDM systems are all IEEE 802.11g WLANs). The analytical error rate expressions for OFDM-to-OFDM interference include the effects of time, frequency and phase offsets between desired and interfering transmissions. These offsets induce spectral leakage at the receiver's DFT output which means that *every* interfering subcarrier will have its energy smeared across the entire OFDM spectrum, thus interfering with *every* desired OFDM subcarrier. The presence of spectral leakage coupled with mapping of the interfering subcarriers results in error rate expressions that have several nested summations. These nested summations make the complete analytical expressions computationally infeasible (evaluating a simple case would require aeons on a modern single-core CPU chip).

Therefore, a computationally efficient algorithm is developed that is a hybrid of two approximation methods. These approximation methods provide acceptable accuracy levels compared with results obtained from Monte Carlo numerical methods. For the case of a single OFDM interferer, a scaled down version of the complete analytical expressions is adopted whereby only the effects of the closest interfering subcarriers to the desired subcarriers are considered. Typically, the closest five interfering subcarriers to the desired subcarrier would contain more than 90% of the interferer's energy. A scaling factor is included in the model to compensate for underestimating the interference power. When there are multiple interferers present, the central limit theorem is used to obtain the upper bound expression, which is computationally very efficient. For non-BPSK mapping schemes, the upper bound expression becomes independent of the number of interferers, the interference mapping scheme, and the time, frequency and phase offsets between desired and interfering transmissions and is dependent only on the desired mapping scheme and the *effective* SINR.

OFDM-to-OFDM interference performance assessments for indoor-to-indoor and outdoor-to-indoor deployment scenarios have been conducted using real RF measurements in two architecturally different buildings at The University of Auckland. Path loss databases obtained via different measurement campaigns over the past decade provided the necessary radio channel information to calculate the effective SINR at the receiver. Results show that for Test Environment A with close proximity neighbouring buildings, a vertically aligned base station deployment at one side of the building would produce the best error rate performance. However, a zigzag, or staggered, deployment best fits Test Environment B which has a single central services core as a salient feature. Results also show that for the Test Environment A, a base station redeployment would be unnecessary if a DS-CDMA network is replaced with an OFDM network while for Test Environment B, a base station redeployment is needed. Thus, the redeployment issue is environment-specific.

The analytical model developed in this thesis is independent of the channel model, synchronisation algorithm, forward error correction code and signal diversity scheme. This allows the analytical model to be transportable across platforms and thus can be used as a module to calculate the raw error rate performance of OFDM-based networks. This module can also be used as an integral part of a larger model that encompasses all the other features present in commercial OFDM systems. Several enhancing features are recommended to be included in the analytical model to improve its usability such as a general OFDM-to-OFDM interference model and non-square QAM constellations.

Appendix A

Derivation of the Separation Distance Between Adjacent Signal Levels, Δ, in Signal Space

A $\sqrt{M}$-ary ASK signal $s_m(t)$, with a pulse shaping function $p(t)$, is given by [39, p. 427]

$$\begin{aligned} s_m(t) &= s_m \varphi(t), \quad 0 \le t \le T_s \\ &= A_m p(t) \cos(2\pi f t), \end{aligned} \tag{A.1}$$

where $\varphi(t)$ is the basis function, T_s is the symbol period, and

$$A_m = \left(2m - 1 - \sqrt{M}\right) A, \quad m = 1, 2, \ldots, \sqrt{M} \tag{A.2}$$

for bipolar symmetric ASK signals and $A > 0$. If we define

$$\varphi(t) \triangleq \sqrt{\frac{2}{E_p}} p(t) \cos(2\pi f t), \tag{A.3}$$

where E_p is the energy of $p(t)$ that is normalised to 1, then

$$\begin{aligned} s_m &= A_m \sqrt{\frac{E_p}{2}} \\ &= \left(2m - 1 - \sqrt{M}\right) A_0, \end{aligned} \tag{A.4}$$

where $A_0 = A\sqrt{\frac{E_p}{2}}$. Therefore,

$$\begin{aligned} \Delta &= |s_m - s_{m-1}| \\ &= 2A_0. \end{aligned} \tag{A.5}$$

Since the average symbol energy of $\sqrt{M}$-ary ASK signal is half that of an M-ary QAM signal [39, p. 464], the average M-ary QAM symbol energy, E_s, can be expressed as

$$\begin{aligned} E_s &= \frac{2}{\sqrt{M}} \sum_{m=1}^{\sqrt{M}} s_m^2 \\ &= \frac{2}{\sqrt{M}} \sum_{m=1}^{\sqrt{M}} \left(2m - 1 - \sqrt{M}\right)^2 A_0^2. \end{aligned}$$

Using the algebraic identities

$$\sum_{x=u}^{v} x = \frac{(v-u+1)(v+u)}{2} \tag{A.6}$$

$$\sum_{x=u}^{v} x^2 = \frac{v(v+1)(2v+1)}{6}, \tag{A.7}$$

E_s becomes

$$\begin{aligned} E_s &= \frac{2}{\sqrt{M}} \frac{\sqrt{M}(M-1)A_0^2}{3} \\ &= \frac{2}{3}(M-1)A_0^2. \end{aligned} \tag{A.8}$$

Given that $E_s = E_b \log_2(M)$ (where E_b is the average energy-per-bit) and equations (A.5) & (A.8), Δ can be expressed as a function of the average energy-per-bit and the QAM level

$$\frac{\Delta}{2} = \sqrt{\frac{3}{2} \frac{E_b \log_2(M)}{(M-1)}}. \tag{6.12}$$

Appendix B

Monte Carlo Numerical Model

The Monte Carlo numerical model used in this thesis to validate the analytical error rate expressions derived in Chapters 6 and 7 simulates an M-ary OFDM system in the presence of noise and interference. The interference can be narrowband or Z-ary QAM OFDM. The numerical model simulates the transmission and reception of an OFDM packet and counts the number of symbol and bit errors for each frame. The simulation stops once the maximum number of bit errors has been reached and then calculates the BER and SER based on the total number of bit/symbol errors and the total number of transmitted bits/symbols. The higher the threshold for the total number of bit errors, the higher the resolution for the BER and SER results. The pseudo code for the numerical model is shown in Algorithm B.1.

Algorithm B.1 Monte Carlo numerical model pseudo code.

inputs: N, M, J, α, ϕ, $\mathbf{Z}$, SIR, E_b/N_0, TotalErrors
outputs: P_s^{MC}, P_b^{MC}
begin
SymbErrors $= 0$ {total number of symbol errors}
BitErrors $= 0$ {total number of bit errors}
Frames $= 0$ {total number of OFDM frames transmitted}
while BitError$<$TotalErrors **do**
    Generate mapped data for one desired OFDM frame {using M and N}
    Pass mapped data through N-point IFFT
    Calculate energy of desired signal frame, E_s
    Generate interfering signal(s) {using J, α, ϕ and $\mathbf{Z}$}
    Calculate the energy of interfering signal(s), E_i
    Adjust E_i such that $E_i = E_s/\text{SIR}$
    Generate AWGN signal and adjust its energy, E_N, such that $E_N = E_s/\left\{\log_2\{M\} \times E_b/N_0\right\}$
    Add the desired OFDM signal, the interfering signal(s) and the AWGN signal
    Pass composite signal through N-point FFT
    De-map the output of the FFT {Estimate transmitted symbols and bits}
    Count the number of symbol errors, SE, and bit errors, BE
    SymbErrors $=$ SymbErrors $+$ SE; BitErrors $=$ BitErrors $+$ BE; Frames $=$ Frames $+ 1$
end while
$P_s^{\text{MC}} = \text{SymbErrors}/\left(N \times \text{Frames}\right)$; $P_b^{\text{MC}} = \text{BitErrors}/\left(N \times \text{Frames} \times \log_2\{M\}\right)$
end

Appendix C

Derivation of Equations (7.7) and (7.8)

$\Psi_{i,g}^{(1)}(\alpha_i, \tau_i)$, Equation (7.7)

The post-DFT interference component due to $\Gamma_{n,i}^{(1)}$ is given by (recall Equation (7.6) and Fig. 7.1)

$$\begin{aligned}
I_k^{(1)} &= \sum_{n=0}^{\tau_i-1} \Gamma_{n,i}^{(1)} e^{-j2\pi kn/N} \\
&= \sum_{n=0}^{\tau_i-1} \sum_{g=0}^{N-1} \frac{D_{i,g}^{(1)} \beta_{i,g}}{N} e^{j[\phi_i + 2\pi(n+[N-\tau_i])(g+\alpha_i)/N]} e^{-j2\pi kn/N} \\
&= \sum_{g=0}^{N-1} \frac{D_{i,g}^{(1)} \beta_{i,g}}{N} e^{j[\phi_i + 2\pi(N-\tau_i)(g+\alpha_i)/N]} \underbrace{\sum_{n=0}^{\tau_i-1} e^{j2\pi n(g+\alpha_i-k)/N}}_{\triangleq X}.
\end{aligned} \tag{C.1}$$

Using the Geometric series expansion defined in Equation (6.6),

$$\begin{aligned}
X &= \frac{1 - e^{j2\pi\tau_i(g+\alpha_i-k)/N}}{1 - e^{j2\pi(g+\alpha_i-k)/N}} \\
&= \frac{-e^{j\pi\tau_i(g+\alpha_i-k)/N}}{-e^{j\pi(g+\alpha_i-k)/N}} \left\{ \frac{e^{j\pi\tau_i(g+\alpha_i-k)/N} - e^{-j\pi\tau_i(g+\alpha_i-k)/N}}{e^{j\pi(g+\alpha_i-k)/N} - e^{-j\pi(g+\alpha_i-k)/N}} \right\} \\
&= \frac{\sin\left[\pi\tau_i\left(g+\alpha_i-k\right)/N\right]}{\sin\left[\pi\left(g+\alpha_i-k\right)/N\right]} e^{j\pi(g+\alpha_i-k)(\tau_i-1)/N}.
\end{aligned} \tag{C.2}$$

$\Psi_{i,g}^{(1)}(\alpha_i, \tau_i)$ is defined as

$$\begin{aligned}
\Psi_{i,g}^{(1)}\left(\alpha_i,\tau_i\right) &\triangleq Xe^{j[\phi_i+2\pi(N-\tau_i)(g+\alpha_i)/N]} \\
&= \frac{\sin\left[\pi\tau_i\left(g+\alpha_i-k\right)/N\right]}{\sin\left[\pi\left(g+\alpha_i-k\right)/N\right]}e^{j\left[\phi_i+\frac{\pi}{N}\{(g+\alpha_i-k)(\tau_i-1)+2(N-\tau_i)(g+\alpha_i)\}\right]} \\
&= \frac{\sin\left[\pi\tau_i\left(g+\alpha_i-k\right)/N\right]}{\sin\left[\pi\left(g+\alpha_i-k\right)/N\right]}e^{j\left[\phi_i+\frac{\pi}{N}\{(g+\alpha_i)(\tau_i-1)-k(\tau_i-1)+2(N-\tau_i)(g+\alpha_i)\}\right]} \\
&= \frac{\sin\left[\pi\tau_i\left(g+\alpha_i-k\right)/N\right]}{\sin\left[\pi\left(g+\alpha_i-k\right)/N\right]}e^{j\left[\phi_i+\frac{\pi}{N}\{(g+\alpha_i)(\tau_i-1+2N-2\tau_i)-k(\tau_i-1)\}\right]}.
\end{aligned}$$

Therefore,

$$\Psi_{i,g}^{(1)}\left(\alpha_i,\tau_i\right)=\frac{\sin\left[\pi\tau_i\left(g+\alpha_i-k\right)/N\right]}{\sin\left[\pi\left(g+\alpha_i-k\right)/N\right]}e^{j\left[\phi_i+\frac{\pi}{N}\{(g+\alpha_i)(2N-\tau_i-1)-k(\tau_i-1)\}\right]}. \tag{7.7}$$

When considering special cases where $\tau_i=0$ and/or $\alpha_i=0$, $\Psi_{i,g}^{(1)}\left(\alpha_i,\tau_i\right)$ becomes

$$\Psi_{i,g}^{(1)}\left(\alpha_i,\tau_i\right)=\begin{cases}0 & \tau_i=0\\ \tau_i e^{j\phi_i}\delta\left[k-g\right] & \tau_i\neq 0,\alpha_i=0,g=k\\ \frac{\sin[\pi\tau_i(g-k)/N]}{\sin[\pi(g-k)/N]}e^{j\left[\phi_i+\frac{\pi}{N}\{g(2N-\tau_i-1)-k(\tau_i-1)\}\right]} & \tau_i\neq 0,\alpha_i=0,g\neq k\\ \text{Equation (7.7)} & \tau_i\neq 0,\alpha_i\neq 0.\end{cases} \tag{C.3}$$

$\Psi_{i,g}^{(2)}\left(\alpha_i,\tau_i\right)$, Equation (7.8)

Similarly, the post-DFT interference component due to $\Gamma_{n,i}^{(2)}$ is given by (recall Equation (7.6) and Fig. 7.1)

$$\begin{aligned}
I_k^{(2)} &= \sum_{n=\tau_i}^{N-1}\Gamma_{n,i}^{(2)}e^{-j2\pi kn/N} \\
&= \sum_{n=\tau_i}^{N-1}\sum_{g=0}^{N-1}\frac{D_{i,g}^{(2)}\beta_{i,g}}{N}e^{j[\phi_i+2\pi(n-\tau_i)(g+\alpha_i)/N]}e^{-j2\pi kn/N} \\
&= \sum_{g=0}^{N-1}\frac{D_{i,g}^{(2)}\beta_{i,g}}{N}e^{j[\phi_i-2\pi\tau_i(g+\alpha_i)/N]}\sum_{n=\tau_i}^{N-1}e^{j2\pi n(g+\alpha_i-k)/N}.
\end{aligned} \tag{C.4}$$

$$\begin{aligned}
Y &\triangleq \sum_{n=\tau_i}^{N-1}e^{j2\pi n(g+\alpha_i-k)/N} \\
&= \underbrace{\sum_{n=0}^{N-1}e^{j2\pi n(g+\alpha_i-k)/N}}_{\triangleq W}-\underbrace{\sum_{n=0}^{\tau_i-1}e^{j2\pi n(g+\alpha_i-k)/N}}_{=X\text{ (Equation (C.2))}}
\end{aligned}$$

$$\begin{aligned}
W &= \frac{1-e^{j2\pi(g+\alpha_i-k)}}{1-e^{j2\pi(g+\alpha_i-k)/N}} \\
&= \frac{-e^{j\pi(g+\alpha_i-k)}}{-e^{j\pi(g+\alpha_i-k)/N}}\left\{\frac{e^{j\pi(g+\alpha_i-k)}-e^{-j\pi(g+\alpha_i-k)}}{e^{j\pi(g+\alpha_i-k)/N}-e^{-j\pi(g+\alpha_i-k)/N}}\right\} \\
&= \frac{\sin\left[\pi\left(g+\alpha_i-k\right)\right]}{\sin\left[\pi\left(g+\alpha_i-k\right)/N\right]}e^{j\pi(g+\alpha_i-k)(N-1)/N}. \qquad \text{(C.5)}
\end{aligned}$$

$\Psi_{i,g}^{(2)}\left(\alpha_i,\tau_i\right)$ is defined as

$$\begin{aligned}
\Psi_{i,g}^{(2)}\left(\alpha_i,\tau_i\right) &\triangleq Ye^{j[\phi_i-2\pi\tau_i(g+\alpha_i)/N]} \\
&= \left(W-X\right)e^{j[\phi_i-2\pi\tau_i(g+\alpha_i)/N]} \\
&= \frac{e^{j[\phi_i-2\pi\tau_i(g+\alpha_i)/N]}}{\sin\left[\pi\left(g+\alpha_i-k\right)/N\right]}\Big\{\sin\left[\pi\left(g+\alpha_i-k\right)\right]e^{j\pi(g+\alpha_i-k)(N-1)/N}- \\
&\quad \sin\left[\pi\tau_i\left(g+\alpha_i-k\right)/N\right]e^{j\pi(g+\alpha_i-k)(\tau_i-1)/N}\Big\}, \qquad \text{(C.6)}
\end{aligned}$$

which is the expression in (7.8). When considering special cases where $\tau_i = 0$ and/or $\alpha_i = 0$, $\Psi_{i,g}^{(2)}\left(\alpha_i,\tau_i\right)$ becomes

$$\Psi_{i,g}^{(2)}\left(\alpha_i,\tau_i\right) = \begin{cases}
Ne^{j\phi_i}\delta\left[k-g\right] & \tau_i = 0, \alpha_i = 0 \\
\frac{\sin[\pi(g+\alpha_i-k)]}{\sin[\pi(g+\alpha_i-k)/N]}e^{j\left[\phi_i+\frac{\pi}{N}(g+\alpha_i-k)(N-1)\right]} & \tau_i = 0, \alpha_i \neq 0 \\
\left(N-\tau_i\right)e^{j[\phi_i-2\pi\tau_i k/N]} & \tau_i \neq 0, \alpha_i = 0, g = k \\
\frac{-\sin[\pi\tau_i(g-k)/N]e^{j\pi(g-k)\left(\tau_i-1\right)/N}}{\sin[\pi(g-k)/N]e^{-j\left[\phi_i-2\pi\tau_i g/N\right]}} & \tau_i \neq 0, \alpha_i = 0, g \neq k \\
\text{Equation (7.8)} & \tau_i \neq 0, \alpha_i \neq 0.
\end{cases} \qquad \text{(C.7)}$$

Appendix D

Derivation of Equation (7.17)

The pdf of the gth subcarrier of $\Gamma_{n,i}^{(\ell)}$ in the I-channel is given by

$$P_{\Gamma}^{I}\left[r|i,g,\ell\right] = \frac{1}{Z_i}\sum_{x_{i,g}^{(\ell)}=1}^{\sqrt{Z_i}}\sum_{y_{i,g}^{(\ell)}=1}^{\sqrt{Z_i}} \delta\left[r - \frac{1}{N}\beta_{i,g}\left|\Psi_{i,g}^{(\ell)}\left(\alpha,\tau,\phi\right)\right|\Omega_{i,g,I}^{(\ell)}\left(x,y,\alpha,\tau,\phi\right)\right]. \tag{7.14}$$

Consider the case when there are two interfering symbols (i.e. $\Gamma_{n,i}^{(1)}$ and $\Gamma_{n,i}^{(2)}$) each with a pdf given by (7.14), the composite interference pdf in the I-channel for two symbols, $P_{I_k}^{I}\left[r|i,g\right]$, is given by

$$\begin{aligned} P_{I_k}^{I}\left[r|i,g\right] &= P_{\Gamma}^{I}\left[r|i,g,\ell=1\right] \star P_{\Gamma}^{I}\left[r|i,g,\ell=2\right] \\ &= P_{i,g}^{(1)}\left[r\right] \star P_{i,g}^{(2)}\left[r\right], \end{aligned} \tag{D.1}$$

where $\star$ is the convolution operator. Since (7.14) is discrete, the convolution operation becomes a convolution sum [131, p. 98] according to (the α, τ and ϕ dependency variables are omitted for clarity)

$$\begin{aligned} P_{I_k}^{I}\left[r|i,g\right] &= \sum_{q=-\infty}^{\infty} P_{i,g}^{(1)}\left[q\right] P_{i,g}^{(2)}\left[r-q\right] \\ &= \frac{1}{Z_i^2}\sum_{q=-\infty}^{\infty}\left\{\sum_{x_{i,g}^{(1)}=1}^{\sqrt{Z_i}}\sum_{y_{i,g}^{(1)}=1}^{\sqrt{Z_i}} \delta\left[q - \frac{\beta_{i,g}}{N}\left|\Psi_{i,g}^{(1)}\right|\Omega_{i,g}^{(1)}\left(x,y\right)\right]\times\right. \\ &\qquad \left.\sum_{x_{i,g}^{(2)}=1}^{\sqrt{Z_i}}\sum_{y_{i,g}^{(2)}=1}^{\sqrt{Z_i}} \delta\left[r - q - \frac{\beta_{i,g}}{N}\left|\Psi_{i,g}^{(2)}\right|\Omega_{i,g}^{(2)}\left(x,y\right)\right]\right\}, \end{aligned}$$

which gives non-zero values at $q = \frac{\beta_{i,g}}{N}\left|\Psi_{i,g}^{(1)}\right|\Omega_{i,g}^{(1)}\left(x,y\right)$ thanks to the sifting property of the Kronecker delta function. Therefore, the pdf for the gth subcarrier of the ith OFDMI is given by

$$P_{I_k}^{I}[r|i,g] = \frac{1}{Z_i^2} \sum_{x_{i,g}^{(1)}=1}^{\sqrt{Z_i}} \sum_{y_{i,g}^{(1)}=1}^{\sqrt{Z_i}} \sum_{x_{i,g}^{(2)}=1}^{\sqrt{Z_i}} \sum_{y_{i,g}^{(2)}=1}^{\sqrt{Z_i}} \delta\left[r - \frac{\beta_{i,g}}{N}\times \left\{\left|\Psi_{i,g}^{(1)}\right| \Omega_{i,g}^{(1)}(x,y) + \left|\Psi_{i,g}^{(2)}\right| \Omega_{i,g}^{(2)}(x,y)\right\}\right]. \tag{D.2}$$

When two subcarriers are considered, the joint pdf is given by

$$\begin{aligned} P_{I_k}^{I}[r|i,\mathbf{g}=[g_1,g_2]] &= P_{I_k}^{I}[r|i,g_1] \star P_{I_k}^{I}[r|i,g_2] \\ &= \sum_{q=-\infty}^{\infty} P_{I_k}^{I}[q|i,g_1]\, P_{I_k}^{I}[r-q|i,g_2] \\ &= \frac{1}{Z_i^4} \sum_{q=-\infty}^{\infty} \left\{ \sum_{x_{i,g_1}^{(1)}=1}^{\sqrt{Z_i}} \sum_{y_{i,g_1}^{(1)}=1}^{\sqrt{Z_i}} \sum_{x_{i,g_1}^{(2)}=1}^{\sqrt{Z_i}} \sum_{y_{i,g_1}^{(2)}=1}^{\sqrt{Z_i}} \delta\left[q - \frac{\beta_i}{N}\times \left\{\left|\Psi_{i,g_1}^{(1)}\right| \Omega_{i,g_1}^{(1)}(x,y) + \left|\Psi_{i,g_1}^{(2)}\right| \Omega_{i,g_1}^{(2)}(x,y)\right\}\right] \times \right. \\ &\quad \left. \sum_{x_{i,g_2}^{(1)}=1}^{\sqrt{Z_i}} \sum_{y_{i,g_2}^{(1)}=1}^{\sqrt{Z_i}} \sum_{x_{i,g_2}^{(2)}=1}^{\sqrt{Z_i}} \sum_{y_{i,g_2}^{(2)}=1}^{\sqrt{Z_i}} \delta\left[r - q - \frac{\beta_i}{N}\times \left\{\left|\Psi_{i,g_2}^{(1)}\right| \Omega_{i,g_2}^{(1)}(x,y) + \left|\Psi_{i,g_2}^{(2)}\right| \Omega_{i,g_2}^{(2)}(x,y)\right\}\right] \right\} \\ &= \frac{1}{Z_i^4} \sum_{g\in\mathbf{g}} \sum_{\ell=1}^{2} \sum_{x_{i,g}^{(\ell)}=1}^{\sqrt{Z_i}} \sum_{y_{i,g}^{(\ell)}=1}^{\sqrt{Z_i}} \delta\left[r - \sum_{p\in\mathbf{g}} \sum_{q=1}^{2} \left\{\frac{\beta_i}{N}\left|\Psi_{i,p}^{(q)}\right| \Omega_{i,p,I}^{(q)}(x,y)\right\}\right]. \end{aligned} \tag{D.3}$$

This process is repeated for every additional subcarrier, and thus for the general case of J OFDMIs each with N subcarriers, the joint pdf is given by

$$P_{I_k}^{I}[r] = \mathcal{F}^{-1}\left\{\prod_{i=1}^{J}\prod_{g=0}^{N-1} \mathcal{F}\left\{P_{I_k}^{I}[r|i,g]\right\}\right\},$$

which is the convolution of (D.2) NJ times with itself giving

$$P_{I_k}^{I}[r] = \left(\prod_{w=1}^{J}\frac{1}{Z_w^{2N}}\right) \sum_{i=1}^{J}\sum_{g=0}^{N-1}\sum_{\ell=1}^{2} \sum_{x_{i,g}^{(\ell)}=1}^{\sqrt{Z_i}} \sum_{y_{i,g}^{(\ell)}=1}^{\sqrt{Z_i}} \delta\left[r - \sum_{d=1}^{J}\sum_{p=0}^{N-1}\sum_{q=1}^{2}\left\{\frac{\beta_d}{N}\left|\Psi_{d,p}^{(q)}\right| \Omega_{d,p,I}^{(q)}(x,y)\right\}\right]. \tag{7.17}$$

Appendix E

Derivation of Equation (7.30)

The pdf of the gth subcarrier of $\Gamma_{n,i}^{(\ell)}$ in the I-channel is given by

$$P_{\Gamma}^{I}\left[r|i,g,\ell\right] = \frac{1}{Z_i}\sum_{x_{i,g}^{(\ell)}=1}^{\sqrt{Z_i}}\sum_{y_{i,g}^{(\ell)}=1}^{\sqrt{Z_i}}\delta\left[r-\frac{1}{N}\beta_{i,g}\left|\Psi_{i,g}^{(\ell)}\left(\alpha,\tau,\phi\right)\right|\Omega_{i,g,I}^{(\ell)}\left(x,y,\alpha,\tau,\phi\right)\right], \tag{7.14}$$

where

$$\begin{aligned}\Omega_{i,g,I}^{(\ell)}\left(x,y,\alpha,\tau,\phi\right) &= \left(2x_{i,g}^{(\ell)}-1-\sqrt{Z_i}\right)\cos\left[\varphi_{i,g}^{(\ell)}\left(\alpha,\tau,\phi\right)\right]- \\ &\quad \left(2y_{i,g}^{(\ell)}-1-\sqrt{Z_i}\right)\sin\left[\varphi_{i,g}^{(\ell)}\left(\alpha,\tau,\phi\right)\right].\end{aligned}$$

The pdf in (7.14) can be re-written as

$$\begin{aligned}P_{\Gamma}^{I}\left[r|i,g,\ell\right] &= \frac{1}{\sqrt{Z_i}}\sum_{x_{i,g}^{(\ell)}=1}^{\sqrt{Z_i}}\delta\left[r-\frac{1}{N}\beta_{i,g}\left|\Psi_{i,g}^{(\ell)}\left(\alpha,\tau,\phi\right)\right|\left(2x_{i,g}^{(\ell)}-1-\sqrt{Z_i}\right)\cos\left[\varphi_{i,g}^{(\ell)}\left(\alpha,\tau,\phi\right)\right]\right]- \\ &\quad \frac{1}{\sqrt{Z_i}}\sum_{y_{i,g}^{(\ell)}=1}^{\sqrt{Z_i}}\delta\left[r-\frac{1}{N}\beta_{i,g}\left|\Psi_{i,g}^{(\ell)}\left(\alpha,\tau,\phi\right)\right|\left(2y_{i,g}^{(\ell)}-1-\sqrt{Z_i}\right)\sin\left[\varphi_{i,g}^{(\ell)}\left(\alpha,\tau,\phi\right)\right]\right] \\ &= X-Y.\end{aligned}$$

Given that X and Y are *independent* and using probability theory, the variance of (7.14), $\sigma_{i,g,\ell,I}^{2}$, is given by [123, p. 213]

$$\begin{aligned}\sigma_{i,g,\ell,I}^{2} &= \mathrm{Var}\left(X-Y\right) \\ &= \mathrm{Var}\left(X+Y\right) \\ &= \mathrm{Var}\left(X\right)+\mathrm{Var}\left(Y\right).\end{aligned} \tag{E.1}$$

Given that X (and Y) is symmetrical around zero (i.e. it has an expected value $E[X]=0$) and all the components in X (and Y) have a discrete probability of $1/\sqrt{Z_i}$,Var (X) is given by (all superscripts, subscripts and dependency variables are omitted for clarity)

$$\begin{aligned}
\text{Var}(X) &= \frac{1}{\sqrt{Z}}\sum_{x=1}^{\sqrt{Z}}\left\{\frac{1}{N}\beta\left|\Psi\right|\left(2x-1-\sqrt{Z}\right)\cos\left[\varphi\right]\right\}^2 \\
&= \underbrace{\frac{\beta^2\left|\Psi\right|^2}{N^2\sqrt{Z}}\cos^2\left[\varphi\right]}_{\triangleq A}\sum_{x=1}^{\sqrt{Z}}\left(2x-1-\sqrt{Z}\right)^2 \\
&= A\sum_{x=1}^{\sqrt{Z}}\left(4x^2-4x+1-4x\sqrt{Z}+2\sqrt{Z}+Z\right) \\
&= A\left\{4\sum_{x=1}^{\sqrt{Z}}x^2-4\left(\sqrt{Z}+1\right)\sum_{x=1}^{\sqrt{Z}}x+\sqrt{Z}\left(\sqrt{Z}+1\right)^2\right\}.
\end{aligned}$$

Using the algebraic identities defined in (A.6) and (A.7), Var (X) becomes

$$\begin{aligned}
\text{Var}(X) &= A\left\{\frac{2}{3}\left(2Z^{\frac{3}{2}}+3Z+\sqrt{Z}\right)-2\sqrt{Z}\left(\sqrt{Z}+1\right)^2+\sqrt{Z}\left(\sqrt{Z}+1\right)^2\right\} \\
&= A\left\{\frac{1}{3}\left(Z^{\frac{3}{2}}-\sqrt{Z}\right)\right\} \\
&= A\left\{\frac{\sqrt{Z}\left(Z-1\right)}{3}\right\} \\
&= \frac{\left(Z-1\right)}{3N^2}\beta^2\left|\Psi\right|^2\cos^2\left[\varphi\right]. \qquad \text{(E.2)}
\end{aligned}$$

Similarly,

$$\text{Var}(Y) = \frac{\left(Z-1\right)}{3N^2}\beta^2\left|\Psi\right|^2\sin^2\left[\varphi\right]. \qquad \text{(E.3)}$$

Therefore,

$$\begin{aligned}
\sigma^2_{i,g,\ell,I} &= \text{Var}(X)+\text{Var}(Y) \\
&= \frac{\left(Z-1\right)}{3N^2}\beta^2\left|\Psi\right|^2\left(\underbrace{\cos^2\left[\varphi\right]+\sin^2\left[\varphi\right]}_{\equiv 1}\right) \\
&= \frac{\left(Z-1\right)}{3N^2}\beta^2\left|\Psi\right|^2. \qquad \text{(E.4)}
\end{aligned}$$

However, if $Z=2$, Var $(Y)=0$ and $\sigma^2_{i,g,\ell,I}$ is given by Var (X) in (E.2). The process is identical for the Q-channel where the expressions for Var (X) and Var (Y) are swapped.

Appendix F

Error Rate Patterns When There is No Spectral Leakage

When $\tau_i = 0\,\forall i$ and $\alpha_i = 0\,\forall i$, no spectral leakage exists after the receiver's DFT. While this scenario is unlikely to occur in practice, it is interesting to observe the effects some of the parameters (J and ϕ in particular) have on the error rate performance. The error rate values presented in this appendix are calculated using the lower bound expressions derived in Section §7.3.3.

F.1 Effect of Changes in J

Fig. F.1 illustrates the effect of changing J on the BER performance of a QPSK-OFDM system in the presence of QPSK-OFDMIs ($\phi_i = 0\,\forall i$) while the SIR is fixed at 10 dB. Each OFDMI has an equal share ($1/J$th) of the total interference energy. It is observed in Fig. F.1 that despite the fact that the total interference energy is constant, the more interferers there are, the worse the BER performance becomes.

This, perhaps surprising, behaviour can be explained as follows: consider the case when $J = 1$ and $\phi = 0$, since each interferer considered in Fig. F.1 is QPSK modulated, there are only two discrete values that the interferer can take in each channel; considering the I-channel (the same applies to the Q-channel), the post-DFT interferer will have the values of $\pm A$ with a probability of 0.5 for each value, where A is just an arbitrary post-DFT voltage value. This configuration results in the BER performance shown in Fig. F.1. However, when a second interferer is added, to maintain a constant interference power as in the first scenario, each interferer will have the discrete values of $\pm A/\sqrt{2}$ with a probability of 0.5 for both values. Since the interferers are added, the pdf of their sum is the convolution of their individual pdfs and the resultant pdf will have three discrete values $\left[-\sqrt{2}A, 0, \sqrt{2}A\right]$ with respective probabilities of [0.25,0.5,0.25]. This means that there is a 50% chance that the interferers will cancel each other out, but there is also a 50% chance that the interferers will displace the desired message point on the signal space by a magnitude of $\sqrt{2}A$, which is greater than in the scenario with one interferer (i.e. a displacement of A versus $\sqrt{2}A$), resulting in higher BERs. This pattern is amplified when further interferers are added until the interference's pdf approximates to a Gaussian pdf and the BER asymptotes to a certain value ($\approx 7.8 \times 10^{-4}$ in Fig. F.1) that is given by the expressions in (8.7) and (6.20). Similar patterns and behaviours have been observed for different OFDM modulation schemes.

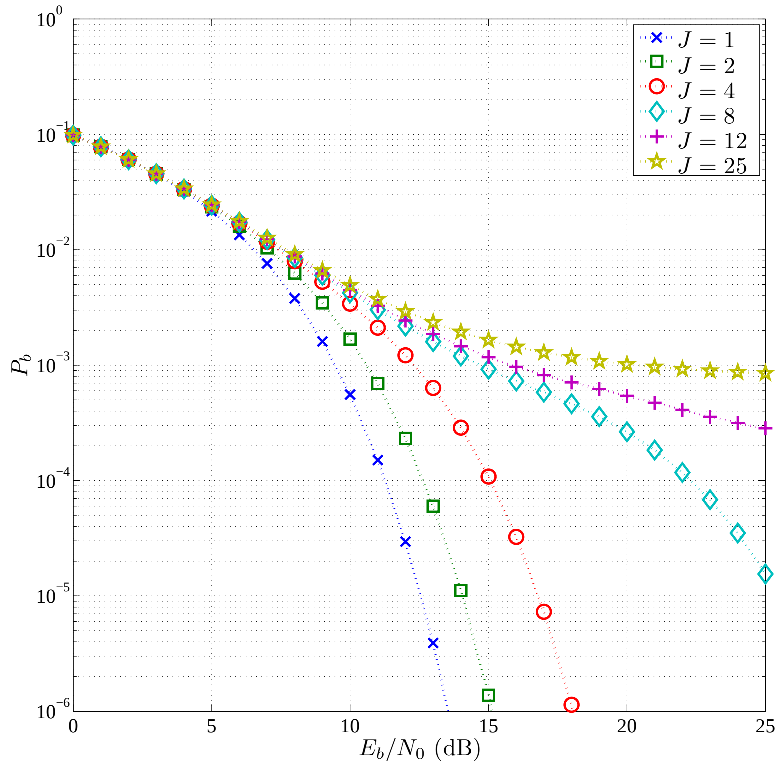

Figure F.1: Probability of bit error, P_b, performance of QPSK-OFDM in the presence of J QPSK-OFDMIs, total SIR is fixed at 10 dB, $\phi_i = 0\,\forall i$. Each OFDMI has $1/J$th of the total interference power.

F.2 Effect of Changes in ϕ

The desired and interfering signals will have a phase offset between them, $\phi_i \sim U\,[0, 2\pi]$. Since the effect of ϕ on the error rates has been considered in the analytical expressions derived in Chapter 7, it is straightforward to show how it impacts the error rates visually.

Fig. F.2 shows the BER performance of a 16QAM-OFDM system in the presence of a single QPSK-OFDMI with different ϕ values and SIR $= 15$ dB. Two things can be observed from the results shown in Fig. F.2: the first, is the effect of ϕ on the BER performance; the phase offset has a significant impact on the BER performance and can be several orders of magnitude more than the $\phi = 0$ case (maximum error rate when $\phi = \pi/4$). The reason $\phi = \pi/4$ gives the worst BER performance is that at that angle, the interfering constellation in signal space is perfectly aligned with the decision axes (boundaries), thus displacing the desired message points closer to the decision boundaries. The second thing to notice is that the effect of ϕ on the BER performance is cyclic and symmetrical around $\phi = \pi/4$ (e.g. P_b performance when $\phi = \pi/6$ is identical to that when $\phi = \pi/3$). So, although ϕ is uniformly distributed between zero and 2π, it is also correct, from a BER performance point of view, to state that $\phi_i \sim U\,[0, \pi/4]$.

Similar patterns have been observed when there are multiple OFDMIs: worst BER performance is observed when $\phi_i = \pi/4\,\forall i$ and best BER performance is observed when $\phi_i = 0\,\forall i$. These findings are true when $Z_i > 2$, however, when $Z_i = 2$, the maximum error rates are observed when $\phi_i = x\pi/2$, where x is an integer.

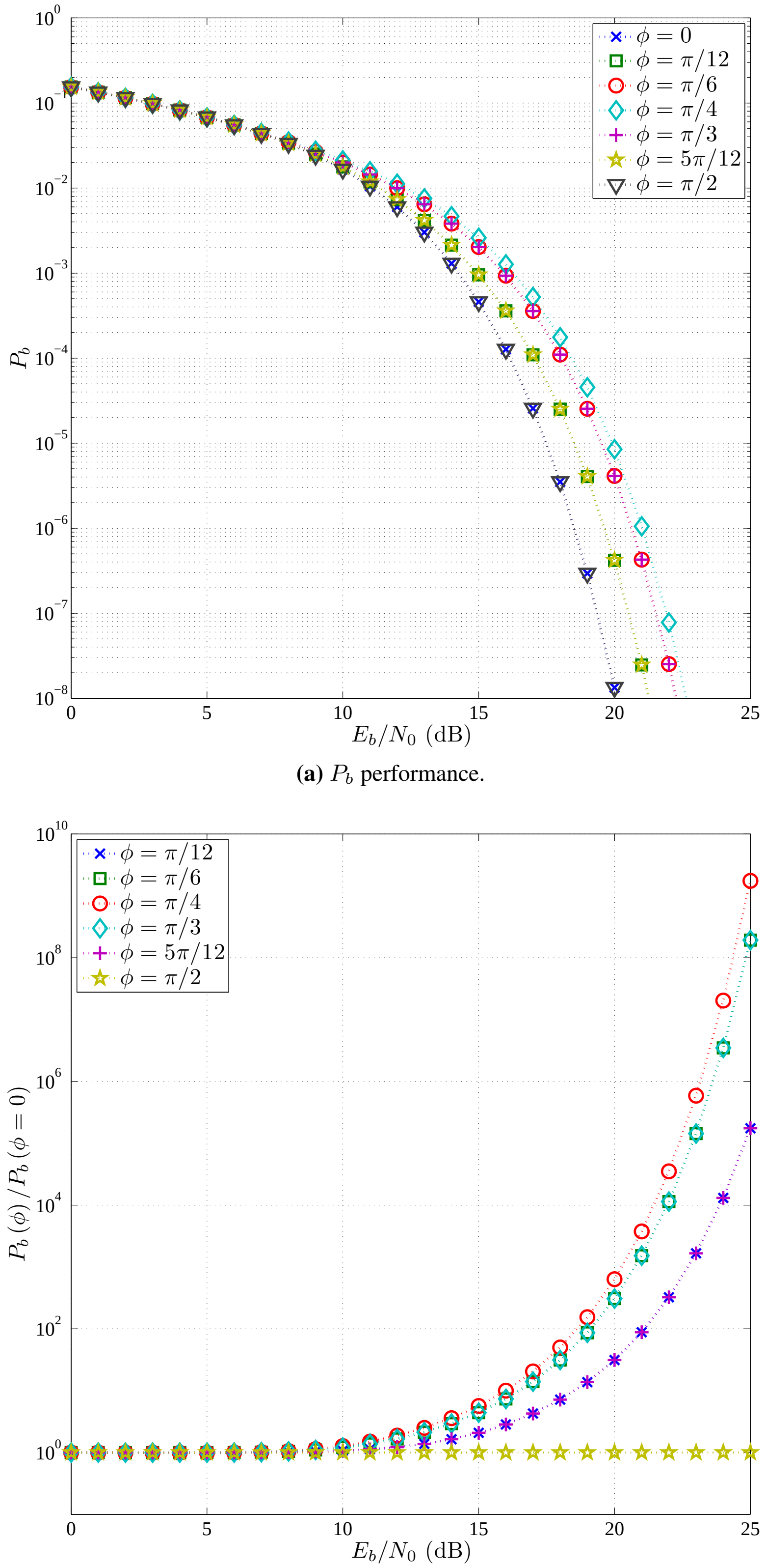

(a) P_b performance.

(b) P_b performance normalised to P_b performance when $\phi = 0$.

Figure F.2: Probability of bit error, P_b, performance of 16QAM-OFDM in the presence of a single QPSK-OFDMI with different phase offsets (SIR = 15 dB).

Appendix G

Measured RF Path Loss Values in Test Environments A and B

The measured path loss values for test environments A and B (Sections §5.2.2 and §5.2.3) are presented here. Each figure gives a contour map[1] of the path loss values (in dB) for the floor of interest given a particular active base station.

For the given base station locations in Fig. 5.4, the path loss values across the third floor of The Science Building are shown in Figs. G.1–G.3. For the given base station locations in Fig. 5.7, the path loss values across the sixth floor of The Engineering Tower (Yang's measurement campaign [108]) are shown in Figs. G.4–G.6.

The path loss values across the eighth floor of The Engineering Tower (Wong's measurement campaign [15]) are shown in Figs. G.7 and G.8.

[1]The path loss values are measured at the locations indicated by •. The contour maps were generated using MATLAB's built-in linear interpolation algorithm.

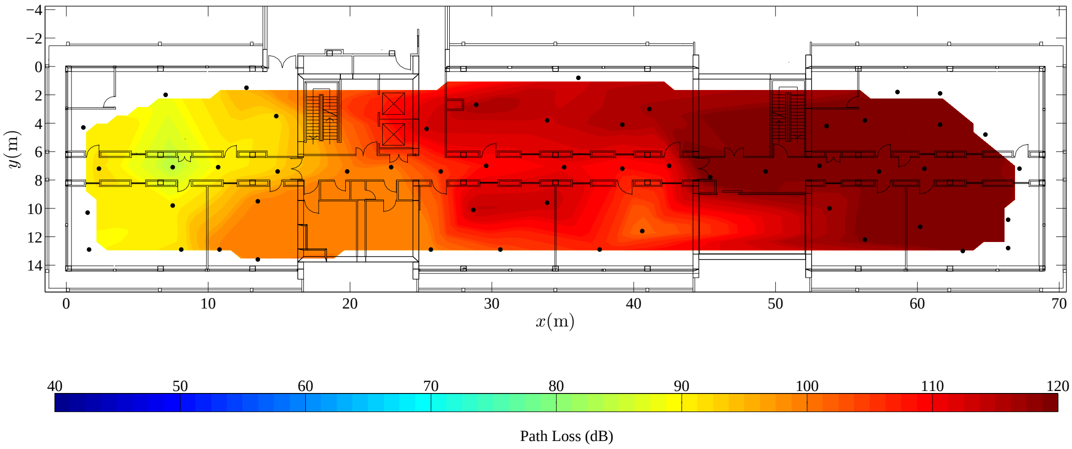

(a) Tx 1A.

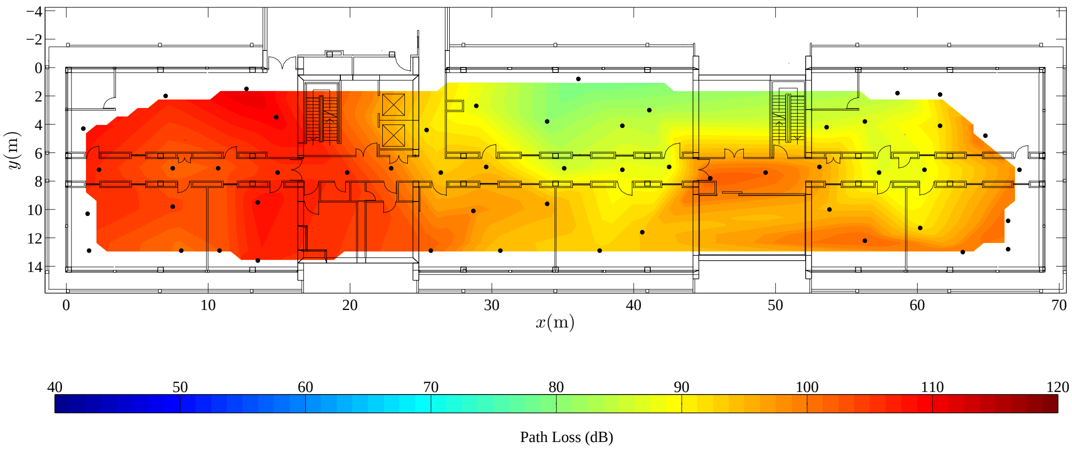

(b) Tx 1B.

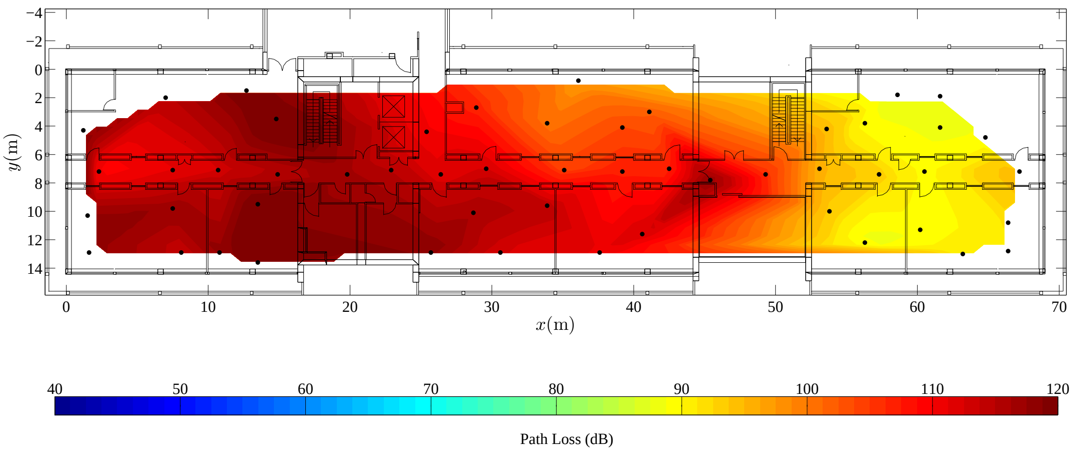

(c) Tx 1C.

Figure G.1: Base stations located on the first floor of the Science Building.

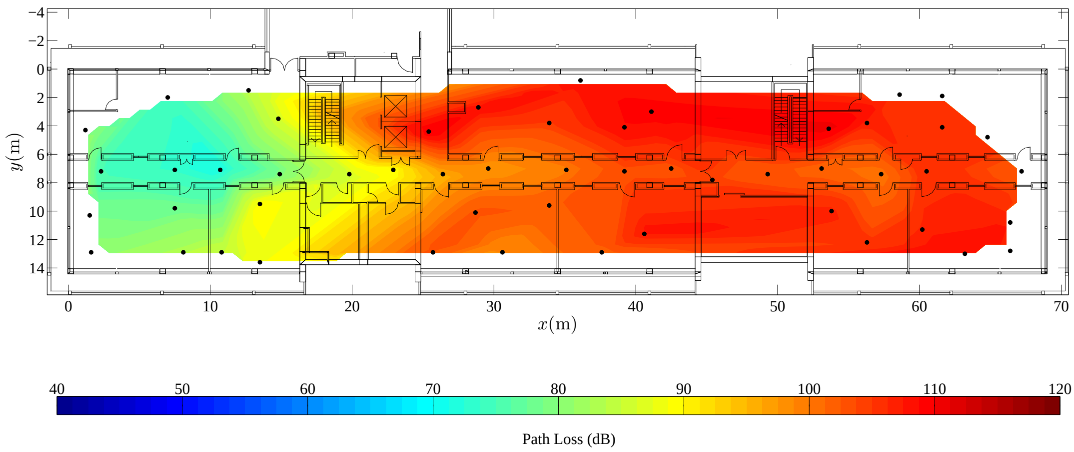

(a) Tx 2A.

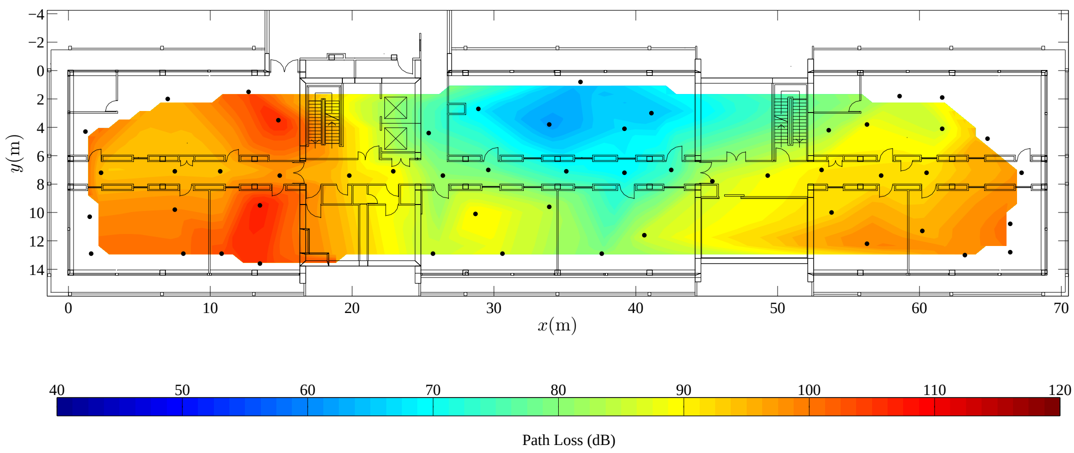

(b) Tx 2B.

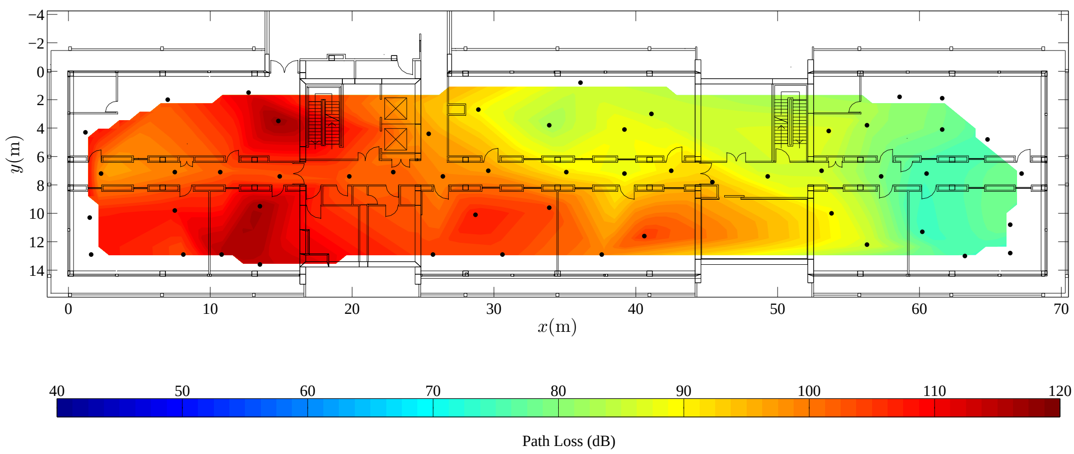

(c) Tx 2C.

Figure G.2: Base stations located on the second floor of the Science Building.

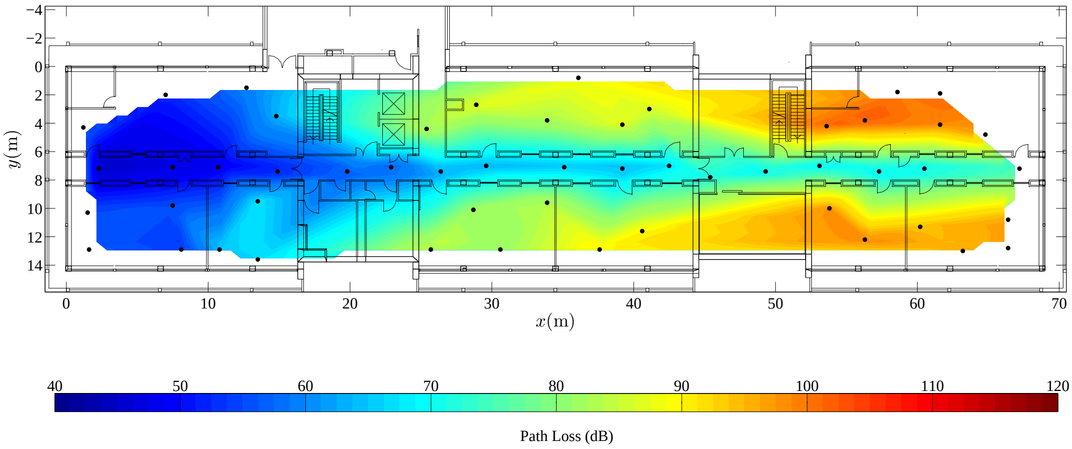

(a) Tx 3A.

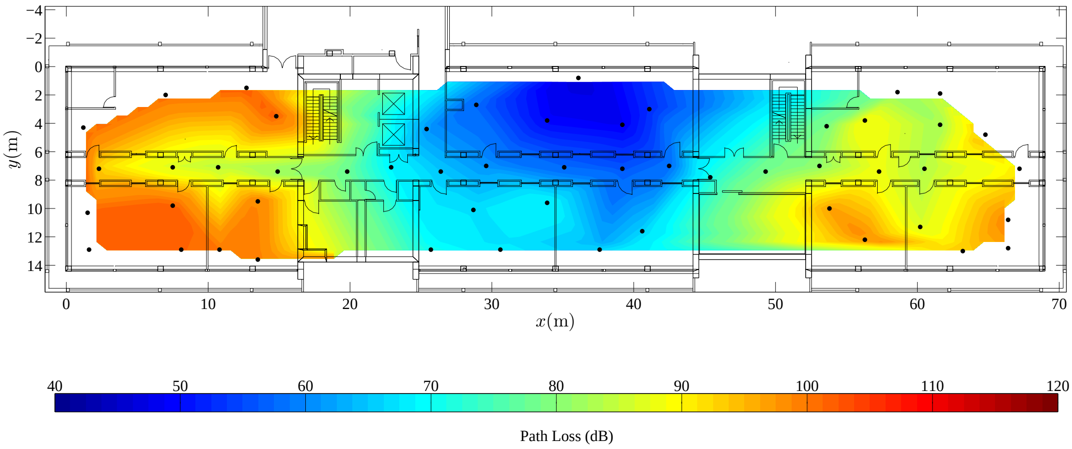

(b) Tx 3B.

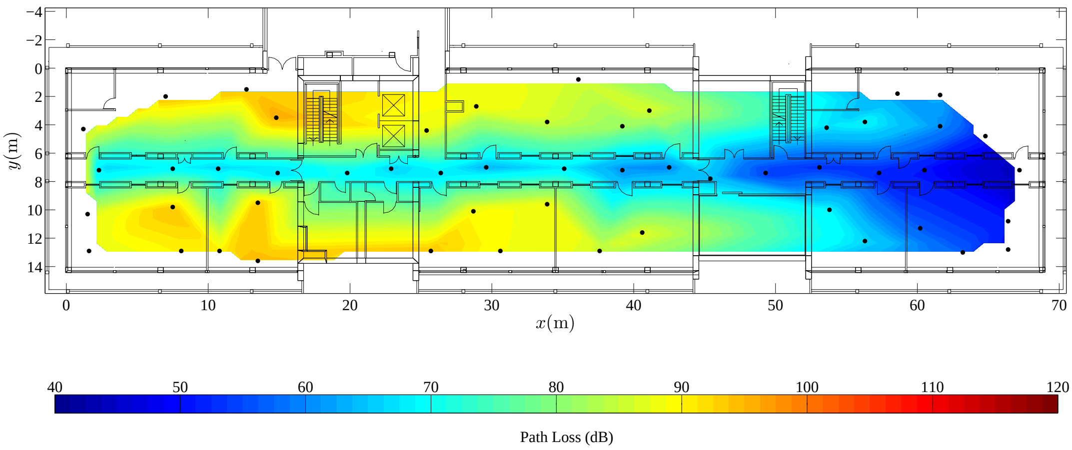

(c) Tx 3C.

Figure G.3: Base stations located on the second floor of the Science Building.

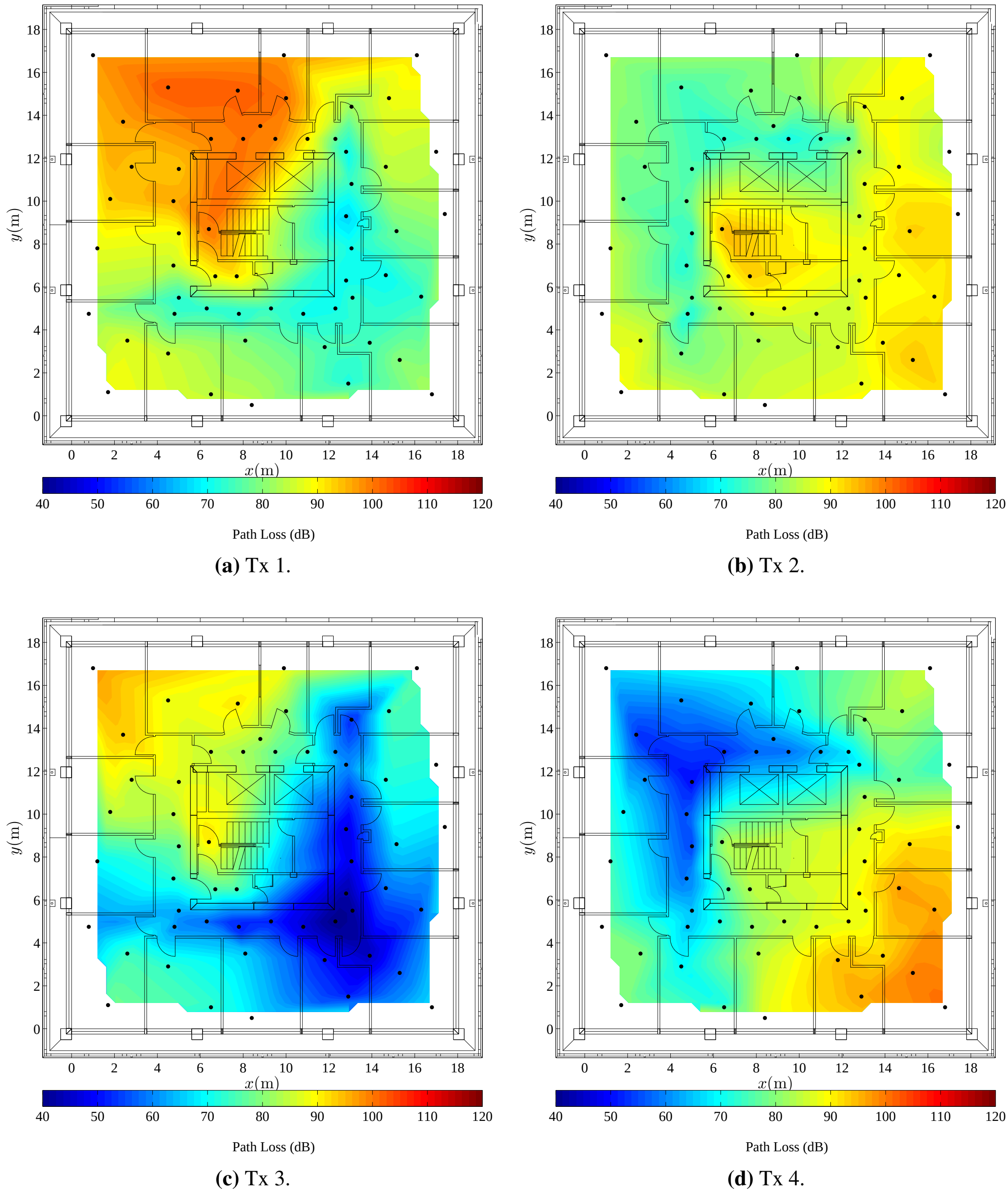

(a) Tx 1.

(b) Tx 2.

(c) Tx 3.

(d) Tx 4.

Figure G.4: Base stations located on levels 5 and 6 (Rx locations on this floor) of the Engineering Tower.

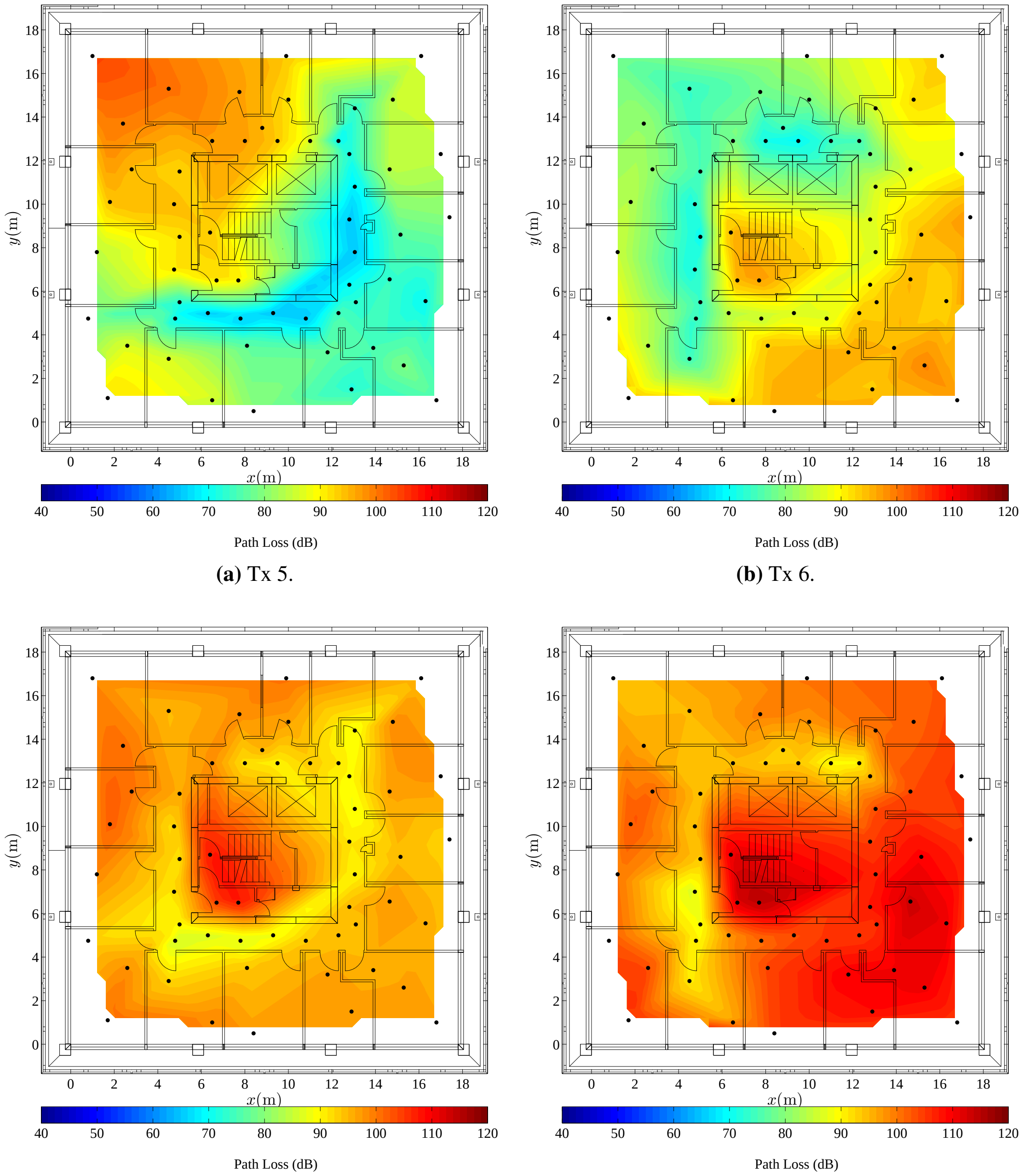

(a) Tx 5.

(b) Tx 6.

(c) Tx 7.

(d) Tx 8.

Figure G.5: Base stations located on levels 7 and 8 of the Engineering Tower.

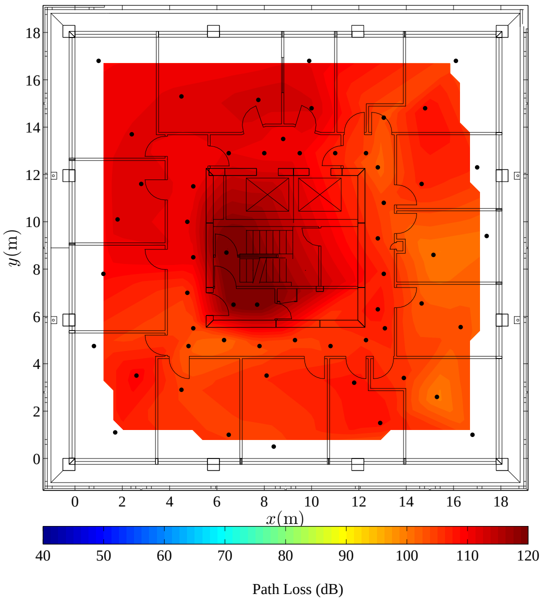

(a) Tx 9.

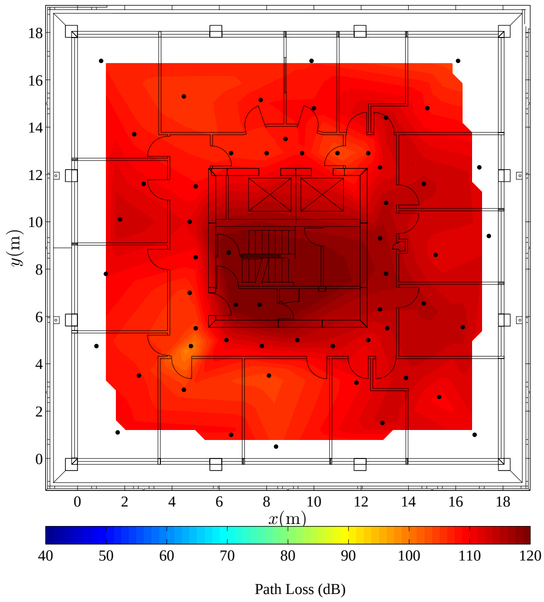

(b) Tx 10.

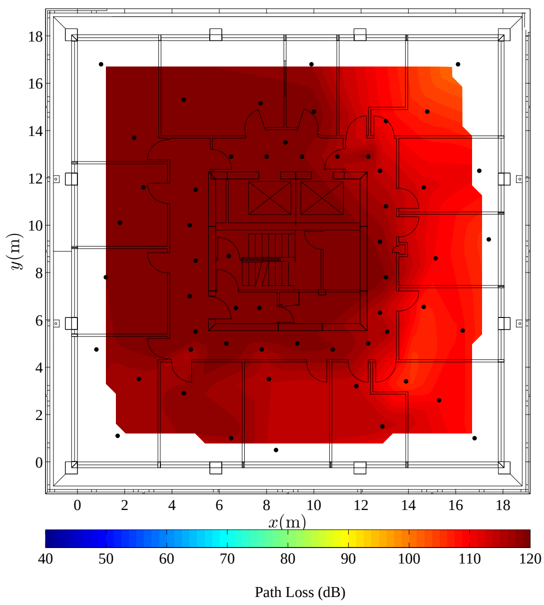

(c) Tx 11.

Figure G.6: Base station located on levels 9 and 10 of the Engineering Tower.

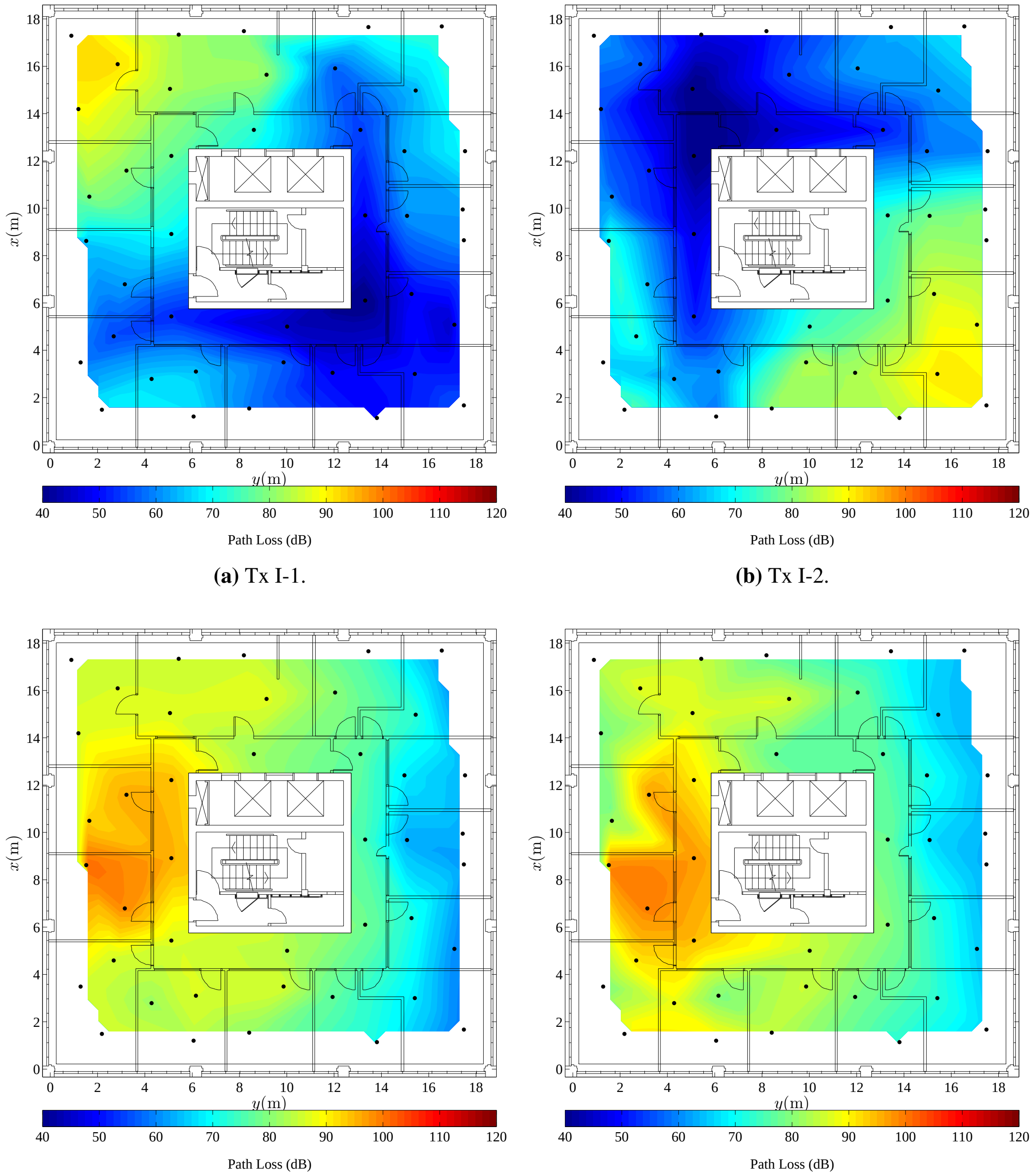

(a) Tx I-1.

(b) Tx I-2.

(c) Tx O-1.

(d) Tx O-2.

Figure G.7: Path loss values for the eighth floor of the Engineering Tower. Wong's measurements [15].

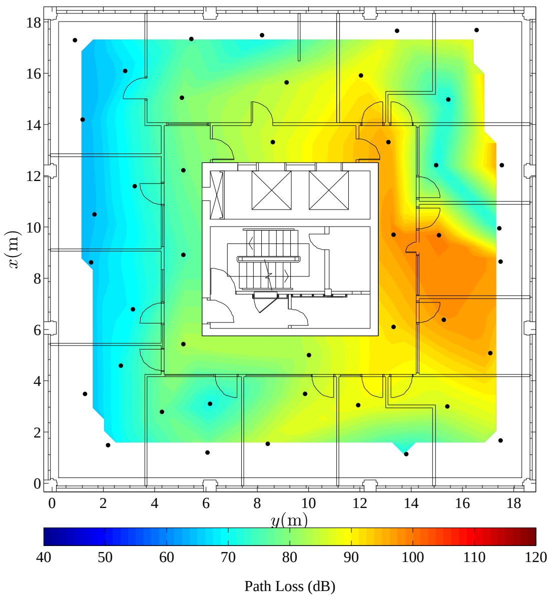

(a) Tx O-3.

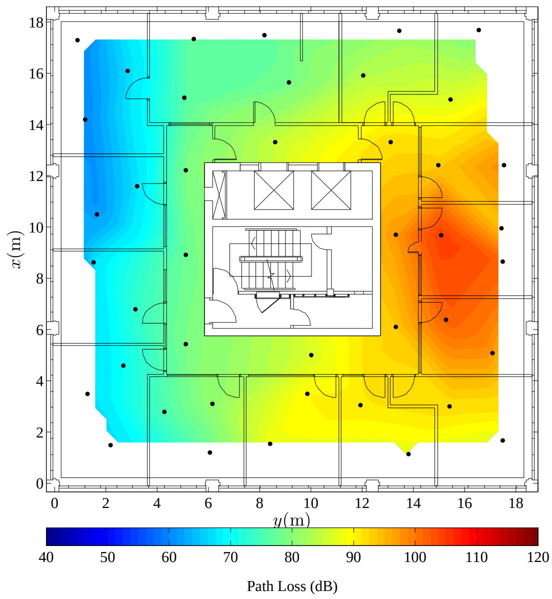

(b) Tx O-4.

Figure G.8: Path loss values for the eighth floor of the Engineering Tower. Wong's measurements [15]. Continued.

Appendix H

Additional Error Rate Performance Results for Test Environments A & B

Bit error rate performances for test environments A and B as a function of different desired QAM level, M, are shown in Figs. H.1–H.7.

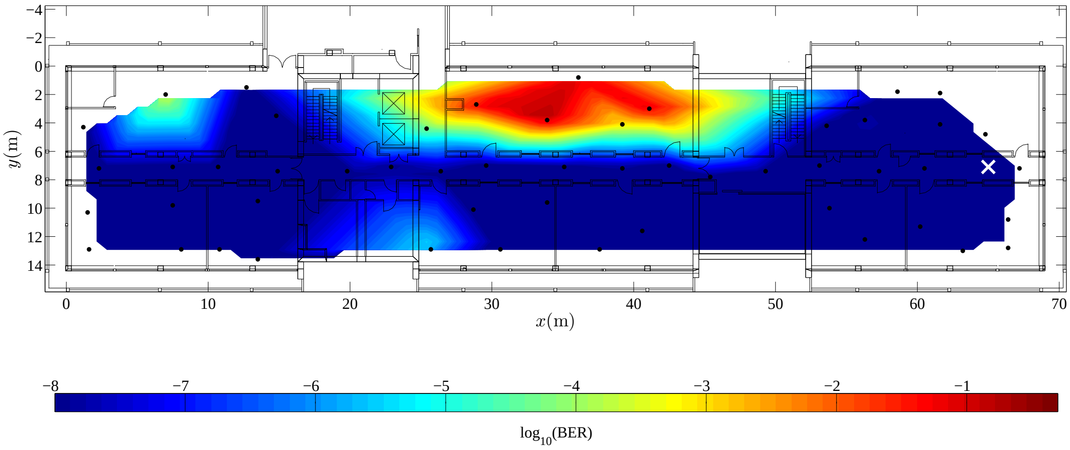

(a) $M = 2$.

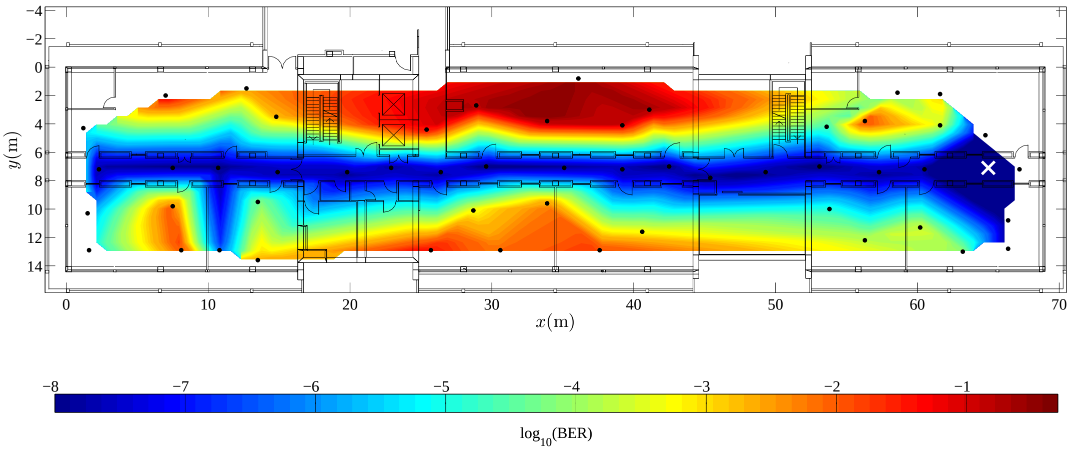

(b) $M = 16$.

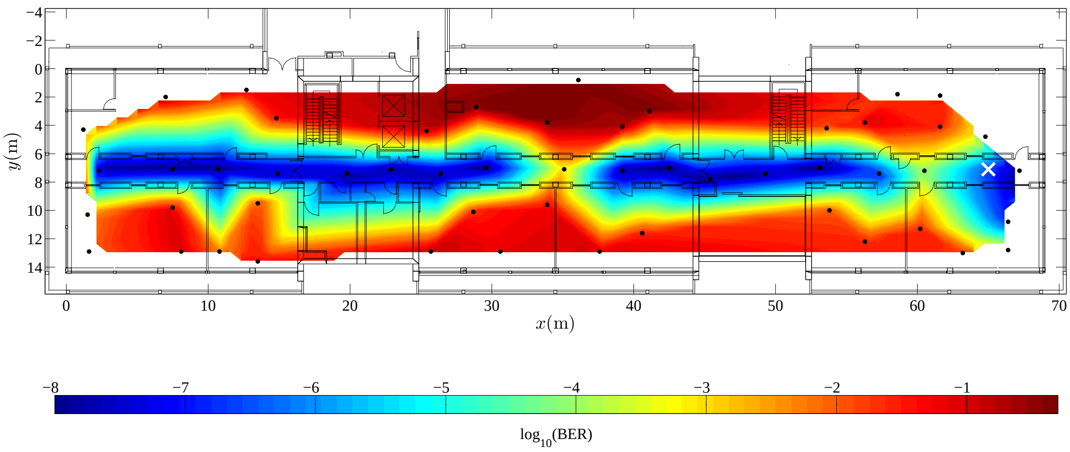

(c) $M = 64$.

Figure H.1: Contour map of $\log_{10}(\text{BER})$ for scenario TEA-I. $\mathbf{Z} = [4,4]$. Location of desired BS is indicated by a white $\times$.

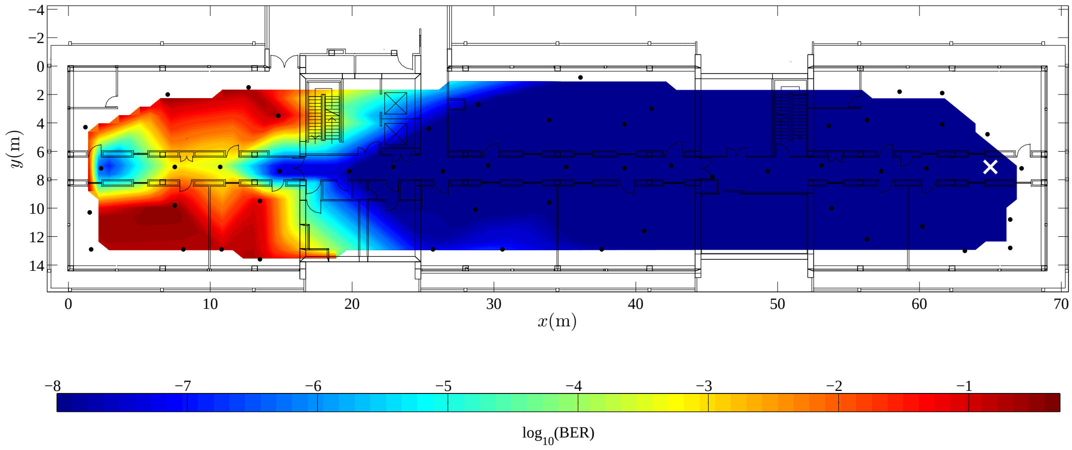

(a) $M = 2$.

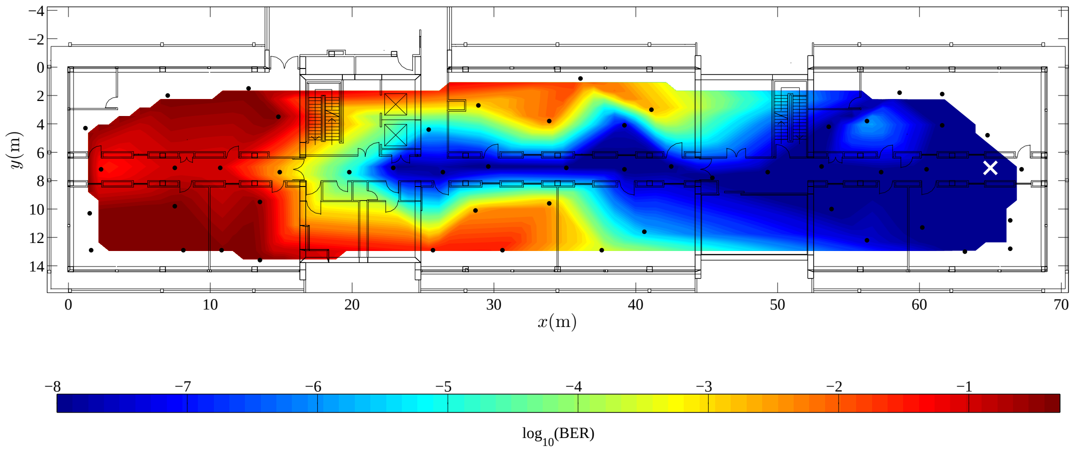

(b) $M = 16$.

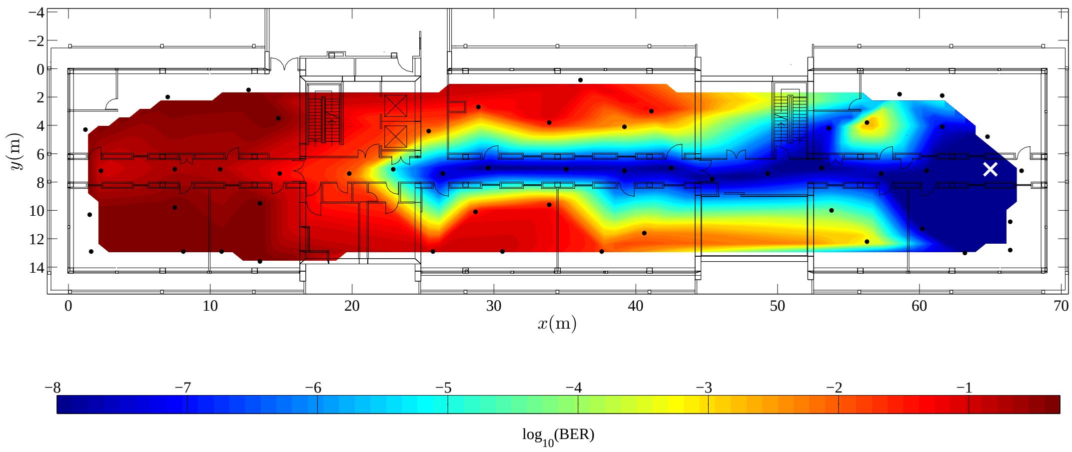

(c) $M = 64$.

Figure H.2: Contour map of $\log_{10}(\text{BER})$ for scenario TEA-II. $\mathbf{Z} = [4{,}4]$. Location of desired BS is indicated by a white $\times$.

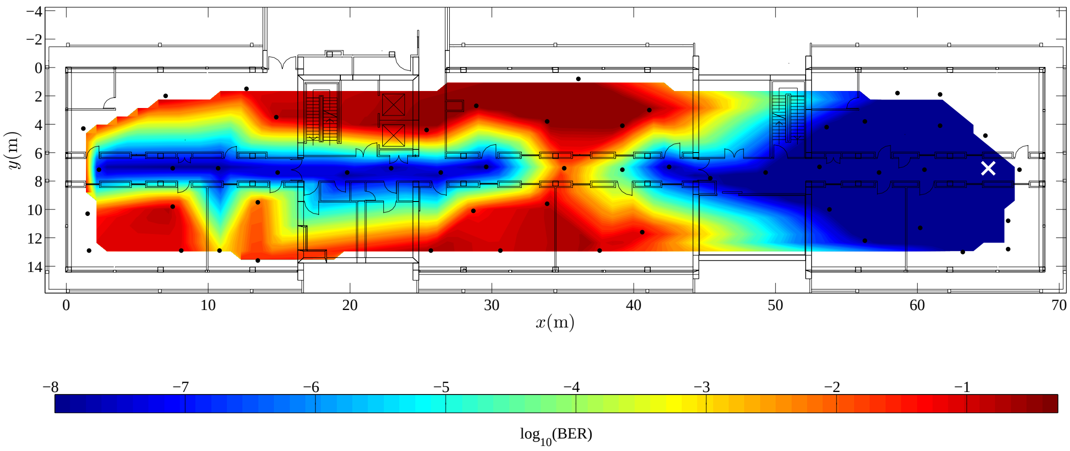

(a) $M = 2$.

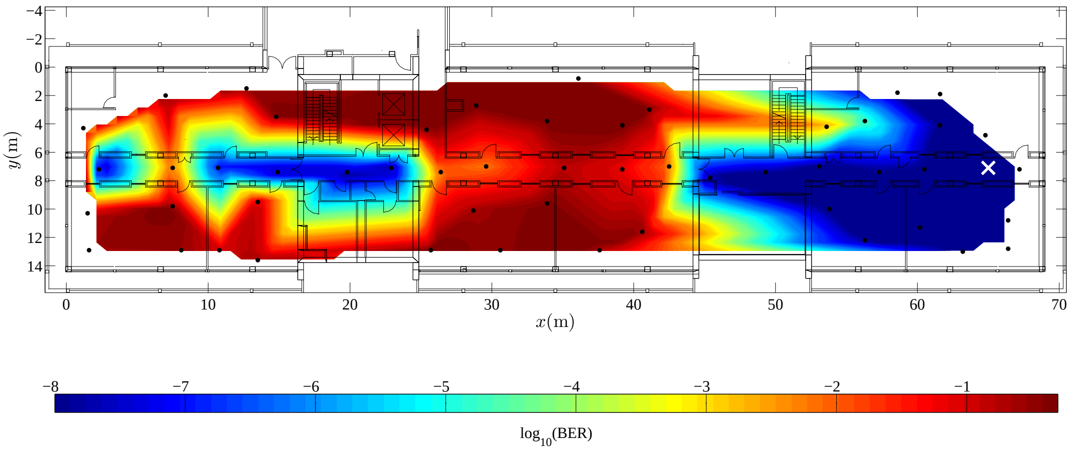

(b) $M = 16$.

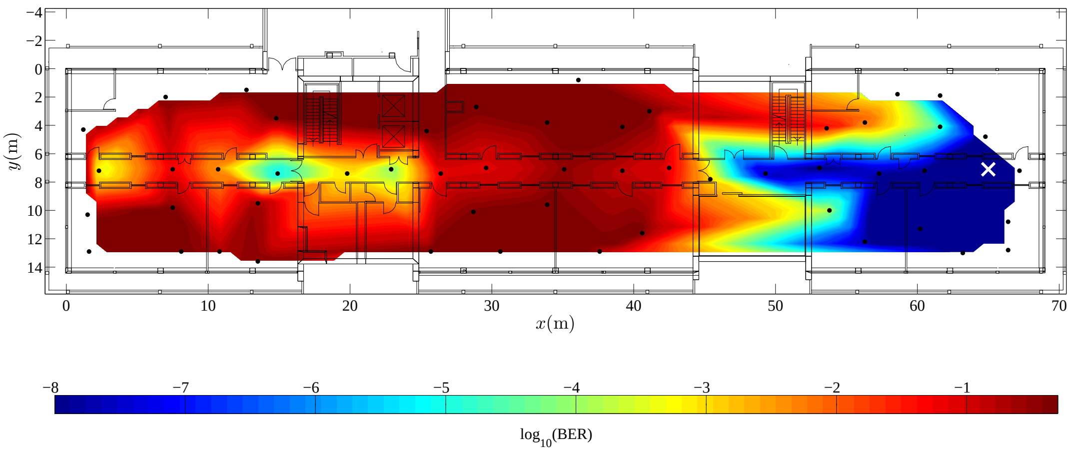

(c) $M = 64$.

Figure H.3: Contour map of $\log_{10}(\text{BER})$ for scenario TEA-III. $\mathbf{Z} = [4,4]$. Location of desired BS is indicated by a white $\times$.

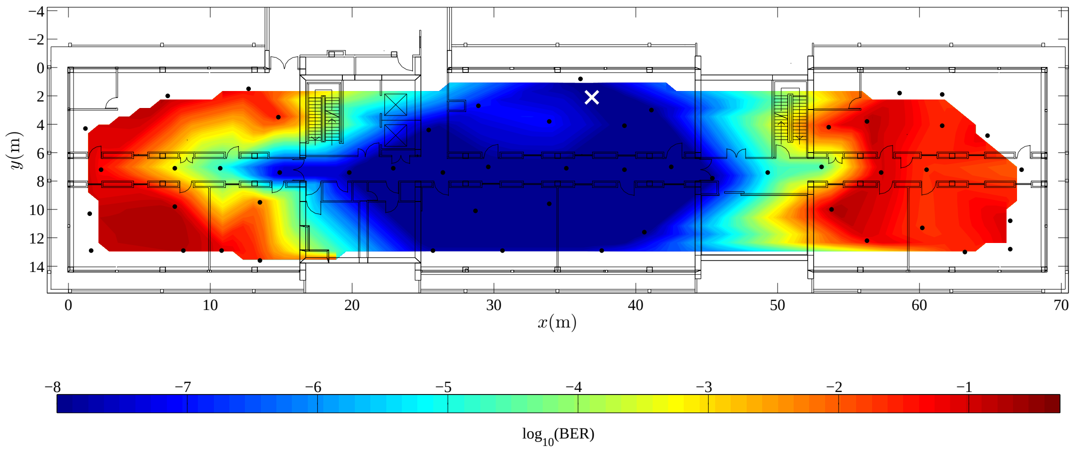

(a) $M = 2$.

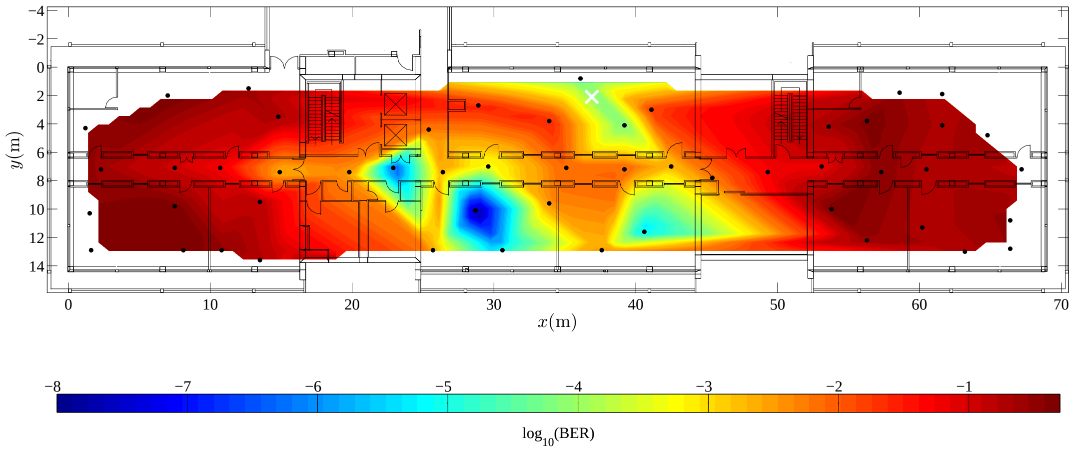

(b) $M = 16$.

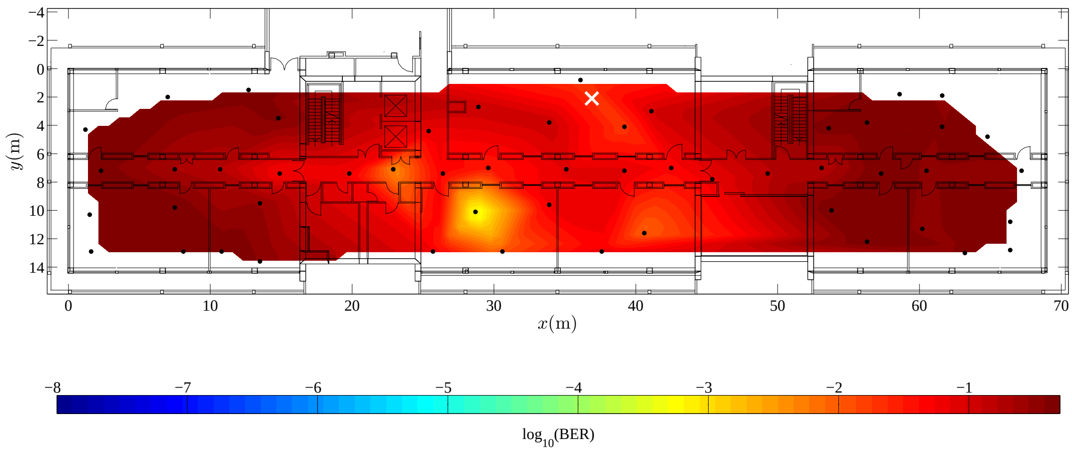

(c) $M = 64$.

Figure H.4: Contour map of $\log_{10}$ (BER) for scenario TEA-IV. $\mathbf{Z} = [4{,}4]$. Location of desired BS is indicated by a white $\times$.

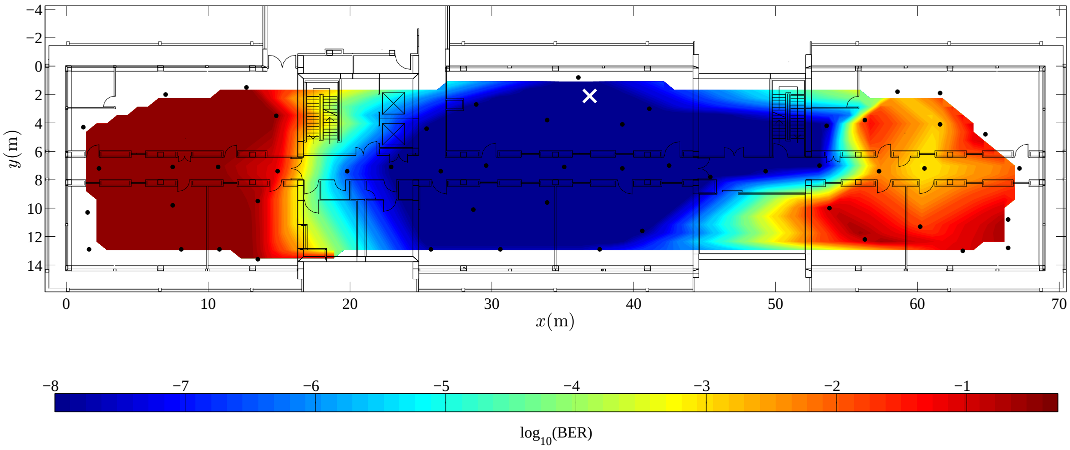

(a) $M = 2$.

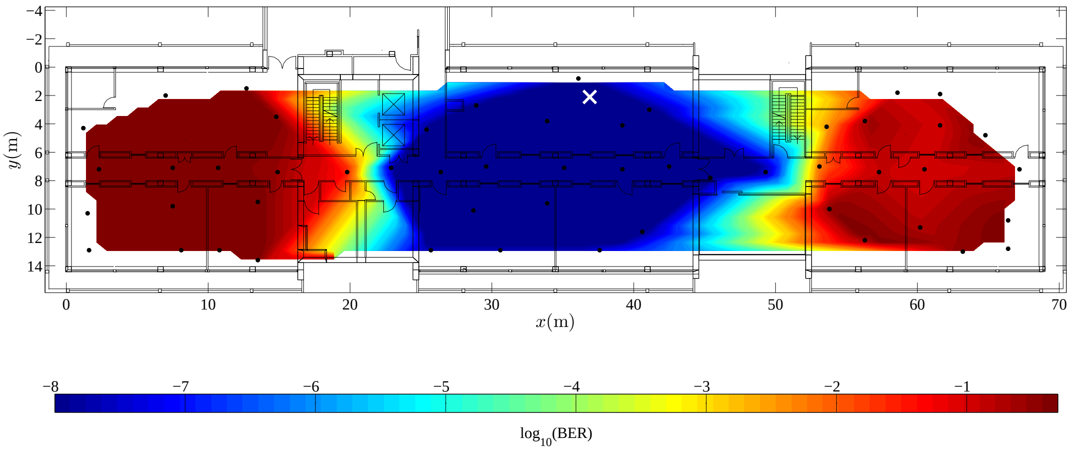

(b) $M = 16$.

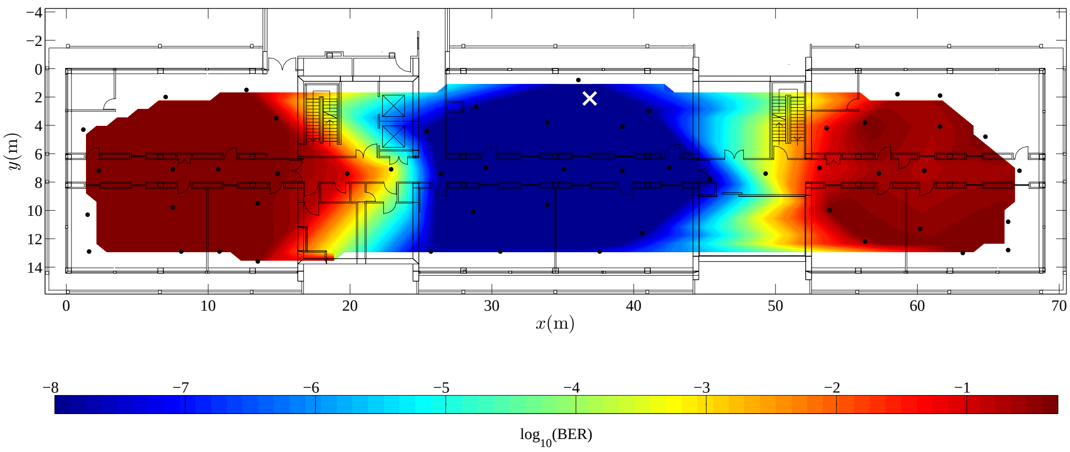

(c) $M = 64$.

Figure H.5: Contour map of $\log_{10}(\text{BER})$ for scenario TEA-V. $\mathbf{Z} = [4{,}4]$. Location of desired BS is indicated by a white $\times$.

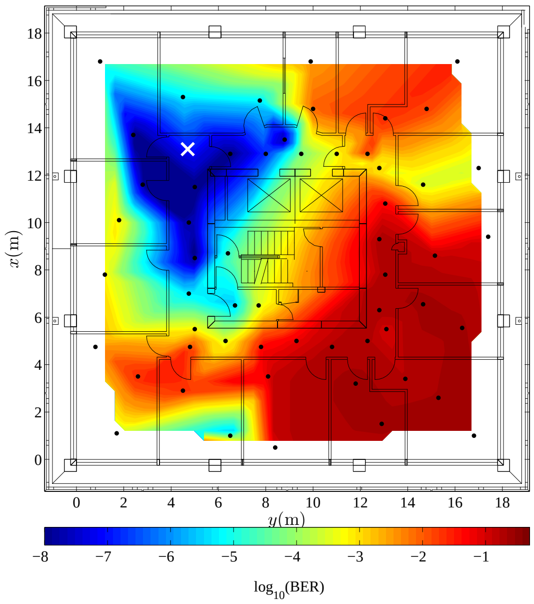

(a) $M = 2$.

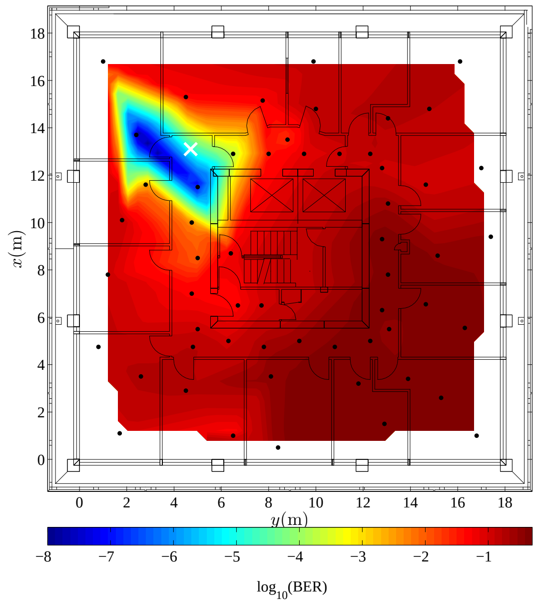

(b) $M = 16$.

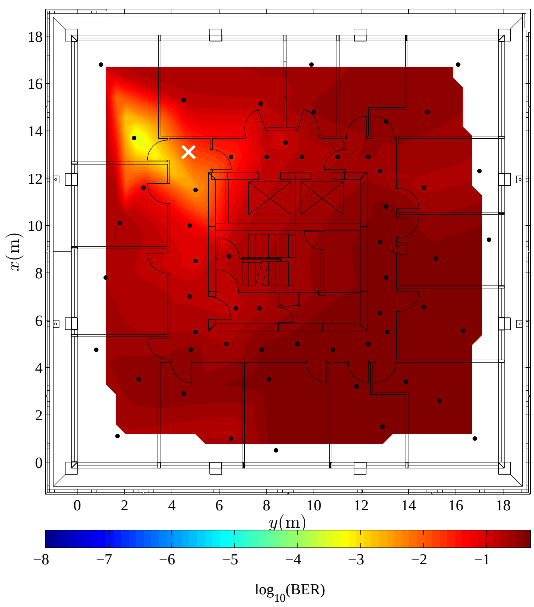

(c) $M = 64$.

Figure H.6: Contour map of $\log_{10}(\mathrm{BER})$ for scenario TEB-I. $Z_i = 4\,\forall i$. Location of desired BS is indicated by a white $\times$.

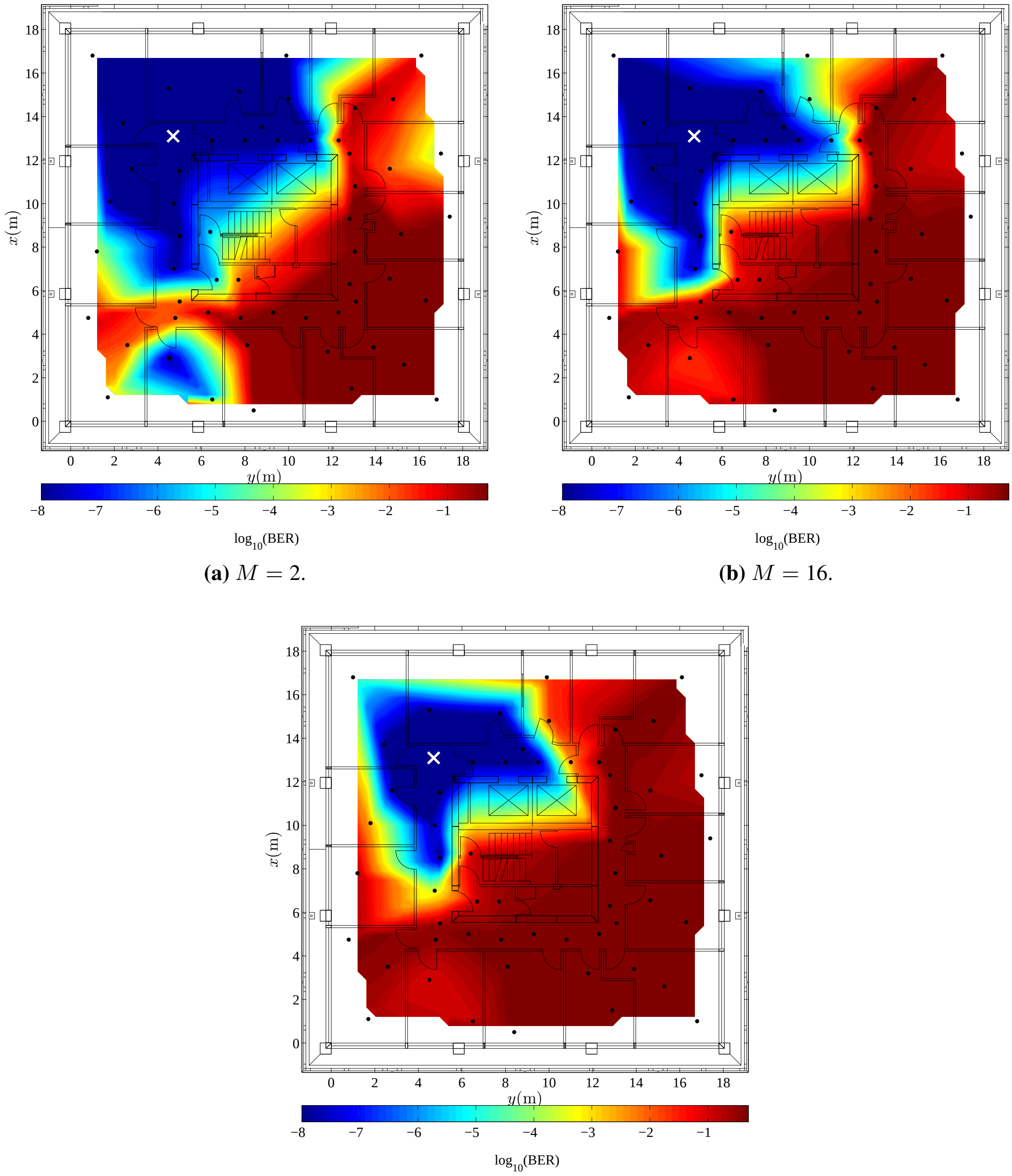

(a) $M = 2$.

(b) $M = 16$.

(c) $M = 64$.

Figure H.7: Contour map of $\log_{10}(\text{BER})$ for scenario TEB-II. $Z_i = 4\,\forall i$. Location of desired BS is indicated by a white $\times$.

References

[1] D. E. Noble, "The history of land-mobile radio communications," *Proceedings of the IRE*, vol. 50, no. 5, pp. 1405–1414, 1962.

[2] J. S. Smith and D. E. Noble, "The history of land-mobile radio communications," *Proc. IEEE*, vol. 51, no. 1, 1963.

[3] V. H. McDonald, "The cellular concept," *Bell Syst. Tech. J.*, vol. 58, no. 1, pp. 15–43, January 1979.

[4] W. R. Young, "Advanced mobile phone services: Introduction, background, and objectives," *Bell Syst. Tech. J.*, vol. 58, no. 1, pp. 1–14, January 1979.

[5] T. S. Rappaport, *Wireless Communications: Principles and Practice*, 2nd ed. Upper Saddle River, NJ: Prentice-Hall, 2002.

[6] S. C. Yang, *OFDMA System Analysis and Design*, ser. mobile communications. Norwood, MA: Artech House, 2010.

[7] 3GPP Group, "LTE." [Online]. Available: http://www.3gpp.org/LTE

[8] IEEE Std 802.16-2004, "Part 16: Air interface for fixed broadband wireless access systems," 2004.

[9] A. F. Molisch, *Wireless Communications*. Chichester, West Sussex, UK: Wiley, 2011.

[10] J. D. Parsons, *The Mobile Radio Propagation Channel*, 2nd ed. Chichester: Wiley, 2000.

[11] S. Haykin, *Communication Systems*, 4th ed. Hoboken, NJ: John Wiley & Sons, Ltd, 2001.

[12] D. V. Sarwate and M. B. Pursley, "Crosscorrelation properties of pseudorandom and related sequences," *Proc. IEEE*, vol. 68, no. 5, pp. 593–619, 1980.

[13] ——, "Correction to "crosscorrelation properties of pseudorandom and related sequences"," *Proc. IEEE*, vol. 68, no. 12, 1980.

[14] K. S. Butterworth, "Performance, Planning and Deployment of DS-CDMA In-Building Wireless Communication Systems," Ph.D. dissertation, The University of Auckland, Auckland, New Zealand, 2000.

[15] A. H. C. Wong, "Antenna Selection and Deployment Strategies for Indoor Wireless Communication Systems," Ph.D. dissertation, The University of Auckland, Auckland, New Zealand, 2005.

[16] D. C. K. Lee, "Indoor Wireless Communication System Performance Enhancement via Environmental Modification," Ph.D. dissertation, The University of Auckland, Auckland, New Zealand, 2007.

[17] A. V. Pais, "The Deployment and Performance of Indoor/Outdoor DS-CDMA Systems with Multiuser Detection," Ph.D. dissertation, The University of Auckland, Auckland, New Zealand, 2007.

[18] A. Goldsmith, *Wireless Communications*. New York: Cambridge University Press, 2005.

[19] S. Pietrzyk, *OFDMA for Broadband Wireless Access*, ser. mobile communications. Norwood, MA: Artech House, 2006.

[20] L. W. Couch, *Digital and Analog Communication Systems*, 7th ed. Upper Saddle River, NJ 07458: Prentice-Hall, 2007.

[21] IEEE Std 802.11a-1999, "Part 11: Wireless LAN medium access control (MAC) and physical layer (PHY) specifications — high speed physical layer in the 5 GHz band," 1999.

[22] IEEE Std 802.11b-1999, "Part 11: Wireless LAN medium access control (MAC) and physical layer (PHY) specifications — Higher-Speed Physical Layer Extension in the 2.4 GHz Band," 1999.

[23] IEEE Std 802.11g-2003, "Part 11: Wireless LAN medium access control (MAC) and physical layer (PHY) specifications — further higher data rate extension in the 2.4 GHz band," 2003.

[24] IEEE Std 802.11n-2009, "Part 11: Wireless LAN Medium Access Control (MAC) and Physical Layer (PHY) Specifications," 2009.

[25] ETSI TS 102 563, "Digital audio broadcasting (DAB); transport of advanced audio coding (AAC) audio," *European Broadcasting Union*, vol. 1.1.1, February 2007.

[26] ETSI EN 302 755, "Digital video broadcasting (DVB); frame structure channel coding and modulation for a second generation digital terrestrial television broadcasting system (DVB-T2)," *European Standard (Telecommunications series)*, vol. 1.1.1, September 2009.

[27] IEEE Std 802.15.1-2002, "Part 15.1: Wireless medium access control (MAC) and physical layer (PHY) specifications for wireless personal area networks (WPANs)," 2002.

[28] J. Zyren, "Overview of the 3GPP Long Term Evolution physical layer," Freescale Semiconductor, White Paper 3GPPEVOLUTIONWP, July 2007.

[29] P. Bello, "Selectrive fading limitations of the KATHRYN modem and some system design considerations," *IEEE Trans. Commun. Technol.*, vol. 13, no. 3, pp. 320–333, 1965.

[30] ——, "Corrections: Error probabilities due to atmospheric noise and flat fading in hf ionospheric communication systems; some techniques for the instantaneous real-time measurement of multipath and doppler spread; selective fading limitations of the KATHRYN modem and some design considerations," *IEEE Trans. Commun. Technol.*, vol. 14, no. 1, 1966.

[31] M. Zimmerman and A. Kirsch, "The AN/GSC-10 (KATHRYN) variable rate data modem for HF radio," *IEEE Trans. Commun. Technol.*, vol. 15, no. 2, pp. 197 –204, 1967.

[32] R. W. Chang, "Synthesis of band-limited orthogonal signals for multichannel data transmission," *Bell Syst. Tech. J*, pp. 1775–1796, December 1966.

[33] R. W. Chang and R. Gibby, "A theoretical study of performance of an orthogonal multiplexing data transmission scheme," *IEEE Trans. Commun. Technol.*, vol. 16, no. 4, pp. 529 –540, 1968.

[34] B. Saltzberg, "Performance of an efficient parallel data transmission system," *IEEE Trans. Commun. Technol.*, vol. 15, no. 6, pp. 805 –811, 1967.

[35] R. W. Chang, "Orthogonal frequency division multiplexing," U.S. Patent 3,488,445, January 6, 1970.

[36] S. Weinstein and P. Ebert, "Data transmission by frequency-division multiplexing using the discrete Fourier transform," *IEEE Trans. Commun. Technol.*, vol. 19, no. 5, pp. 628 –634, 1971.

[37] B. Hirosaki, "An Orthogonally Multiplexed QAM System Using the Discrete Fourier Transform," *IEEE Trans. Commun.*, vol. 29, no. 7, pp. 982 – 989, Jul. 1981.

[38] B. Hirosaki, S. Hasegawa, and A. Sabato, "Advanced Groupband Data Modem Using Orthogonally Multiplexed QAM Technique," *IEEE Trans. Commun.*, vol. 34, no. 6, pp. 587 – 592, Jun. 1986.

[39] F. Xiong, *Digital Modulation Techniques*, 2nd ed. Norwood, MA: Artech House, 2006.

[40] U.-K. Kwon, D. Kim, and G.-H. Im, "Amplitude clipping and iterative reconstruction of MIMO-OFDM signals with optimum equalization," *IEEE Trans. Wireless Commun.*, vol. 8, no. 1, pp. 268–277, 2009.

[41] X. H. Wu, A. A. Kishk, and A. W. Glisson, "MIMO-OFDM radar for direction estimation," *IET Radar, Sonar & Navigation*, vol. 4, no. 1, pp. 28–36, 2010.

[42] M. Mohammadnia-Avval, C. Snow, and L. Lampe, "Error-rate analysis for bit-loaded coded MIMO-OFDM," *IEEE Trans. Veh. Technol.*, vol. 59, no. 5, pp. 2340–2351, 2010.

[43] P.-L. Chiu, L.-Z. Huang, L.-W. Chai, and Y.-H. Huang, "Interpolation-based QR decomposition and channel estimation processor for MIMO-OFDM system," *IEEE Trans. Circuits Syst. I*, vol. 58, no. 5, pp. 1129–1141, 2011.

[44] W.-Q. Wang, "Space–time coding MIMO-OFDM SAR for high-resolution imaging," *IEEE Trans. Geosci. Remote Sens.*, vol. 49, no. 8, pp. 3094–3104, 2011.

[45] A. J. Coulson, "Bit error rate performance of OFDM in narrowband interference with excision filtering," *IEEE Trans. Wireless Commun.*, vol. 5, no. 9, pp. 2484–2492, September 2006.

[46] S.-G. Huang and C.-H. Hwang, "Improvement of active interference cancellation: avoidance technique for OFDM cognitive radio," *IEEE Trans. Wireless Commun.*, vol. 8, no. 12, pp. 5928–5937, 2009.

[47] C. Snow, L. Lampe, and R. Schober, "Impact of WiMAX interference on MB-OFDM UWB systems: analysis and mitigation," *IEEE Trans. Commun.*, vol. 57, no. 9, pp. 2818 –2827, 2009.

[48] O. El Ayach, S. W. Peters, and R. W. Heath, "The feasibility of interference alignment over measured MIMO-OFDM channels," *IEEE Trans. Veh. Technol.*, vol. 59, no. 9, pp. 4309–4321, 2010.

[49] A. J. Coulson, "Wideband interference in pilot symbol assisted OFDM systems," in *Proc. Australian Communications Theory Workshop (AusCTW)*, 2010, pp. 1–6.

[50] D. Qu, Z. Wang, and T. Jiang, "Extended active interference cancellation for sidelobe suppression in cognitive radio OFDM systems with cyclic prefix," *IEEE Trans. Veh. Technol.*, vol. 59, no. 4, pp. 1689–1695, 2010.

[51] P. Torio and M. G. Sanchez, "Intrasymbol interference in OFDM," *IEEE Trans. Consum. Electron.*, vol. 56, no. 2, pp. 447–449, 2010.

[52] J. Zhang and J. Meng, "Robust narrowband interference rejection for power-line communication systems using IS-OFDM," *IEEE Trans. Power Del.*, vol. 25, no. 2, pp. 680–692, 2010.

[53] J.-L. Yu and Y.-C. Lin, "Space–time-coded MIMO ZP-OFDM systems: Semiblind channel estimation and equalization," *IEEE Trans. Circuits Syst. I*, vol. 56, no. 7, pp. 1360–1372, 2009.

[54] D. N. Liu and M. P. Fitz, “Iterative map equalization and decoding in wireless mobile coded OFDM,” *IEEE Trans. Commun.*, vol. 57, no. 7, pp. 2042–2051, 2009.

[55] B. Wu, Y. Shang, and H. Xiang, “Combined equalisation and code assignment for expanded time-frequency OFDM system,” *Electronics Letters*, vol. 46, no. 7, pp. 534–536, 2010.

[56] N. Prasad, L. Venturino, and X. Wang, “Diversity-multiplexing tradeoff analysis for OFDM systems with subcarrier grouping, linear precoding, and linear detection,” *IEEE Trans. Inf. Theory*, vol. 56, no. 12, pp. 6078–6096, 2010.

[57] P. Cheng, M. Tao, Y. Xiao, and W. Zhang, “V-OFDM: On performance limits over multi-path rayleigh fading channels,” *IEEE Trans. Commun.*, vol. 59, no. 7, pp. 1878–1892, 2011.

[58] E. Panayirci, H. Dogan, and H. V. Poor, “Low-complexity MAP-based successive data detection for coded OFDM systems over highly mobile wireless channels,” *IEEE Trans. Veh. Technol.*, vol. 60, no. 6, pp. 2849–2857, 2011.

[59] A. B. Awoseyila, C. Kasparis, and B. G. Evans, “Robust time-domain timing and frequency synchronization for OFDM systems,” *IEEE Trans. Consum. Electron.*, vol. 55, no. 2, pp. 391–399, 2009.

[60] J. Chen, M. Li, and Y. Kuo, “Adaptive OFDM synchronization algorithm in frequency selective fading channels,” *IEEE Trans. Consum. Electron.*, vol. 55, no. 4, pp. 1841–1846, 2009.

[61] A. Filippi and S. Serbetli, “OFDM symbol synchronization using frequency domain pilots in time domain,” *IEEE Trans. Wireless Commun.*, vol. 8, no. 6, pp. 3240–3248, 2009.

[62] E. C. Kim, J. Yang, and J. Y. Kim, “Novel OFDM frame synchronization and frequency offset compensation scheme for wireless multimedia communication systems,” *IEEE Trans. Consum. Electron.*, vol. 55, no. 3, pp. 1141–1148, 2009.

[63] T.-C. Wei, W.-C. Liu, C.-Y. Tseng, and S.-J. Jou, “Low complexity synchronization design of an OFDM receiver for DVB-T/H,” *IEEE Trans. Consum. Electron.*, vol. 55, no. 2, pp. 408–413, 2009.

[64] X. Q. Jin and J. M. Tang, “Optical OFDM synchronization with symbol timing offset and sampling clock offset compensation in real-time IMDD systems,” *IEEE Photonics Journal*, vol. 3, no. 2, pp. 187–196, 2011.

[65] C. Snow, L. Lampe, and R. Schober, “Error rate analysis for coded multicarrier systems over quasi-static fading channels,” *IEEE Trans. Commun.*, vol. 55, no. 9, pp. 1736–1746, 2007.

[66] M. Chiani and A. Giorgetti, “Coexistence Between UWB and Narrow-Band Wireless Communication Systems,” *Proc. IEEE*, vol. 97, no. 2, pp. 231–254, Feb. 2009.

[67] C. Eduardo, R. Alberto, F. Detlef, and F. Joaquim, “On the evaluation of MB-OFDM UWB interference effects on a WiMAX receiver,” *EURASIP Journal on Wireless Communications and Networking*, vol. 2010, 2010.

[68] M.-C. L. Lee, “Performance of OFDM in In-Building Wireless Communication Environments,” Master’s thesis, The University of Auckland, Auckland, New Zealand, 2001.

[69] I. Kalet, “The multitone channel,” *IEEE Trans. Commun.*, vol. 37, no. 2, pp. 119–124, 1989.

[70] A. Czylwik, “Adaptive OFDM for wideband radio channels,” in *Proc. IEEE Global Communications Conf. GLOBECOM*, vol. 1, 1996, pp. 713–718.

[71] T. Keller and L. Hanzo, “Adaptive multicarrier modulation: a convenient framework for time-frequency processing in wireless communications,” *Proc. IEEE*, vol. 88, no. 5, pp. 611–640, 2000.

[72] ——, "Prolog to adaptive multicarrier modulation: a convenient framework for time-frequency processing in wireless communications," *Proc. IEEE*, vol. 88, no. 5, pp. 609–610, 2000.

[73] L. Hanzo, M. Munster, B. J. Choi, and T. Keller, *OFDM and MC-CDMA for Broadband Multi-User Communications, WLANs and Broadcasting*. Chichester, West Sussex, England: John Wiley & Sons, Ltd, 2003.

[74] G. Cariolaro and F. Vagliani, "An OFDM scheme with a half complexity," *IEEE J. Sel. Areas Commun.*, vol. 13, no. 9, pp. 1586 –1599, Dec. 1995.

[75] K. Chang, I. Bahl, and V. Nair, *RF and Microwave Circuit Component Design for Wireless Systems*. New York: Wiley, 2002.

[76] N. Blaunstein and J. B. Anderson, *Multipath Phenomena in Cellular Networks*, ser. mobile communications. Norwood, MA: Artech House, 2002.

[77] M. Speth, S. Fechtel, G. Fock, and H. Meyr, "Optimum receiver design for wireless broad-band systems using OFDM—Part I," *IEEE Trans. Commun.*, vol. 47, no. 11, pp. 1668 –1677, Nov. 1999.

[78] J. Heiskala and J. Terry, *OFDM Wireless LANs: A Theoretical and Practical Guide*. Indianapolis, Indiana, USA: Sams Publishing, 2002.

[79] P. Toutier, R. Monnier, and P. Lopez, "Multicarrier modem for HDTV terrestrial broadcasting," *Signal Processing: Image Communication*, vol. 5, no. 5–6, pp. 379–403, December 1993.

[80] F. Daffara and O. Adami, "A new frequency detector for orthogonal multicarrier transmission techniques," in *Proc. IEEE 45th Vehicular Technology Conf*, vol. 2, 1995, pp. 804–809.

[81] J.-J. van de Beek, M. Sandell, M. Isaksson, and P. Ola Borjesson, "Low-complex frame synchronization in OFDM systems," in *Proc. Fourth IEEE Int Universal Personal Communications. 1995. Record. Conf*, 1995, pp. 982–986.

[82] M. Sandell, J.-J. van de Beek, and P. Borjesson, "Timing and frequency synchronization in OFDM systems using cyclic prefix," in *Proc. Int. Symp. Synchronization, Saalbau, Essen, Germany*, December 14-15 1995, pp. 16–19.

[83] J.-J. van de Beek, M. Sandell, and P. Borjesson, "ML estimation of time and frequency offset in OFDM systems," *IEEE Trans. Signal Process.*, vol. 45, no. 7, pp. 1800 –1805, Jul 1997.

[84] N. Lashkarian and S. Kiaei, "Class of cyclic-based estimators for frequency-offset estimation of OFDM systems," *IEEE Trans. Commun.*, vol. 48, no. 12, pp. 2139–2149, 2000.

[85] W. D. Warner and C. Leung, "OFDM/FM frame synchronization for mobile radio data communications," *IEEE Trans. Veh. Technol.*, vol. 42, no. 3, pp. 302–313, 1993.

[86] F. Classen and H. Meyr, "Frequency synchronization algorithms for OFDM systems suitable for communication over frequency selective fading channels," in *Proc. IEEE 44th Vehicular Technology Conf*, 1994, pp. 1655–1659.

[87] T. M. Schmidl and D. C. Cox, "Robust frequency and timing synchronization for OFDM," *IEEE Trans. Commun.*, vol. 45, no. 12, pp. 1613–1621, Dec. 1997.

[88] U. Lambrette, M. Speth, and H. Meyr, "OFDM burst frequency synchronization by single carrier training data," *IEEE Commun. Lett.*, vol. 1, no. 2, pp. 46–48, 1997.

[89] S. H. Muller-Weinfurtner, "On the optimality of metrics for coarse frame synchronization in OFDM: a comparison," in *Proc. Ninth IEEE Int. Personal, Indoor and Mobile Radio Communications Symp.*, vol. 2, 1998, pp. 533–537.

[90] F. Tufvesson, O. Edfors, and M. Faulkner, "Time and frequency synchronization for OFDM using PN-sequence preambles," in *Proc. 50th IEEE Vehicular Technology Conf.*, vol. 4, 1999, pp. 2203–2207.

[91] E. Sourour and G. E. Bottomley, "Effect of frequency offset on DS-SS acquisition in slowly fading channels," in *Proc. IEEE Wireless Communications and Networking Conf.*, 1999, pp. 569–573.

[92] M. Morelli and U. Mengali, "An improved frequency offset estimator for OFDM applications," *IEEE Commun. Lett.*, vol. 3, no. 3, pp. 75–77, 1999.

[93] ——, "Carrier-frequency estimation for transmissions over selective channels," *IEEE Trans. Commun.*, vol. 48, no. 9, pp. 1580–1589, 2000.

[94] H. Minn, M. Zeng, and V. K. Bhargava, "On timing offset estimation for OFDM systems," *IEEE Commun. Lett.*, vol. 4, no. 7, pp. 242–244, 2000.

[95] A. J. Coulson, "Maximum likelihood synchronization for OFDM using a pilot symbol: analysis," *IEEE J. Sel. Areas Commun.*, vol. 19, no. 12, pp. 2495–2503, Dec 2001.

[96] ——, "Maximum likelihood synchronization for OFDM using a pilot symbol: algorithms," *IEEE J. Sel. Areas Commun.*, vol. 19, no. 12, pp. 2486–2494, Dec. 2001.

[97] T. Keller, L. Piazzo, P. Mandarini, and L. Hanzo, "Orthogonal frequency division multiplex synchronization techniques for frequency-selective fading channels," *IEEE J. Sel. Areas Commun.*, vol. 19, no. 6, pp. 999–1008, 2001.

[98] J. Li, G. Liu, and G. B. Giannakis, "Carrier frequency offset estimation for OFDM-based WLANs," *IEEE Signal Process. Lett.*, vol. 8, no. 3, pp. 80–82, 2001.

[99] K. Shi and E. Serpedin, "Coarse frame and carrier synchronization of OFDM systems: a new metric and comparison," *IEEE Trans. Wireless Commun.*, vol. 3, no. 4, pp. 1271–1284, 2004.

[100] R. H. Clarke, "A Statistical Theory of Mobile-Radio Reception," *Bell Syst. Tech. J.*, vol. 47, pp. 957–1000, July 1968.

[101] D. C. Cox, "Multipath delay spread and path loss correlation for 910-MHz urban mobile radio propagation," *IEEE Trans. Veh. Technol.*, vol. 26, no. 4, pp. 340–344, Nov 1977.

[102] K. W. Sowerby, "Outage Probability in Mobile Radio Systems," Ph.D. dissertation, Department of Electrical and Electronic Engineering, The University of Auckland, Auckland, New Zealand, May 1989.

[103] H. Suzuki, "A Statistical Model for Urban Radio Propogation," *IEEE Trans. Commun.*, vol. 25, no. 7, pp. 673–680, 1977.

[104] K. Yee, "Numerical solution of initial boundary value problems involving Maxwell's equations in isotropic media," *IEEE Trans. Antennas Propag.*, vol. 14, no. 3, pp. 302–307, 1966.

[105] A. Taflove and S. C. Hagness, *Computational Electrodynamics: The Finite-Difference Time-Domain Method*, 3rd ed. Boston: Artech House, 2005.

[106] A. C. M. Austin, "Interference modelling for indoor wireless systems using the Finite-Difference Time-Domain method," Ph.D. dissertation, Department of Electrical and Computer Engineering, The University of Auckland, Auckland, New Zealand, June 2011.

[107] M. J. Neve, K. W. Sowerby, A. G. Williamson, G. B. Rowe, J. C. Batchelor, and E. A. Parker, "Physical layer engineering for indoor wireless systems in the twenty-first century," in *Proc. Loughborough Ant. Prop. Conf. (LAPC)*, 2010, pp. 72–78.

[108] Y. H. Yang, "Wireless Propagation in Aged Care Facilities," Master's thesis, The University of Auckland, Auckland, New Zealand, 2010.

[109] J. Lu, K. B. Letaief, J. C. I. Chuang, and M. L. Liou, "M-PSK and M-QAM BER computation using signal-space concepts," *IEEE Trans. Commun.*, vol. 47, no. 2, pp. 181–184, Feb. 1999.

[110] M. Abramowitz and I. A. Stegun, *Handbook of Mathematical Functions*, 9th ed. New York: Dover Publications, Inc., 1972.

[111] L. B. Milstein and P. Das, "An analysis of a real-time transform domain filtering digital communication system–part I: narrow-band interference rejection," *IEEE Trans. Commun.*, vol. 28, no. 6, pp. 816–824, 1980.

[112] E. Masry and L. Milstein, "Performance of DS spread-spectrum receiver employing interference-suppression filters under a worst-case jamming condition," *IEEE Trans. Commun.*, vol. 34, no. 1, pp. 13–21, 1986.

[113] J. Morrow, R. K. and J. S. Lehnert, "Bit-to-bit error dependence in slotted DS/SSMA packet systems with random signature sequences," *IEEE Trans. Commun.*, vol. 37, no. 10, pp. 1052–1061, 1989.

[114] L. B. Milstein, T. S. Rappaport, and R. Barghouti, "Performance evaluation for cellular CDMA," *IEEE J. Sel. Areas Commun.*, vol. 10, no. 4, pp. 680–689, May 1992.

[115] K. G. Filis and S. C. Gupta, "Overlay of cellular CDMA on FSM," *IEEE Trans. Veh. Technol.*, vol. 43, no. 1, pp. 86–98, 1994.

[116] S. D. Sandberg, "Adapted demodulation for spread-spectrum receivers which employ transform-domain interference excision," *IEEE Trans. Commun.*, vol. 43, no. 9, pp. 2502–2510, 1995.

[117] J. Wang and L. B. Milstein, "Interference suppression for CDMA overlay of a narrowband waveform," *Electronics Letters*, vol. 31, no. 24, pp. 2074–2075, 1995.

[118] L. B. Milstein, "Interference rejection techniques in spread spectrum communications," *Proc. IEEE*, vol. 76, no. 6, pp. 657–671, 1988.

[119] P. J. Marshall, "The coexistence of DS-CDMA mobile radio systems and fixed services," Ph.D. dissertation, Department of Electrical and Electronic Engineering, The University of Auckland, Auckland, New Zealand, September 1997.

[120] J. Park, C. Kang, and D. Hong, "Effect of Bluetooth interference on OFDM systems," *Electronics Letters*, vol. 40, no. 23, pp. 1496–1498, 11 Nov. 2004.

[121] M. D. Springer, *The Algebra of Random Variables*. New York: Wiley, 1979.

[122] R. E. Ziemer, W. H. Tranter, and D. R. Fannin, *Signals & Systems: Continuous and Discrete*, 4th ed. Upper Saddle River, NJ: Prentice-Hall, 1998.

[123] A. Papoulis and S. U. Pillai, *Probability, Random Variables and Stochastic Processes*, 4th ed. New York: McGraw-Hill, 2002.

[124] R. D. Yates and D. J. Goodman, *Probability and Stochastic Processes: A Friendly Introduction For Electrical and Computer Engineers*. New York: Wiley, 1999.

[125] S. Namik, K. W. Sowerby, and M. J. Neve, "Are DS-CDMA indoor system deployments appropriate for OFDM networks?" in *2012 Australian Communications Theory Workshop (AusCTW) (AusCTW'12)*, Wellington, New Zealand, Jan. 2012, pp. 72–77.

[126] K. S. Butterworth, K. W. Sowerby, and A. G. Williamson, "Base station placement for in-building mobile communication systems to yield high capacity and efficiency," *IEEE Trans. Commun.*, vol. 48, no. 4, pp. 658–669, 2000.

[127] S. Tirró, Ed., *Satellite Communication Systems Design*. Springer, June 1993.

[128] R. Pickholtz, L. Milstein, and D. Schilling, "Spread spectrum for mobile communications," *IEEE Trans. Veh. Technol.*, vol. 40, no. 2, pp. 313–322, May 1991.

[129] Y. S. Cho, J. Kim, W. Y. Yang, and C. G. Kang, *MIMO-OFDM Wireless Communications with MATLAB*. Singapore: Wiley, 2010.

[130] H. G. Myung, J. Lim, and D. J. Goodman, "Single carrier FDMA for uplink wireless transmission," *IEEE Veh. Technol. Mag.*, vol. 1, no. 3, pp. 30–38, 2006.

[131] S. Haykin and B. V. Veen, *Signals and Systems*, 2nd ed. Hoboken, NJ: John Wiley & Sons, Ltd, 2003.